
METAL-ORGANIC FRAMEWORKS: DEFECTS, SPECTROSCOPY AND CATALYSIS

ISBN: 978-90-9033046-4

Printed by Ridderprint | www.ridderprint.nl
Ridderprint B.V., Ohmweg 31, Alblasserdam 2952 BD, Nederland

Cover Art by Thomas Hartman Illustrated Science – THIS B.V. -

METAL-ORGANIC

FRAMEWORKS: DEFECTS,

SPECTROSCOPY AND

CATALYSIS

Metaal-Organische Structuren: Defecten, Spectroscopie en Katalyse
(met een samenvatting in het Nederlands)

Proefschrift

*ter verkrijging van de graad van doctor aan de Universiteit Utrecht
op gezag van de rector magnificus, Prof. dr. H. R. B. M. Kummeling, ingevolge het
besluit van het college voor promoties in het openbaar te verdedigen
op woensdag 29 april 2020
door
Miguel Rivera-Torrente
geboren op 24 november 1991 te Madrid, Spanje*

Promotor: Prof. Dr. ir. B. M. Weckhuysen

This PhD thesis was accomplished with financial support from the European Union's Horizon 2020 research and innovation programme under the Marie Skłodowska-Curie grant agreement No. 641887 (project acronym: DEFNET) and the Netherlands Center for Multiscale Catalytic Energy Conversion (MCEC).

*Dedicada a mi familia,
Miguel Rivera Torrente*

"The scientist is motivated primarily by curiosity and a desire for truth." "History proves abundantly that pure science, undertaken without regard to applications to human needs, is usually ultimately of direct benefit to mankind." — Irving Langmuir

"Yo soy yo y mi circunstancia, y si no la salvo a ella no me salvo yo." (Meditaciones del Quijote, 1914) — José Ortega y Gasset

TABLE OF CONTENTS

Chapter 1

General Introduction and Fundamental Concepts in the Chemistry of Metal-Organic Frameworks for Catalysis

Chapter 2

Advanced Spectroscopy and Structural Characterization of MIL-100 and HKUST-1 Metal-Organic Framework Materials

PART A. Lattice Disorder in Metal-Organic Framework-Supported Metal Catalysts: Origins and Effects

Chapter 3

Pd Nanoparticles Supported on MIL-100(Fe) and BASOLITE® F300 Metal-Organic Frameworks

PART B. Generation of Defects in Metal-Organic Frameworks for Catalysis: Spectroscopy and Characterization

Chapter 4

Defect Sites in Zeotypic Cr Metal-Organic Frameworks: Ethylene Polymerization and *In-situ* Spectroscopy

PART C. Micro-Spectroscopy Studies of Defect-Engineered and Functional [Cu₃(BTC)₂] and Guest@[Cu₃(BTC)₂] Materials

Chapter 5

Advanced Micro-Spectroscopy Studies of Defect-Engineered [Cu₃(BTC)_{2-x}(CYDC)_x] Materials

Chapter 6

HKUST-1 Metal-Organic Framework Crystals Loaded with Tetracyanoquinodimethane: Effects of Water on Host-Guest Chemistry and Electro-Conductivity

Chapter 7

Summary, Concluding Remarks and Perspectives

Nederlandse Samenvatting

Acknowledgements

Appendix A. List of Publications and Presentations at Conferences

Appendix B. List of Abbreviations

About the Author

Chapter 1

General Introduction and Fundamental Concepts in the Chemistry of Metal-Organic Frameworks for Catalysis

In this Chapter, the general concepts by which coordination chemistry, catalysis, defects in crystalline compounds and spectroscopy are governed will be presented as a brief introduction for the research presented in this PhD thesis. Metal-Organic Frameworks (MOFs), given the fact that they are a subclass of Coordination Polymers (CPs), have been developed from compounds interesting at the fundamental level, to functional porous solids that have the potential of becoming industrially relevant materials. They may be used in a manifold of applications, including gas storage, drug delivery, electroconductive materials or catalysis. Performance in such applications may be further tailored by the introduction of defects, redox-sites or guest molecules that alter their physicochemical properties. However, these approaches may be victims of their own success, being necessary to find a compromise between stability (as MOFs are coordination compounds, with relatively low bond enthalpies); and boosting the mentioned functional properties.

PREFACE

Metal-Organic Frameworks (MOFs) have become an increasingly important class of porous materials over the last 20 years, showing potential in a whole array of fields, such as gas storage and separation, drug delivery and biomedicine, sensing or electronic applications.¹ The distinction between the terms “metal-organic framework” and “coordination polymer” has been the subject of much debate.²⁻⁵ According to the International Union for Pure and Applied Chemistry (IUPAC) recommendations published in 2013,⁶ and the Commission on MOFs of the International Zeolite Association (IZA),^{7,8} a MOF, “...is a *Coordination Network (CN)* with organic ligands containing potential voids.” Complementarily, a Coordination Network is “...a coordination entity is an ion or neutral molecule that is composed of a central atom, usually that of a metal, to which is attached a surrounding array of atoms or groups of atoms, each of which is called a ligand”, thus, clarifying the fact that MOFs are subclass of Coordination Polymer Compounds (CPCs). If porosity is a property of a coordination polymer, one can then talk about Porous Coordination Polymers (PCPs), a term that now corresponds to the same definition of MOF. We can then conclude that the abbreviations MOF and PCP can be used indistinctively and interchangeable for these materials, although the former has been traditionally used by solid-state scientists and crystallographers, and the latter, by coordination and synthetic (organic and inorganic) chemists.

In this PhD thesis, the term “Metal-Organic Framework” and the abbreviation “MOF” will be consistently used, as it is widely employed in the literature closely related to porous material characterization and heterogeneous catalysis. Moreover, despite the IUPAC and the IZA recommendations to use topological descriptors or molecular formulas, we will refer to the investigated structures by their abbreviations: MIL, for Matériaux de l’Institut Lavoisier; and HKUST, for Hong-Kong University of Science and Technology; due to the familiarity of the community with such materials (*e.g.* MIL-100, MIL-101 and HKUST-1), and the existence of abundant reports on their structure.

GENERAL INTRODUCTION

1.1. FUNDAMENTAL CONCEPTS

The research described in this PhD thesis focuses on Metal-Organic Framework (MOF) materials, and the implications of their structural point defects and lattice disorder in catalysis as demonstrated by various spectroscopic and microscopic techniques. In order to provide the reader with a basis set, we will describe several fundamental concepts (*e.g.* coordination compounds, crystal lattices, catalysis or spectroscopy) in the following subsections.

1.1.1 Coordination Chemistry

A coordination compound consists of a metal atom (acceptor) with which ligand atoms or molecules (donors) interact *via* coordination bonds, generally $2e^-$, 2 or 3 centre bonds in which the donor provides an electron pair, *i.e.* Lewis acid-metal base adducts, making them dipolar bonds.⁹ If the ligand provides more than one pair, it is called a polydentate ligand. Coordination bonds are typically in the orders of $100\text{-}200\text{ kJ}\cdot\text{mol}^{-1}$ (depending on many factors, such as the type of ligand as well as the type of metal and its oxidation state), being the interaction between *s* and *p* orbitals with the *d* orbitals of metals the most important ones, and may exhibit configurational isomerism or exchange reactions. In order to provide a reference point, in silicon oxide (SiO_2), *i.e.* silica or porous aluminosilicates such as zeolites, Si-O bonds have a formation enthalpy at standard conditions of $452\text{ kJ}\cdot\text{mol}^{-1}$, more than twice the one of common coordination bonds. A way of predicting the stability of transition metal complexes is the $18e^-$ rule, by which complexes showing a closed shell configuration are more stable. To explain some of their properties, the Crystal Field Theory (CFT), and the more complex Ligand Field Theory (LFT) and Molecular Orbital Theory (MOT), which included bond covalency into their models and that were introduced for those cases in which CFT fails, have provided a quantum chemical explanation of electronic transitions. Important to highlight for the content of this PhD thesis are the electronic transitions for *d*-metals complexes (Figure 1.1). Naturally, the *d*-orbitals of a metal cation are degenerate (at the same energy level).

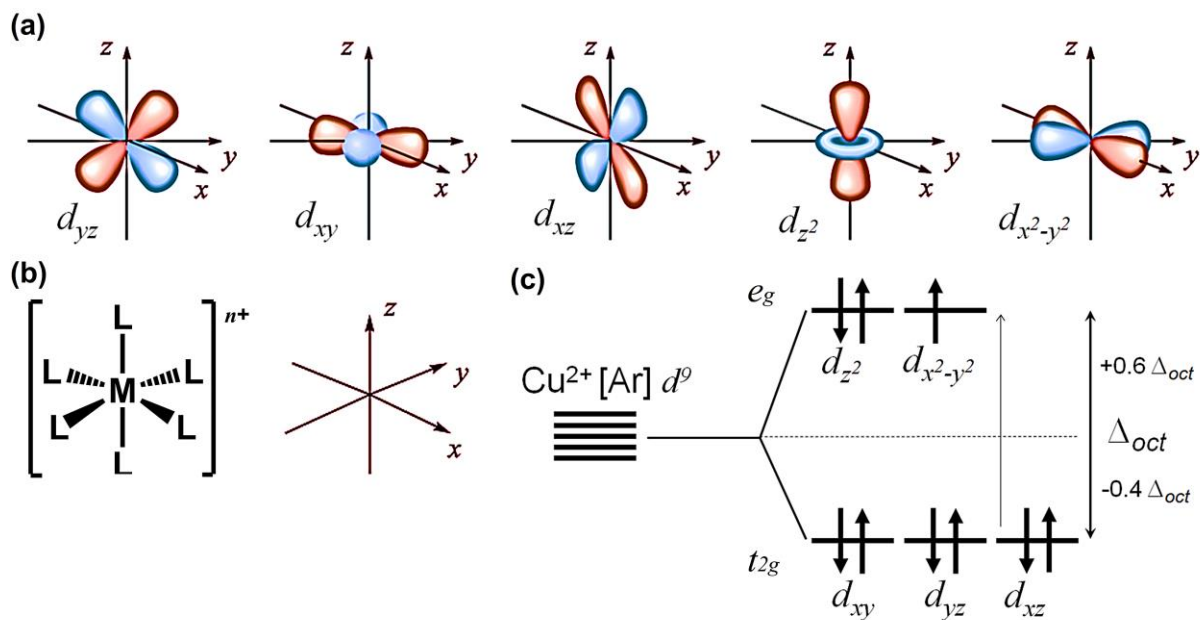


Figure 1.1. (a) Geometry of the d -orbitals in a transition metal and their spatial orientation on an arbitrary x,y,z axis. (b) General scheme of an octahedral coordination complex with the metal atom (M) in the centre and the ligands (L) around. (c) Diagram of an octahedral Cu^{2+} complex ($[\text{Ar}]d^9$) showing the possible d - d transition from the t_{2g} to the e_g term, including the Ligand Field Splitting Energy (LFSE).

However, when the ligands (negative charges in the CFT) approach the metal, orbitals increase/decrease in energy to stabilize charges, as they are repelled by the surrounding electrons. Destabilization energies will depend on the geometry, oxidation state and ligands. Particularly relevant for this PhD thesis, is the octahedral geometry of d^9 metals, such as Cu^{2+} ; or d^5 , such as Cr^{3+} , given the fact that materials based on these metals are the subject of study. For octahedral geometry, the orbitals are stabilized in two terms (t_{2g} and e_g , a set of multiple orbitals each) as described in Figure 1.1c, with an energy difference Δ_{oct} or Δ_0 , the Crystal Field Splitting Energy (CFSE) or Ligand Field Splitting Energy (LFSE). The electronic configuration of Cu^{2+} is $[\text{Ar}]d^9$, and according to Hund's rules, the Aufbau and Pauli's exclusion principle, one orbital can accommodate one additional electron. If a certain energy equal or higher to the spin pairing energy is supplied, one electron is promoted from the lower to the higher energy level, giving rise to the so-called d - d transitions. The typical energy range for these transitions is 390-700 nm and is the reason for which many complexes exhibit colour. Orbital splitting is related to magnetic, optical and electronic properties as well of coordination compounds.¹⁰

Coordination theory was first established by Alfred Werner (1866-1919), among others, who obtained the Nobel Prize in 1913.¹¹ Since then, it has been developed as a field on its own, resulting in major fundamental and technological advances for chemistry and science. Metal coordination complexes are ubiquitous in catalysis, and have been the cornerstone for modern homogeneous catalysis.^{12, 13} A major example was the discovery of the chloridotris(triphenylphosphane)rhodium(I) $[\text{RhCl}(\text{PPh}_3)_3]$ compound, an extremely active catalyst for olefin hydrogenations, for which Sir Geoffrey Wilkinson (1921-1996) received the Nobel Prize in 1973. The development and study of coordination compounds for catalysis has, thus, become a major field of inorganic chemistry since then.

1.1.2 Coordination Polymers

Polydentate ligands have been identified above as those which can donate more than one electron pair to a metal centre. A single ligand molecule can be bonded to two or more metal atoms forming chains or networks of coordination complexes, *i.e.* coordination polymers. For instance, iron (II,III) hexacyanide $(\text{Fe}_4[\text{Fe}(\text{CN})_6]_3 \cdot x\text{H}_2\text{O})$, known since the early 18th century and probably the first example of a Coordination Polymer (CP) in history, has iron cations octahedrally coordinated to cyanide groups by either the C or the N atom depending on the crystallographic position.¹⁴

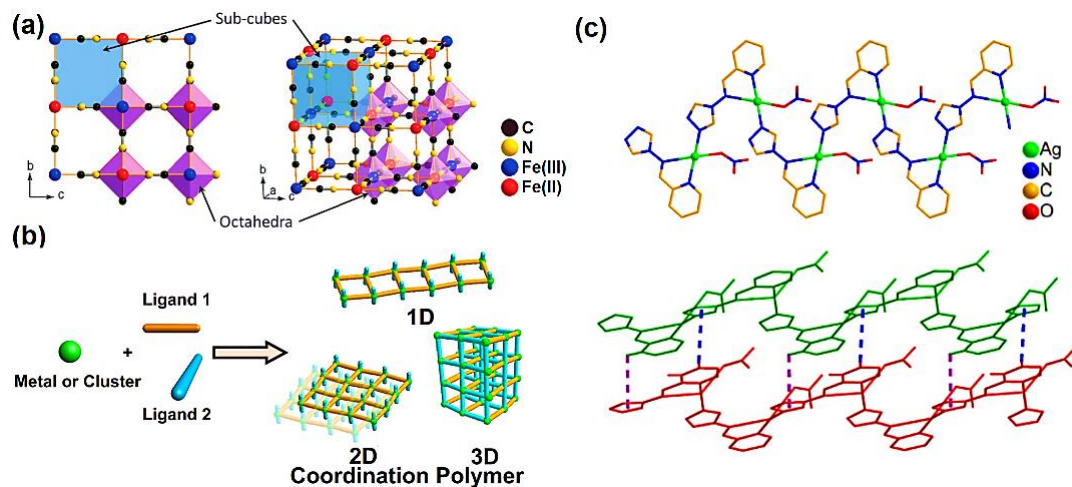


Figure 1.2. (a) Structure of $(\text{Fe}_4[\text{Fe}(\text{CN})_6]_3 \cdot x\text{H}_2\text{O}$ showing different types of octahedral iron and coordination modes of CN^- ligands. (b) Different dimensionalities of coordination polymers. (c) Example of a Coordination Polymer (CP) formed by 4-(pyridine-2-yl)methylene amino-1,2,4-triazole and Ag^+ ions. The chains stack into dense crystals due to $\pi-\pi$ interactions of the triazolyl aromatic rings.¹⁵

More complex organic moieties can be used to coordinate the metal centres and, depending on the components, CPCs can form 1-D, 2-D or 3-D structures. At the macroscale, they often appear as dense phases, stacked *via* van der Waals interactions or H-bonding (Figure 1.2b),¹⁶ forming robust (non-) crystalline lattices. Although they were already known in the past, the term “coordination polymer” did not appear until 1964.¹⁷ These compounds have been very much developed, starting from discrete molecules that could oligomerize; up to multi-linker and multi-metal, hierarchically structured, porous materials in which the cavities and properties can be tuned,¹⁸⁻²² as a subfield combining organic, coordination and solid-state chemistry.

1.1.3 Crystal Lattices and Defects

A crystal structure consists of an array of atoms, molecules or ions ordered in the 3-D space in a periodic manner forming a lattice and with certain symmetry operations that can be applied to the smallest repeating ensemble of components, the Unit Cell (UC).²³ The symmetry arrangements of the UCs are defined according to one of the 230 so-called, space groups reported for all existing crystalline solids. Solids formed under real conditions often contain defects, due to local differences in energy (T , P , ΔG or μ), that arise from non-ideal arrangements of the lattice caused by those very differences in chemical potentials and energy landscapes. Traditionally, crystallographic defects are divided into four categories (with a schematic representation of each shown in Figure 1.3):

Point defects: atoms displaced, added or removed from single lattice points (see Figure 3a for exemplary representations of some types): ion vacancy (A), interstitial impurity (B), displacement (C) or ion (D); surface edge (E) or kink (F).

Line: line and screw dislocations leading to surface terraces and edges.

Planar: stacking faults, grain or antiphase boundaries.

Bulk: voids, cracks and macropores on the structure, or precipitates that nucleate on a growing crystal.

Further details on a systematized classification and properties of defects in crystals and their solid-state chemistry can be found in the literature.^{9, 11, 24, 25} However, as the theory

of crystal lattices lays upon the bases of topological mathematics (a sub field of geometry and set theory), the definition of a defect is somewhat complex.²⁶ For the sake of simplicity, the word defect in this manuscript refers to deviations of the ideal structure obtained for a given topology by means of crystallographic analysis, corresponding to the seminal papers in which the structure or compound was reported.

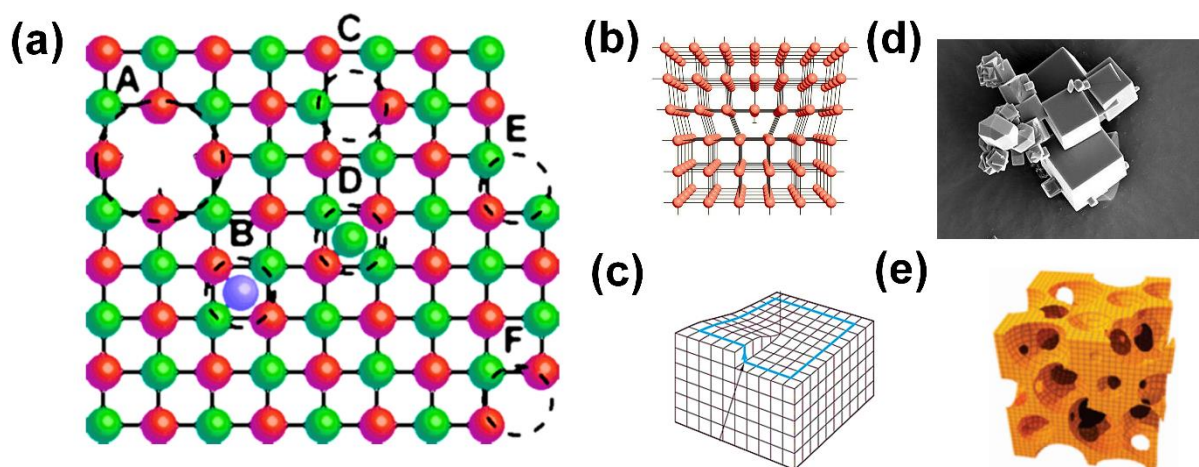


Figure 1.3. (a) Representation of a crystal lattice with different types of defects noted in the list above. Examples of different defects: line, (b) edge dislocation and (c) screw dislocation; and bulk, (d) intertwined crystals due to grain boundaries and (e) bulk microporous voids in a lattice.

For instance, HKUST-1(Cu) consists of 1,3,5-benzenetricarboxylate (BTC) ligands bonded to Cu²⁺ cations. Thus, defects may appear in the form of nanosized impurities, non-coordinated BTC molecules, reduced oxidation states (such as Cu⁺) or intercalated non-coordinating linkers. Analogously, heterogeneities in the crystallization process may lead to amorphous regions with different physicochemical properties than those of a perfect array of atoms or molecules. As such, fast crystallization,²⁷ modulators,²⁸ the use of aggressive reagents that partially collapse the structure or harsh activation conditions²⁹ have shown to generate these defects (diffraction peak broadening or interpenetration³⁰) and may be treated as defects in this document.

1.1.4 Catalysis and Kinetics of Chemical Reactions

Chemical reactions occur when atoms or molecules collide with each other at an energy higher to the one needed for the bond cleavage or formation events to happen.³¹ This

energy is known as activation energy (E_a), which was first introduced by Svante Arrhenius (1859-1927) in 1889, and is dependent on temperature and concentration of the reagents. Arrhenius equation (eq. 1) correlates the reaction rate constant (k) with its activation energy as follows:

$$k = A \cdot e^{(-\frac{E_a}{k_B T})} \quad (\text{Eq. 1.1})$$

where A is the pre-exponential factor (which describes the probability of more or less successful collisions, mainly depends on size and mass of the molecules), k_B is the Boltzmann constant and T is temperature. Catalysts are substances that upon interaction with the reacting atoms or molecules facilitating bond cleavage or formation, *i.e.* decrease the activation energy of a given reaction (see Figure 1.4). This, in turn, increases the rate of the chemical process (k) allowing for reactions to occur faster (or to occur at all, if the E_a is too high). Important to note is that catalysis is a kinetic phenomenon, so it does not alter the thermodynamics (ΔG_r) of the reaction.

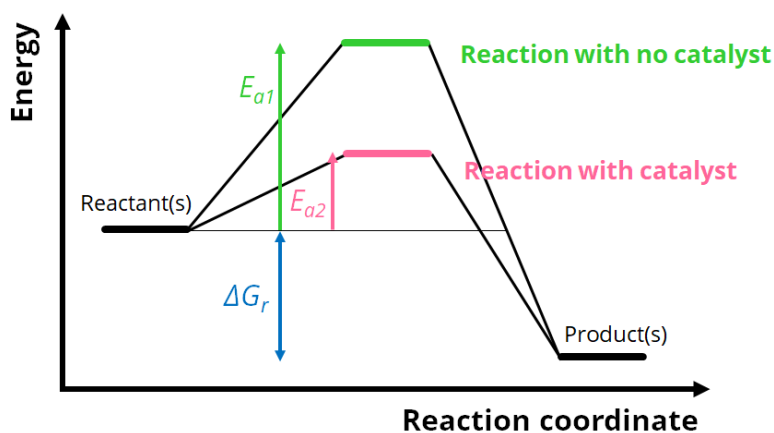


Figure 1.4. Energy diagram of a catalysed reaction with a lower activation (E_{a2} , pink) energy barrier to be overcome compared to an uncatalyzed reaction (E_{a1} , green). Note that catalysis is a kinetic phenomenon, the free energy of the reaction (blue, thermodynamics) remains unaffected.

If the catalyst is present in the same phase as the reagents (typically in solution), the term used is homogeneous catalysis (or biocatalysis if the catalysts are enzymes or bio-based systems). When a gas or liquid are contacted with a solid material that decreases the activation energy, we refer to it as heterogeneous catalysis. Catalysis and the development of catalytic processes is at the heart of chemical research and industry, for approximately 80% of all chemical transformations in the world proceed with a catalyst.

Extensive literature is available for the interested reader in the various fundamental aspects relevant for catalysis.^{32, 33} It is the intersection between catalysis and material science where the scope this PhD thesis lies. We will present in the following sections how MOFs may be used as catalysts or gas sorbents, and what the impact of defects (*vide supra*) is on the physicochemical properties of both type of functional materials.

1.1.5 Electronic Structure of Matter and Spectroscopy

Energy states of an electron in atoms or molecules corresponds to the eigenstates of the Hamiltonian operator of each electron. Chemical bonds in molecules result from electrons in the atomic orbitals shifting to bonding ($\sigma, \pi, \delta, \dots$) and anti-bonding ($\sigma^*, \pi^*, \delta^*, \dots$) created molecular orbitals, that are in lower and higher energy, respectively. Important to note that in the case of solids, the molecular orbitals result into a continuum of energy levels (bands). In the case of metals, the bands lie on the so-called Fermi level (E_F), the electrochemical potential above which they can flow across the atom array of the solid. In the case of semi-conductors and insulators, electrons populate lower energy states, the difference between E_F and those being called, a bandgap. Association into molecules or solids leads to an overall favourable energy balance compared to the isolated atoms. The energy of a molecular state corresponds to the molecular Hamiltonian:

$$E = E_{vib} + E_{elec} + E_{rot} + E_{nuc} + E_{trans} \quad (\text{Eq. 1.2})$$

where each term corresponds to the vibrational, electronic, rotational, nuclear or translational energy of each state. Each energy state can be described by terms given by the general expression:

$$^{2S+1}\Lambda_{\Omega,(g/u)}^{(+/-)} \quad (\text{Eq. 1.3})$$

where S is the total spin quantum number, Λ and Ω are the projections of the orbital and total angular momentum along the internuclear axis, (g/u) describe the symmetry of the state; and note the reflection symmetry along an arbitrary plane containing the internuclear axis. Upon absorbing photons of the appropriate energy (*i.e.* wavelength or frequency), electrons undergo transitions from a lower (the ground-state, if it happens to be the lowest possible) to a higher energy (excited) state. These electronic transitions can be combined with a vibrational or rotational in what are called rovibronic transitions.

Analogously, an excited state can release energy (*i.e.* photons) to decay to a lower energy state. If the energy is high enough (typically for X-ray or γ -rays), not only excitation but also ionization (*i.e.* abstraction of electrons in different orbital levels or ‘shells’) may be observed. Typical terminology for these emission processes relates the s , p , d , ... orbitals to the K , L , $M\dots$ transitions. A broad array of phenomena, such as fluorescence, phosphorescence or secondary electron emission, can occur during these energy exchange processes as shown in Figure 1.5.

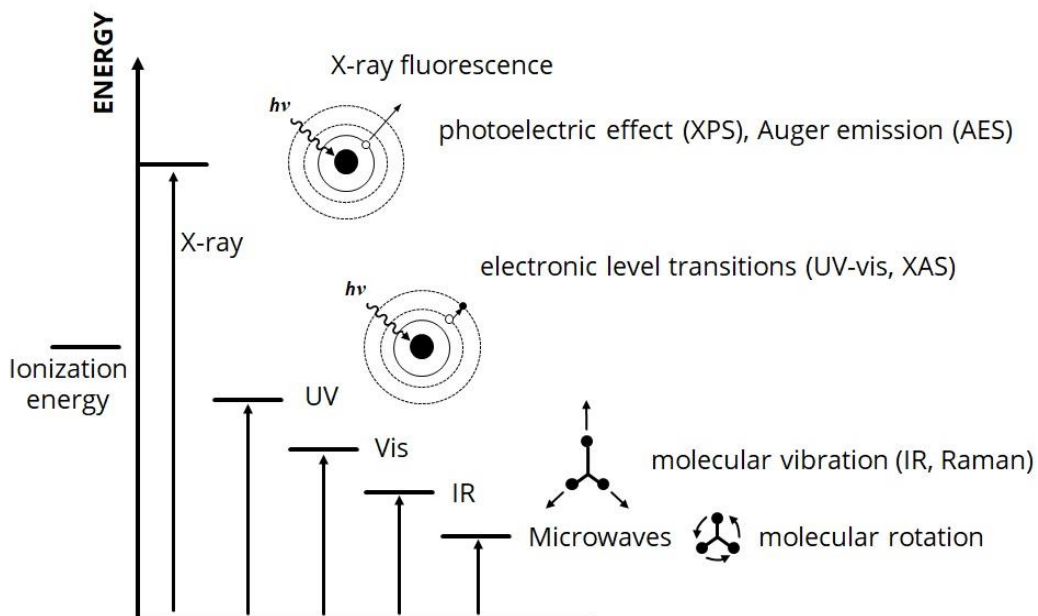


Figure 1.5. Different energy ranges and possible interactions with the typical techniques (in brackets) that are used in materials characterization.

Note that in this section we have described the absorption and emission of energies (*i.e.* inelastic processes). However, an incident photon beam may be not only absorbed, but also scattered. The intensity and patterns by which photons (and electrons), depends on the spatial arrangement of a matter (crystal structure), and maybe used for structural characterization of materials (*e.g.* X-ray Diffraction (XRD) or Small-Angle X-ray Scattering (SAXS)).³¹ Spectroscopy is the study of the interaction between electromagnetic radiation (light) and matter, and the field that deals with understanding the phenomena that occur therein in order to describe them mathematically. These processes vary depending on the type of the incident radiation, as well as on the composition and structure of the matter (material) under study. Developing (spectroscopic) tools for such purpose is integral part

of the field, and lays at the interface between physics, chemistry and materials science. As mentioned, for each part of the electromagnetic spectrum, one (or several) types of spectroscopy exist and may be used to study different features of chemical or physical substances. The main subject of this PhD thesis lays around crystalline (see Section 1.1.c), metal-organic coordination (see Section 1.1.a. and 1.1.b.) compounds. Thus, different matters require different techniques, such as spatial arrangement (XRD, SAXS, and X-ray Pair Distribution Function (PDF)), strength and nature of chemical bonds (IR or Raman spectroscopy) or electronic transitions between orbitals (UV-Vis spectroscopy). In the following parts of this Chapter, an overview of the different spectroscopic tools that can be used for those different parameters will be presented to the reader as a guide for understanding the fundamental challenges and advances described in Chapters 2 to 6.

1.2 METAL-ORGANIC FRAMEWORKS

As defined above, Metal-Organic Frameworks (MOFs) consist of organic polydentate ligands (linkers) bonded to metal cations or clusters (nodes) resulting in 2-D or 3-D network structures with potential porous cavities.¹⁹ In fact, MOFs often show coordination clusters that have been previously observed and isolated with their putative monodentate ligand counterparts. The clusters have been referred to as Secondary Building Units (SBUs) in the literature and are tremendously diverse in geometry, oxidation state and composition.^{34, 35} For instance, the HKUST-1 topology shows the so-called Paddle-Wheel (PW) clusters,³⁶ in which two metal atoms are coordinated in octahedral geometry to four carboxylate molecules (Figure 1.7a). A vast number of PW complexes are known in coordination chemistry and a few have been used as guidelines for the preparation of porous coordination polymers by different groups.³⁷ For example the group of Fischer prepared Ru and Rh analogues of HKUST-1 by pre-synthesizing $\text{Ru}_2(\text{OAc})_4$ and $\text{Rh}_2(\text{OAc})_4$ with PW structure.³⁸⁻⁴² However, one can imagine that non-polymeric multi-metallic clusters can serve as a guideline for the discovery of new structures that consist of the 2- or 3D infinite space extension of such clusters, leading to the generation of new MOF structures based on monomeric coordination compounds in the future.

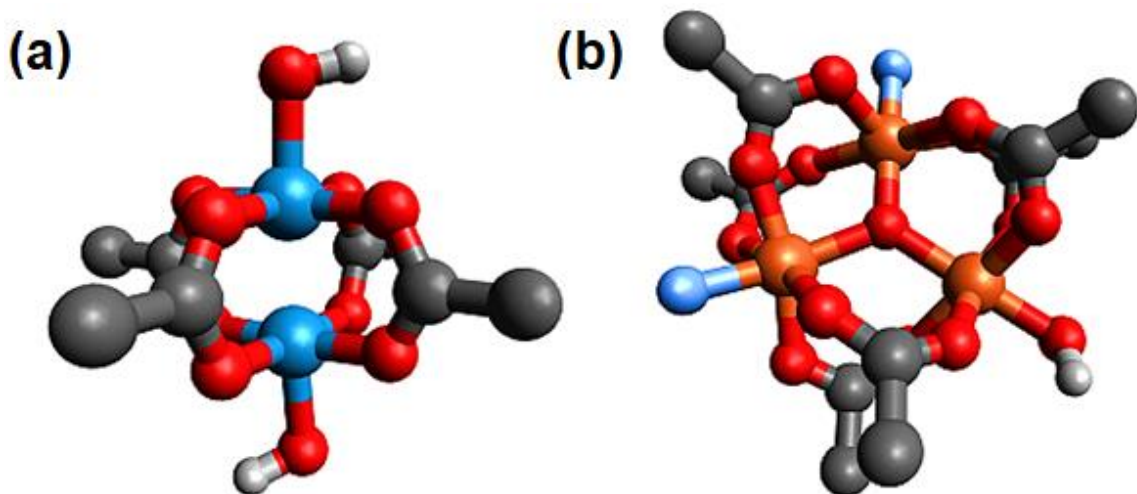


Figure 1.7 (a) Paddle-wheel (PW) cluster present in the HKUST-1 topology and (b) trimer cluster present in the zeotype MIL-100(Fe) topology (C, grey; O, red; Cu, blue; F, light blue; Fe, orange; H, white; linker molecules are omitted for clarity). Fluorine is typically present as a residual counter-anion from synthesis procedures.

Another example is the trimer cluster present in the MIL-100 and MIL-101 topologies. In this case, three metal cations around a bridging oxygen adopt the octahedral geometry ligated to four carboxylate molecules (Figure 1.7b). This building block is present in different topologies, *e.g.* MIL-127, MIL-88, MIL-89, and just as previously mentioned for HKUST-1, it may be used as a molecular precursor for crystal formation.⁴³ For instance, Wongsakulphasatch *et al.*⁴⁴ prepared mixed-metal molecular precursors by reacting $\text{Ni}(\text{OAc})_2$, $\text{Co}(\text{OAc})_2$ or $\text{Mg}(\text{OAc})_2$ and $\text{Fe}(\text{OAc})_2$ to yield the trimers, which were then mixed with the 3,3',5,5'-azobenzenetetracarboxylic acid ligand (TazbH_4) to obtain mixed-metal analogues of MIL-127(Fe). This example clearly shows the potential of prefabricated coordination clusters or complexes for the preparation of MOFs with different properties. The research described in Chapters 2 to 5 is devoted to topologies that are built upon these two SBUs, *i.e.* paddle-wheels and oxo-trimmers for HKUST-1 and MIL-100, respectively.

Research in the field of MOFs came to fruition after the pioneering reports by Robson,⁴⁵ Kitagawa,⁴⁶ Yaghi^{47, 48} at the end of the last century. Thereafter, an increasing number of framework structure topologies combining different polytopic linkers (*e.g.*, phosphonates, azolates, thiols and carboxylates) with metal ions (alkaline-earth,

transition and main group) or clusters (mostly oxidic) have been published, reaching up to ~60000 different structures.⁴⁹ The interest of MOFs is linked mainly to two key features of these functional materials: the tunability of their different components (*i.e.*, linkers and nodes), as just mentioned; and their record surface areas (up to ~10000 m²/g for ultra-high surface area MOFs).¹ Many structures have shown other interesting properties, such as non-linear photon absorption,⁵⁰ sensing,⁵¹ luminescence⁵² or electrical conductivity,⁵³ leading to new avenues in MOF design.

However, a very reduced number of those structures show permanent porosity upon solvent removal, as well as thermal and chemical stabilities, which are crucial for several applications. Certain trends, in terms of metal, linker and topology composing these frameworks, have been identified by a number of authors,^{54, 55} who highlighted the necessity of exploiting the properties of these structures (Figure 1.8a, b). In fact, only very few MOF topologies (including slightly modified analogues) have been thoroughly studied due to their potential in these different applications. One can establish a certain analogy with zeolite chemistry, in which the ensemble of topologies formed by the FAU, MFI, MOR, BEA and FER architectures is often called “the big five” (although CHA could be arguably added to this list) due to their widespread use.⁵⁶ A similar list comprising the MOF structures shown in Figure 1.8a, b, which can be easily prepared and are air stable for periods of time (except for MOF-5) can be established as well. Although other topologies (*e.g.* MIL-68, MIL-88, MOF-808, NU-1000) have been also intensively studied and merit to be included, we chose these 7 structures based on the literature and their potential industrial applications. Some of them can be prepared with different linkers and metals that yield the same structure, their stability varying with those components. Not only stability, but also straightforward synthesis methods, cheap raw materials and physical properties needed for their use as functional solids, such as shaping, are required.⁵⁷⁻⁶⁰ The number of patents filed related to MOFs has been steadily increasing over the last few years, but the first commercial successes have been only very recently achieved, highlighting that widespread use of MOFs is still to come.^{61, 62} The current trend is to further implement continuous, reproducible production methods, and to tackle further technological challenges hindering their use.^{63, 64} Proof of this is the number of start-ups

recently founded, in addition to traditional large chemical manufacturing businesses (Table 1.1). Despite all this, MOF researchers still target now *niche* applications, such as use in heat pumps, electronics or biomedicine.

Table 1.1. Different start-ups and large companies involved in MOF research, production or application worldwide.⁶⁵⁻⁶⁸

Name	FOUNDATION	Location	Application
Framergy	2011	USA	Low-cost MOF gas sorbents
ProfMOF	2016	Norway	Large-scale production
MOF Apps	2013	Norway	Customized MOF production
MOF Technologies	2012	UK	MOFs for gas sorbents
Immaterial Labs Ltd	2017	UK	MOFs for gas storage/separation
Numat Technologies, inc	2012	USA	MOF for toxic gas storage
Inmundo Tech	2013	USA	Large-scale production of MOFs
MOFWORX	-	Australia	Large-scale prod. of MOFs for CO ₂ capture
Materials Center TU Dresden	-	Germany	MOF supply in research quantities
Mosaic Materials	2016	USA	MOFs for CO ₂ and hydrocarbon separations
Rimo Therapeutics	2016	USA	MOFs for cancer therapy
MOFgen	2017	UK	MOFs in biomedicine
NovoMOF AG	2017	Switzerland	Customized MOF production
BASF SE	1865	Germany	Production and use of MOFs
Strem Chemicals Inc.	1964	USA	Commercialization of MOFs or MOF building blocks
Johnson Matthey plc	1817	UK	Research in production and use of MOFs

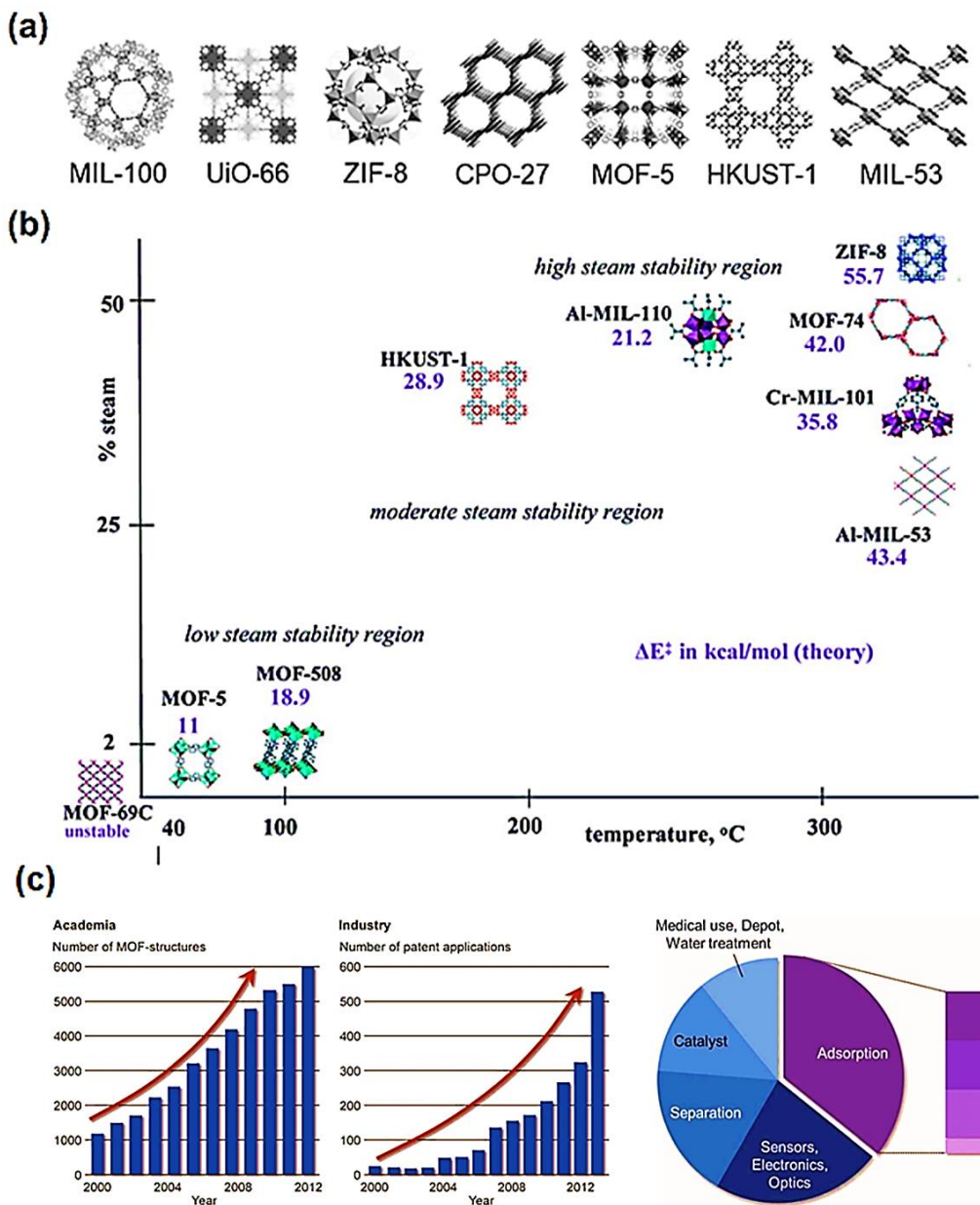


Figure 1.8 (a) Schematic representation of some of the most studied MOF topologies and (b) hydrothermal stability of several structures described above, showing the calculated ΔE of the ligand displacement by a water molecule at a given temperature and concentration (%steam). Adapted from reference [54]. Copyright © American Chemical Society, 2009. (c) Evolution of the number of structures and filed patents over the past years. Different applications of the filed patents (does not include the latest in biomedical applications). Adapted from reference [62]. Copyright © John Wiley & Sons, 2015.

Bearing this in mind, the research carried out in this PhD thesis deals with the potential properties of HKUST-1(Cu) as gas sorbent, redox catalyst and host material for electrically conductive devices. Additionally, properties of MIL-100 as a mildly acidic, catalyst support (*i.e.* host material for metal nanoparticles) and a catalyst itself (upon mixing with an activator) were the subject of this PhD work. Thus, the study of physicochemical

parameters that can be tailored for those specific applications has been investigated by means of structural and textural characterization techniques, as well as testing their performance in the aforementioned applications. A detailed summary of techniques for probing acidity, oxidation state, coordination geometry or sorption thermodynamics of gases is presented in further sections: HKUST-1 (Section 1.5.1) and MIL-100 (Section 1.5.2).

1.3 DEFECTS AND DISORDER IN METAL-ORGANIC FRAMEWORKS

As described in Section 1.1.c, crystal lattices naturally contain structural defects in the form of missing atoms, dislocations or kinks. In Section 1.2, MOFs have been described as crystalline, porous coordination compounds, which may, indeed, exhibit defects of their own nature. This subject has been extensively researched and reviewed by many groups, whereby defects have been used as a tool itself to alter the properties of MOFs.^{62, 69-73} The classification of defects in MOFs, just as for lattices, may vary from one text to another, and usually comprises defects at different length-scales (Figure 1.9) and compositions for a given topology. For example, variations or absence of the metal atoms (or clusters) (Figure 1.9a) or organic linker molecules (Figure 1.9b) may be missing at certain parts of the lattice, *i.e.* defects at the atomic or molecular scale, that upon clustering may reveal effects at the mesoscale (larger pores) (Figure 1.9d, h). Mixing of different components is typically referred as multivariate (MTV)-MOFs,^{1, 74, 75} (Figure 1.9a-c) and is truly one of the main advantages of MOFs as solid, molecular materials. In some cases, not only changes in the backbone itself, but also the presence of metal nanoparticles (NPs) or guest molecules are considered as heterogeneities in the ideal lattice (Figure 1.9f-g). In brief, the definition of the term 'defect' has been somewhat flexibly applied for convenience at different points in time in the scientific literature. In this PhD thesis, the research described in Chapter will deal with one or several types of the defects presented in Figure 1.9. A detailed description of the nature of those defects will be provided in each Chapter, as well as the techniques that allow for their study. Again, except in the case of a few frameworks that can accommodate large amounts of defects,⁷⁶ they generally appear in low concentrations, and require very sensitive characterization techniques in order to determine their nature and properties.

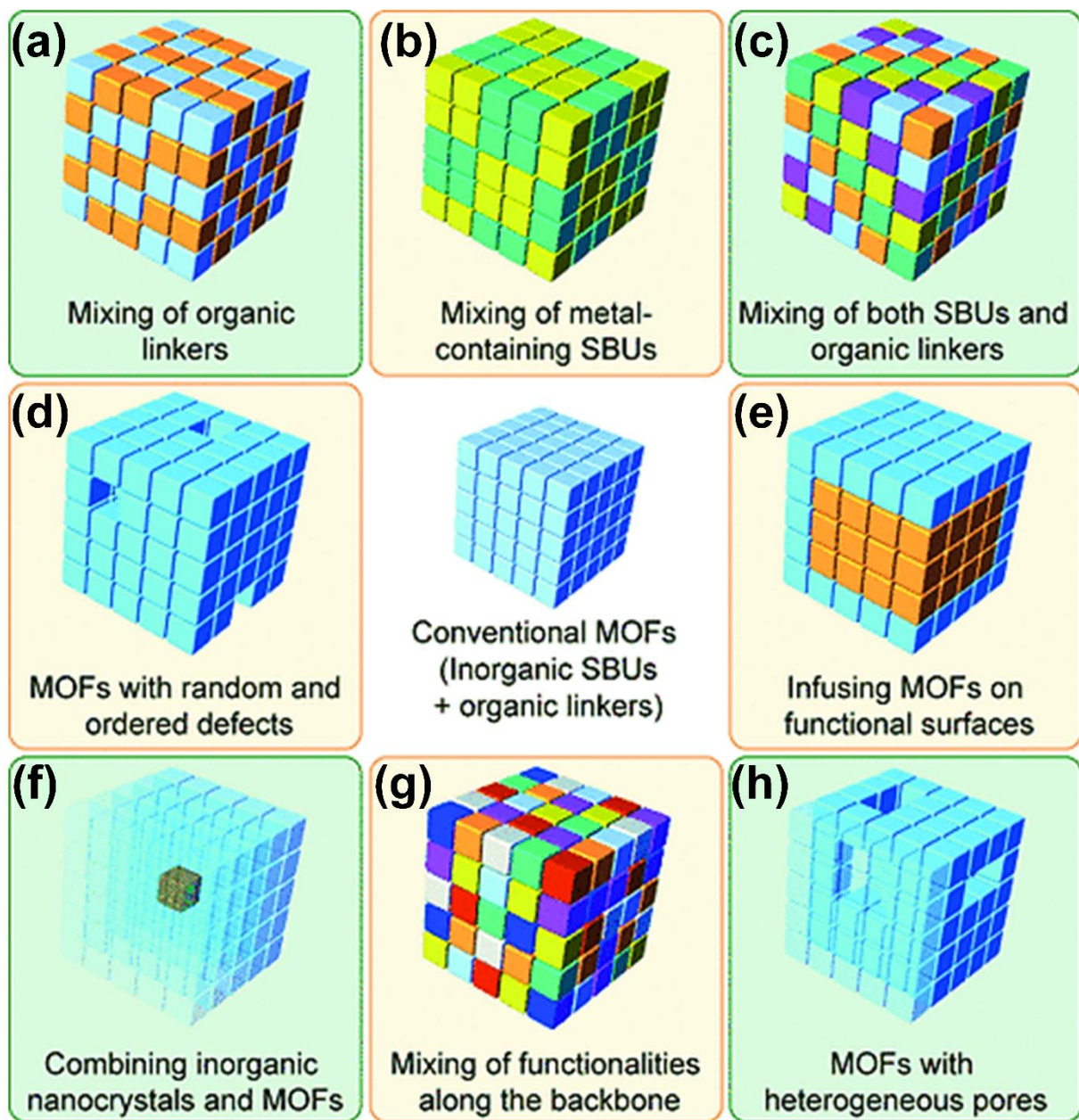


Figure 1.9. Different compositional heterogeneities of MOFs that stem from combining linkers, metals, defects, SBUs and/or metal nanoparticles according to Furukawa *et al.*⁶². Copyright © John Wiley & Sons, 2017. As mentioned earlier, the concept of defect from the viewpoint of inorganic chemistry, group theory or material science may vary and encompasses many different perspectives.

Important to mention is that one of the most studied topologies in which multiple kinds of defects appear is UiO-66. As demonstrated by different research groups,^{28,77} by adding monodentate or mineral acids of different strengths (*i.e.*, hydrochloric, formic, acetic or trifluoroacetic acid), different molar amounts of them remain coordinated after crystallization along with the terephthalate linker. Upon thermal treatment under

vacuum, the monodentate acid molecules are removed, leaving additional Zr⁴⁺ Lewis acid sites (LAS) and -OH Brønsted acid sites (BAS) available for gas sorption and catalysis (Figure 1.10).⁷⁸⁻⁸⁰ Above a certain threshold, the amount of defects leads to missing zirconium oxohydroxide, *i.e.* [Zr₆(μ₃-O)₄(μ₃-OH)₄]¹²⁻, clusters, and thus, to a lattice with different symmetry; as well as to the presence of small mesopores, as shown by Cliffe *et al.*⁸¹ by means of advanced modelling and X-ray scattering and diffraction techniques.

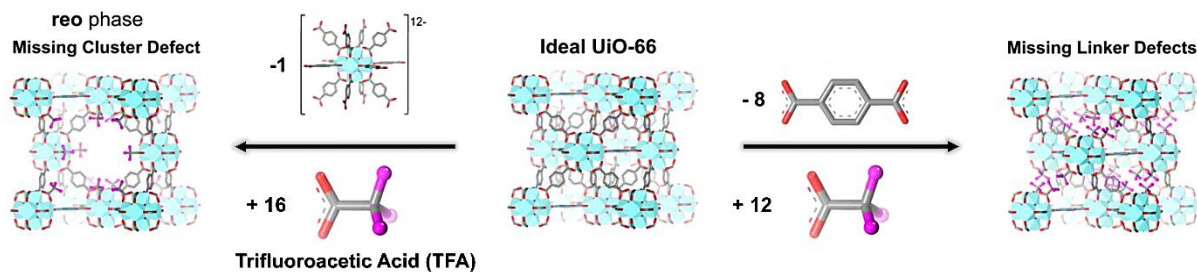


Figure 1.10. Addition of different molar amounts of trifluoroacetic acid (TFA) to the synthesis of UiO-66 leads to the formation of defects in the form of: missing terephthalate linkers (right), or missing Zr₆ nodes (left).

Missing linkers may modify an extremely wide variety of properties (*e.g.* chemical potential, reducibility, coordination geometry, magnetic properties),^{69, 82, 83} thus, altering MOF performance in a manifold of applications. Defect linkers may also be purposefully introduced, as demonstrated by Marx *et al.*, who co-crystallized partially coordinating 3,5-pyridine-dicarboxylic acid with 1,3,5-benzenetricarboxylic acid to yield defect-engineered HKUST-1 materials, which contain easily reducible Cu²⁺ sites and porosity.⁸⁴ This will be further discussed in Chapters 4 and 5. In brief, there are multiple strategies to use defect-linkers as a tool for improving the performance of materials in different applications. As mentioned, missing nodes may result in the formation of mesopores, enhancing mass transport and diffusion through their pores. However, alternative pathways for the formation of large pores have been described in the literature. For instance, etching with strong acids or plasma,^{85, 86} high temperature treatments⁸⁷ or simply fast crystallization processes result in defective crystals at the macroscale (Figure 1.11c).⁸⁸

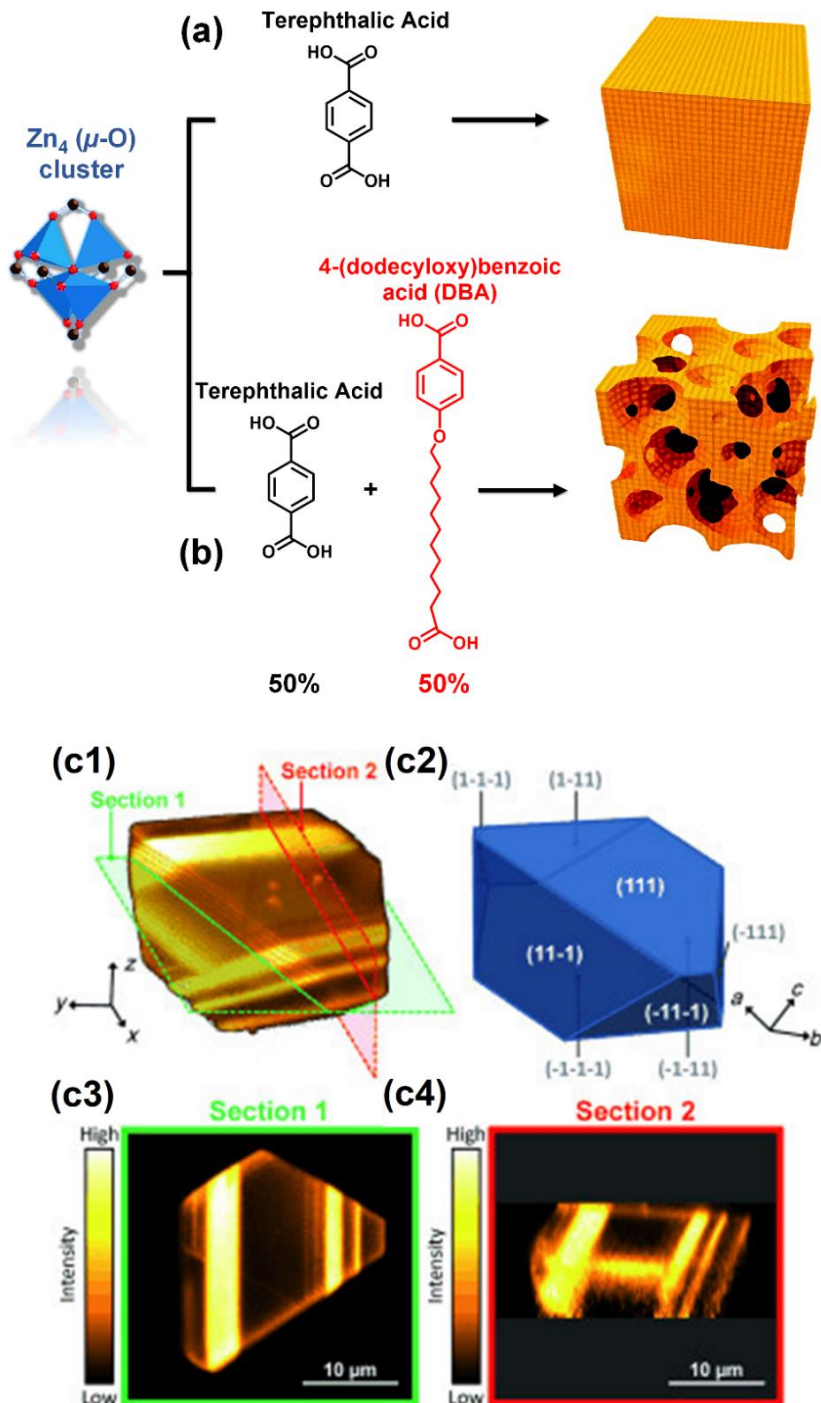


Figure 1.11. Co-crystallizing long-chain carboxylates with terephthalic acid and zinc nitrate results in MOF-5 with defects at the macro-scale, *i.e.* large pores (b), in contrast with the ideal microporous, defect-free structure (a). Adapted from reference [89]. Copyright © American Chemical Society, 2009. Different parameters, such as crystallization time, temperature and molar ratios affect the number of defects in HKUST-1, as demonstrated by Ameloot *et al.* by means of confocal fluorescence microscopy with furfuryl alcohol. A scheme (c2) shows the different lattice planes of the three-dimensional image (c1) of a crystal. Sections (c3) and (c4) reveal certain crystalline plane defects along which fluorescence is more intense, indicating a higher density of Brønsted acid sites. Adapted from reference [90]. Copyright © John Wiley & Sons, 2009.

In Figure 1.11a and b, when long-chain carboxylates are introduced in the synthesis mixture together with terephthalic acid, the ideal MOF-5 structure shows large mesopores observable by SEM.⁸⁹ Long crystallization times may also affect the nucleation-growth processes occurring, since MOF structures are not always thermodynamic products, but rather kinetically stable stages of the mixture.^{91, 92} Thus, a number of -COOH groups along certain planes or within the pores remain unbonded (*i.e.* defect sites). In Figure 1.11c, HKUST-1 crystals show defective planes observed by Confocal Fluorescence Microscopy (CFM) after BAS catalyzed the oligomerization of furfuryl alcohol (*i.e.* naturally occurring defects). In fact, as reported by Dodson *et al.*,²⁹ something apparently trivial such as thermal desolvation, may severely affect the crystallinity of MOFs, leading to losses in porosity, defect or mesopore formation (Figure 1.12). This is due to capillary forces of the solvent leaving the micropores, as well as fast heating ramps that induce local gas hotspots that can break bonds and partially collapse crystals.

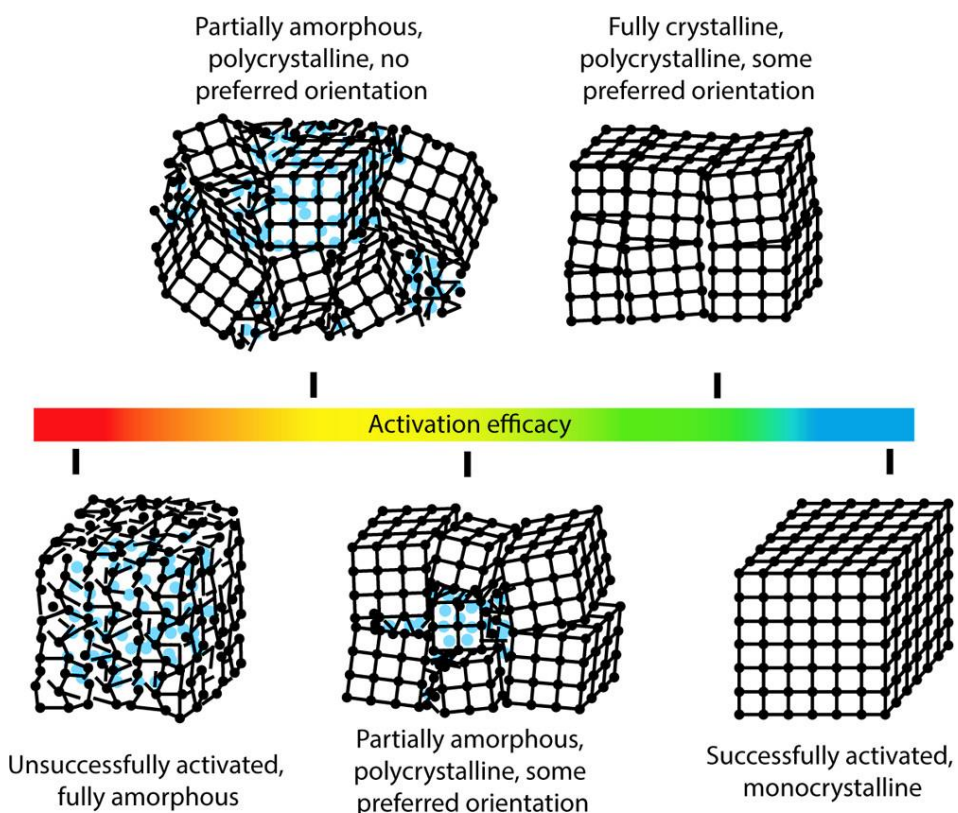


Figure 1.12. Different landscapes of lattice collapse that may occur during MOF thermal desolvation, depending on the conditions (pre-solvent exchange with non-coordinating solvents, *e.g.* hydrocarbons) and topology, different degrees of crystallinity are obtained. Adapted from reference [29]. Copyright © American Chemical Society, 2018.

Thus, it is important to keep in mind that MOFs are very dynamic materials, a property that stems from the fact that they are molecular structures in which bonds (coordination and covalent) possess many degrees of freedom for rotation and rearrangement. This leads to the possibility of MOFs having a relatively high degree of disorder at the long range, a recently studied field in MOF chemistry, given the fact that some MOF topologies may behave like glasses.⁹³

In this regard, the group of Bennet has⁹⁴⁻⁹⁷ demonstrated how a variety of MOFs may reach amorphous states without bond cleavage (especially in the case of soft ion pairs, *e.g.* Zn-N that show high affinity) (Figure 1.13). Thus, Bennett *et al.* prepared the amorphous compositional analogue from an ideal lattice of ZIF-4 by ball-milling and a treatment at high temperatures (723 K).⁹⁸ ZIF-4 undergoes amorphization and recrystallization into a Zn azolate dense phase by following the former and later steps, respectively.

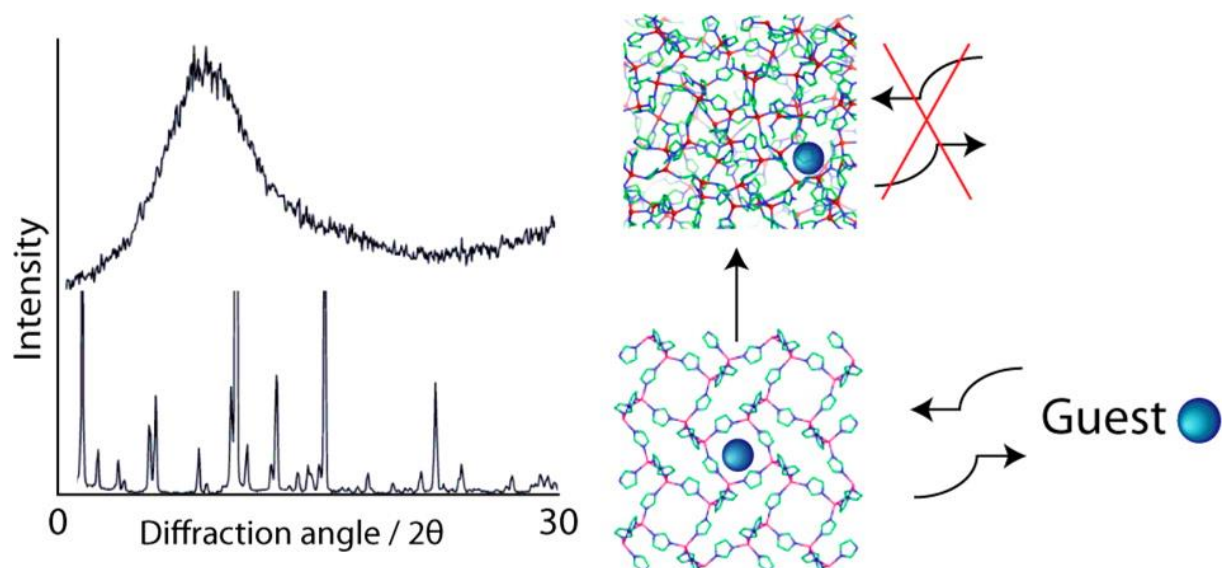


Figure 1.13. Scheme showing how thermal or mechanical treatment of certain zeolitic imidazolate frameworks (ZIFs) may lead to non-crystalline porous structures with different properties (*e.g.* physical, textural, host-guest chemistry). Adapted from reference [97]. Copyright © American Chemical Society, 2018.

This consists of yet another type of ‘defective’ metal-organic material compared to the parent networks. In Chapter 2, the effect of lattice disorder, *i.e.* an amorphous metal-organic structure, on two different compositional analogues of MIL-100(Fe) as supports

for metal nanoparticles will be studied. This shows that this type of long-range defects plays a critical role in different aspects of MOF chemistry, such as gas sorption or catalysis.

Finally, compositionally heterogeneous materials can be made by introducing metallic nanoparticles (NPs) or guest molecules into the porous structure of MOFs.⁹⁹⁻¹⁰¹ A number of different routes have been investigated for the preparation of these composites: i) impregnation, drying and reduction of metallic NP precursor, ii) deposition or ship-in-a-bottle fabrication of colloidally stabilized NPs,¹⁰² iii) chemical vapor infiltration (CVI)¹⁰³ and (to a less extent) iv) solid grinding. When particles are located inside the pores of the MOF lattice, these composites are often referred to as NP@MOF or M@MOFs (where M = metal).

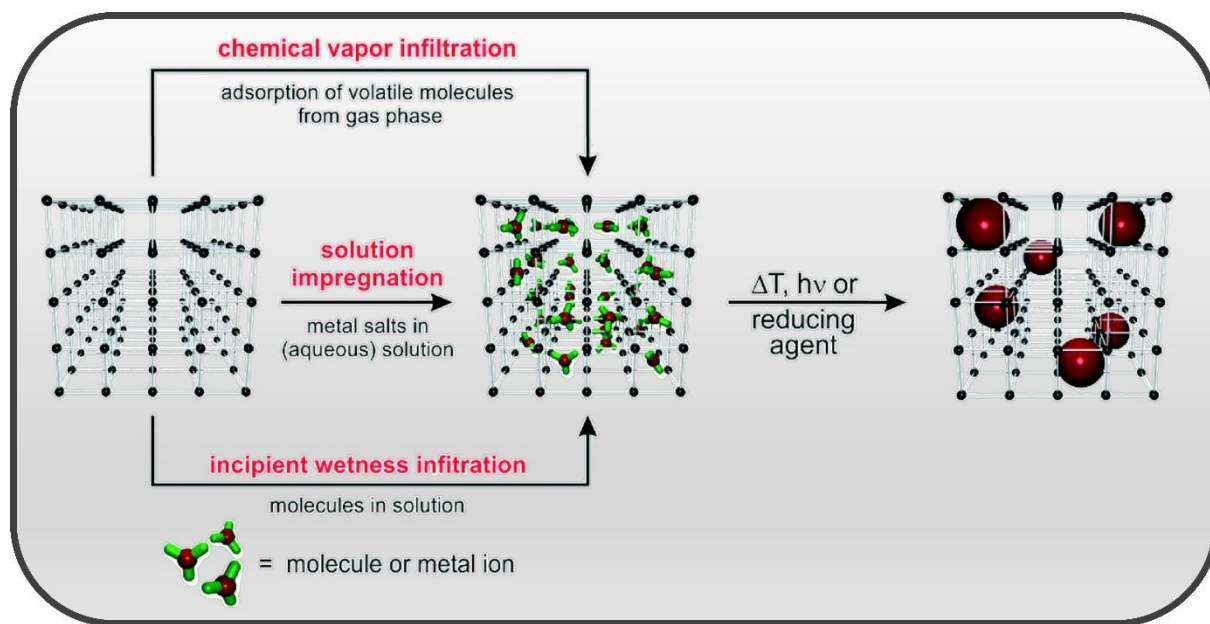


Figure 1.14. Scheme of the most commonly used strategies for the synthesis of NP@MOFs from salts or organometallic compounds of the NP precursor. Adapted from reference [99]. Copyright © Royal Society of Chemistry, 2015.

These composites have shown potential in applications, such as enhanced gas storage, catalysis or gas sensing.¹⁰⁴ A number of questions as for how the synthesis method, the porosity and the nature of the metal affect nanoparticle formation, location and dispersion, remain open.¹⁰⁵⁻¹¹⁰ It is worth mentioning that Pd is by far the most studied metal for these kind of composites, given its use both for catalytic applications (*e.g.*,

hydrogenations, oxidations and C-C coupling) and energy or hydrogen storage. A detailed description on these issues, and more specifically, of the uses in catalysis of metallic nanoclusters and nanoparticles embedded in MOFs is presented in Section 1.4.2.

1.4 METAL-ORGANIC FRAMEWORKS IN CATALYSIS

As described before, one of the major interest of MOFs is as heterogeneous catalysts. A number of authors have highlighted the strong competition that MOFs have with other porous functional materials (*e.g.* zeolites and porous silicas), due to their low stability and relatively high cost (Figure 1.15).¹¹¹⁻¹¹³ Nevertheless, their utility under appropriate conditions for the synthesis of complex molecules is undisputable, and has been extensively shown since Fujita *et al.* reported the first example of catalysis by MOFs in 1994. They showed the acidic properties of the active Cd²⁺ cations in [Cd(4,4'-bpy)₂](NO₃)₂ for the cyanosilylation of aldehydes.¹¹⁴

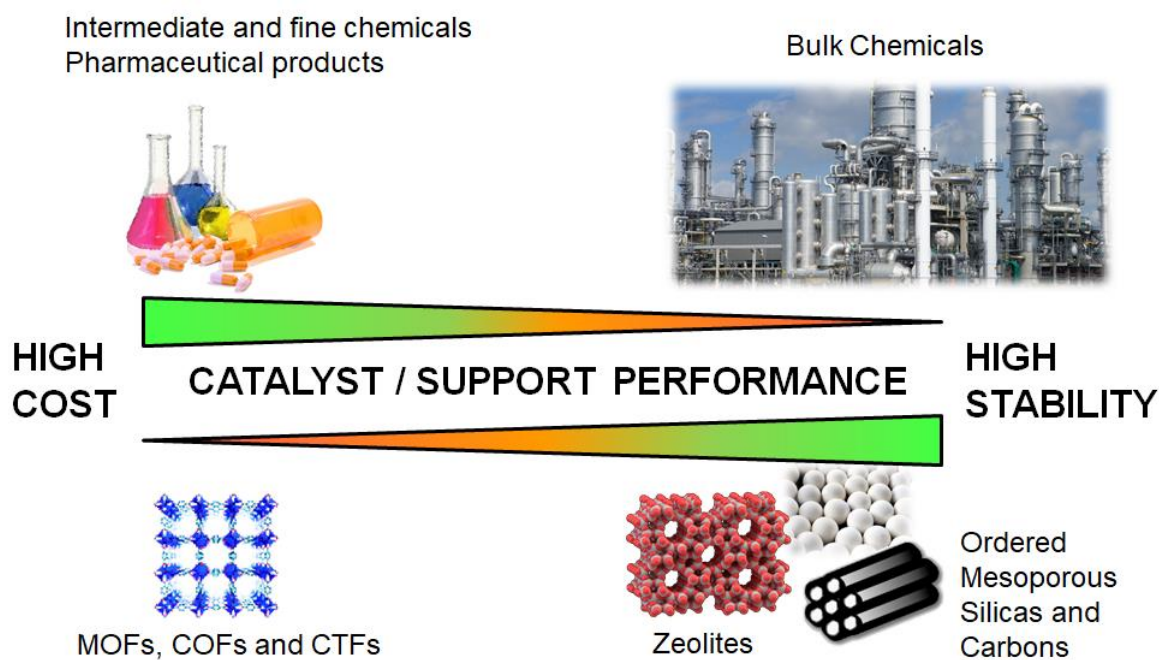


Figure 1.15. The role that MOFs play in catalysis is related to the price/performance ratio, in which high-value products, such as fine chemicals and pharmaceutical products, are the most valuable target applications for these functional materials relative to *e.g.* zeolites and ordered mesoporous silicas and carbons.

MOFs have shown their potential in hydrogenation, oxidation, carbonylation, C-C and C-N bond formation, metathesis or C-H activation (and even of CH₄, in which ΔH⁰_{f(C-H)} = 415

$\text{kJ}\cdot\text{mol}^{-1}$; thanks to their weak-field ligands and ability to stabilize high-spin states, *e.g.* Fe^{IV}) reactions among others.¹¹⁵⁻¹¹⁸ In this regard, outstanding examples of how MOFs can be used either as acid/redox solids, functional supports or single-site catalysts have been recently published. In this regard, several strategies have been used to make use of MOFs in heterogeneous catalysis. Thus, although the use of MOFs as sacrificial templates for metal@C and other complex composites,¹¹⁹⁻¹²⁵ or/and photo(electro-)catalysis¹²⁶⁻¹²⁸ is worth mentioning, a detailed discussion lays beyond the scope of this PhD thesis.

1.4.1 Metal-Organic Frameworks as Single-Site Catalysts

One of the advantages of MOFs compared to other heterogeneous catalysts is the fact that they possess a very well-defined structure. This allows for a very clear distinction of the active sites playing an actual role during the catalytic process.

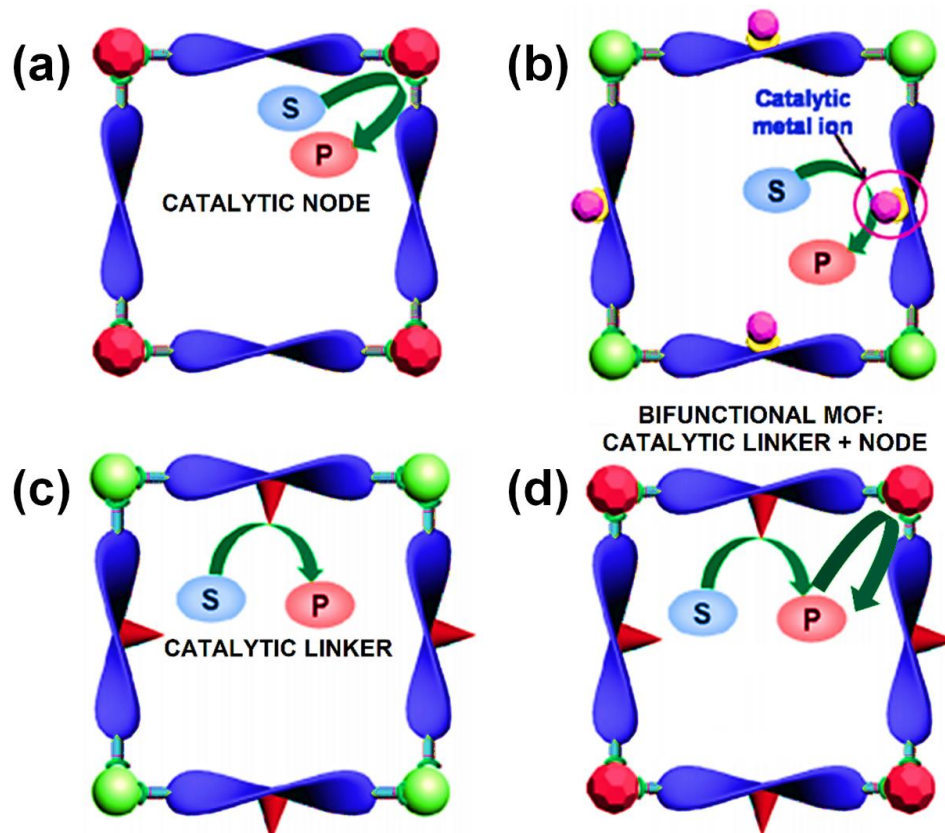


Figure 1.16. Different possibilities for single-site MOF catalysts: (a) metal atoms or nodes (usually coordinatively unsaturated sites) act as Lewis acid sites;¹²⁹ (b) metal atoms or complexes grafted to the nodes act as supported homogeneous catalysts;¹³⁰ (c) functional groups on the linker (*e.g.* thiourea)¹³¹ may act as organocatalyst analogues; and (d) two or more of the previous approaches may be combined into a multifunctional catalyst.¹³²

As mentioned earlier, MOFs can be easily post-treated in order to either remove (*e.g.*, OH groups and capping anions) or introduce reactive species, such as redox-active cations or coordination complexes anchored to their organic struts. In order to show the potential of all these strategies, we will describe the most relevant examples of each below.

a) Metal-Organic Frameworks Containing Coordinatively Unsaturated Sites and

Lattice Defects. As mentioned before, some topologies have metal centres or clusters that form Coordinatively Unsaturated Sites (CUS) upon removal of hydroxy ligands by thermal treatment under vacuum. This results in exposed Lewis sites M^{n+} , that can also suffer from auto-reduction and form $M^{(n-1)+}$ sites, showing redox behaviour.¹³³⁻¹³⁵ Purposefully incorporated redox-active atoms have been used for catalysis as well, taking advantage of particular coordination available in MOFs that allows for typically restricted spin-states.¹³⁶⁻¹⁴⁰ For instance, MIL-100(Fe) may be dehydrated to generate LAS (either Fe^{2+} or Fe^{3+}) on the metallic trimer clusters that are able to catalyse epoxide ring openings, hydrocarbon oxidations or aldol condensations.¹⁴¹ HKUST-1(Cu) exhibits a similar behaviour upon dehydration,¹²⁹ yielding Cu^{2+} and Cu^+ sites that catalyse the rearrangement of α -pinene oxide to campholenic aldehyde or the cyclization of citronellal to isopulegol. In a more recent example, Agirrezabal-Telleria *et al.*¹⁴² showed how thermally treated HKUST-1(Ru) forms $Ru^+/Ru^{2+}/Ru^{3+}$ sites that catalyse dimerization of ethylene to 1-butene highly selectively. Formation of these different sites, their study by means of spectroscopy and their utility in gas sorption and catalysis will be described in Chapter 2.

b) Metal-Organic Frameworks as Anchors for Asymmetric Catalysts or Single Atoms.

Another approach is to introduce organometallic complexes in the pores either during or after the MOF synthesis, which can be anchored through covalent interaction to the linker or interacting *via* van der Waals interactions with cationic or anionic sites (either at the nodes or the linker). This has shown to be an extremely successful approach, achieving activities and selectivities comparable, and sometimes surpassing, those of the homogeneous complexes, or even showing different types of reactivity.¹⁴³ For instance, Corma *et al.* showed how a Au^{3+} -Schiff base complex attached to NH₂-MOF-5 was more

active in the gas-phase hydrogenation of 1,3-butadiene than any other gold catalyst to date, as well as in amine cyclization.¹⁴⁴ Other very powerful examples involving metal complexes can be found in the literature, and the reader is referred to them.^{130, 145-157} Not only metal complexes, but also chiral linkers or ligands, *e.g.* 2,2'-Bis(diphenylphosphino)-1,1'-binaphthyl (BINAP) or [1,1'-binaphthalene]-2,2'-diol (BINOL), have shown excellent properties in asymmetric catalysis when attached to MOFs.¹⁵⁸⁻¹⁶⁶ These have the potential to bring MOF (together with COFs) catalysts to the next level, since no other porous materials can be designed to inherently have chiral motifs in their structure. Another interesting strategy has been to use the metal nodes, which show structural and chemical similarities to their corresponding metal oxides, as support materials for atoms or complexes. Some groups have developed a number of catalysts using the OH groups in the MOF as anchoring points for metal atoms or complexes introduced mainly by Atomic Layer Deposition (ALD) or post-synthetic metalation in solution, and that have shown very interesting results in catalysis.¹⁶⁷⁻¹⁸⁸

1.4.2 Metal-Organic Frameworks as Support for Catalytic Metal Nanoparticles and Clusters

As described above, the pores of a MOF can be infiltrated (either after or during formation) with reactive species that sit next to reacting sites of the surface. The advantage compared to other supports are the interplay between MOF (host) and guest,^{101, 105, 189-191} due to pore confinement effects; as well as high loadings (due to their much larger surface area)^{103, 192, 193} and reduced sintering arising from the pore structures.^{194, 195} Thus, metal salts and precursors can be introduced by many different strategies, and after thermal treatment, photolysis or liquid-phase reduction, metal atoms aggregate resulting in supported clusters (< 1 nm) or nanoparticles (NPs) that can be used as metal catalysts. Not only metals, but also other species, such as enzymes¹⁹⁶ or polyoxometallates¹⁹⁷, can be used, as well as combinations of all these to prepare new catalyst compositions. Concerning the synthetic methods, wet and incipient wetness impregnation,^{198, 199} Chemical Vapor Deposition (CVD),^{193, 200} and solid grinding,^{201, 202} as well as ship-in-a-bottle and bottle-around-a-ship protocols with colloidal particles have been described,¹⁰⁰ each one with its own peculiarities.^{99, 101, 203-207} A spectacular example

of this strategy has been reported by Fortea-Pérez *et al.*,²⁰⁸ who prepared Pd₄ clusters sitting next to anionic sites of the MOF and that can catalyse carbene transfer reactions. More recently, Mon *et al.* showed clusters of two Pt⁰ atoms inside the pores of a Cu,Ca-containing MOF with thioalkyl chains (Pt-S interactions) or Fe³⁺ sites within a Ni,Cu-MOF that are active in various industrially relevant reactions, proving the generality of this strategy for further studies in catalysis.^{209, 210} More recently, Chen *et al.* have also demonstrated how Pt single atoms sitting next to the CUS of MIL-101(Cr) catalyse CO₂ hydrogenation to methanol with high Turnover Frequencies (TOFs).²¹¹

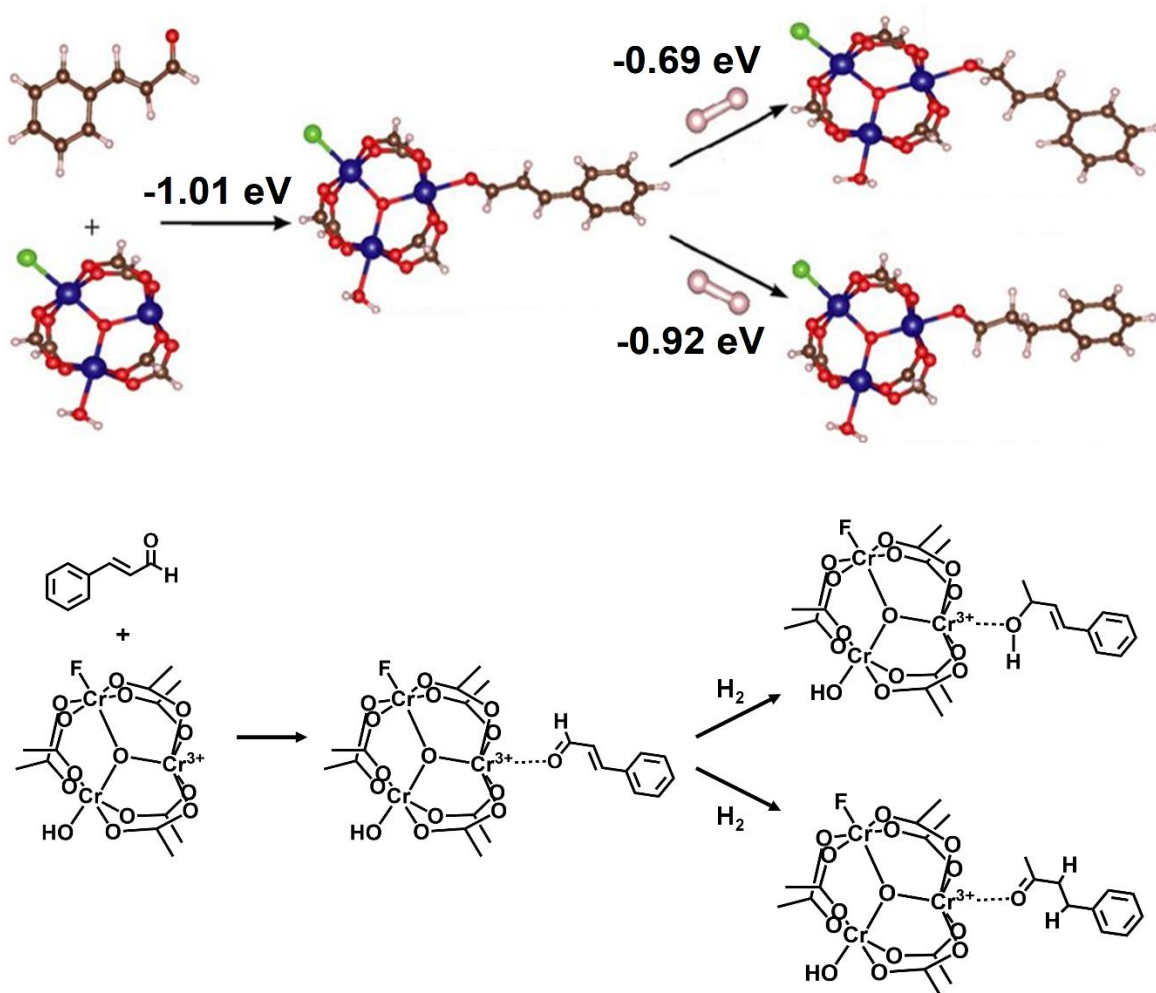


Figure 1.17. Schematic of cinnamaldehyde hydrogenation, showing the calculated adsorption energies (ΔH_E) of the substrate to the Cr³⁺ sites of the MIL-101(Cr) framework (-1.01 eV), and the free energy for the hydrogenation reactions yielding hydrocinnamaldehyde (-0.92 eV) or cinnamyl alcohol (-0.69 eV). These differences in energy lead to important differences in selectivity. Adapted and reprinted from reference [189]. Copyright © Nature Publishing Group, 2016.

Analogously, Zhao *et al.* showed that when Pt nanoparticles are embedded into different layers of MIL-101(Cr), the selectivity for the hydrogenation of cinnamaldehyde is affected by the interaction of the carbonyl group rather than the olefinic bond with the Cr³⁺ CUS sites in the framework. This interaction results in a lower free energy for hydrogenation towards hydro-cinnamaldehyde compared to cinnamyl alcohol (Figure 1.17), as demonstrated by Density Functional Theory (DFT) calculations. These examples show how MOFs may become the catalysts of choice for selected reactions where selectivity is key.

1.5. SCOPE AND OUTLINE OF THE PhD THESIS

As shown in the preceding sections, Metal-Organic Frameworks (MOFs) are relatively new materials consisting of molecular building blocks that may be highly dynamic in nature and structure (*e.g.* oxidation state and coordination geometry of the metals, presence of defects, spatial arrangement, formation of catalytically active sites and hosting of guest molecules), and a number of scientific questions concerning how deviations from ideality remain unanswered.

In order to address those issues, a general introduction on the fundamentals of the most important concepts of coordination and crystal chemistry, chemical kinetics, spectroscopy or defects, are described in this Chapter, **Chapter 1**. The Chapter is intended as an introduction to familiarize the reader with MOF materials and their potential use as porous hosts and functional materials, more specifically, as solid catalysts and electroconductive materials. As mentioned, MOFs are highly complex materials, so a review of the most interesting techniques for studying issues related to that is presented in **Chapter 2**. Mainly, vibrational and X-ray spectroscopy techniques in combination with probe molecules (*i.e.*, CO, NO, CD₃CN or pyridine) have been used to assess the properties of the metals in the lattice. These techniques have been highlighted due to their specific importance for gas sorption, binding of guests (such as during a catalytic process or that impart functionality, as shown in Chapter 6). Not only the metals *per se*, but also the 3D arrangement of the lattice (ordered or disordered, *i.e.* a specific type of defect) can affect the properties of the surface. In **Chapter 3**, we have studied the deposition of Pd molecular species and subsequent growth into metallic nanoparticles, which is greatly affected by the ordering of the MOF lattice. We have compared two compositional

analogues, MIL-100(Fe) and Basolite®F300 as supports for Pd nanoparticles, as well as the influence of the deposition technique. First, a detailed analysis of the structures by XRD, PDF, Raman spectroscopy, gas sorption and FT-IR spectroscopy with pyridine as probe molecule showed differences in polarity which revealed crucial for the latter size of Pd particles.

A different type of defects was studied in **Chapter 4**, where defects were potentially generated *in-situ* in the zeotypes (artificial materials based on the structure of zeolites) MIL-100 and MIL-101 frameworks. We rendered the frameworks catalytically active by mixing the materials with a co-catalyst (diethyl aluminium chloride), and studied by means of *in-situ* spectroscopy techniques (FT-IR spectroscopy with CO as probe molecule and UV-Vis spectroscopy) the fate of the metal sites and the framework structure. By analysing the morphology and molecular properties of the resulting polymer from the polymerization of ethylene, we proposed a mechanistic pathway and tentatively assigned the differences in reactivity to the pore cavities of each analogue.

Other than strong reagents, an alternative way of generating defect sites is the purposeful introduction of non-coordinating linkers. An insightful study on the properties of defect-engineered HKUST-1 materials settled the ground for the DEFNET consortium,⁷⁶ the funding partner of this PhD project. In **Chapter 5**, we have tried to shed more light on issues such as the morphology of the mesopores, the effect on crystal size and the spatial distribution of the defect linker at the interparticle level. By using SAXS, Wide-Angle X-ray Scattering (WAXS), Scanning Electron Microscopy (SEM) and Raman microscopy for the issues described before, respectively, we have added one layer of knowledge to what is known of defect-engineered HKUST-1 frameworks. Additionally, a large set of bulk techniques (*i.e.*, UV-vis, Electron Paramagnetic Resonance (EPR), FT-IR spectroscopy with NO- and Pyridine as probe molecules) were used to further study the nature of the Cu⁺/Cu²⁺ redox sites, although due to their highly dynamic nature, a detailed description remains elusive.

Not only defects can be introduced into the lattice, but other types of functionalization can be done into the archetypal HKUST-1 framework. In **Chapter 6**, we have addressed the issue of spatial distribution by means of microscopy, but now of a functional guest molecule (*i.e.*, 7,7,8,8-tetracyanoquinodimethane), rather than of defects, as described in

Chapter 5. Loading from the gas-phase results in a composite (Guest@MOF) material, with high electroconductivity. However, the mechanism of electron conduction is still a matter of debate; the location and arrangement of the guest molecules probably playing an important role. Thus, we used advanced microscopy (*i.e.*, Raman and FT-IR) techniques along with Principal Component Analysis (PCA), and a series of bulk characterization techniques to study the location of TCNQ within large HKUST-1 crystals. Moreover, we have studied the effect that water has on the distribution and performance of this material, showing that it does impact the properties of the material.

Finally, **Chapter 7**, serves as a summary of the results presented in this PhD thesis and includes potential future experiments and lines of research to deepen our understanding of defects in MOFs, and their use as functional materials.

1.7. REFERENCES

1. H. Furukawa, K. E. Cordova, M. O'Keeffe and O. M. Yaghi, *Science*, 2013, **341**, 1230444.
2. M. Fromm Katharina, L. Sagué Jorge and L. Mirolo, *Macromol. Symp.*, 2010, **291-292**, 75-83.
3. S. R. Batten, N. R. Champness, X.-M. Chen, J. Garcia-Martinez, S. Kitagawa, L. Ohrstrom, M. O'Keeffe, M. P. Suh and J. Reedijk, *CrystEngComm*, 2012, **14**, 3001-3004.
4. D. J. Tranchemontagne, J. L. Mendoza-Cortes, M. O'Keeffe and O. M. Yaghi, *Chem. Soc. Rev.*, 2009, **38**, 1257-1283.
5. K. Biradha, A. Ramanan and J. J. Vittal, *Cryst. Growth Des.*, 2009, **9**, 2969-2970.
6. N. G. Connelly, T. Damhus, R. M. Hartshorn and A. T. Hutton, *Nomenclature of Inorganic Chemistry: IUPAC Recommendations*, Royal Society of Chemistry, 2005, 367
7. R. Batten Stuart, R. Champness Neil, X.-M. Chen, J. Garcia-Martinez, S. Kitagawa, L. Öhrström, M. O'Keeffe, M. Paik Suh and J. Reedijk, *Terminology of metal-organic frameworks and coordination polymers (IUPAC Recommendations 2013)*, Pure App. Chem., **85**, 1715 - 1724.
8. <http://www.iza-online.org/MOF/MOFForIZA.pdf>.
9. F. A. Cotton and G. J. Wilkinson, *Advanced Inorganic Chemistry*, 1972, John Wiley & Sons, New Jersey.
10. G. L. Miessler, P. J. Fischer and D. A. Tarr, *Inorganic Chemistry*, 2014, Pearson Education Inc., London.
11. A. G. Sharp and C. E. Housecroft, *Inorganic Chemistry*, 2005, Pearson Prentice Hall, London.
12. P. W. N. M. van Leeuwen and J. C. Chadwick, *Homogeneous Catalysis: Understanding the Art*, 2011, Wiley-VCH, Weinheim.
13. A. Behr and P. Neubert, *Applied Homogeneous Catalysis*, 2012, Wiley-VCH, Weinheim.
14. H. J. Buser, D. Schwarzenbach, W. Petter and A. Ludi, *Inorg. Chem.*, 1977, **16**, 2704-2710.
15. Y. Jin Lin, M. Li Meng, B. Dang Dong, Y. Bai and N. Zheng Yan, *Z. Naturforsch. B*, 2013, **68**, 284-288.
16. S. Kitagawa and K. Uemura, *Chem. Soc. Rev.*, 2005, **34**, 109-119.
17. J. C. Bailar, *Interscience Publishers*, 1964.
18. J. R. Long and O. M. Yaghi, *Chem. Soc. Rev.*, 2009, **38**, 1213-1214.
19. L. MacGillivray, *Metal-Organic Frameworks*, 2010, John Wiley & Sons. Inc, New Jersey.
20. S. L. James, *Chem. Soc. Rev.*, 2003, **32**, 276-288.
21. S. Kitagawa, R. Kitaura and S.-i. Noro, *Angew. Chem. Int. Ed.*, 2004, **43**, 2334-2375.
22. M. Schröder, *Metal-Organic Frameworks*, 2010, Springer-Verlag, Berlin.
23. C. Kittel, *Introduction to Solid State Physics*, 2005, John Wiley & Sons, Inc., New York.
24. C. Giacovazzo, H. L. Monaco, G. Artioli, D. Viterbo, M. Milanesio, G. Gilli, P. Gilli, G. Zanotti, G. Ferraris and M. Catti, *Fundamentals of Crystallography*, 2011, Oxford University Press, Oxford.
25. L. Smart and E. Moore, *Solid State Chemistry: An Introduction*, 2012, CRC Press, Boca Raton.

-
26. J. H. Conway and N. J. A. Sloane, *Sphere Packings, Lattices and Groups*, 1988, Springer-Verlag, Berlin.
27. U. Ravon, M. Savonnet, S. Aguado, M. E. Domine, E. Janneau and D. Farrusseng, *Micropor. Mesopor. Mater.*, 2010, **129**, 319-329.
28. F. Vermoortele, B. Bueken, G. Le Bars, B. Van de Voorde, M. Vandichel, K. Houthoofd, A. Vimont, M. Daturi, M. Waroquier, V. Van Speybroeck, C. Kirschhock and D. E. De Vos, *J. Am. Chem. Soc.*, 2013, **135**, 11465-11468.
29. R. A. Dodson, A. G. Wong-Foy and A. J. Matzger, *Chem. Mater.*, 2018, **30**, 6559-6565.
30. R. J. Marshall, C. T. Lennon, A. Tao, H. M. Senn, C. Wilson, D. Fairn-Jimenez and R. S. Forgan, *J. Mater. Chem. A*, 2018, **6**, 1181-1187.
31. P. Atkins and J. De Paula, *Physical Chemistry*, 2006, Oxford University Press, Oxford.
32. M. Boudart, B. H. Davis and H. Heinemann, *Handbook of Heterogeneous Catalysis*, 2008, Wiley-VCH, Weinheim.
33. K. P. de Jong, *Synthesis of Solid Catalysts*, 2009, Wiley-VCH, Weinheim, 1-11.
34. M. J. Kalmutzki, N. Hanikel and O. M. Yaghi, *Sci. Adv.*, 2018, **4**, eaat9180.
35. M. Eddaoudi, D. B. Moler, H. Li, B. Chen, T. M. Reineke, M. O'Keeffe and O. M. Yaghi, *Acc. Chem. Res.*, 2001, **34**, 319-330.
36. S. S. Y. Chui, S. M. F. Lo, J. P. H. Charmant, A. G. Orpen and I. D. Williams, *Science*, 1999, **283**, 1148-1150.
37. M. Köberl, M. Cokoja, W. A. Herrmann and F. E. Kühn, *Dalton Trans.*, 2011, **40**, 6834-6859.
38. W. R. Heinz, T. Kratky, M. Drees, A. Wimmer, O. Tomanec, S. Günther, M. Schuster and R. A. Fischer, *Dalton Trans.*, 2019, **48**, 12031-12039.
39. W. Zhang, O. Kozachuk, R. Medishetty, A. Schneemann, R. Wagner, K. Khaletskaya, K. Epp and R. A. Fischer, *Eur. J. Inorg. Chem.*, 2015, **2015**, 3913-3920.
40. O. Kozachuk, I. Luz, F. X. Llabrés i Xamena, H. Noei, M. Kauer, H. B. Albada, E. D. Bloch, B. Marler, Y. Wang, M. Muhler and R. A. Fischer, *Angew. Chem. Int. Ed.*, 2014, **53**, 7058-7062.
41. H. Noei, O. Kozachuk, S. Amirjalayer, S. Bureekaew, M. Kauer, R. Schmid, B. Marler, M. Muhler, R. A. Fischer and Y. Wang, *J. Phys. Chem. C*, 2013, **117**, 5658-5666.
42. O. Kozachuk, K. Yusenko, H. Noei, Y. Wang, S. Walleck, T. Glaser and R. A. Fischer, *Chem. Commun.*, 2011, **47**, 8509-8511.
43. H. Reinsch and N. Stock, *Dalton Trans.*, 2017, **46**, 8339-8349.
44. S. Wongsakulphasatch, F. Nouar, J. Rodriguez, L. Scott, C. Le Guillouzer, T. Devic, P. Horcajada, J. M. Grenèche, P. L. Llewellyn, A. Vimont, G. Clet, M. Daturi and C. Serre, *Chem. Commun.*, 2015, **51**, 10194-10197.
45. B. F. Hoskins and R. Robson, *J. Am. Chem. Soc.*, 1990, **112**, 1546-1554.
46. S. i. Noro, S. Kitagawa, M. Kondo and K. Seki, *Angew. Chem. Int. Ed.*, 2000, **39**, 2081-2084.
47. O. M. Yaghi, H. Li and T. L. Groy, *J. Am. Chem. Soc.*, 1996, **118**, 9096-9101.
48. O. M. Yaghi and H. Li, *J. Am. Chem. Soc.*, 1995, **117**, 10401-10402.
49. G. Ferey, *Chem. Soc. Rev.*, 2008, **37**, 191-214.
50. L. R. Mingabudinova, V. V. Vinogradov, V. A. Milichko, E. Hey-Hawkins and A. V. Vinogradov, *Chem. Soc. Rev.*, 2016, **45**, 5408-5431.
51. L. E. Kreno, K. Leong, O. K. Farha, M. Allendorf, R. P. Van Duyne and J. T. Hupp, *Chem. Rev.*, 2012, **112**, 1105-1125.
52. J. J. Perry, C. A. Bauer and M. D. Allendorf, *Metal-Organic Frameworks*, 2011, Wiley-VCH, Weinheim, 267-308.
53. L. Sun, G. Campbell Michael and M. Dincă, *Angew. Chem. Int. Ed.*, 2016, **55**, 3566-3579.
54. J. J. Low, A. I. Benin, P. Jakubczak, J. F. Abrahamian, S. A. Faheem and R. R. Willis, *J. Am. Chem. Soc.*, 2009, **131**, 15834-15842.
55. T. Devic and C. Serre, *Chem. Soc. Rev.*, 2014, **43**, 6097-6115.
56. V. Van Speybroeck, K. Hemelsoet, L. Joos, M. Waroquier, R. G. Bell and C. R. A. Catlow, *Chem. Soc. Rev.*, 2015, **44**, 7044-7111.
57. M. Gaab, N. Trukhan, S. Maurer, R. Gummaraju and U. Müller, *Micropor. Mesopor. Mater.*, 2012, **157**, 131-136.
58. A. U. Czaja, N. Trukhan and U. Müller, *Chem. Soc. Rev.*, 2009, **38**, 1284-1293.
59. B. Yilmaz, N. Trukhan and U. Müller, *Chin. J. Catal.*, 2012, **33**, 3-10.
60. B. Böhringer, R. Fischer, R. Lohe Martin, M. Rose, S. Kaskel and P. Küsgens, *Metal-Organic Frameworks*, 2011, Wiley-VCH, Weinheim.
61. T. Faust, *Nat. Chem.*, 2016, **8**, 990-991.
-

-
62. H. Furukawa, U. Müller and O. M. Yaghi, *Angew. Chem. Int. Ed.*, 2015, **54**, 3417-3430.
63. M. P. Batten, M. Rubio-Martinez, T. Hadley, K.-C. Carey, K.-S. Lim, A. Polyzos and M. R. Hill, *Curr. Opin. Chem. Eng.*, 2015, **8**, 55-59.
64. A. Czaja, E. Leung, N. Trukhan and U. Müller, *Metal-Organic Frameworks*, 2011, Wiley-VCH, Weinheim.
65. <https://www.chemistryworld.com/feature/mofs-find-a-use/2500508.article>.
66. <https://eic.rsc.org/feature/mofs-head-to-market/2000100.article>.
67. <https://news.uchicago.edu/article/2016/01/29/uchicago-rimo-therapeutics-complete-first-ucgo-startup-license>.
68. <https://cen.acs.org/articles/95/i24/Round-two-MOF-commercialization.html>.
69. S. Dissegna, K. Epp, W. R. Heinz, G. Kieslich and R. A. Fischer, *Adv. Mater.*, 2018, **30**, 1704501.
70. J. Canivet, M. Vandichel and D. Farrusseng, *Dalton Trans.*, 2016, **45**, 4090-4099.
71. Z. Fang, B. Bueken, D. E. De Vos and R. A. Fischer, *Angew. Chem. Int. Ed.*, 2015, **54**, 7234-7254.
72. Z. Fang, B. Bueken, D. E. De Vos and R. A. Fischer, *Angew. Chem. Int. Ed.*, 2015, **54**, 7234-7254.
73. D. S. Sholl and R. P. Lively, *J. Phys. Chem. Lett.*, 2015, **6**, 3437-3444.
74. X. Kong, H. Deng, F. Yan, J. Kim, J. A. Swisher, B. Smit, O. M. Yaghi and J. A. Reimer, *Science*, 2013, **341**, 882-885.
75. H. Deng, C. J. Doonan, H. Furukawa, R. B. Ferreira, J. Towne, C. B. Knobler, B. Wang and O. M. Yaghi, *Science*, 2010, **327**, 846-850.
76. Z. Fang, J. P. Dürholt, M. Kauer, W. Zhang, C. Lochenie, B. Jee, B. Albada, N. Metzler-Nolte, A. Pöpll, B. Weber, M. Muhler, Y. Wang, R. Schmid and R. A. Fischer, *J. Am. Chem. Soc.*, 2014, **136**, 9627-9636.
77. G. C. Shearer, S. Chavan, J. Ethiraj, J. G. Vitillo, S. Svelle, U. Olsbye, C. Lamberti, S. Bordiga and K. P. Lillerud, *Chem. Mater.*, 2014, **26**, 4068-4071.
78. G. C. Shearer, S. Chavan, S. Bordiga, S. Svelle, U. Olsbye and K. P. Lillerud, *Chem. Mater.*, 2016, **28**, 3749-3761.
79. J. Hajek, C. Caratelli, R. Demuynck, K. De Wispelaere, L. Vanduyfhuys, M. Waroquier and V. Van Speybroeck, *Chem. Sci.*, 2018, **9**, 2723-2732.
80. D. M. Driscoll, D. Troya, P. M. Usov, A. J. Maynes, A. J. Morris and J. R. Morris, *J. Phys. Chem. C*, 2018, **122**, 14582-14589.
81. M. J. Cliffe, W. Wan, X. Zou, P. A. Chater, A. K. Kleppe, M. G. Tucker, H. Wilhelm, N. P. Funnell, F.-X. Coudert and A. L. Goodwin, *Nat. Commun.*, 2014, **5**, 4176.
82. Y. Zhang, S. N. Riduan and J. Wang, *Chem. Eur. J.*, 2017, **23**, 16419-16431.
83. M. Lammert, M. T. Wharmby, S. Smolders, B. Bueken, A. Lieb, K. A. Lomachenko, D. D. Vos and N. Stock, *Chem. Commun.*, 2015, **51**, 12578-12581.
84. S. Marx, W. Kleist and A. Baiker, *J. Catal.*, 2011, **281**, 76-87.
85. J. Koo, I.-C. Hwang, X. Yu, S. Saha, Y. Kim and K. Kim, *Chem. Sci.*, 2017, **8**, 6799-6803.
86. J. B. DeCoste, J. A. Rossin and G. W. Peterson, *Chem. Eur. J.*, 2015, **21**, 18029-18032.
87. S. Gadipelli and Z. Guo, *Chem. Mater.*, 2014, **26**, 6333-6338.
88. S. Furukawa, J. Reboul, S. Diring, K. Sumida and S. Kitagawa, *Chem. Soc. Rev.*, 2014, **43**, 5700-5734.
89. K. M. Choi, H. J. Jeon, J. K. Kang and O. M. Yaghi, *J. Am. Chem. Soc.*, 2011, **133**, 11920-11923.
90. R. Ameloot, F. Vermoortele, J. Hofkens, F. C. De Schryver, D. E. De Vos and M. B. J. Roeffaers, *Angew. Chem. Int. Ed.*, 2013, **52**, 401-405.
91. M. J. Van Vleet, T. Weng, X. Li and J. R. Schmidt, *Chem. Rev.*, 2018, **118**, 3681-3721.
92. A. K. Cheetham, G. Kieslich and H. H. M. Yeung, *Acc. Chem. Res.*, 2018, **51**, 659-667.
93. J. Hou, C. W. Ashling, S. M. Collins, A. Krajnc, C. Zhou, L. Longley, D. N. Johnstone, P. A. Chater, S. Li, M.-V. Coulet, P. L. Llewellyn, F.-X. Coudert, D. A. Keen, P. A. Midgley, G. Mali, V. Chen and T. D. Bennett, *Nat. Commun.*, 2019, **10**, 2580.
94. T. D. Bennett, A. K. Cheetham, A. H. Fuchs and F.-X. Coudert, *Nat. Chem.*, 2017, **9**, 11-16.
95. T. D. Bennett, T. K. Todorova, E. F. Baxter, D. G. Reid, C. Gervais, B. Bueken, B. Van de Voorde, D. De Vos, D. A. Keen and C. Mellot-Draznieks, *Phys. Chem. Chem. Phys.*, 2016, **18**, 2192-2201.
96. T. D. Bennett, A. H. Fuchs, A. K. Cheetham and F.-X. Coudert, *Dalton Trans.*, 2016, **45**, 4058-4059.
97. T. D. Bennett and A. K. Cheetham, *Acc. Chem. Res.*, 2014, **47**, 1555-1562.
98. T. D. Bennett, S. Cao, J. C. Tan, D. A. Keen, E. G. Bithell, P. J. Beldon, T. Friscic and A. K. Cheetham, *J. Am. Chem. Soc.*, 2011, **133**, 14546-14549.
99. C. Rosler and R. A. Fischer, *CrystEngComm*, 2015, **17**, 199-217.
100. C. Rösler, D. Esken, C. Wiktor, H. Kobayashi, T. Yamamoto, S. Matsumura, H. Kitagawa and R. A. Fischer, *Eur. J. Inorg. Chem.*, 2014, **2014**, 5514-5521.
101. Q. Yang, Q. Xu and H.-L. Jiang, *Chem. Soc. Rev.*, 2017, **46**, 4774-4808.

-
102. J. Juan-Alcañiz, J. Gascon and F. Kapteijn, *J. Mater. Chem.*, 2012, **22**, 10102-10118.
103. I. Luz, C. Rösler, K. Epp, F. X. Llabrés i Xamena and R. A. Fischer, *Eur. J. Inorg. Chem.*, 2015, **2015**, 3904-3912.
104. J. Yu, C. Mu, B. Yan, X. Qin, C. Shen, H. Xue and H. Pang, *Materials Horizons*, 2017, **4**, 557-569.
105. D. E. Coupry, J. Butson, P. S. Petkov, M. Saunders, K. O'Donnell, H. Kim, C. Buckley, M. Addicoat, T. Heine and P. A. Szilágyi, *Chem. Commun.*, 2016, **52**, 5175-5178.
106. P. Á. Szilágyi, D. M. Rogers, I. Zaiser, E. Callini, S. Turner, A. Borgschulte, A. Züttel, H. Geerlings, M. Hirscher and B. Dam, *J. Mater. Chem. A*, 2017, **5**, 15559-15566.
107. P. Guo, Q. Fu, C. Yıldız, Y.-T. Chen, K. Ollegott, C. Froese, W. Kleist, R. A. Fischer, Y. Wang, M. Muhler and B. Peng, *Catal. Sci. Technol.*, 2019, **9**, 3703-3710.
108. J. D. Butson, H. Kim, K. Murugappan, M. Saunders, C. E. Buckley, D. S. Silvester and P. Á. Szilágyi, *ChemPhysChem*, 2019, **20**, 745-751.
109. T. Wang, L. Gao, J. Hou, S. J. A. Herou, J. T. Griffiths, W. Li, J. Dong, S. Gao, M.-M. Titirici, R. V. Kumar, A. K. Cheetham, X. Bao, Q. Fu and S. K. Smoukov, *Nat. Commun.*, 2019, **10**, 1340.
110. Y.-Z. Chen, B. Gu, T. Uchida, J. Liu, X. Liu, B.-J. Ye, Q. Xu and H.-L. Jiang, *Nat. Commun.*, 2019, **10**, 3462.
111. A. Corma, H. García and F. X. Llabrés i Xamena, *Chem. Rev.*, 2010, **110**, 4606-4655.
112. J. Gascon, A. Corma, F. Kapteijn and F. X. Llabrés i Xamena, *ACS Catal.*, 2014, **4**, 361-378.
113. J. Liang, Z. Liang, R. Zou and Y. Zhao, *Adv. Mater.*, 2017, **29**, 1701139.
114. M. Fujita, Y. J. Kwon, S. Washizu and K. Ogura, *J. Am. Chem. Soc.*, 1994, **116**, 1151-1152.
115. J. Lee, O. K. Farha, J. Roberts, K. A. Scheidt, S. T. Nguyen and J. T. Hupp, *Chem. Soc. Rev.*, 2009, **38**, 1450-1459.
116. H. Wee Lik, L. Alaerts, J. A. Martens and D. De Vos, *Metal-Organic Frameworks*, 2011, Wiley-VCH, Weinheim.
117. C. J. Doonan and C. J. Sumby, *CrystEngComm*, 2017, **19**, 4044-4048.
118. K. T. Dinh, M. M. Sullivan, P. Serna, R. J. Meyer, M. Dincă and Y. Román-Leshkov, *ACS Catal.*, 2018, **8**, 8306-8313.
119. V. P. Santos, T. A. Wezendonk, J. J. D. Jaén, A. I. Dugulan, M. A. Nasalevich, H.-U. Islam, A. Chojecki, S. Sartipi, X. Sun, A. A. Hakeem, A. C. J. Koeken, M. Ruitenbeek, T. Davidian, G. R. Meima, G. Sankar, F. Kapteijn, M. Makkee and J. Gascon, *Nat. Commun.*, 2015, **6**, 6451.
120. W. Xia, R. Zou, L. An, D. Xia and S. Guo, *Ener. Environ. Sci.*, 2015, **8**, 568-576.
121. L. Oar-Arteta, T. Wezendonk, X. Sun, F. Kapteijn and J. Gascon, *Mater. Chem. Front.*, 2017, **1**, 1709-1745.
122. T. A. Wezendonk, V. P. Santos, M. A. Nasalevich, Q. S. E. Warringa, A. I. Dugulan, A. Chojecki, A. C. J. Koeken, M. Ruitenbeek, G. Meima, H.-U. Islam, G. Sankar, M. Makkee, F. Kapteijn and J. Gascon, *ACS Catal.*, 2016, **6**, 3236-3247.
123. L. Oar-Arteta, T. Wezendonk, X. Sun, F. Kapteijn and J. Gascon, *Nanotechnology in Catalysis*, 2017, Wiley-VCH, Weinheim.
124. Y.-Z. Chen, R. Zhang, L. Jiao and H.-L. Jiang, *Coord. Chem. Rev.*, 2018, **362**, 1-23.
125. R. V. Jagadeesh, K. Murugesan, A. S. Alshammari, H. Neumann, M.-M. Pohl, J. Radnik and M. Beller, *Science*, 2017, **358**, 326-332.
126. M. A. Nasalevich, M. van der Veen, F. Kapteijn and J. Gascon, *CrystEngComm*, 2014, **16**, 4919-4926.
127. L. Zeng, X. Guo, C. He and C. Duan, *ACS Catal.*, 2016, **6**, 7935-7947.
128. Y. Li, H. Xu, S. Ouyang and J. Ye, *Phys. Chem. Chem. Phys.*, 2016, **18**, 7563-7572.
129. L. Alaerts, E. Séguin, H. Poelman, F. Thibault-Starzyk, P. A. Jacobs and D. E. De Vos, *Chem. Eur. J.*, 2006, **12**, 7353-7363.
130. A. Grigoropoulos, A. I. McKay, A. P. Katsoulidis, R. P. Davies, A. Haynes, L. Brammer, J. Xiao, A. S. Weller and M. J. Rosseinsky, *Angew. Chem. Int. Ed.*, 2018, **57**, 4532-4537.
131. Y. Luan, N. Zheng, Y. Qi, J. Tang and G. Wang, *Catal. Sci. Technol.*, 2014, **4**, 925-929.
132. A. M. Rasero-Almansa, A. Corma, M. Iglesias and F. Sánchez, *ChemCatChem*, 2014, **6**, 1794-1800.
133. D. M. D'Alessandro, *Chem. Commun.*, 2016, **52**, 8957-8971.
134. A. Lieb, H. Leclerc, T. Devic, C. Serre, I. Margiolaki, F. Mahjoubi, J. S. Lee, A. Vimont, M. Daturi and J.-S. Chang, *Micropor. Mesopor. Mater.*, 2012, **157**, 18-23.
135. J. Szanyi, M. Daturi, G. Clet, D. R. Baer and C. H. F. Peden, *Phys. Chem. Chem. Phys.*, 2012, **14**, 4383-4390.
136. D. Osadchii, A. I. Olivos Suarez, Á. Szécsényi, G. Li, M. A. Nasalevich, A. I. Dugulan, P. Serra-Crespo, E. J. M. Hensen, S. L. Veber, M. V. Fedin, G. Sankar, E. A. Pidko and J. Gascon, *ACS Catal.*, 2018, **8**, 5542-5548

-
137. C. K. Brozek and M. Dincă, *J. Am. Chem. Soc.*, 2013, **135**, 12886-12891.
138. D. J. Xiao, E. D. Bloch, J. A. Mason, W. L. Queen, M. R. Hudson, N. Planas, J. Borycz, A. L. Dzubak, P. Verma, K. Lee, F. Bonino, V. Crocellà, J. Yano, S. Bordiga, D. G. Truhlar, L. Gagliardi, C. M. Brown and J. R. Long, *Nat. Chem.*, 2014, **6**, 590-595.
139. A. F. Cozzolino, C. K. Brozek, R. D. Palmer, J. Yano, M. Li and M. Dincă, *J. Am. Chem. Soc.*, 2014, **136**, 3334-3337.
140. P. Verma, K. D. Vogiatzis, N. Planas, J. Borycz, D. J. Xiao, J. R. Long, L. Gagliardi and D. G. Truhlar, *J. Am. Chem. Soc.*, 2015, **137**, 5770-5781.
141. A. Dhakshinamoorthy, M. Alvaro, P. Horcajada, E. Gibson, M. Vishnuvarthan, A. Vimont, J.-M. Grenèche, C. Serre, M. Daturi and H. Garcia, *ACS Catal.*, 2012, **2**, 2060-2065.
142. I. Agirrezabal-Telleria, I. Luz, M. A. Ortúñoz, M. Oregui-Bengoechea, I. Gandarias, N. López, M. A. Lail and M. Soukri, *Nat. Commun.*, 2019, **10**, 2076.
143. G. Bauer, D. Ongari, X. Xu, D. Tiana, B. Smit and M. Ranocchiari, *J. Am. Chem. Soc.*, 2017, **139**, 18166-18169.
144. X. Zhang, F. X. Llabrés i Xamena and A. Corma, *J. Catal.*, 2009, **265**, 155-160.
145. A. Burgun, J. Coghlan Campbell, M. Huang David, W. Chen, S. Horike, S. Kitagawa, F. Alvino Jason, F. Metha Gregory, J. Sumby Christopher and J. Doonan Christian, *Angew. Chem. Int. Ed.*, 2017, **56**, 8412-8416.
146. J. Canivet, S. Aguado, Y. Schuurman and D. Farrusseng, *J. Am. Chem. Soc.*, 2013, **135**, 4195-4198.
147. L. Braglia, E. Borfecchia, L. Maddalena, S. Øien, K. A. Lomachenko, A. L. Bugaev, S. Bordiga, A. V. Soldatov, K. P. Lillerud and C. Lamberti, *Catal. Today*, 2017, **283**, 89-103.
148. S. Øien, G. Agostini, S. Svelle, E. Borfecchia, K. A. Lomachenko, L. Mino, E. Gallo, S. Bordiga, U. Olsbye, K. P. Lillerud and C. Lamberti, *Chem. Mater.*, 2015, **27**, 1042-1056.
149. D. Yang, S. O. Odoh, T. C. Wang, O. K. Farha, J. T. Hupp, C. J. Cramer, L. Gagliardi and B. C. Gates, *J. Am. Chem. Soc.*, 2015, **137**, 7391-7396.
150. J. Yuan, A. M. Fracaroli and W. G. Klemperer, *Organometallics*, 2016, **35**, 2149-2155.
151. A. Chołuj, A. Zieliński, K. Grela and M. J. Chmielewski, *ACS Catal.*, 2016, **6**, 6343-6349.
152. F. L. Morel, X. Xu, M. Ranocchiari and J. A. van Bokhoven, *Chemistry of Organo-Hybrids*, 2015, Wiley-VCH, Weinheim.
153. D. T. Genna, L. Y. Pfund, D. C. Samblanet, A. G. Wong-Foy, A. J. Matzger and M. S. Sanford, *ACS Catal.*, 2016, **6**, 3569-3574.
154. M. D. Korzynski, D. F. Consoli, S. Zhang, Y. Roman-Leshkov and M. Dinca, *J. Am. Chem. Soc.*, 2018, **140**, 6956-6960.
155. R. J. Comito, Z. Wu, G. Zhang, J. A. Lawrence, M. D. Korzyński, J. A. Kehl, J. T. Miller and M. Dincă, *Angew. Chem. Int. Ed.*, 2018, **57**, 8135 -8139.
156. H. D. Park, M. Dinca and Y. Roman-Leshkov, *J. Am. Chem. Soc.*, 2018, **140**, 10669-10672.
157. M. T. Huxley, A. Burgun, H. Ghodrati, C. J. Coghlan, A. Lemieux, N. R. Champness, D. M. Huang, C. J. Doonan and C. J. Sumby, *J. Am. Chem. Soc.*, 2018, **140**, 6416-6425.
158. M. Yoon, R. Srirambalaji and K. Kim, *Chem. Rev.*, 2012, **112**, 1196-1231.
159. S.-H. Cho, B. Ma, S. T. Nguyen, J. T. Hupp and T. E. Albrecht-Schmitt, *Chem. Commun.*, 2006, 2563-2565.
160. A. Hu, H. L. Ngo and W. Lin, *J. Am. Chem. Soc.*, 2003, **125**, 11490-11491.
161. F. Song, C. Wang, J. M. Falkowski, L. Ma and W. Lin, *J. Am. Chem. Soc.*, 2010, **132**, 15390-15398.
162. C.-D. Wu, A. Hu, L. Zhang and W. Lin, *J. Am. Chem. Soc.*, 2005, **127**, 8940-8941.
163. J. M. Falkowski, T. Sawano, T. Zhang, G. Tsun, Y. Chen, J. V. Lockard and W. Lin, *J. Am. Chem. Soc.*, 2014, **136**, 5213-5216.
164. L. Ma, J. M. Falkowski, C. Abney and W. Lin, *Nat. Chem.*, 2010, **2**, 838-846.
165. T. Sawano, N. C. Thacker, Z. Lin, A. R. McIsaac and W. Lin, *J. Am. Chem. Soc.*, 2015, **137**, 12241-12248.
166. L. Ma, C. Abney and W. Lin, *Chem. Soc. Rev.*, 2009, **38**, 1248-1256.
167. A. E. Platero-Prats, A. Mavrandonakis, L. C. Gallington, Y. Liu, J. T. Hupp, O. K. Farha, C. J. Cramer and K. W. Chapman, *J. Am. Chem. Soc.*, 2016, **138**, 4178-4185.
168. I. S. Kim, O. K. Farha, J. T. Hupp, L. Gagliardi, K. W. Chapman, C. Cramer and A. B. F. Martinson, *ECS Trans.*, 2016, **75**, 93-99.
169. R. C. Klet, T. C. Wang, L. E. Fernandez, D. G. Truhlar, J. T. Hupp and O. K. Farha, *Chem. Mater.*, 2016, **28**, 1213-1219.
170. S. Ahn, N. E. Thornburg, Z. Li, T. C. Wang, L. C. Gallington, K. W. Chapman, J. M. Notestein, J. T. Hupp and O. K. Farha, *Inorg. Chem.*, 2016, **55**, 11954-11961.
-

-
171. L. C. Gallington, I. S. Kim, W.-G. Liu, A. A. Yakovenko, A. E. Platero-Prats, Z. Li, T. C. Wang, J. T. Hupp, O. K. Farha, D. G. Truhlar, A. B. F. Martinson and K. W. Chapman, *J. Am. Chem. Soc.*, 2016, **138**, 13513-13516.
172. A. W. Peters, Z. Li, O. K. Farha and J. T. Hupp, *ACS Appl. Mater. Interfaces*, 2016, **8**, 20675-20681.
173. A. B. Thompson, D. R. Pahls, V. Bernales, L. C. Gallington, C. D. Malonzo, T. Webber, S. J. Tereniak, T. C. Wang, S. P. Desai, Z. Li, I. S. Kim, L. Gagliardi, R. L. Penn, K. W. Chapman, A. Stein, O. K. Farha, J. T. Hupp, A. B. F. Martinson and C. C. Lu, *Chem. Mater.*, 2016, **28**, 6753-6762.
174. Z. Li, N. M. Schweitzer, A. B. League, V. Bernales, A. W. Peters, A. B. Getsoian, T. C. Wang, J. T. Miller, A. Vjunov, J. L. Fulton, J. A. Lercher, C. J. Cramer, L. Gagliardi, J. T. Hupp and O. K. Farha, *J. Am. Chem. Soc.*, 2016, **138**, 1977-1982.
175. V. Bernales, A. B. League, Z. Li, N. M. Schweitzer, A. W. Peters, R. K. Carlson, J. T. Hupp, C. J. Cramer, O. K. Farha and L. Gagliardi, *J. Phys. Chem. C*, 2016, **120**, 23576-23583.
176. W. Bury, O. K. Farha, J. T. Hupp and J. E. Mondloch, US Patent, *US20150031908A1*, 2015.
177. W. Bury, O. K. Farha, J. T. Hupp and J. E. Mondloch, US Patent, *US20150031908A1*, 2015.
178. I. S. Kim, J. Borycz, A. E. Platero-Prats, S. Tussupbayev, T. C. Wang, O. K. Farha, J. T. Hupp, L. Gagliardi, K. W. Chapman, C. J. Cramer and A. B. F. Martinson, *Chem. Mater.*, 2015, **27**, 4772-4778.
179. A. W. Peters, Z. Li, O. K. Farha and J. T. Hupp, *ACS Nano*, 2015, **9**, 8484-8490.
180. R. C. Klet, S. Tussupbayev, J. Borycz, J. R. Gallagher, M. M. Stalzer, J. T. Miller, L. Gagliardi, J. T. Hupp, T. J. Marks, C. J. Cramer, M. Delferro and O. K. Farha, *J. Am. Chem. Soc.*, 2015, **137**, 15680-15683.
181. S. T. Madrahimov, J. R. Gallagher, G. Zhang, Z. Meinhart, S. J. Garibay, M. Delferro, J. T. Miller, O. K. Farha, J. T. Hupp and S. T. Nguyen, *ACS Catal.*, 2015, **5**, 6713-6718.
182. J. E. Mondloch, W. Bury, D. Fairén-Jimenez, S. Kwon, E. J. DeMarco, M. H. Weston, A. A. Sarjeant, S. T. Nguyen, P. C. Stair, R. Q. Snurr, O. K. Farha and J. T. Hupp, *J. Am. Chem. Soc.*, 2013, **135**, 10294-10297.
183. P. Ji, J. B. Solomon, Z. Lin, A. Johnson, R. F. Jordan and W. Lin, *J. Am. Chem. Soc.*, 2017, **139**, 11325-11328.
184. K. Manna, P. Ji, Z. Lin, F. X. Greene, A. Urban, N. C. Thacker and W. Lin, *Nat. Commun.*, 2016, **7**, 12610.
185. P. Ji, K. Manna, Z. Lin, A. Urban, F. X. Greene, G. Lan and W. Lin, *J. Am. Chem. Soc.*, 2016, **138**, 12234-12242.
186. S. Kim In, Z. Li, J. Zheng, A. E. Platero-Prats, A. Mavrandakis, S. Pellizzeri, M. Ferrandon, A. Vjunov, L. C. Gallington, T. E. Webber, N. A. Vermeulen, R. L. Penn, R. B. Getman, C. J. Cramer, K. W. Chapman, D. M. Camaioni, J. L. Fulton, J. A. Lercher, O. K. Farha, J. T. Hupp and A. B. F. Martinson, *Angew. Chem. Int. Ed.*, 2018, **57**, 909-913.
187. X. Zhang, Z. Huang, M. Ferrandon, D. Yang, L. Robison, P. Li, T. C. Wang, M. Delferro and O. K. Farha, *Nat. Catal.*, 2018, **1**, 356-362.
188. S. Ahn, S. L. Nauert, C. T. Buru, M. Rimoldi, H. Choi, N. M. Schweitzer, J. T. Hupp, O. K. Farha and J. M. Notestein, *J. Am. Chem. Soc.*, 2018, **140**, 8535-8543.
189. M. Zhao, K. Yuan, Y. Wang, G. Li, J. Guo, L. Gu, W. Hu, H. Zhao and Z. Tang, *Nature*, 2016, **539**, 76-80.
190. Y. Fang, Z. Xiao, J. Li, C. Lollar, L. Liu, X. Lian, S. Yuan, S. Banerjee, P. Zhang and H. C. Zhou, *Angew. Chem. Int. Ed.*, 2018, **57**, 5283-5287.
191. B. Aguilera, Q. Sun, X. Wang, E. O'Rourke, M. Al-Enizi Abdullah, A. Nafady and S. Ma, *Angew. Chem. Int. Ed.*, 2018, **57**, 10107-10111.
192. M. Müller, S. Hermes, K. Kähler, M. W. E. van den Berg, M. Muhler and R. A. Fischer, *Chem. Mater.*, 2008, **20**, 4576-4587.
193. M. Muller, O. I. Lebedev and R. A. Fischer, *J. Mater. Chem.*, 2008, **18**, 5274-5281.
194. X. Fan, R. Vakili, E. Gibson, S. Chansai, S. Xu, P. Wells, C. Hardacre, A. Walton and N. Al-Janabi, *ChemCatChem*, 2018, **10**, 4238-4242.
195. C. L. Whitford, C. J. Stephenson, D. A. Gómez-Gualdrón, J. T. Hupp, O. K. Farha, R. Q. Snurr and P. C. Stair, *J. Phys. Chem. C*, 2017, **121**, 25079-25091.
196. X. Lian, Y. Fang, E. Joseph, Q. Wang, J. Li, S. Banerjee, C. Lollar, X. Wang and H.-C. Zhou, *Chem. Soc. Rev.*, 2017, **46**, 3386-3401.
197. J. Juan-Alcaniz, M. G. Goesten, E. V. Ramos-Fernandez, J. Gascon and F. Kapteijn, *New J. Chem.*, 2012, **36**, 977-987.
198. E. V. Ramos-Fernandez, C. Pieters, B. van der Linden, J. Juan-Alcañiz, P. Serra-Crespo, M. W. G. M. Verhoeven, H. Niemantsverdriet, J. Gascon and F. Kapteijn, *J. Catal.*, 2012, **289**, 42-52.
199. K. Leus, P. Concepcion, M. Vandichel, M. Meledina, A. Grirrane, D. Esquivel, S. Turner, D. Poelman, M. Waroquier, V. Van Speybroeck, G. Van Tendeloo, H. Garcia and P. Van Der Voort, *RSC Adv.*, 2015, **5**, 22334-22342.
-

-
200. S. Hermes, M.-K. Schröter, R. Schmid, L. Khodeir, M. Muhler, A. Tissler, R. W. Fischer and R. A. Fischer, *Angew. Chem. Int. Ed.*, 2005, **44**, 6237-6241.
201. H.-L. Jiang, Q.-P. Lin, T. Akita, B. Liu, H. Ohashi, H. Oji, T. Honma, T. Takei, M. Haruta and Q. Xu, *Chem. Eur. J.*, 2011, **17**, 78-81.
202. T. Ishida, M. Nagaoka, T. Akita and M. Haruta, *Chem. Eur. J.*, 2008, **14**, 8456-8460.
203. A. Dhakshinamoorthy and H. Garcia, *Chem. Soc. Rev.*, 2012, **41**, 5262-5284.
204. M. Meilikhov, K. Yusenko, D. Esken, S. Turner, G. Van Tendeloo and R. A. Fischer, *Eur. J. Inorg. Chem.*, 2010, **2010**, 3701-3714.
205. H. R. Moon, D.-W. Lim and M. P. Suh, *Chem. Soc. Rev.*, 2013, **42**, 1807-1824.
206. P. Falcaro, R. Ricco, A. Yazdi, I. Imaz, S. Furukawa, D. MasPOCH, R. Ameloot, J. D. Evans and C. J. Doonan, *Coord. Chem. Rev.*, 2016, **307**, 237-254.
207. C. R. Kim, T. Uemura and S. Kitagawa, *Chem. Soc. Rev.*, 2016, **45**, 3828-3845.
208. F. R. Fortea-Pérez, M. Mon, J. Ferrando-Soria, M. Boronat, A. Leyva-Pérez, A. Corma, J. M. Herrera, D. Osadchii, J. Gascon, D. Armentano and E. Pardo, *Nat. Mater.*, 2017, **16**, 760.
209. M. Mon, M. A. Rivero-Crespo, J. Ferrando-Soria, A. Vidal-Moya, M. Boronat, A. Leyva-Pérez, A. Corma, J. C. Hernández-Garrido, M. López-Haro, J. J. Calvino, G. Ragazzon, A. Credi, D. Armentano and E. Pardo, *Angew. Chem. Int. Ed.*, 2018, **0**.
210. M. Tejeda-Serrano, M. Mon, B. Ross, F. Gonell, J. Ferrando-Soria, A. Corma, A. Leyva-Pérez, D. Armentano and E. Pardo, *J. Am. Chem. Soc.*, 2018, **140**, 8827-8832.
211. Y. Chen, H. Li, W. Zhao, W. Zhang, J. Li, W. Li, X. Zheng, W. Yan, W. Zhang, J. Zhu, R. Si and J. Zeng, *Nat. Commun.*, 2019, **10**, 1885.

Chapter 2

Advanced Spectroscopy and Structural Characterization of MIL-100 and HKUST-1 Metal-Organic Framework Materials

In this Chapter, a review of the spectroscopic characterization techniques that can be used for assessing the properties of two specific MOF topologies will be provided. Namely, the different properties of MIL-100 and MIL-101 (which are isoreticular) as well as the HKUST-1 structures, have been studied by means of different spectroscopic tools. We will emphasize the study of coordinatively unsaturated sites (CUS) arising from the removal of counterions at high temperature, their acidic properties as Lewis sites and the use of in-situ and operando techniques. Temperature treatments and the presence of non-coordinating linkers can also lead to the reduced oxidation states of the metals, a phenomenon with implications in catalysis or gas separation. It is important to mention that this chapter is focused on the used advanced characterization tools that provide additional insight into the crystal lattices, rather than resolving their structure (e.g. X-ray and neutron diffraction, Rietveld refinement; or electron diffraction techniques).

Parts of this Chapter are reported in the following manuscript: "Spectroscopy, Microscopy, Diffraction and Scattering of Archetypal Metal-Organic Frameworks: Formation, Spatial Heterogeneities and Thin-Films", M. Rivera-Torrente, M. Filez, L. D. B. Mandemaker, G. Delen, B. Seoane, F. Meirer, B. M. Weckhuysen, *Chem. Soc. Rev.*, **2020**, in preparation.

2.1 INTRODUCTION

The fact that Metal-Organic Frameworks (MOFs) are typically crystalline has allowed for the use of single-crystal and powder X-ray Diffraction (XRD) with the subsequent Pawley fits and Rietveld refinements for framework structure solution to determine their structures, which renders them “easy” to characterize compared to other types of solid-state materials.^{1, 2} However, a whole array of properties, such as surface reactivity, framework dynamics, magnetic momenta or acidity, requires the use of advanced spectroscopy beyond crystallography, that needs to be properly combined with other characterization techniques to study textural and stability properties, and supported by theory if possible, to fully understand their properties. Abundant literature is available on these subjects.³⁻⁸ In the particular case of catalysis, understanding acid/redox properties of the metal cations is crucial. Important contributions utilizing *in-situ* studies have been made over the past 10 years for the most relevant MOF topologies. To introduce the topologies that have been used in this PhD thesis, a description of their most relevant features and how they have been studied in the past will be done in the following subsections. This includes electronic, vibrational and X-ray spectroscopy, as well as *in-situ* and *operando* studies of the MOFs under working (either catalysis or gas separation) conditions.

2.2 MIL-100 and MIL-101

MIL-100 and MIL-101 have been intensively studied since they were first reported by Férey *et al.* in the mid-2000s.^{9, 10} They consist of 1,3,5-benzenetricarboxylate (BTC) and 1,4-benzenedicarboxylate (BDC), respectively, and μ_3 -O-centered trinuclear inorganic clusters $M_3(\mu_3\text{-O})(O_2C\text{-R})_6$, where $M = Cr^{3+}$, Fe^{3+} ,¹¹ Al^{3+} ,¹² $V^{3+/4+}$,¹³ Sc^{3+} ,¹⁴ Ti^{3+} ,¹⁵ Mn^{3+16} or In^{3+} .¹⁷ In the as-synthesized form, each metallic centre is in an octahedral environment coordinated by one common μ_3 -O atom, shared with the other two metallic centres building the cluster, four oxygen atoms from the organic linker and one terminal ligand. While two metallic octahedra per cluster are coordinated by terminal aqua ligands, the third terminal ligand is an anionic species, typically either a hydroxido ligand or a halide anion (such as F^- or Cl^- , depending on the synthesis conditions), needed to compensate the negative default

charge per inorganic cluster of the framework. The μ_3 -O-centered trinuclear clusters are then linked through the organic moieties to form hybrid supertetrahedra, which further assemble into a 3D porous framework having the zeolite MTN topology. This topology possesses two different types of mesoporous cages of 25 Å and 29 Å (MIL-100) and 29 Å and 34 Å (MIL-101), delimited by microporous pentagonal and hexagonal windows of 5 Å and 8.6 Å (MIL-100) and 12 Å and 14.7 Å (MIL-101). A scheme is provided in Figure 2.1. Depending on the metal and the activation procedure, MIL-100 and MIL-101 have been reported to possess Brunnauer-Emmett-Teller (BET) areas up to 2300 and 4100 $\text{m}^2\cdot\text{g}^{-1}$, respectively, exceptional hydrothermal stability and a relatively high thermal stability. This set of properties, together with the presence of Coordinatively Unsaturated Sites (CUS) in the inorganic Secondary Building Units (SBUs) upon activation and the presence of mesoporous cages, makes these MOF frameworks one of the topologies of choice for study in different fields.¹⁸

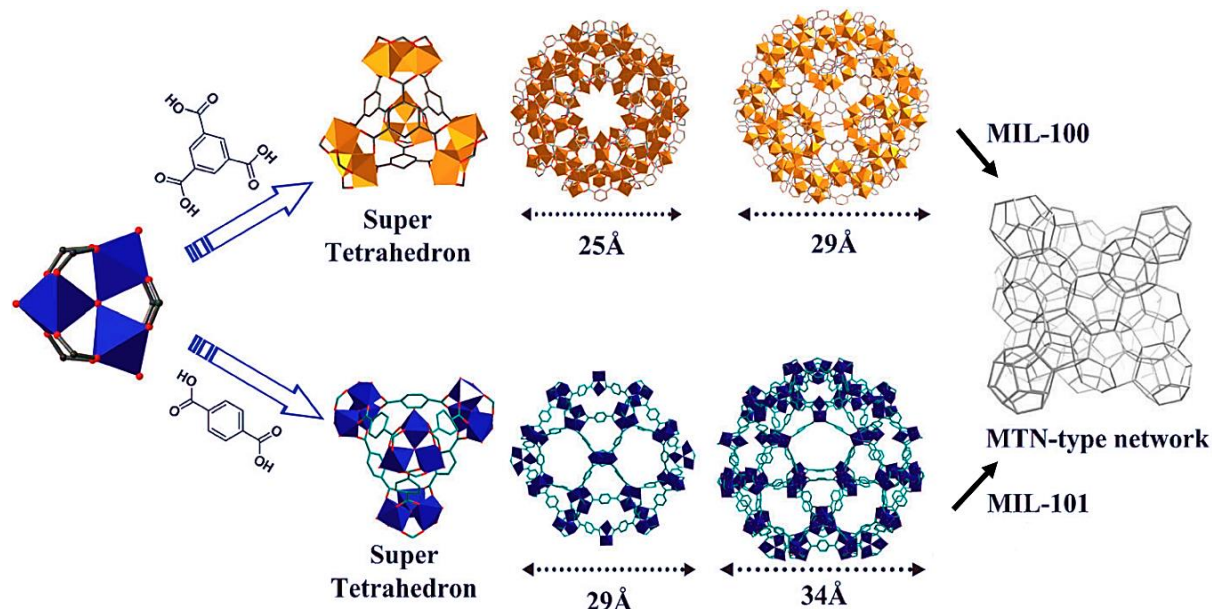


Figure 2.1. Structure of MIL-100 and 101 formed by μ_3 -O-centered trinuclear metallic clusters linked through the organic linker into a supertetrahedron, which further assembles into a porous framework having the MTN topology. Reprinted from reference [19]. Copyright © American Chemical Society, 2013.

Exposed CUS can act as Lewis acid sites, binding gas or liquid molecules during a separation process; or promoting bond cleavage in a certain molecule during catalysis. MIL-100 and MIL-101 have been reported to exhibit CUS upon removal of the terminal

ligands present at the apical positions of the metallic octahedra forming the inorganic μ_3 -O-centered clusters. Vimont *et al.*^{20, 21} studied the nature of the terminal ligands coordinating the chromium atoms in MIL-100(Cr), with chemical composition $(Cr^{III})_3OF_{0.85}(OH)_{0.15}(H_2O)_2 \cdot nH_2O$, as a function of the MOF outgassing temperature, as measured by Fourier Transform Infrared (FT-IR) spectroscopy (Table 2.1).

Table 2.1. Wavenumbers and modes of the infrared bands assigned to different water species of MIL-100(Cr) upon dehydration. Adapted from reference [21].

Water species	$\nu_3 (\nu_{as}) [\text{cm}^{-1}]$	$\nu_1 (\nu_s) [\text{cm}^{-1}]$	$\nu_2 + \nu_3 [\text{cm}^{-1}]$	$\nu_2 + \delta(H_2O) [\text{cm}^{-1}]$
$H_2O \rightarrow Cr^{3+}$ (species 1)	3700	3608	5274	1596
$H_2O \rightarrow Cr^{3+}$ (species 1')	3683	3595	5265	1604
$H_2O \cdots H_2O \rightarrow Cr$ (species 2)	3680	3588	5252	1603
$H_2O \cdots H_2O \rightarrow Cr$	3670	2950	5320	1650

Upon degassing at 573 K, only two bands were observed in the 3700-3000 cm⁻¹ range: the stretching modes of Cr-OH species and the aromatic C-H of the terephthalate moieties (at 3585 cm⁻¹ and 3090 cm⁻¹, respectively), with no $\nu(OH)$ bands ascribed to water. The absence of bands in the 5400 - 5000 cm⁻¹ range, in which the $\nu + \delta(H_2O)$ combination mode of water should be obtained, further corroborated the complete removal water molecules, pointing to the generation of open metal sites at this activation temperature. When the degassing temperature was decreased to 423 K and 373 K, new bands appeared in the 5300 - 5200 cm⁻¹ and 3800 - 3500 cm⁻¹ ranges, attributed to the formation of two different water species coordinated to the unsaturated metal sites. The formation of two different species was related to the metal centers heterogeneity, due to a heterogeneous distribution of the anionic terminal ligands (in this case fluoride anions), being 0, 1 or 2 per trinuclear inorganic cluster. When the outgassing temperature was further decreased, new bands were observed, which corresponded to the appearance of new Cr-H₂O/H₂O water species, not directly bound to the metal, but H-bonded to the previously adsorbed Cr-H₂O water species instead.

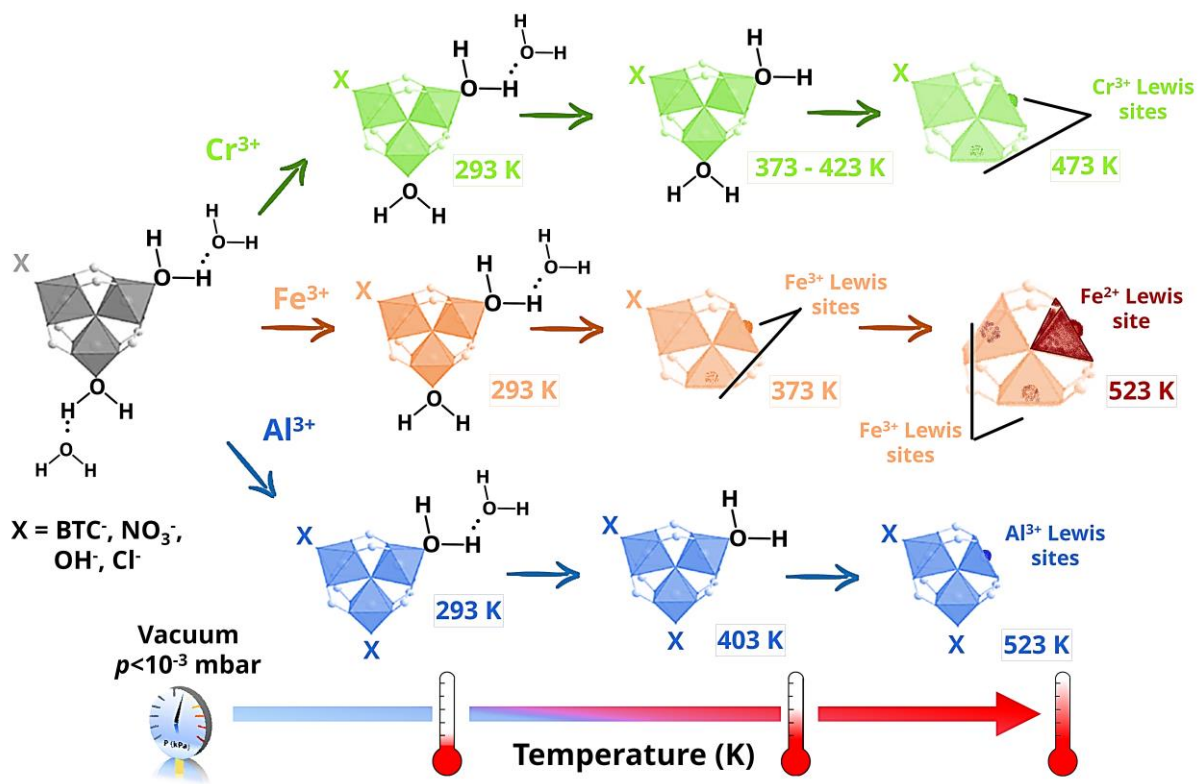


Figure 2.2 Location and interaction of water molecules with the open metal sites present in the inorganic trimers of MIL-100 as a function of the MOF outgassing temperature for different for different MIL-100 analogues.

In contrast to MIL-100(Cr), for which CUS with only a single oxidation state were observed, *i.e.* Cr³⁺, the infrared spectra acquired for MIL-100(Fe) showed two different bands at 618 and 597 cm⁻¹, corresponding to the $\nu_{as}(\text{Fe}^{\text{III}}_3\text{O})$ and $\nu_{as}(\text{Fe}^{\text{II}}_3\text{O})$ vibrations modes, respectively.²² This partial reduction of Fe at higher outgassing temperatures was further confirmed by ⁵⁷Fe Mössbauer spectroscopy and it was related to the partial removal of terminal anionic ligands at 523 K (Figure 2.2). In the case of MIL-100(Al), FT-IR spectroscopy and solid-state Nuclear Magnetic Resonance (NMR) studies pointed to a different scenario, in which only one of the two terminal aqua ligands per trinuclear cluster can be removed.^{23,24} This different behaviour was related to the presence of different impurities, in particular NO₃⁻ from the metal salt used for the MOF synthesis and H₃BTC, probably coordinated to the aluminium open metal sites. In a further step, several research groups evaluated the Brønsted and Lewis acidity of different MIL-100 analogues by infrared spectroscopy using different basic probe molecules. To this end, CO is one the most widely used probe to evaluate protonic acidity. When probing Brønsted acid sites, CO

interacts with protons, leading to shifts in both the $\nu(\text{OH})$ and $\nu(\text{CO})$ IR bands, so that the larger the shift, the stronger the acidity. M-OH species (only observed for Al and Cr-based analogues, but not in the case of MIL-100(Fe) and MIL-100(V)) gave rise to $\Delta\nu(\text{OH}) = 90$ and 86 cm^{-1} for MIL-100(Cr) and MIL-100(Al), respectively, showing a fairly weak acidity, close to that of silanol groups in silicalite ($\Delta\nu(\text{OH}) = 100 \text{ cm}^{-1}$). The highest Brønsted acidity was observed for the M-H₂O species, where the water molecules were located in the cation coordination sphere.²⁵ In this case, the $\Delta\nu(\text{OH})$ value was 160 cm^{-1} , close to that of alkali-exchanged faujasite ($\Delta\nu(\text{OH}) = 160 \text{ cm}^{-1}$) or P-OH groups of phosphated silica ($\Delta\nu(\text{OH}) = 180 \text{ cm}^{-1}$). Interestingly, as demonstrated by Vimont and co-workers, this Brønsted acidity can be modified by substituting the coordinated water by different OH-containing organic molecules, paving the way to the fine tuning of the acidic properties of MOFs.²⁰ Furthermore, Brønsted acid sites can be converted into Lewis acid sites upon framework dehydration, which can be also probed with different probe molecules (Table 2.2). As expected, in the case of MIL-100(Fe) two different $\nu(\text{CO})$ bands were observed in the $2170 - 2166 \text{ cm}^{-1}$ and $2192 - 2173 \text{ cm}^{-1}$ ranges, which is assigned to CO adsorbed on Fe²⁺ and Fe³⁺ CUS, respectively.²⁶ Moreover, for MIL-100(Al) half of the CUS calculated for MIL-100(Cr) and MIL-100(Fe) were obtained, in line with the presence of different impurities previously observed by infrared and NMR spectroscopy.²⁴

Table 2.2. Amount of coordinatively unsaturated sites (CUS) reported by Vimont *et al.*,²¹ Leclerc *et al.*²² and Volkinger *et al.*²⁴ for different MIL-100 analogues together with the wavenumbers of several coordinated probe molecules on the different frameworks.

MIL-100 analogue	M ²⁺ CUS [$\mu\text{mol}\cdot\text{g}^{-1}$]	M ³⁺ CUS [$\mu\text{mol}\cdot\text{g}^{-1}$]	Total M CUS [$\mu\text{mol}\cdot\text{g}^{-1}$]
MIL-100(Cr) _{523 K}	-	3500	3500
MIL-100(Fe) _{423 K}	45	1895	1940
MIL-100(Fe) _{523 K}	850	2810	3660
MIL-100(Al) _{523 K}	-	1800	1800
MIL-100 analogue	$\nu(\text{CO}) [\text{cm}^{-1}]$	$\text{CD}_3\text{CN } \nu(\text{CN}) [\text{cm}^{-1}]$	$\nu_7 \text{ pyridine} [\text{cm}^{-1}]$
Cr ³⁺ (MIL-100(Cr))	2207, 2200, 2196	2305	1015
Fe ³⁺ (MIL-100(Fe))	2192 – 2173	2304	1014
Al ³⁺ (MIL-100(Al))	2195 – 2184	2326 – 2321	1018

Very recent studies by Gómez-Pozuelo *et al.* with CD₃CN as a probe and catalytic testing show that the Sc and V analogues possess even a higher amount of Lewis sites mmol than MIL-100(Fe) upon dehydration (*ca.* 2600, 2300 and 1500 µmol·g⁻¹ after evacuation at 523 K overnight, respectively).²⁷ This series of works highlight the importance of a thorough characterization of open metal sites in MOFs, since the different activation conditions, coordinated molecules or chemical composition influence the nature, concentration and strength of the framework acid sites. In addition to evaluate the acidity of MOFs, infrared spectroscopy has also been proven as a very powerful tool to study the interaction of CUS with different adsorbates. For instance, Leclerc *et al.*²² examined the influence of the different open metal sites present in MIL-100(Fe), *i.e.* Fe²⁺ and Fe³⁺ on the adsorption of several probe molecules, particularly CO, propene and propyne, able to interact through π -backdonation, and CO₂, pyridine and propane, not able to provide such interaction. FT-IR spectroscopy pointed to a more important role of Fe²⁺ sites, despite their weaker acidity, due to their ability to strongly interact with CO, propene and propyne via π -backdonation, as indicated by the redshifts observed in the $\nu(\text{C-O})$, $\nu(\text{C=C})$, $\nu(\text{C}\equiv\text{C})$ and $\nu(\text{C}\equiv\text{H})$ bands. Indeed, the additional electron in Fe²⁺ *d*-orbitals enables the formation of more stable metal-adsorbate complexes by the transfer of electron density from the *d* orbitals of the Fe²⁺ metal centres to the π^* antibonding orbitals of certain molecules. Yoon *et al.*²⁸ and Wuttke *et al.*²⁶ took advantage of the stronger interaction of Fe²⁺ sites with unsaturated gas molecules, and studied the separation of propene from propane through breakthrough experiments using equimolar propene:propane mixtures. Specifically, Wuttke *et al.* have applied *operando* FT-IR spectroscopy and studied the propene:propane separation performance with and without selectively poisoning the Fe²⁺ sites. In line with previous studies, the adsorption capacity for C₃H₆ is markedly higher without blocking the Fe²⁺ sites, leading to separation factors over 100, which drop to 5.3 upon Fe²⁺ NO poisoning. Further insight into the adsorption of different molecules can be obtained through variable-temperature infrared (VTIR) spectroscopy, which, as shown by Palomino *et al.*²⁹ for H₂ adsorption on MIL-100(Cr) and MIL-101(Cr), allows for the determination of the corresponding values of standard adsorption enthalpy (ΔH_0) and entropy (ΔS_0). Two special cases for understanding the formation of CUS and binding properties in the MIL-100 series are the Sc and the Al analogue, in which solid-state NMR was particularly useful.

The formation of acid Sc^{3+} sites in MIL-100(Sc) remained elusive until Giovine *et al.*^[30] reported on the formation of penta-coordinated sites upon dehydration. A comparison with Sc_3BTB_2 , which shows similar Sc sites, was established, and combining DFT calculations and multinuclear techniques (namely, Resonance-Echo Saturation-Pulse Double-Resonance (RESPDOR ^{13}C -{ ^{45}Sc }), 2- and 3-dimensional Multi-Quantum Magic Angle Spinning (2-3D MQ-MAS ^{45}Sc -{ ^1H }) and Cross-Polarization (CP MAS)), they were able to quantify the number of CUS Sc^{3+} based on their coordination numbers and the asymmetric polarization of the $\text{Sc}_3(\mu_3\text{O})$ clusters. In some cases, additional techniques, such as Electron Paramagnetic Resonance (EPR), have been combined with NMR for characterizing CUS in MIL-100 materials, allowing the authors to reach conclusions that could not be drawn from vibrational techniques. For instance, Barth, Hartman and others^[31] studied the adsorption of NO in MIL-100(Al) by means of DRIFTS, multinuclear NMR and EPR spectroscopies. In a first instance, there are weakly interacting NO with the π -electrons of the aromatic linkers (band at 1861 cm^{-1}) and physisorbed and gaseous NO (1854 and 1874 cm^{-1} , respectively). While no evident bands pointing to $[\text{Al}^{3+}\cdots\text{NO}]$ adducts were observed in the DRIFTS spectra, EPR showed that electrophilic Al^{3+} can polarize NO and transform it into NO^+ . Moreover, the evolution of adsorbed species could be studied as a function of temperature to corroborate that hypothesis. Such type of weak ionic interactions cannot be detected efficiently by FT-IR spectroscopy, while coupling EPR and DFT calculations allowed for an accurate description of this issue.^[32] In order to avoid any confusion with different Al adsorption sites, $^{27}\text{Al}\{{^1\text{H}}\}$ Heteronuclear Correlation (HETCOR) upon dehydration of the MOF was used in another work,^[33] showing the presence of $\text{Al}(\text{OH})_3$ deposits that play a minor role in NO adsorption. In brief, even for a complex case of weak, ionic interactions, the authors were able to obtain an accurate description with adding magnetic resonance spectroscopy to the toolbox of vibrational techniques. EPR and NMR with probe molecules have been extensively used by others successfully in different frameworks,^[34-36] sometimes being able to discriminate between competing adsorbing molecules of very similar nature.^[37]

Thus, beyond the use of well-known basic probe molecules to study MOF acidity, the use of different probe molecules as well as the implementation of more sophisticated

approaches, such as *operando* studies, can give mechanistic insight into catalytic or separation processes, allow for the identification active species and even enable the evaluation of adsorption thermodynamics.

2.3 HKUST-1

Along with MOF-5, the topology known as HKUST-1 (Hong-Kong University of Science and Technology-1)^[38] or MOF-199^[39] has been one of the most studied MOF structures in the past 20 years, and is amongst the few being produced industrially, as Basolite® C300 (BASF), among other commercial names.

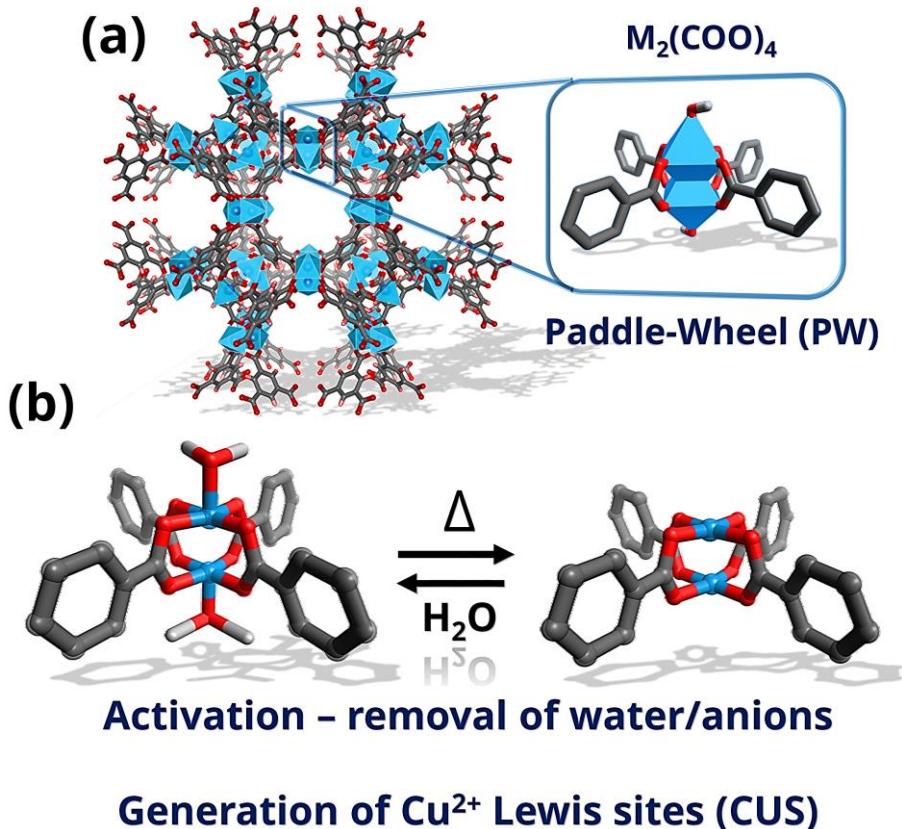


Figure 2.3. (a) Square-shaped pores of 0.9 nm x 0.9 nm dimensions of HKUST-1 formed viewed along the [100] axis; (b) archetypal paddle-wheel and scheme of the formation of CUS by desolvation by release of solvent molecules (C, grey; O, pink; light green, metal; and blue, counter anion or solvent molecule).

In the MOF community, HKUST-1 has become an archetypal example of the MOF branch constructed from well-defined paddle-wheel SBU, which exhibit CUS upon solvent

removal. The framework consists of four carboxylate units connected to dinuclear cationic clusters (see Figure 2.3) with either counter anions (*i.e.*, X⁻ or NO₃⁻) or solvent molecules (*i.e.*, H₂O) on the axial positions. The crystallographic structure relies on the *tbo* topology in space group *Fm*³*m*. Other properties that promoted the study of HKUST-1 are their relative robustness (stable in air for several days or weeks)⁴⁰ and the myriad of metals that can be introduced into the HKUST-1 nodes, including Zn,⁴¹ Mo,⁴² Ru,⁴³ Ni,⁴⁴ Cr⁴⁵ or Fe.⁴⁶ In addition, mixed oxidation states⁴⁷ and radicals⁴⁸ have been observed under certain conditions, which renders this MOF very interesting for applications involving redox chemistry. Recently, several groups^[49] have reported the on-purpose introduction of defective, non-coordinating linkers into the HKUST-1 structure. The resulting metal sites exhibiting increased coordinative undercoordination show increased Lewis acidity,^[50] thus enhancing their potential for adsorptive and catalytic applications.

The formation of CUS in HKUST-1 prompted the use of advanced techniques to study the process of desolvation and gas sorption. Interestingly, Peterson *et al.* first reported neutron diffraction measurements on D₂-loaded Cu₃(BTC)₂, which suggest that adsorbate molecules are bound to metal sites.⁵¹ However, to add true chemical information, a wide range of complementary characterization tools, such as XRD, EPR, X-ray Absorption Spectroscopy (XAS), UV-Vis-NIR spectroscopy, Raman spectroscopy and FT-IR spectroscopy with probe molecules (*e.g.*, with CO, CO₂, NO and H₂), have aided in understanding the framework metal-adsorbate interaction. Excellent review articles on this topic are available for the reader.^{3-6, 52-54} Other gas molecules, including energy carriers,⁵⁵ such as H₂ or industrially relevant O₂⁵⁶ or SH₂⁵⁷, and a combination of spectroscopic tools have also been used to study the adsorptive properties of HKUST-1(Cu) and their Cr/Zn/Ru analogues at various temperatures. This is summarized in Table 2.3.

Table 2.3 Summary of the different spectroscopic tools used for the study of HKUST-1/gas interactions.

Metal cation	Spectroscopic tools used	Adsorbed (or desorbed) gases	Reference
Cu	PXRD, EXAFS, XANES, Raman, DR UV-vis-NIR (CO and H ₂ probed FT-IR at 77K)	Desolvation	[54]
	PXRD, Raman, DR UV-vis-NIR, solution ¹ H NMR	Desolvation (chemical activation)	[58]
	Inelastic neutron scattering (INS)	CD ₄ (at 77 K)	[59]
	INS	CO ₂ (at 20 K)	[60]
	INS, neutron diffraction	H ₂ (at 4-5K)	[61, 62]
	Neutron diffraction	D ₂ (at 4-5K)	[51]
	Low-temperature thermal-desorption spectroscopy (TDS)	H ₂ /D ₂	[63]
	<i>In-situ</i> FT-IR, μ -XRF, Synchrotron-based PXRD, pair distribution function analysis	I ₂ and H ₂ O (at 348 K)	[64]
	<i>In-situ</i> FT-IR	CO, CO ₂ , NO, N ₂ , H ₂ (20-77 K)	[65]
	PXRD, XANES, DR UV-vis-NIR, FT-IR	SH ₂ (298 K)	[57]
NH₂-Cu-HKUST-1	XPS, NEXAFS	H ₂ O, NO (at 298 K)	[66]
	PXRD, XANES, EXAFS, DR UV-vis-NIR, FT-IR, <i>cw</i> EPR, HYSCORE	H ₂ O, NH ₃ (298 K)	[67]
	Synchrotron XPS, APXPS, NEXAFS, AES	H ₂ O, NH ₃ (298 K)	[68]
Cu_{2.97}:Zn_{0.03}	solid-state ¹ H MAS NMR, <i>in-situ</i> FT-IR	NO (298 K)	[69, 70]
	ENDOR, HYSCORE, <i>cw</i> EPR	HD, D ₂ , H ₂ and ¹³ CO ₂ / ¹³ CO	[71], [72]
	¹³ C MAS NMR	¹³ CO, CO ₂ (213-353 K)	[73]
Cr	PXRD, DR UV-vis-NIR, <i>in-situ</i> FT-IR, XANES, neutron powder diffraction	Desolvation and O ₂ (variable temperature)	[56]
	Neutron powder diffraction, INS, <i>in-situ</i> FT-IR	H ₂ , D ₂ (30-80 K)	[74]
Ru	PXRD, UHV-XPS, UHV-labelled C ¹⁶ O/C ¹⁸ O-probed FT-IR (at 90 K)	Desolvation	[75]

A notable example of the multi-spectroscopic investigation of adsorptive properties of Cu²⁺ sites in HKUST-1 is the sorption of gas phase, dry and wet ammonia (NH₃). In particular, understanding their molecular adsorption mechanisms has proven crucial to predict the effect on distortion and/or degradation of the paddle-wheel SBU and long-range order of the HKUST-1 framework.

In a thorough study, Borfecchia *et al.* showed that phase changes are induced in the HKUST-1 framework only when NH₃ (1:1 mol Cu:NH₃, 298 K) is adsorbed after water sorption on Cu sites, revealed by XRD.⁶⁷ In the case of dry ammonia, the crystallinity is preserved, being possible to introduce water again even after evacuation of NH₃ without amorphization or phase change, suggesting an important role of water in the degradation mechanism of the framework. Diffuse reflectance (DR) UV-vis spectra of the dry samples (Figure 2.4a) with adsorbed NH₃ showed a slight red shift of the Cu²⁺ *d-d* transition peak from 585 nm (activated) to 745 nm (+NH₃), which is similar to the peak of the hydrated sample at 725 nm, as expected for these two σ -donors (H₂O and NH₃).

Far-IR spectroscopy (Figure 2.4b) showed that dehydration blue-shifted all the bands corresponding to Cu-O and Cu-Cu, due to the increased donation of the carboxylate ligands. Introduction of NH₃ restored the IR spectrum to that of the hydrated one. These spectral features indicate that NH₃ is bonded to the open Cu²⁺ sites *via* the lone pair in a similar fashion to H₂O molecules, thus, decreasing the Cu-O bond strength with the carboxylates due to increased electron density around the Cu centre.

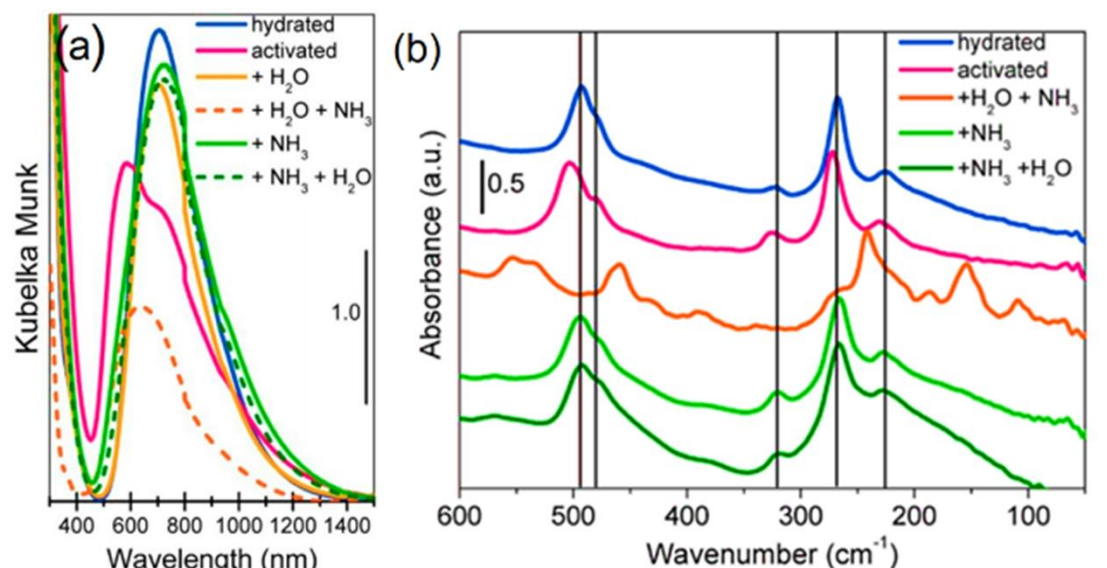


Figure 2.4. Spectroscopic analysis of the different HKUST-1 samples activated and upon introduction of ammonia under different conditions (dry and wet): (a) Diffuse Reflectance (DR) UV-Vis spectroscopy and (b) far-IR spectroscopy of the as-prepared (blue line), activated (pink line), and activated + NH₃ (green line) sample. (c) Different states of the Cu Paddle Wheel (PW) units under the different conditions reported. Adapted and modified from reference [67]. Copyright © American Chemical Society 2012.

This was further corroborated by XANES, namely by two pre-edge features that change when 50 mbar eq. pressure of NH₃ are introduced, indicating an effective interaction of ammonia molecules with Cu centres. Surprisingly, EXAFS fitting of the recorded spectra, together with simulations, indicated an elongation of the Cu-O_{carboxylate} bonds of more than double than in the case of water, as probably due to higher basicity ammonia ($pK_a = 9.24$), thus, decreasing the Cu-O bond strength (as well as no degradation of the framework,

seen in PXRD). Thus, it was possible to obtain a full chemical and electronic description of the metal centres and the framework by this array of techniques (Figure 2.4c).

Interestingly, and in contrast with other published works, the sample did not show any signs of reduction from Cu²⁺ to Cu⁺ nor any mixed valence states upon activation. The g_{\parallel} values obtained with EPR confirmed this finding, and shed some light on the magnetic properties of Cu with adsorbed NH₃.^[76] In any case, it was confirmed that only humid NH₃ transformed HKUST-1 readily, being possible to adsorb and desorb dry ammonia without major structural changes. As mentioned, not only the primary Cu atom or paddle-wheel cluster, but the whole structure is affected, making necessary to use a holistic approach for the study of these features. On the other hand, even if a very detailed picture was obtained, the mechanism by which the framework is destroyed was still not clarified. Thus, Nijem *et al.*^[68] used a surface approach consisting of an Ambient Pressure X-ray Photoelectron Spectroscopy (AP-XPS) and Near-Edge X-ray Absorption Fine Structure (NEXAFS) study of dry and humid NH₃ adsorption by an HKUST-1 thin-film (thickness 100 nm). In their study, one additional challenge had to be faced: although different spots of the sample were measured, in order to avoid beam-induced reduction, they have observed the presence of the L₃ Cu⁺ peak at *ca.* 935.3 eV in the NEXAFS spectra (see Figure 2.5a), indicating Cu⁺ in the material, in contrast with the previous study. They have estimated ~ 3.5 at% of the total Cu to be Cu⁺ (later increased up to ~10% with increasing H₂O pressure), which they attributed to missing-linker defects.

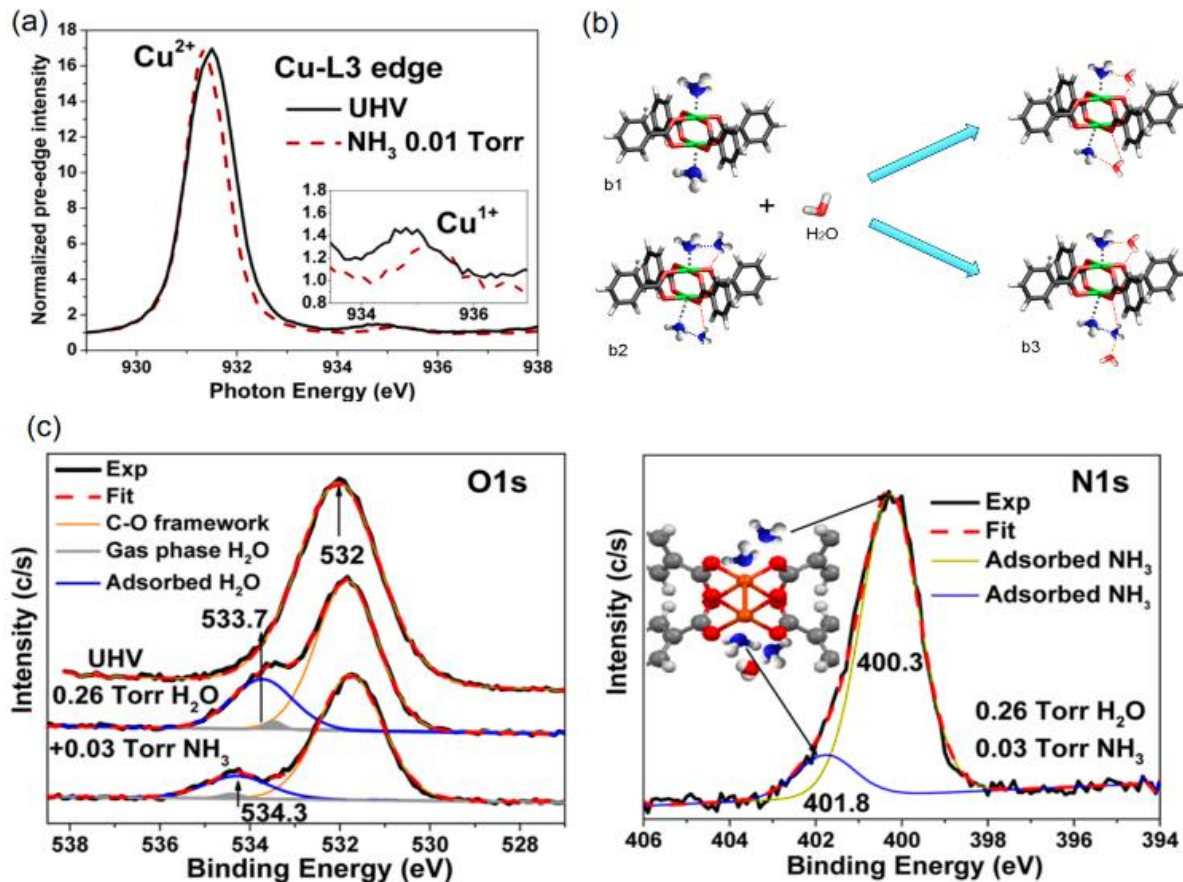


Figure 2.5. (a) L₃ Cu²⁺ edge (inset shows L₃ Cu¹⁺) in the Near-Edge X-ray Absorption Fine Structure (NEXAFS) spectra of a HKUST-1 thin-film without and with 0.01 Torr of NH₃ adsorbed. (b) Possible cooperative interactions between adsorbed water and ammonia molecules (C, grey; O, red; H, white; N, blue; and Cu, green). (c) O 1s and N 1s scans of the humid NH₃ sorption Ambient Pressure X-ray Photoelectron Spectroscopy (AP-XPS) experiments of a HKUST-1 thin-film. Adapted and reprinted from reference [68]. Copyright © American Chemical Society 2015.

Despite observing this difference between the Cu sites, experiments with humid NH₃ revealed a complex interplay between water and ammonia molecules in their coordination to Cu²⁺ clusters (Figure 2.5b1 and 2.5b2). Depending on the NH₃ pressure and presence of water, it was proven that H₂O coordinates to secondary ammonia molecules *via* hydrogen bonding (Figure 2.5b3). Moreover, additional interactions with the BTC linkers (namely the oxygen atom) can appear as the coverage increases. As it can be seen in Figure 2.5c, a shoulder at 533.7 eV seen in the O 1s scan appeared when 0.26 Torr of H₂O were introduced, indicating physisorbed Cu^{2+...}OH₂ species. With 0.03 Torr of NH₃, a shift of +0.6 eV, which was linked to the formation of [O₂H_{...}H₃N_{...}Cu²⁺] species. The shoulder at 401.8 eV further corroborated the existence of such interactions, as described

in the model in the inset of the N 1s scan of Figure 2.5c. This is in line with what Borfecchia *et al.* had hypothesized, *i.e.* ammonia can be reversibly adsorbed by HKUST-1, being water the major factor of degradation. These studies are a good showcase of how complementary *in-situ* spectroscopies can provide a full and detailed snapshot of each step during CUS \cdots X (X = host) interactions. In addition, such a multi-spectroscopic approach allows to describe the parameters, which may induce framework degradation/perturbation, such as gas pressure or the nature of gas phase species themselves. Not only different characterization tools but also the types of substrates, *i.e.* bulk powder vs. thin films, can offer alternative routes for gaining uncovered information which is not directly accessible/relevant in other sample configurations. Nonetheless, one should be very careful when applying this type of studies to highly porous materials, since exceptional physical and chemical phenomena can occur upon downsizing the MOF from bulk to nanoscale dimensions.

As mentioned above, the desolvation process affects the clusters (more specifically the metal atoms) in two different ways: change in the coordination geometry and increase in the partial positive charge (δ^+). Consequently, this has prompted the study of the redox properties of the material, which can determine the efficiency in, for instance, selective adsorption or catalysis. Spectroscopy has played a crucial role in the elucidation of such features, as it will be described in the following lines. Characterization of the Fe framework revealed the presence of both oxidation states in the HKUST-1 analogue of formula $[\text{Fe}_2(\text{H}_2\text{O})_2(\text{BTC})_{4/3}]\text{Cl}\cdot 4.5(\text{DMF})$.⁴⁶ Although no successful attempts of desolvation have been reported for this structure, Mössbauer spectroscopy of the DMF containing material showed curves with a double isomer shifts of $\delta = 0.41 \text{ mm s}^{-1}$ and 1.08 mm s^{-1} ; and quadrupole-splitting values $\Delta E = 0.78 \text{ mm s}^{-1}$ and 1.66 mm s^{-1} , which correspond to Fe^{2+} and Fe^{3+} species, respectively. In addition, the integral under the curves yielded a 49:51 ratio, indicating a 1:1 ratio of each oxidation state. When carefully designed, Fe-Fe distances and coordination environments in these MOF materials can be similar to those seen in enzymes, as it has been shown for other topologies.⁷⁷

Mixed-valence states have also been observed in the Ru analogue ($\text{Ru}^{3+}/\text{Ru}^{2+}/\text{Ru}^{\delta+}$), as reported by the group of Fischer after deconvolution of XPS spectra.⁴³ Two different Ru species were identified: Ru^{3+} and Ru^{2+} , as confirmed by XANES analysis of both the precursors and the obtained MOF materials. Similar MOF materials were further analysed by FT-IR spectroscopy with CO as probe molecule and the experimental data compared to DFT calculations.⁷⁵ Although two signals were observed (both for labelled C^{16}O , at 2171 cm^{-1} and 2137 cm^{-1} ; and C^{18}O experiments, at 2120 cm^{-1} and 2085 cm^{-1}), pointing to two oxidation states, theoretical support concluded that Cl^- are still present, presenting a more complex scenario (possible chloroformyl and CO-Cl species) than purely physically adsorbed CO on mixed-valence nodes.

Partially reduced clusters can also be found in the defective linker-containing analogues of HKUST-1 prepared following Baiker's strategy (Figure 2.6b).^{47,78,79} For instance, in Figure 2.6a, XPS spectra of defective HKUST-1(Ru), with increasing molar amounts of 3,5-pyridinedicarboxylic acid (Pydc) as low-coordinating linker, show a gradual shift on the characteristic Ru^{2+} doublets towards lower energies, indicating the formation of $\text{Ru}^{\delta+}$.

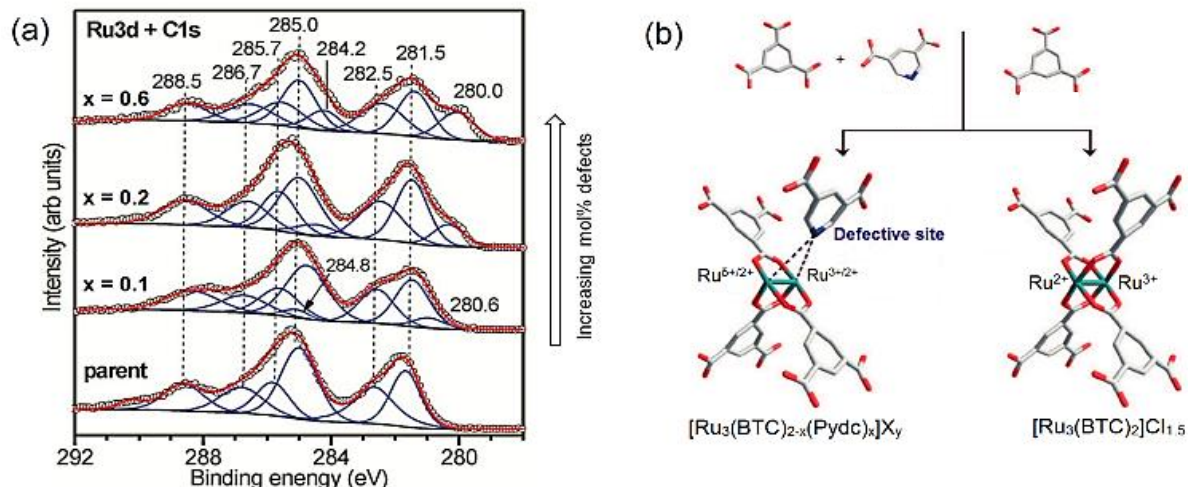
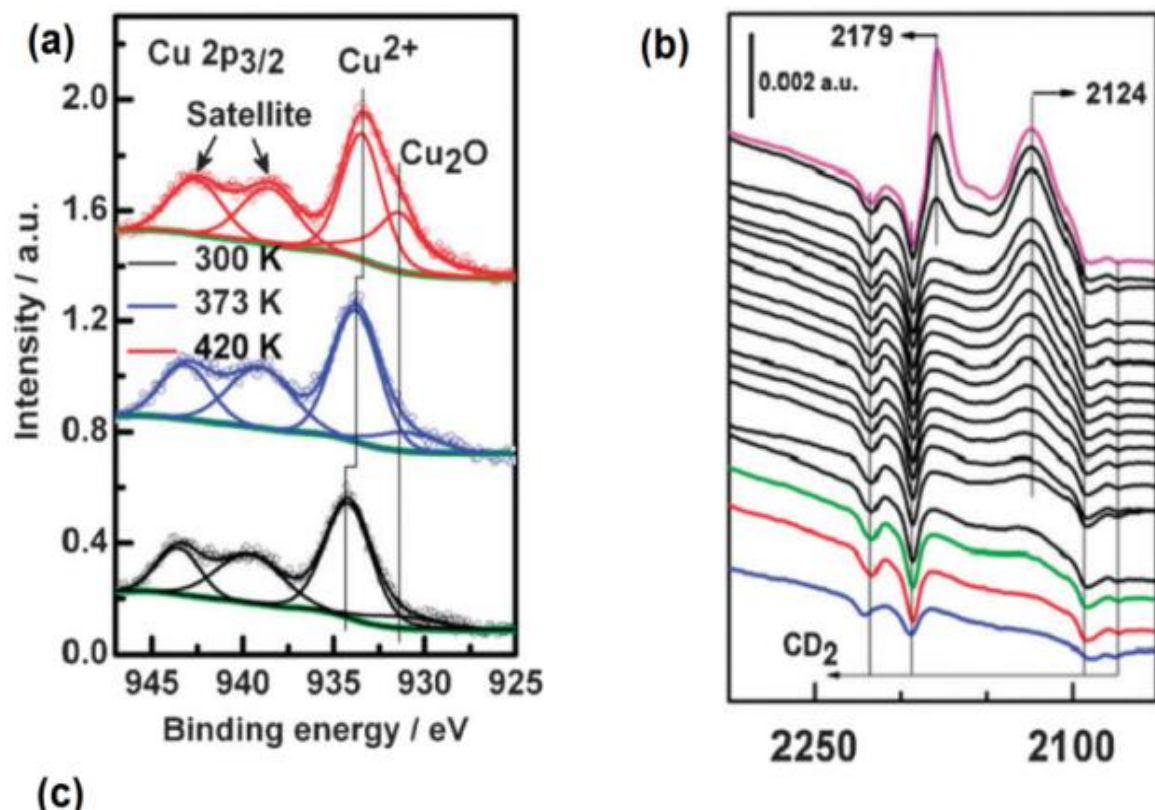


Figure 2.6. (a) X-ray Photoelectron Spectroscopy (XPS) analysis of defect-engineered HKUST-1 (Ru) crystals with increasing defect molar amount (x indicates the targeted amount of pydc per cluster) showing the peaks of Ru^{3+} at 281.5 and 285.4 eV and Ru^{2+} at 282.5 and 286.6 eV. The latter is gradually shifted, indicating the presence of $\text{Ru}^{\delta+}$ (284.2 and 280.0 eV). (b) Model of parent and defective clusters including mixed-valence $\text{Ru}^{3+/2+/}\delta+$ species. Adapted and reprinted from reference [47] Copyright © John Wiley and Sons, 2014.

This shift is accompanied by a decrease in the intensity of the Cl 2p XPS peak, reinforcing their hypothesis. This report shows that, even in clusters showing multiple oxidation states, the introduction of defective ligands can further reduce the paddlewheel.

Similar to the case of Ru, partially reduced Cu⁺/Cu²⁺ ions have been previously observed in defective HKUST-1 (Cu) (XPS and FT-IR spectroscopy with CO as probe at 90 K). However, it was a matter of discussion whether the reduction of Cu was due to the thermal activation procedure or inherent to the presence of defect clusters.⁴⁹ In fact, the formation of Cu⁺ has been the focus of different studies that tried to elucidate whether the Cu⁺ evidences were extra-framework cations, defective clusters, Cu₂O impurities arising from the synthesis procedure or just reduced Cu atoms in perfectly coordinated paddlewheels. Their presence was first reported by the group of de Vos, when FT-IR with CO as probe showed a band at 2123 cm⁻¹, in addition to that at 2179 cm⁻¹ (which indicates the presence of Cu²⁺-CO species), and which is still present at low CO coverage. This phenomenon was attributed to enhanced back-bonding in the case of Cu⁺ (Cu⁺ (5σ) → C≡O π*) than for Cu²⁺,⁸⁰ and a higher temperature or lower pressure is necessary to desorb the CO. The reason for this finding was first attributed to CO acting as a reductant during the measurement. However, Bordiga *et al.* later assigned such band (at 2127 cm⁻¹ in their study) to copper (I) oxide impurities rather than to the reduction of HKUST-1(Cu), although XRD patterns did not indicate the presence of such compound.⁶⁵ As mentioned above, thin-films have been used as “model systems” to study certain properties of MOFs. For an in-depth analysis of the Cu⁺ formation issue, Wöll and co-workers⁸¹ observed similar spectral features in XPS and experiments with FT-IR spectroscopy in combination with CO as probe molecule of a ~60 nm HKUST-1 (Cu) film grown over a self-assembled monolayer (SAM). In Figure 2.7a the spectral region of Cu 2p_{3/2} shows increasing amounts of Cu₂O (assigned to be at 931.0–931.4 eV), while in Figure 2.7b the FT-IR spectroscopy data revealed a band at 2124 cm⁻¹, which was attributed to Cu₂O. In addition, no corresponding XRD peaks could be observed (even for amounts as high as ~42% of Cu reduced).



T/K	Binding energy/eV		Intensity/a.u		Ratio $\frac{\text{Cu}^+}{\text{Cu}^++\text{Cu}^{2+}}$
	Cu ²⁺	Cu ₂ O	Cu ²⁺	Cu ₂ O	
300	934.2	931.4	1.433	0.213	12.9%
373	933.8	931.0	1.556	0.3	16.2%
420	933.4	931.4	1.424	1.027	41.9%

Figure 2.7. (a) X-ray Photoelectron Spectroscopy (XPS) data of the HKUST-1/SAM thin film activated at different temperatures, (b) FT-IR spectroscopy with CO as probe molecule and (c) Cu²⁺/Cu⁺ ratios calculated from the XPS data. Adapted and reprinted from reference [81]. Copyright © Royal Society of Chemistry, 2011.

Nonetheless, in a later report Szanyi, Daturi and co-workers⁸² used NO, NO₂, CH₃OH and CO as probes for FT-IR spectroscopy in bulk HKUST-1(Cu), and proved that Cu can undergo auto-reduction at high temperature under vacuum. Co-feeding of NO and CO showed the selective binding of CO to Cu⁺ species, which could be later re-oxidized *in-situ* to Cu²⁺ by nitric oxide. Experiments with CH₃OH showed that it can be dissociated to methoxy species (2956 and 2852 cm⁻¹, ν (C-H) bound to Cu⁺) after activation under vacuum at 473

K. Once again, the thin-film approach was used by St. Petkov *et al.*⁸³ who prepared a high-quality film of about 40 layers of HKUST-1(Cu) and with the aid of quantum chemical calculations, attributed the presence of Cu⁺ to low-coordinated defect clusters rather than cuprous oxide, which is in agreement with the previous FT-IR and XPS data provided by the group of Wöll. This concept has been further extended to other HKUST-1-like SURMOFs⁸⁴ or paddle-wheel Cu-MOFs⁸⁵ with defects. Not only by annealing, but also electron (e^-) beams or X-rays can reduce Cu (or create defects) in HKUST-1. This has been studied by several groups by means of Ambient Pressure Photoelectron Spectroscopy (APPES), XPS and NEXAFS, revealing that exposure time to the photon flux promotes the reduction to Cu⁺.⁸⁶ Recent studies show that in addition to beam damage and thermal treatment, exposure to ambient conditions leads to the formation of Cu⁺ sites as well. Todaro *et al.* reported the evolution of the Cu PWs over time, as modelled and determined by XRD, SEM, Raman and EPR.^{87,88} Exposure for more than 20 days results in the hydrolysis of Cu-O bonds and destructive interactions with H₂O that generate EPR-silent Cu⁺ sites and a decrease in the Raman intensity of Cu-O bonds. This has been further corroborated by XAFS,⁸⁹ and surface studies combining IRRAS and XPS.⁹⁰ Not only in the case of HKUST-1, but also in other topologies, such as CPO-27, or MFU-4L, the presence of these redox Cu²⁺ to Cu⁺ process has been observed.^{91,92} This pair could have important implications in the use of MOFs for olefin separations, as shown for the Fe²⁺ to Fe³⁺ pair in MIL-100 in the previous sections.

Summarizing, despite many studies have been devoted to the cause of formation and nature of reduced sites, total agreement is yet to be reached. Nevertheless, it is clear that a large fraction of Cu⁺ sites, that can be tuned by different procedures, is present in HKUST-1. Practical application of Cu reducibility has been already proven in, for example, the use of MOFs for delivery of nitrous oxide as a vasodilator agent. As shown for carbon monoxide, σ -bonding and π -backdonation were enhanced in the case of Cu⁺ versus Cu²⁺ for nitric oxide (NO) based on the photoelectron spectra, serving as an example of the uses that reduced HKUST-1(Cu) may find.⁶⁶

2.4 CONCLUSIONS

In this Chapter, an overview is presented of the different spectroscopic techniques currently available for the characterization of MOF materials. This has been illustrated for two different MOF topologies, namely the MIL-100 and MIL-101 structures, next to the HKUST-1 structures, which both will be discussed in this PhD thesis in more detail. More specifically, we have provided information on the formation and nature of coordinatively unsaturated sites (CUS) as gathered by diffraction, scattering, spectroscopy and microscopy methods. Given the Lewis acidic nature of CUS sites in the MIL-100 and HKUST-1 topologies, *in-situ* characterization tools along with probe molecules, *e.g.* CO, CO₂, NO, H₂, NH₃, pyridine or CD₃CN, have been extensively used to better understand their surface chemistry, and potential applications in sorption and catalysis. Similar information can be obtained for HKUST-1 structures. Also, the coordination geometry, oxidation states, abundance of sites and presence of defects can be studied in great detail by *e.g.* FT-IR, UV-vis, NMR, EPR, XPS, SAXS-WAXS and XAS. For both structures, it became clear that this approach has helped to unravel the different possibilities for (potential) applications of these functional materials as well as to determine the impact of temperature treatments, beam damage or exposure to different conditions, thereby helping to define what reaction environments may lead to function, such as sorption, separation and catalysis.

2.5 REFERENCES

1. F. Gandara and T. D. Bennett, *International Union of Crystallography Journal (IUCrJ)*, 2014, **1**, 563-570.
2. A. J. Howarth, A. W. Peters, N. A. Vermeulen, T. C. Wang, J. T. Hupp and O. K. Farha, *Chem. Mater.*, 2017, **29**, 26-39.
3. F. Bonino, C. Lamberti and S. Bordiga, in *The Chemistry of Metal-Organic Frameworks: Synthesis, Characterization, and Applications*, Wiley-VCH, Weinheim, 2016, 657-690.
4. F. Bonino, C. Lamberti, S. Chavan, J. G. Vitillo and S. Bordiga, in *Metal Organic Frameworks as Heterogeneous Catalysts*, The Royal Society of Chemistry, Cambridge, 2013, 76-142.
5. S. Bordiga, F. Bonino, K. P. Lillerud and C. Lamberti, *Chem. Soc. Rev.*, 2010, **39**, 4885-4927.
6. E. Borfecchia, D. Gianolio, G. Agostini, S. Bordiga and C. Lamberti, in *Metal Organic Frameworks as Heterogeneous Catalysts*, The Royal Society of Chemistry, Cambridge, 2013, 143-208.
7. M. G. O'Brien, A. M. Beale and B. M. Weckhuysen, *Chem. Soc. Rev.*, 2010, **39**, 4767-4782.
8. A. M. Beale, S. D. M. Jacques and B. M. Weckhuysen, *Chem. Soc. Rev.*, 2010, **39**, 4656-4672.
9. G. Férey, C. Serre, C. Mellot-Draznieks, F. Millange, S. Surblé, J. Dutour and I. Margiolaki, *Angew. Chem. Int. Ed.*, 2004, **43**, 6296-6301.
10. G. Férey, C. Mellot-Draznieks, C. Serre, F. Millange, J. Dutour, S. Surblé and I. Margiolaki, *Science*, 2005, **309**, 2040-2042.

-
11. P. Horcajada, S. Surble, C. Serre, D.-Y. Hong, Y.-K. Seo, J.-S. Chang, J.-M. Grenèche, I. Margiolaki and G. Férey, *Chem. Commun.*, 2007, 2820-2822.
12. C. Volkringer, D. Popov, T. Loiseau, G. Férey, M. Burghammer, C. Riekel, M. Haouas and F. Taulelle, *Chem. Mater.*, 2009, **21**, 5695-5697.
13. A. Lieb, H. Leclerc, T. Devic, C. Serre, I. Margiolaki, F. Mahjoubi, J. S. Lee, A. Vimont, M. Daturi and J.-S. Chang, *Micro. Meso. Mater.*, 2012, **157**, 18-23.
14. L. Mitchell, B. Gonzalez-Santiago, J. P. S. Mowat, M. E. Gunn, P. Williamson, N. Acerbi, M. L. Clarke and P. A. Wright, *Catal. Sci. Technol.*, 2013, **3**, 606-617.
15. J. A. Mason, L. E. Darago, W. W. Lukens and J. R. Long, *Inorg. Chem.*, 2015, **54**, 10096-10104.
16. H. Reinsch and N. Stock, *CrystEngComm*, 2013, **15**, 544-550.
17. F. Zhang, X. Zou, W. Feng, X. Zhao, X. Jing, F. Sun, H. Ren and G. Zhu, *J. Mater. Chem.*, 2012, **22**, 25019-25026.
18. S. Bhattacharjee, C. Chen and W.-S. Ahn, *RSC Adv.*, 2014, **4**, 52500-52525.
19. W. Xuan, C. Zhu, Y. Liu and Y. Cui, *Chem. Soc. Rev.*, 2012, **41**, 1677-1695.
20. A. Vimont, H. Leclerc, F. Maugé, M. Daturi, J.-C. Lavalley, S. Surblé, C. Serre and G. Férey, *J. Phys. Chem. C*, 2007, **111**, 383-388.
21. A. Vimont, J.-M. Goupil, J.-C. Lavalley, M. Daturi, S. Surblé, C. Serre, F. Millange, G. Férey and N. Audebrand, *J. Am. Chem. Soc.*, 2006, **128**, 3218-3227.
22. H. Leclerc, A. Vimont, J.-C. Lavalley, M. Daturi, A. D. Wiersum, P. L. Llewellyn, P. Horcajada, G. Férey and C. Serre, *Phys. Chem. Chem. Phys.*, 2011, **13**, 11748-11756.
23. M. Haouas, C. Volkringer, T. Loiseau, G. Férey and F. Taulelle, *J. Phys. Chem. C*, 2011, **115**, 17934-17944.
24. C. Volkringer, H. Leclerc, J.-C. Lavalley, T. Loiseau, G. Férey, M. Daturi and A. Vimont, *J. Phys. Chem. C*, 2012, **116**, 5710-5719.
25. J. Jiang and O. M. Yaghi, *Chem. Rev.*, 2015, **115**, 6966-6997.
26. S. Wuttke, P. Bazin, A. Vimont, C. Serre, Y.-K. Seo, Y. K. Hwang, J.-S. Chang, G. Férey and M. Daturi, *Chem. Eur. J.*, 2012, **18**, 11959-11967.
27. G. Gómez-Pozuelo, C. P. Cabello, M. Opanasenko, M. Horáček and J. Čejka, *ChemPlusChem*, 2016, **82**, 152-159.
28. J. W. Yoon, Y.-K. Seo, Y. K. Hwang, J.-S. Chang, H. Leclerc, S. Wuttke, P. Bazin, A. Vimont, M. Daturi, E. Bloch, P. L. Llewellyn, C. Serre, P. Horcajada, J.-M. Grenèche, A. E. Rodrigues and G. Férey, *Angew. Chem. Int. Ed.*, 2010, **49**, 5949-5952.
29. G. T. Palomino, C. P. Cabello and C. O. Areán, *Eur. J. Inorg. Chem.*, 2011, **2011**, 1703-1708.
30. R. Giovine, C. Volkringer, S. E. Ashbrook, J. Trébosc, D. McKay, T. Loiseau, J.-P. Amoureux, O. Lafon and F. Pourpoint, *Chem. Eur. J.*, 2017, **23**, 9525-9534.
31. B. Barth, M. Mendt, A. Pöpll and M. Hartmann, *Micropor. Mesopor. Mater.*, 2015, **216**, 97-110.
32. M. Mendt, B. Barth, M. Hartmann and A. Pöpll, *J. Chem. Phys.*, 2017, **147**, 224701.
33. A. H. Khan, B. Barth, M. Hartmann, J. Haase and M. Bertmer, *J. Phys. Chem. C*, 2018, **122**, 12723-12730.
34. A. Nandy, A. C. Forse, V. J. Witherspoon and J. A. Reimer, *J. Phys. Chem. C*, 2018, **122**, 8295-8305.
35. C. Zhao, H. Meng, M. Nie, L. Jiang, C. Wang and T. Wang, *J. Phys. Chem. C*, 2018, **122**, 4635-4640.
36. A. M. Sheveleva, A. V. Anikeenko, A. S. Poryvaev, D. L. Kuzmina, I. K. Shundrina, D. I. Kolokolov, A. G. Stepanov and M. V. Fedin, *J. Phys. Chem. C*, 2017, **121**, 19880-19886.
37. T. Wittmann, A. Mondal, C. B. L. Tschense, J. J. Wittmann, O. Klimm, R. Siegel, B. Corzilius, B. Weber, M. Kaupp and J. Senker, *J. Am. Chem. Soc.*, 2018, **140**, 2135-2144.
38. S. S. Y. Chui, S. M. F. Lo, J. P. H. Charmant, A. G. Orpen and I. D. Williams, *Science*, 1999, **283**, 1148-1150.
39. D. J. Tranchemontagne, J. R. Hunt and O. M. Yaghi, *Tetrahedron*, 2008, **64**, 8553-8557.
40. S. P. Gavrish and Y. D. Lampeka, *Theor. Exper. Chem.*, 2013, **49**, 130-134.
41. Z. G.-S. F. Qian-Rong, X. Ming-Hong, Z. Da-Liang, S. Xin, W. Gang, T. Ge, T. Lu-Lu, X. Ming, Q. Shi-Lun, *Chem. J. Chin. Uni.*, 2004, **25**, 1016-1018.
42. M. Kramer, U. Schwarz and S. Kaskel, *J. Mater. Chem.*, 2006, **16**, 2245-2248.
43. O. Kozachuk, K. Yusenko, H. Noei, Y. Wang, S. Walleck, T. Glaser and R. A. Fischer, *Chem. Commun.*, 2011, **47**, 8509-8511.
44. P. Maniam and N. Stock, *Inorg. Chem.*, 2011, **50**, 5085-5097.
45. C. R. Wade and M. Dinca, *Dalton Trans.*, 2012, **41**, 7931-7938.
46. L. Xie, S. Liu, C. Gao, R. Cao, J. Cao, C. Sun and Z. Su, *Inorg. Chem.*, 2007, **46**, 7782-7788.

-
47. O. Kozachuk, I. Luz, F. X. Llabrés i Xamena, H. Noei, M. Kauer, H. B. Albada, E. D. Bloch, B. Marler, Y. Wang, M. Muhler and R. A. Fischer, *Angew. Chem. Int. Ed.*, 2014, **53**, 7058-7062.
48. C. H. Hendon and A. Walsh, *Chem. Sci.*, 2015, **6**, 3674-3683.
49. Z. Fang, J. P. Dürholt, M. Kauer, W. Zhang, C. Lochenie, B. Jee, B. Albada, N. Metzler-Nolte, A. Pöppl, B. Weber, M. Muhler, Y. Wang, R. Schmid and R. A. Fischer, *J. Am. Chem. Soc.*, 2014, **136**, 9627-9636.
50. R. Ameloot, F. Vermoortele, J. Hofkens, F. C. De Schryver, D. E. De Vos and M. B. J. Roeffaers, *Angew. Chem. Int. Ed.*, 2013, **52**, 401-405.
51. V. K. Peterson, Y. Liu, C. M. Brown and C. J. Kepert, *J. Am. Chem. Soc.*, 2006, **128**, 15578-15579.
52. I. Senkovska and V. Bon, *The Chemistry of Metal-Organic Frameworks: Synthesis, Characterization, and Applications*, 2016, Wiley-VCH, Weinheim.
53. M. Mendt, M. Šiménas and A. Pöppl, *The Chemistry of Metal-Organic Frameworks: Synthesis, Characterization, and Applications*, 2016, Wiley-VCH, Weinheim.
54. C. Prestipino, L. Regli, J. G. Vitillo, F. Bonino, A. Damin, C. Lamberti, A. Zecchina, P. L. Solari, K. O. Kongshaug and S. Bordiga, *Chem. Mater.*, 2006, **18**, 1337-1346.
55. K.-S. Lin, A. K. Adhikari, C.-N. Ku, C.-L. Chiang and H. Kuo, *Int. J. Hydr. Ener.*, 2012, **37**, 13865-13871.
56. L. J. Murray, M. Dinca, J. Yano, S. Chavan, S. Bordiga, C. M. Brown and J. R. Long, *J. Am. Chem. Soc.*, 2010, **132**, 7856-7857.
57. J. Ethiraj, F. Bonino, C. Lamberti and S. Bordiga, *Micropor. Mesopor. Mater.*, 2015, **207**, 90-94.
58. H. K. Kim, W. S. Yun, M.-B. Kim, J. Y. Kim, Y.-S. Bae, J. Lee and N. C. Jeong, *J. Am. Chem. Soc.*, 2015, **137**, 10009-10015.
59. J. Getzschmann, I. Senkovska, D. Wallacher, M. Tovar, D. Fairen-Jimenez, T. Düren, J. M. van Baten, R. Krishna and S. Kaskel, *Micropor. Mesopor. Mater.*, 2010, **136**, 50-58.
60. H. Wu, J. M. Simmons, G. Srinivas, W. Zhou and T. Yildirim, *J. Phys. Chem. Lett.*, 2010, **1**, 1946-1951.
61. Y. Liu, C. M. Brown, D. A. Neumann, V. K. Peterson and C. J. Kepert, *J. Alloy. Compd.*, 2007, **446-447**, 385-388.
62. M. C. Brown, Y. Liu, T. Yildirim, V. K. Peterson and C. J. Kepert, *Nanotechnology*, 2009, **20**, 204025.
63. I. Krkljus and M. Hirscher, *Micropor. Mesopor. Mater.*, 2011, **142**, 725-729.
64. D. F. Sava, K. W. Chapman, M. A. Rodriguez, J. A. Greathouse, P. S. Crozier, H. Zhao, P. J. Chupas and T. M. Nenoff, *Chem. Mater.*, 2013, **25**, 2591-2596.
65. S. Bordiga, L. Regli, F. Bonino, E. Groppo, C. Lamberti, B. Xiao, P. S. Wheatley, R. E. Morris and A. Zecchina, *Phys. Chem. Chem. Phys.*, 2007, **9**, 2676-2685.
66. N. Nijem, H. Bluhm, M. L. Ng, M. Kunz, S. R. Leone and M. K. Gilles, *Chem. Commun.*, 2014, **50**, 10144-10147.
67. E. Borfecchia, S. Maurelli, D. Gianolio, E. Groppo, M. Chiesa, F. Bonino and C. Lamberti, *J. Phys. Chem. C*, 2012, **116**, 19839-19850.
68. N. Nijem, K. Fürsich, H. Bluhm, S. R. Leone and M. K. Gilles, *J. Phys. Chem. C*, 2015, **119**, 24781-24788.
69. A. H. Khan, K. Peikert, M. Fröba and M. Bertmer, *Micropor. Mesopor. Mater.*, 2015, **216**, 111-117.
70. K. Peikert, L. J. McCormick, D. Cattaneo, M. J. Duncan, F. Hoffmann, A. H. Khan, M. Bertmer, R. E. Morris and M. Fröba, *Micropor. Mesopor. Mater.*, 2015, **216**, 118-126.
71. B. Jee, M. Hartmann and A. Pöppl, *Mol. Phys.*, 2013, **111**, 2950-2966.
72. B. Jee, P. St. Petkov, G. N. Vayssilov, T. Heine, M. Hartmann and A. Pöppl, *J. Phys. Chem. C*, 2013, **117**, 8231-8240.
73. F. Gul-E-Noor, M. Mendt, D. Michel, A. Pöppl, H. Krautscheid, J. Haase and M. Bertmer, *J. Phys. Chem. C*, 2013, **117**, 7703-7712.
74. K. Sumida, J.-H. Her, M. Dincă, L. J. Murray, J. M. Schloss, C. J. Pierce, B. A. Thompson, S. A. Fitzgerald, C. M. Brown and J. R. Long, *J. Phys. Chem. C*, 2011, **115**, 8414-8421.
75. H. Noei, O. Kozachuk, S. Amirjalayer, S. Bureekaew, M. Kauer, R. Schmid, B. Marler, M. Muhler, R. A. Fischer and Y. Wang, *J. Phys. Chem. C*, 2013, **117**, 5658-5666.
76. A. Pöppl, S. Kunz, D. Himsl and M. Hartmann, *J. Phys. Chem. C*, 2008, **112**, 2678-2684.
77. D. J. Xiao, E. D. Bloch, J. A. Mason, W. L. Queen, M. R. Hudson, N. Planas, J. Borycz, A. L. Dzubak, P. Verma, K. Lee, F. Bonino, V. Crocellà, J. Yano, S. Bordiga, D. G. Truhlar, L. Gagliardi, C. M. Brown and J. R. Long, *Nat. Chem.*, 2014, **6**, 590-595.
78. W. Zhang, M. Kauer, O. Halbherr, K. Epp, P. Guo, M. I. Gonzalez, D. J. Xiao, C. Wiktor, F. X. Liabrés i Xamena, C. Wöll, Y. Wang, M. Muhler and R. A. Fischer, *Chem. Eur. J.*, 2016, **22**, 14297-14307.
79. S. Marx, W. Kleist and A. Baiker, *J. Catal.*, 2011, **281**, 76-87.
80. L. Alaerts, E. Séguin, H. Poelman, F. Thibault-Starzyk, P. A. Jacobs and D. E. De Vos, *Chem. Eur. J.*, 2006, **12**, 7353-7363.
-

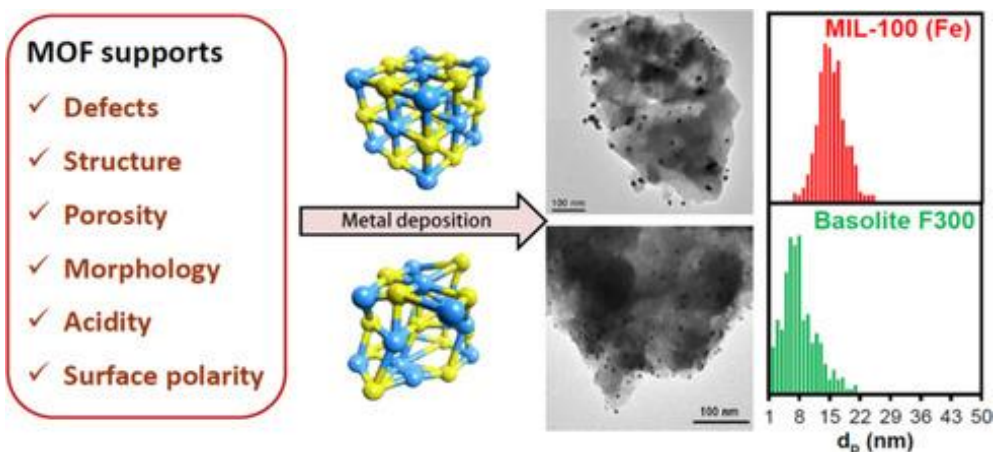
-
81. O. Shekhah, J. Liu, R. A. Fischer and C. Woll, *Chem. Soc. Rev.*, 2011, **40**, 1081-1106.
82. J. Szanyi, M. Daturi, G. Clet, D. R. Baer and C. H. F. Peden, *Phys. Chem. Chem. Phys.*, 2012, **14**, 4383-4390.
83. P. St. Petkov, G. N. Vayssilov, J. Liu, O. Shekhah, Y. Wang, C. Wöll and T. Heine, *ChemPhysChem*, 2012, **13**, 2025-2029.
84. Z. Wang, H. Sezen, J. Liu, C. Yang, S. E. Roggenbuck, K. Peikert, M. Fröba, A. Mavrandonakis, B. Supronowicz, T. Heine, H. Gliemann and C. Wöll, *Micropor. Mesopor. Mater.*, 2015, **207**, 53-60.
85. C.-Y. Wang, P. Ray, Q. Gong, Y. Zhao, J. Li and A. D. Lueking, *Phys. Chem. Chem. Phys.*, 2015, **17**, 26766-26776.
86. A. S. Duke, E. A. Dolgopolova, R. P. Galhenage, S. C. Ammal, A. Heyden, M. D. Smith, D. A. Chen and N. B. Shustova, *J. Phys. Chem. C*, 2015, **119**, 27457-27466.
87. M. Todaro, G. Buscarino, L. Sciortino, A. Alessi, F. Messina, M. Taddei, M. Ranocchiari, M. Cannas and F. M. Gelardi, *J. Phys. Chem. C*, 2016, **120**, 12879-12889.
88. M. Todaro, A. Alessi, L. Sciortino, S. Agnello, M. Cannas, F. M. Gelardi and G. Buscarino, *J. Spectr.*, 2016, , 8074297.
89. M. Todaro, L. Sciortino, F. M. Gelardi and G. Buscarino, *J. Phys. Chem. C*, 2017, **121**, 24853-24860.
90. K. Müller, N. Vankova, L. Schöttner, T. Heine and L. Heinke, *Chem. Sci.*, 2019, **10**, 153-160.
91. N. Drenchev, M. H. Rosnes, P. D. C. Dietzel, A. Albinati, K. Hadjiivanov and P. A. Georgiev, *J. Phys. Chem. C*, 2018, **122**, 17238-17249.
92. M. H. Mohamed, Y. Yang, L. Li, S. Zhang, J. P. Ruffley, A. G. Jarvi, S. Saxena, G. Veser, J. K. Johnson and N. L. Rosi, *J. Am. Chem. Soc.*, 2019, 2019, 141, 33, 13003-13007.

PART A

Lattice Disorder in Metal Organic Framework-Supported Metal Catalysts: Origins and Effects

Chapter 3

Pd Nanoparticles Supported on MIL-100(Fe) and BASOLITE® F300 Metal-Organic Frameworks



ABSTRACT

Metal-Organic Frameworks (MOFs) show great promise as supports for metal nanoparticles because of their high tunability, pore accessibility and surface area. Depending on the synthesis route, MOFs may contain defects. In this Chapter, we show that highly crystalline MIL-100(Fe) and disordered Basolite® F300 with identical iron 1,3,5-benzenetricarboxylate composition exhibit very divergent properties when used as support for Pd nanoparticle deposition. While MIL-100(Fe) shows a regular MTN-zeotype crystal structure with two types of cages, Basolite® F300 lacks long-range order beyond 8 Å and has a single pore system. The medium-range configurational linker-node disorder in Basolite® F300 results in a reduced number of Lewis acid sites, yielding more hydrophobic surface properties compared to hydrophilic MIL-100(Fe). The hydrophilic/hydrophobic nature of MIL-100(Fe) and Basolite® F300 impacts the amount of Pd and particle size distribution of Pd nanoparticles deposited during colloidal synthesis and dry impregnation methods, respectively. Additionally, infiltration of an organopalladium compound from the gas-phase and subsequent reduction under H₂ atmosphere resulted in different size distributions, further corroborating the effect of lattice disorder in particle growth. Preliminary tests in the solvent-free hydrogenation of cyclohexene in the slurry phase show that Pd/FeBTC materials prepared by impregnation

are comparable to other Pd supported catalysts. We argue that polar (apolar) solvents/precursors attractively interact with hydrophilic (hydrophobic) MOF surfaces, thereby obtaining an increasing control over e.g. the metal nanoparticle size distribution.

The results described in this Chapter are reported in the following manuscript: "Metal-Organic Frameworks as Catalyst Supports: Influence of Lattice Disorder on Metal Nanoparticle Formation", M. Rivera-Torrente, M. Filez, R. Hardian, E. Reynolds, B. Seoane, M.-V. Coulet, F. E. Oropeza Palacio, J. P. Hofmann, R. A. Fischer, A. L. Goodwin, P. L. Llewellyn, B. M. Weckhuysen, *Chem. Eur. J.* **2018**, 24, 7498 –7506.

3.1 INTRODUCTION

As described in Chapter 1, Metal Organic Frameworks (MOFs) are an important family of porous compounds, which consist of metal nodes interconnected by organic linkers forming a crystalline network with potential voids.¹⁻³ By varying the metal and linker type, the MOF properties can be altered and their pore space modified according to functional and diffusional needs. This tunability, together with exceptionally high specific surface areas and very rich post- and pre-synthetic chemistries, has generated keen interest within the scientific community, and MOFs have become the target of intense academic and industrial research. One particular function for which MOFs show strong potential is as hosts for metal nanoparticles in a diverse set of applications, ranging from chemical sensing⁴ to gas storage⁵ and catalysis.⁶ Indeed, MOFs have emerged as an attractive alternative to classic heterogeneous metal oxide or carbon supports, owing to their structural variability, opening the way for the synthesis of application-tailored supports.⁷⁻¹² However, despite the potential of MOFs as porous supports, the initial solvent wettability, transport and anchoring of the metal precursors on the MOF surface, as well as subsequent metal nanoparticle formation, are not well-understood and impede control over the nanoparticle properties and stability.¹³

Defect-engineering is becoming an increasingly important discipline in MOF science.^{14, 15} Whether it is by on-purpose introduction or natural occurrence, the presence of disordered domains may perturb the original MOF framework, thereby influencing the pore and channel structure.¹⁶ When it comes to the use of MOFs as supports, the presence of these disordered domains has the potential to play a key role.¹⁷ For example, the introduction of disorder may result in mesopore formation, which allows for a more rapid diffusion of liquids or gases. Furthermore, Lewis (M^{n+}) and Brønsted acid –OH and –COOH groups can arise from linker defects or adsorbed molecules on exposed metal sites.¹⁷⁻²¹ Nonetheless, up to now, the effect of disorder when using a MOF as a support for metal nanoparticles has not been investigated in great detail, hampering the use of defect engineering as a synthetic tool for the rational design of the deposition of metal nanoparticles.

In this Chapter, the goal is to gain fundamental insight into the impact of the lattice disorder on metal deposition and metal nanoparticle formation in various MOF host materials. In particular, our study focusses on the use of two different supports, namely: (1) defect-free MIL-100(Fe), possessing the MTN (named after Socony Mobil Thirty-Nine) zeolite framework type, and (2) its non-crystalline Basolite® F300 analogue,²² containing structural defects (such as kinks, grain boundaries, cracks or voids) owing to the synthesis protocol used for its preparation in an industrial environment.^{23, 24}

In order to understand how structural spatial arrangement modifies physicochemical properties, a wide variety of spectroscopic and textural characterization methods have been used in this Chapter on both defect-free MIL-100(Fe) and disordered Basolite® F300. Based on this, a more complete picture, as shown in Figure 3.1a, emerges on the structure and properties of these two materials. Heterogeneously Pd-catalysed reactions, *e.g.* Suzuki-Miyaura couplings, C-N bond formation, hydrogenation or oxidations, in which MOFs play the role of support, have been and still are the target of much research.^{25, 26} Thereafter, either impregnation of different Pd metal precursors, deposition of colloidal nanoclusters or infiltration of an organopalladium from the gas-phase, have been carried out to shed light on the effect of MOF lattice disorder on metal NP deposition. It will be shown that the disordered framework of MOF materials, *i.e.* non-periodic ordering of metal nodes and organic linkers, has a strong impact on surface polarity. Thus, the Pd content, the Pd nanoparticle size as well as the related Pd nanoparticle distribution within the MOF material can be rationalized accordingly. It will be shown that the properties of Pd nanoparticles are dependent on the precursor- and solvent-type, as a result of support surface polarity and diffusion properties, as outlined in Figure 3.1.

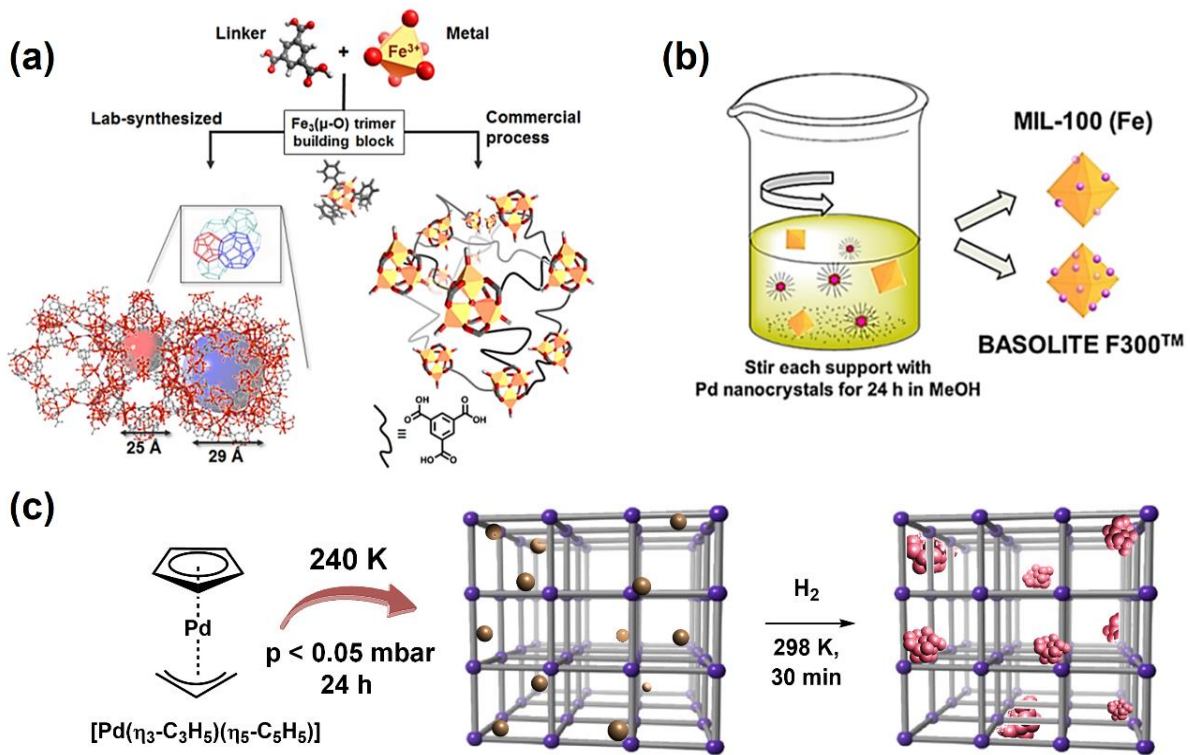


Figure 3.1 (a) Schematic of the different materials obtained from a Fe^{3+} source and trimesic acid (H_3BTC). Depending on the synthesis conditions, either highly crystalline MIL-100(Fe) or disordered, porous iron (III) 1,3,5-benzenetricarboxylate can be obtained, with the subsequent change in properties. (b) and (c) Schematic of the two approaches alternative to Incipient Wetness Impregnation (IWI) used for the synthesis of supported Pd nanoparticles: (b) Colloidal Particle Deposition (CPD) of Pd and (c) Chemical Vapour Infiltration (CVI) of $[\text{Pd}(\eta_3\text{-C}_3\text{H}_5)(\eta_5\text{-C}_5\text{H}_5)]$ with the subsequent reduction to Pd nanoparticles.

3.2 EXPERIMENTAL SECTION

3.2.1. Materials Synthesis

MIL-100(Fe), with molecular formula $\text{Fe}_3(\mu_3\text{-O})(\text{C}_6\text{H}_4\text{O}_4)_3\text{X}_3(\text{H}_2\text{O})_3 \cdot n\text{H}_2\text{O}$ ($\text{X} = \text{NO}_3^-$ or OH^- , $n \sim 11\text{-}14$) was synthesized as described in literature.²⁷ In brief, iron nitrate nonahydrate ($\text{Fe}(\text{NO}_3)_3 \cdot 9 \text{ H}_2\text{O}$, Sigma-Aldrich, $\geq 99.999\%$, 33.7 g, 0.08 mol) and 1,3,5-benzenetricarboxylate (H_3BTC , $\text{C}_9\text{H}_6\text{O}_6$, Sigma-Aldrich, $\geq 99\%$, 15.8 g, 0.08 mol) were mixed in 50 mL of water in a 100 mL round-bottom flask equipped with a reflux condenser. The mixture was heated at 368 K for 24 h and stirred at 300 rpm. Then, the powder was recovered by centrifugation and washed thoroughly with water and ethanol (VWR International, $\geq 96\%$). Basolite® F300 was purchased from Sigma-Aldrich. In order to remove trapped unreacted H_3BTC and other impurities, both MOFs were soaked in N,N -

dimethylformamide (C_3H_7NO , DMF, Sigma-Aldrich, $\geq 98\%$) at 353 K for 12 h. The solvent was then removed and replaced by a 68 mM ammonium fluoride (NH_4F , Sigma-Aldrich, $\geq 98\%$) aqueous solution at 353 K for 6 h. Then, the powders were recovered by centrifugation and dried in an oven at 393 K in air for 16 h.

3.2.2. Impregnation of Pd Precursors

Prior to the solution infiltration of the Pd precursor, the materials were activated in vacuum at 423 K for 12 h and kept in the flask during the addition. The corresponding amount of palladium (II) 2,4-pentanedionate ($Pd(acac)_2$, Sigma-Aldrich, $\geq 99\%$) to attain 1.5 wt% Pd was dissolved in chloroform ($CHCl_3$, Sigma-Aldrich, 99 %, anhydrous) and infiltrated into the degassed pores of the materials by adding it dropwise to the powder at room temperature and with constant stirring. The materials were then dried at 298 K for 24 h in Ar and then calcined at 423 K with a heat ramp of $2\text{ K}\cdot\text{min}^{-1}$ for 2 h in a N_2 flow of $50\text{ mL}\cdot\text{min}^{-1}$, time after which the gas feed was switched to H_2 flow of $50\text{ mL}\cdot\text{min}^{-1}$ for the reduction, and the temperature kept constant for 2 h more, then cooled down to room temperature naturally. No specific passivation method was used. In the case of sodium (II) tetrachloropalladate (Na_2PdCl_4 , Sigma-Aldrich, $\geq 99\%$), the corresponding amount to attain 1 wt% Pd was dissolved in deionized water. The MOF supports were degassed as described previously and the Pd solution added to the powder dropwise while stirring under vacuum. The impregnated powder was then dried at room temperature in Ar atmosphere for 16 h and calcined at 423 K for 2 h in a N_2 flow of $50\text{ mL}\cdot\text{min}^{-1}$ with a heat ramp of $2\text{ K}\cdot\text{min}^{-1}$ after which the gas feed was switched to H_2 flow of $50\text{ mL}\cdot\text{min}^{-1}$, and the temperature kept constant for 2 h more, then cooled down to room temperature naturally. No specific passivation method was used. Metal loading was confirmed by ICP-AES, (Pd wt%), Basolite[®] F300: 1.62; MIL-100(Fe): 1.78.

3.2.3. Synthesis and Deposition of Colloidal Pd Nanocrystals

Colloidally stabilized Pd nanocrystals were prepared as described in literature.²⁸ Monodisperse Pd nanoparticles of ~5 nm were synthesized according to an already reported procedure.²⁸ Briefly, $Pd(acac)_2$ (0.2 g, 0.9 mmol, 98%, Sigma-Aldrich) was placed in a dry three-neck 50 mL round-bottom flask equipped with a condenser and a

thermometer, and previously purged with vacuum ($5 \cdot 10^{-2}$ mbar) and Ar cycles for 3 times. Then, trioctylphosphine (1 mL, 0.83 mg, 2.2 mmol, 97%, Sigma-Aldrich) was added under magnetic stirring yielding an orange solution. Thereafter, 10 mL of oleylamine (44.9 mmol, $\geq 98\%$, Sigma-Aldrich) were added to the slurry and heated to 533 K for 45 min, the yellow-orange solution turning into a deep dark brown oil. After cooling at room temperature, 50 mL of methanol (99%, VWR International) were added and the mixture centrifuged. The brown oil was recovered, redispersed in tetrahydrofuran (THF, Chromasolv HPLC grade, Sigma-Aldrich) and separated by centrifugation. The particles were then suspended in methanol until further use. To deposit the Pd nanocrystals, 100 mg of MOF were mixed under magnetic stirring with 10 mL of methanol at room temperature. Then, a suspension containing 66.6 mg of colloidal Pd in 5 mL of methanol was added dropwise to the MOF suspension, and the mixture stirred for 24 h at 298 K. Thereafter, the powder was recovered by centrifugation, washed with 10 mL of methanol, separated and carefully washed with 10 mL of *n*-hexane (Sigma-Aldrich, 99.9%) in order to remove the excess of oleylamine (Sigma-Aldrich, $\geq 98\%$). The solid composites were then dried at 353 K in air for 5 h and stored in air for further analysis. Metal loading was confirmed by ICP-AES, (Pd wt%), Basolite[®] F300: 0.32; MIL-100(Fe): 0.2.

3.2.4. Chemical Vapour Infiltration of Allyl Cyclopentadienyl Palladium

Chemical Vapour Infiltration (CVI) experiments were carried out by following a slightly modified procedure from literature.⁶ Prior to the gas-phase deposition experiments, the MOFs were activated under vacuum ($p < 10^{-3}$ mbar) at 423 K for 20 h and introduced into a Ar filled ($O_2 < 1$ ppm, $H_2O < 1$ ppm) BraunTM glovebox. For each experiment, MOF (25 mg, ~ 0.03 mmol) and allyl cyclopentadienyl palladium (75 mg, 0.35 mmol, $[Pd(\eta_3-C_3H_5)(\eta_5-C_5H_5)]$, Strem Chemicals, 98%) powders were placed in a Schlenk flask without contact and under the strict exclusion of light inside the drybox. The flask was then evacuated to $p = 5 \cdot 10^{-2}$ mbar and left at 240 K for 24 h. Then, the MOF powder was recovered, inserted into a Fisher-Porter bottle which was pressurized at 2 bar of H_2 (Westfalen, 99.999%) and introduced into an oil-bath at 298 K. The MOF was then stored under air until further analysis. Metal loading was confirmed by ICP-AES, (Pd wt%), Basolite[®] F300: 1.78; MIL-100(Fe): 3.95.

3.2.5. Materials Characterization

X-ray Diffraction (XRD) patterns were obtained by a Bruker-AXS D2 Phaser powder X-ray diffractometer in Bragg-Brentano geometry, using $\text{Co K}_{\alpha1,2} = 1.79026 \text{ \AA}$, operated at 30 kV. Measurements were carried out between 2 and 30° using a step size of 0.05° and a scan speed of 1 s. Simulated patterns were obtained by processing the corresponding .cif files with Mercury 3.7® ($\lambda = 1.79026 \text{ \AA}$, FWHM = 0.2). *X-ray total scattering Pair Distribution Function (X-ray PDF)* measurements were performed using powder samples of Basolite® F300 and MIL-100(Fe) that were loaded in 0.5 mm borosilicate capillaries and mounted on a PANalytical Empyrean diffractometer equipped with a Mo X-ray tube ($\lambda = 0.71 \text{ \AA}$, $Q_{\max} = 17.7 \text{ \AA}^{-1}$), Mo focussing mirror and scintillation point detector. Divergence 1°, anti-scatter 1/4° and Soller (0.04 rad) slits were used to adjust the incident beam profile; a programmable receiving slit, set to a height of 1 mm, was used for the diffracted beam. Total scattering data were collected over the angular range $2.75 > 2\theta > 140^\circ$, yielding data with useable $Q_{\max} = 15 \text{ \AA}^{-1}$. These data were corrected for background, Compton, and multiple scattering and beam attenuation by the sample container using the *GudrunX* package.²⁹ The normalized structure factor $F(Q)$ was converted to the PDF in the form of the $D(r)$ function as defined in ref. [30]. *Raman spectroscopy* was obtained with a Renishaw™ *InVia* microscope, equipped with a 532 nm laser operating at 0.11 mW power output with a 50x objective, a 1200 l/mm grating, 4 accumulations and 10 seconds/acc acquisition time. *X-ray Photoelectron Spectroscopy (XPS)* experiments were performed by using a Thermo Scientific K-Alpha spectrometer equipped with a monochromatic small-spot X-ray source and a 180° double focusing hemispherical analyser with a 128-channel delay line detector. Spectra were obtained using an aluminium anode ($\text{Al K}_{\alpha} = 1486.6 \text{ eV}$) operated at 72 W and a spot size of 400 μm. Survey scans and high-resolution scans of the separate regions were measured at constant pass energies of 200 eV and 50 eV, respectively. The background pressure of the Ultra-High Vacuum (UHV) chamber was $2 \cdot 10^{-8} \text{ mbar}$. Sample charging was compensated for by the use of an electron flood gun, and binding energy calibration was done by setting the peak as reference for all samples to a Binding Energy (BE) of 284.8 eV, which corresponds to a combination of phenyl (sp₂) and adventitious carbon (sp₃), according to previously reported procedures. Fitting of the spectra (BE, Full Width at Half Maximum (FWHM), peak shape, asymmetry, number of

species) was carried out with CasaXPS[©] software, version 2.3.16. *Fourier Transform Infrared (FT-IR)* spectroscopy measurements were recorded on a PerkinElmer System 2000 instrument (16 scans, 4 cm⁻¹ resolution, DTGS detector, cell with KBr windows). The materials were prepared in a press tool by pressing ~10 mg of powder into self-supported pellets (2 cm² area), which were then activated at 448 K for 3 h at p < 10⁻⁵ mbar. After cooling down the cell with liquid N₂ temperature to 85 K, a 10 % CO/He v/v (Linde AG, 99.998 % purity) mixture was introduced to an equilibrium pressure of 100 mbar, and was then desorbed stepwise at constant temperature, until reaching total evacuation again at a pressure of ~10⁻⁵ mbar. When pyridine (Py) was used as a probe molecule, similar pellets were placed into a cell as the one de-scribed above and the spectra recorded with a ThermoFisher Nicolet iS5 spectrometer (32 scans, 4 cm⁻¹ resolution, DTGS detector). The pellet was evacuated by heating in a cell at 498 K (ramp of 10 K·min⁻¹) for 24 h at p < 10⁻⁵ mbar, which was then cooled down to 323 K. At that temperature, pyridine (redistilled, 99.9 %, Sigma-Aldrich) vapour was introduced into the cell and the equilibrium pressure set to 15 mbar. Spectra were recorded in adsorption mode up to 60 min after introduction of the gas. *Thermogravimetric Analysis (TGA)* of the samples was done in a PerkinElmer Pyris 1 TGA equipment. A heating ramp of 5 K·min⁻¹ starting from 323 K to 1073 K under a 10 mL·min⁻¹ of either O₂ and N₂ atmosphere was used for the analysis. *N₂ adsorption isotherms* were measured at 77 K on a Micromeritics ASAP 2010 apparatus. Prior to the measurements, samples were activated at 298 K under primary vacuum until the pressure reached 1 mbar and then switched to secondary vacuum at 443 K for 16 h. The measurement temperature was controlled with liquid N₂ at 77 K. Adsorption equilibrium was assumed when the variation of the cell pressure was 5 % for minimum and maximum period of 9 min and 30 min, respectively. *Methanol adsorption isotherms* were measured at 298 K on BELmax apparatus (MicrotracBEL). Prior to the measurements, samples were activated to 443 K under secondary vacuum for 16 h. Prior to performing methanol adsorption, methanol (analyte) was flash-frozen with liquid nitrogen and then evacuated under dynamic vacuum 3 times in order to remove dissolved gases from the reservoir. The measurement temperature was controlled with a water bath at 298 K and with the dosing manifold controlled at 313 K to avoid unwanted condensation effects. Helium was used to estimate the dead volume prior to the methanol adsorption-desorption

measurements. Adsorption equilibrium was assumed when the variation of the cell pressure was 0.5 % for a min. period of 5 min. *Elemental analysis of the content of Pd, Fe, O and C* was measured by Atomic Absorption Spectroscopy (AAS) after combustion of the samples with V₂O₅ at Mikroanalytisches Laboratorium Kolbe (Mülheim an der Ruhr, Germany). Pd content was determined by digestion of the samples in aqua regia (3/1 v:v of HCl/HNO₃) at high temperature, atomization by Inductively Coupled Plasma (ICP) technique and analysis by Atomic Emission Spectroscopy (AES). *Scanning Electron Microscopy (SEM)* images were recorded on a PhenomPro X microscope operated at 10 kV. The powder samples were supported on carbon tape deposited over Al stabs (FEI stabs) and inserted in the microscope vacuum chamber without Au coating. *Transmission Electron Microscopy (TEM)* images were recorded in the bright-field imaging mode by using a JEOL2011, a Tecnai T12 or a Tecnai T20FEG transmission electron microscope operated at 120 kV (the two former) or 200 kV, respectively. Samples were casted onto holey carbon coated 300 mesh Cu grids from methanol suspensions. The mean particle size of Pd was calculated from at least 200 different particles observed by using TEM.

3.2.6. Catalytic Testing

For catalytic testing we have selected the liquid-phase cyclohexene hydrogenation as model reaction. The catalytic hydrogenation of cyclohexene was conducted in a high-pressure stainless-steel Parr reactor. Typically, 30 mg of Pd/MOF catalyst were mixed with 30 mL of cyclohexene (Sigma-Aldrich, 99%) in the reactor with mechanical stirring (500 rpm). Thereafter, the reactor was heated to the desired temperature (323 or 343 K) and pressurized to 5 bar of H₂ (99.999%, Linde AG, Germany). Aliquots of the reaction were drawn *via* a 3-way valve, dissolved in CDCl₃ (99.96%, Cambridge Isotope Laboratories, USA) and product concentration monitored by ¹H Nuclear Magnetic Resonance (NMR) making use of a Agilent MRF instrument (400 MHz, Me₄Si set as δ = 0 ppm, solvent peaks used as a reference) at 298 K, and 16 scans of ¹H nuclei.

3.3 RESULTS AND DISCUSSION

To gain new insights into the role of disorder on the use of MOFs as catalyst supports, two MOF materials have been selected as hosts to deposit Pd metal nanoparticles, namely, i)

lab-synthesized non-defective MIL-100(Fe) and ii) commercial non-crystalline Basolite® F300 iron 1,3,5-benzenetricarboxylate. As described below, these materials have a similar iron 1,3,5-benzenetricarboxylate composition (although the molecular formula of Basolite® F300 remains largely unknown), yet their properties differ significantly. Thereafter, Pd nanoparticles are introduced following three different approaches. These approaches, as outlined in Figure 3.1., include: i) Incipient Wetness Impregnation (IWI), ii) Colloidal Particle Deposition (CPD) and iii) Chemical Vapour Infiltration (CVI).

3.3.1. Materials Characterization

a) Crystallinity. X-ray Diffraction (XRD) of MIL-100(Fe) and Basolite® F300 supports, as shown in Figure 3.2, a sharp contrast in structural order at longer length ranges between both samples. In the case of MIL-100(Fe), that crystallizes in a face-centered cubic *fcc* structure of the *Fd̄3m* group, XRD displays sharp diffraction peaks at 2.4°, 3.9° and 4.6°, corresponding to the (111), (220) and (311) crystallographic planes of MIL-100(Fe), respectively (Figure 3.2a). This indicates that the synthesized material indeed has the MTN-zeotype framework structure. On the other hand, Basolite® F300 presents a smooth XRD pattern, in contrast to previous literature,²³ characteristic of a non-crystalline solid, thus preventing the assignment to a given crystalline structure. To further understand MIL-100(Fe) and Basolite® F300 structure at the short and intermediate range, X-ray Pair Distribution Function (PDF) analysis was conducted on both materials under study. The local environment of Fe atoms in MIL-100(Fe) and Basolite® F300 shows very similar first (Fe-O), second (Fe-C) and third (Fe-Fe) coordination shells (Figure 3.2b). The distance of the Fe-O bond is 2.08 and 2.12 Å for MIL-100(Fe) and Basolite® F300, respectively. Further, Fe-C and Fe-Fe distances were measured to be 3.4 Å and 3.2 Å; and 4.6 and 4.5 Å, for MIL-100(Fe) and Basolite® F300, respectively. These similar bond distances suggest minor structural changes between both materials in the first three coordination shells around Fe atoms.³¹

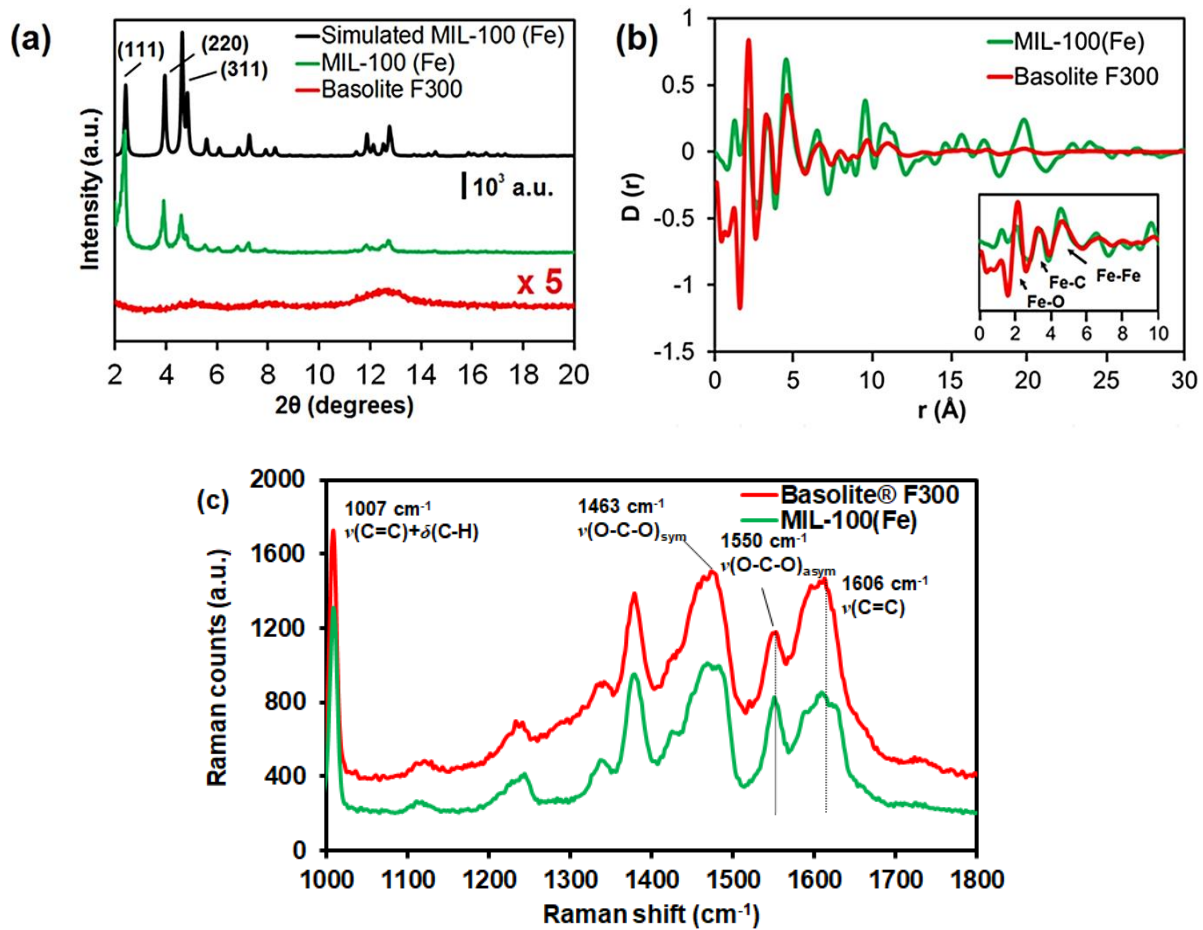


Figure 3.2 (a) X-ray Diffraction (XRD) and (b) normalized probability $D(r)$ obtained from X-ray total scattering of (green) MIL-100(Fe) and (red) Basolite® F300 supports. Inset shows first, second and third coordination shells together with the corresponding assigned bonds. (c) Raman spectra showing the fingerprint bands of BTC of both MOF.

However, the structural arrangement at intermediate and long ranges differs strongly from one support to the other. Beyond *ca.* 8 Å, Basolite® F300 shows very low PDF intensity, which corroborates the lack of long-range order, as observed in XRD. MIL-100(Fe) on the other hand shows intense signal features. Collectively, these results show that both MIL-100(Fe) and Basolite® F300 possess at the local scale oxo-centered trimers of iron octahedra. These, however, are assembled through BTC ligands into a disordered lattice, with structural amorphisation at length scales beyond the trimer building block. Therefore, we can conclude that Basolite® F300 is structurally perturbed compared to the highly ordered MIL-100(Fe) material. Additional Raman spectroscopy reveals that the band intensity ratio of 1606 cm^{-1} $\nu(\text{C=C})$ to 1550 cm^{-1} $\nu(\text{O-C-O})_{\text{asymmetric}}$ is higher for Basolite® F300 compared to MIL-100(Fe) (Figure 3.2c).³² This suggests that O-C-O bond vibrations are less intense for disordered Basolite® F300, as a consequence of the

increased O-C-O bond disorder due to structural perturbation. This observation further suggests that structural disorder affects bond vibrations.

b) Porosity. MOF framework crystallinity or the lack thereof has a potential impact on the pore network geometry. N₂ isotherms acquired at 77 K (Figure 3.3a) showed a type I behaviour for both crystalline MIL-100(Fe) and disordered Basolite® F300, typical of microporous materials. This implies that no meso- and macroporosity is introduced in Basolite® F300 due to the perturbed metal-linker organization. Aside from their similar isotherm type, multiple differences are present between both materials. First, the MIL-100(Fe) and Basolite® F300 BET surface areas amount to 1040 m²/g and 685 m²/g, respectively. Owing to the difference in synthetic protocols, the surface area of MIL-100(Fe) differs from the one reported by the group of Férey, suggesting not as well crystallized material (also observed in the XRD peak broadness).³³ Even though Férey and co-workers have reported MIL-100(Fe) with even higher crystallinity, here we aim to compare MIL-100(Fe) obtained by simple and scalable synthesis protocols that do not involve the presence of HF to Basolite® F300.

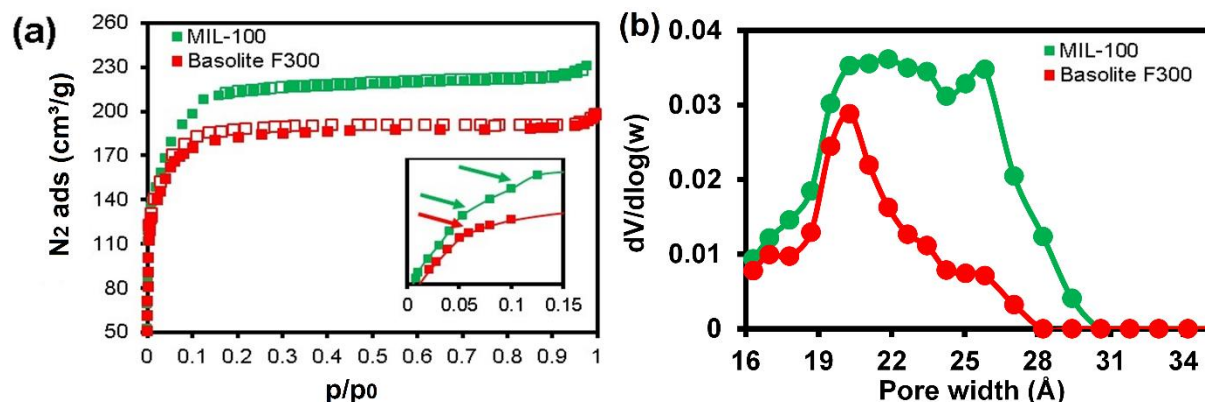


Figure 3.3 (a) N₂ adsorption isotherm at 77 K (inset shows the low-pressure $p/p_0 \leq 0.015$ range with different steps indicated by the arrows) and (b) pore size distribution of both materials derived from the N₂ adsorption data by the Non-Local Density Functional Theory (NLDFT) method, that was used here to get a simple estimate of the pore size distribution. Arrows indicate each type of cage in the structure corresponding to the steps in the isotherm.

In addition, their respective pore volumes differ from 0.45 cm³/g for MIL-100(Fe) to 0.29 cm³/g for Basolite® F300. Therefore, the overall loss in crystallinity observed for Basolite®

F300 relative to MIL-100(Fe) causes a decrease in the porosity of these microporous materials. This porosity loss is also reflected in the maximal N₂ uptake at p/p₀ > 0.95 which decreases from 220 cm³/g for MIL-100(Fe) to 190 cm³/g for Basolite® F300. A detailed investigation of the MIL-100(Fe) isotherm in the low relative pressure regime – p/p₀ between 0.05 and 0.15 – shows two steps, corresponding to the filling of the two different cages (Figure 3.3a inset).³³ As the experimentally determined pore size of MIL-100(Fe) is reported to be in the limit between micropore and mesopore,³⁴⁻³⁶ the use of Non-Local Density Functional Theory (NLDFT) to evaluate the pore size distribution is considered to be the best method compared to the Barrett-Joyner-Halenda (BJH) method, that is applicable only for mesoporous materials. The challenge in the NLDFT method, however, is that there are no perfect kernels known for MOFs. In this Chapter, we have considered to apply NLDFT with a model of nitrogen on silica with a cylindrical pore as it shows the best result. Indeed, our results are comparable to previous reports that used DFT methods.

As can be observed, the overall loss in crystallinity observed for Basolite® F300 relative to MIL-100(Fe) causes a decrease in the porosity of these materials. The loss of porosity in Basolite® F300 may also affect the acidity and hydrophilicity of the material that will be further discussed. The estimated NLDFT pore size distribution of MIL-100(Fe) exhibits a bimodal shape, where the two *modi* are centered at ~18-23 Å and ~25-27 Å (Figure 3.3b), corresponding to the two cages of the zeotypic structure. In contrast, Basolite® F300 exhibits a single visually observable step in the low-pressure regime. Estimation of the pore size distribution logically yields a monomodal pore size distribution, centered around 18-22 Å, though with lower abundances relative to MIL-100(Fe). This suggests that the bimodal pore system of MIL-100(Fe) is not present in Basolite® F300, possibly due to the disordered nature of this compound.

c) Acidity. The Basolite® F300 structure is strongly perturbed compared to the crystalline MIL-100(Fe), yielding a lack of long-range order beyond 8 Å and a well-defined pore network. Whilst order in the pore system may not be a requirement for many applications, such configurationally perturbed linker-node organization can induce changes in the

acidic properties of these materials, which is substantiated here by the use of probe-molecule Fourier Transform Infrared (FT-IR) spectroscopy. Prior to pyridine-probed (Py) FT-IR, the supports were dried at 498 K under secondary vacuum ($p < 10^{-3}$ mbar) for 16 h to remove terminal aqua and hydroxido ligands bound to Fe^{3+} Lewis acid Coordinatively Unsaturated Sites (CUS).³⁷ The Py FT-IR spectra show two main bands at 1070 and 1042 cm^{-1} , corresponding to the ν_{18a} and ν_{12} asymmetrical ring stretching modes of pyridine, respectively (Figure 3.4a).³⁸ No spectral shifts are observed after prolonged pyridine exposure in any of the samples, indicating no interaction with the MOF surface affecting those modes. The FT-IR band at 1014 cm^{-1} corresponds to pyridine interacting with Fe^{3+} sites, *i.e.* Py… Fe^{3+} , while the IR band at 1007 cm^{-1} relates to reduced Fe^{2+} centres.³⁹

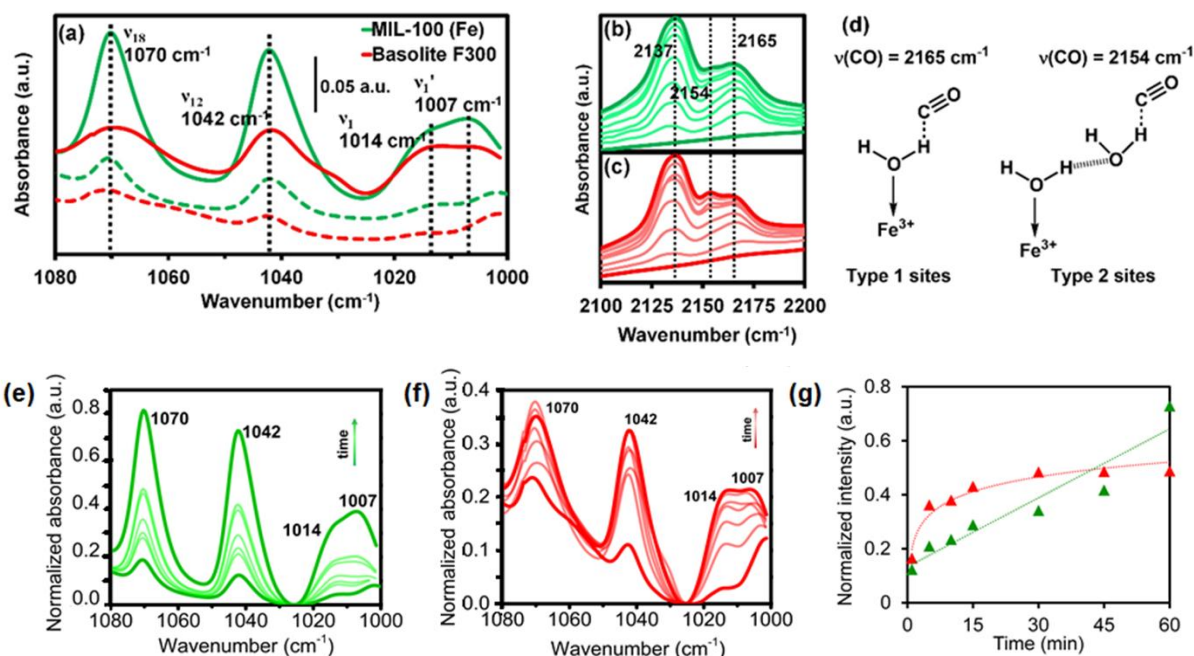


Figure 3.4 FT-IR spectra showing the 1100 – 1000 cm^{-1} region of (green) MIL-100(Fe) and (red) Basolite® F300 1 min and 60 min after introducing 15 mbar of pyridine at 323 K. Spectra were recorded in transmission mode on ~10 mg pellets. (b) Basolite® F300 and (c) MIL-100(Fe) at different CO pressures (from 10^{-2} mbar to 100 mbar) at 85 K. (d) Schematic representation of the vibrational modes assigned to the bands of CO bonded to different $\text{H}_2\text{O}-\text{Fe}^{3+}$ species and physisorbed CO (2137 cm^{-1}), adapted from reference [17]. Pyridine-probe FT-IR spectra of (e) MIL-100(Fe) and (f) Basolite® F300 after dosing 10 mbar of pyridine. The spectra go from 1 min after dosing up to 60 min (bold curves). (g) Evolution of the normalized intensity of the band at 1042 cm^{-1} (see main text for assignment) with time. Absorbance has been normalized both to baseline and to Brunauer-Emmett-Teller (BET) surface area of each material.

Evolution of the normalized intensity of the FT-IR band at 1042 cm^{-1} over time (Figure 3.4g) reveals that pyridine uptake reaches a steady state for Basolite® F300 after 30 min, while it increases linearly up to 60 min in the case of MIL-100(Fe). This indicates that a higher amount of pyridine can be adsorbed, suggesting that there are more adsorption sites per unit surface area thus, a higher number of acid sites in the case of MIL-100(Fe). Moreover, the relative intensity of the IR bands at 1014 and 1007 cm^{-1} is different at similar adsorption times. This indicates that the redox properties of Fe sites are different for each MOF, as previously reported by the group of García.⁴⁰ They might be associated to steric or electronic constraints particular of each material, although further experiments would be necessary to elucidate them.

Dhakshinamoorthy *et al.*⁴⁰ observed a correlation in intensity between the ν_7 mode at 1007 cm^{-1} and the sharp $\nu(\text{OH})$ vibrational band at 3575 cm^{-1} , assigned to the free carboxylic groups (both from unreacted trimesic acid and point defects), which they connected to PyH⁺ sites of -OH groups arising from those defects and impurities. In this Chapter, the IR band at 1007 cm^{-1} was observed in the FT-IR spectra of both materials after pyridine dosing, but no effect on the 2000 - 3600 cm^{-1} region was observed. This implies that both materials have a certain amount of reduced Fe²⁺ sites, but no significant amount of linker defects are observed. When comparing the spectral band intensities in Figure 3.4a, Basolite® F300 clearly possesses less Lewis acid sites compared to MIL-100(Fe). However, the nature of these Lewis acid sites that both supports possess is very similar.⁴⁰ In order to study the Brønsted acidity arising from the OH groups coordinating Fe³⁺ sites, the CO probe molecules are adsorbed onto the support at 85 K, after drying the sample at 448 K for 3 h at $p < 10^{-3}$ mbar. In both supports, very similar IR bands at 2165, 2154 and 2138 cm^{-1} appear upon insertion of CO in the cell (Figure 3.4b and Figure 3.4c). Specifically, the IR bands at 2165 and 2154 cm^{-1} correspond to the CO stretching vibrations interacting with the acidic -OH groups bonded to iron in multimeric species: [Fe³⁺--OH₂]…C≡O and [Fe³⁺--OH₂--OH₂]…C≡O, respectively (Figure 3.4d); while the IR band at 2137 cm^{-1} corresponds to CO physisorbed in the pores. All in all, from the spectroscopic analysis, it can be deduced that the nature of Brønsted or Lewis acid sites in both Basolite® F300 and MIL-100(Fe) materials is very similar. No significant linker-node under-

coordination could be detected for structurally more disordered Basolite® F300, due to the absence of the $\nu(\text{OH})$ vibrational band at 3575 cm^{-1} . However, a lower number of Lewis acid sites, could be substantiated for Basolite® F300, as suggested by the lower band intensities across the Py FT-IR range from $1000\text{-}1080 \text{ cm}^{-1}$ for Basolite® F300 compared to MIL-100(Fe).

c) Hydrophilicity. The differing Lewis acidity for Basolite® F300 and MIL-100(Fe) at the molecular scale could potentially impact the polarity of the materials as a whole, and their hydrophilicity on a more macroscopic level.

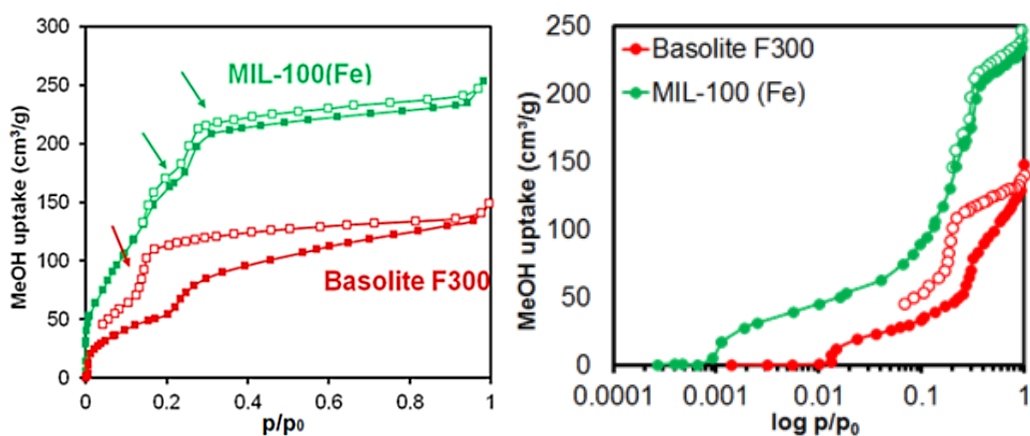


Figure 3.5 Methanol sorption isotherms acquired at 298 K of both supports along with the plot of methanol uptake $\text{vs. } \log p/p_0$. Before adsorption measurement, both samples were degassed at 443 K for 16 h under secondary vacuum ($p < 10^{-3} \text{ bar}$). Arrows indicate different steps corresponding to the filling of each type of pore (2 for MIL-100(Fe) and 1 for Basolite® F300).

To evaluate this hydrophilicity, or affinity towards polar molecules, methanol (MeOH) isotherms were collected at 298 K for MIL-100(Fe) and Basolite® F300 (Figure 3.5). MeOH filling of the pore systems of these materials is in full agreement with N_2 physisorption: the MIL-100(Fe) MeOH isotherm displays two steps resulting from MeOH filling of each cage type; while Basolite® F300 shows only one step as a result of the filling of a monomodal pore system. Second, hydrophilicity of each material can be obtained via the Henry's constant from the MeOH isotherms as reported in literature (Figure 3.5).⁴¹ For MIL-100(Fe) and Basolite® F300, Henry's constant values are $4.2 \cdot 10^{-6}$ and $2.2 \cdot 10^{-6} \text{ mol.g}^{-1}\text{Pa}^{-1}$, respectively, evidencing a more hydrophilic surface for MIL-100(Fe) than for

Basolite® F300 (Table 3.1). This is in accordance with the maximal methanol uptake of 253 cm³/g for MIL-100(Fe) compared to 149 cm³/g for Basolite® F300 at p/p₀ = 0.95. Even when normalizing to the higher surface area of MIL-100(Fe) relative to Basolite® F300 (BET_{MIL-100}/BET_{Basolite} = 1.52), MIL-100(Fe) adsorbs 12 % more MeOH per unit surface area compared to Basolite® F300. This is also the case when normalized to the pore volume of both materials (V_p _{MIL-100}/ V_p _{Basolite} = 1.55), corresponding to 11% more MeOH adsorbed per unit pore volume.

Table 3.1. Overview of the physicochemical properties of the two iron (III) 1,3,5-benzenetricarboxylate materials under study as obtained with various physicochemical characterization methods.

	Basolite® F300	MIL-100(Fe)
Composition (activated)	unknown	Fe ₃ (μ ₃ -O)(C ₆ H ₄ O ₄) ₃ X ₃ (H ₂ O) ₃ ·nH ₂ O (X = NO ₃ ⁻ or OH ⁻)
Structure	disordered	crystalline
Space group	-	F̄3dm
Fe-O bond distance (Å)^a	2.12	2.08
Brønsted acid sites^{c,b,f}	Fe ³⁺ ...OH ₂	Fe ³⁺ ...OH ₂
Lewis acid sites^c	Fe ³⁺ /Fe ²⁺	Fe ³⁺ /Fe ²⁺
MeOH uptake (cm³/g)^d	149	253
K_H (MeOH)^d	2.2·10 ⁻⁶	4.2·10 ⁻⁶
N₂ BET area (m²/g)^e	685	1040
V_p (cm³/g)^e	0.29	0.45
Fe (%)^{f,g}	3.9 (19.6)	4.8 (20.3)
C (%)^{f,g}	63.7 (37.0)	59.4 (37.7)
O (%)^{f,g}	32.1 (n.a.)	35.8 (n.a.)
Adsorbed species (wt%)^h	22	29

^a Obtained from X-ray total scattering. ^b Measured with Pyridine-probed FT-IR spectroscopy; ^c and CO-probed FT-IR spectroscopy. ^d Calculated from MeOH sorption isotherm at 298 K; ^e and N₂ sorption isotherm at 77 K. ^f Surface composition determined from X-ray photoelectron spectroscopy (XPS) data. ^g Values in brackets correspond to bulk elemental composition in wt% determined by elemental analysis of the materials combusted with V₂O₅. ^h Obtained from Thermogravimetical Analysis (TGA).

In the case of MIL-100(Fe), the higher hydrophilicity can be correlated to an increased polarity of the material, induced by Lewis acidity.^{42, 43} The higher number of Lewis acid sites for MIL-100(Fe) relative to Basolite® F300 predicts a higher surface polarity and

hydrophilicity for MIL-100(Fe). This is indeed confirmed by the MeOH adsorption isotherms, and further suggested by pyridine-probe FT-IR experiments. Additionally, Thermogravimetric Analysis (TGA) was applied to further corroborate the stronger hydrophilicity of MIL-100(Fe) and the results are shown in Figure 3.6. The results show that MIL-100(Fe) has ~29 wt% loss of adsorbed species upon heating to 423 K under Ar flow, corresponding to adsorbed water, in contrast to ~22 wt% for Basolite® F300 (22 wt%) (Table 3.1). TGA of both materials under O₂ flow (10 mL·min⁻¹) revealed a similar trend, in which the release of adsorbed water and DMF was ~28 wt% for MIL-100(Fe) and ~15 wt% for Basolite® F300. When comparing the Fe content calculated from the Fe₂O₃ residue, Basolite® F300 showed to contain 18.9 wt% Fe, in contrast to MIL-100(Fe), for which only 15.4 wt% Fe was observed. These minor differences may correspond to nanosized impurity deposits undetectable by other techniques, as previously found in the literature.⁴⁴

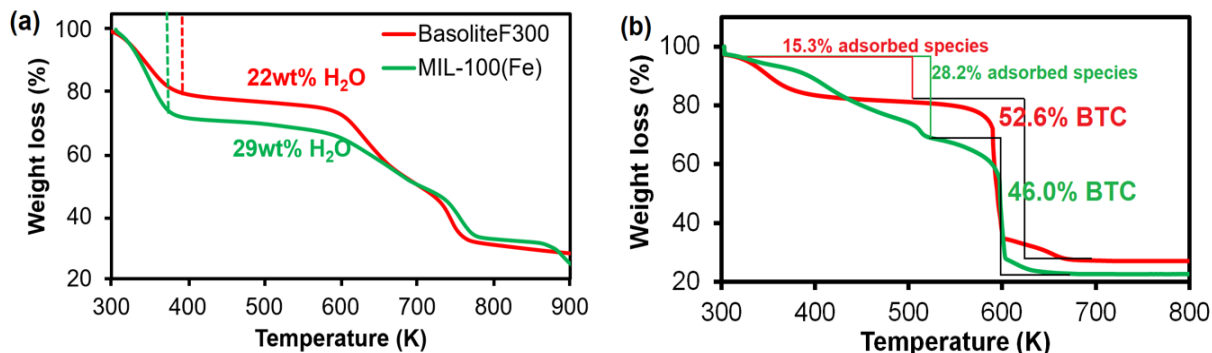
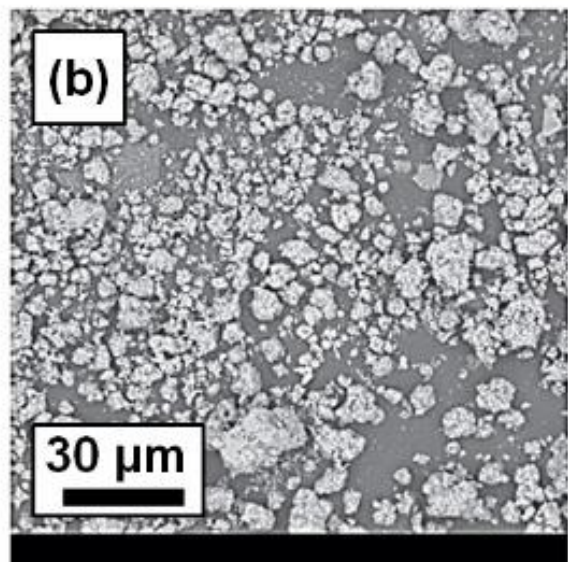
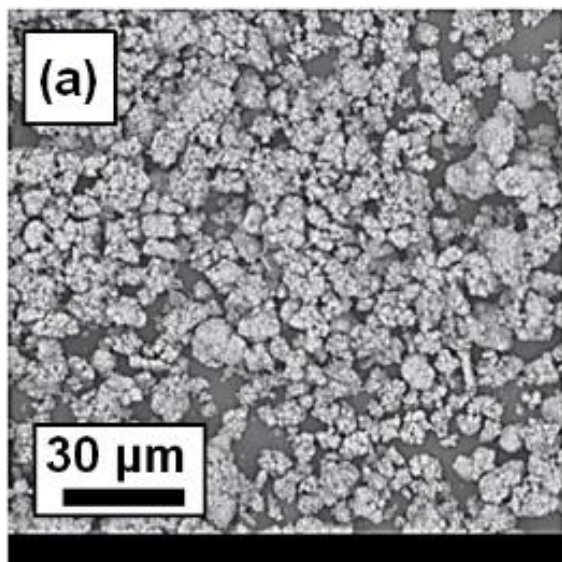
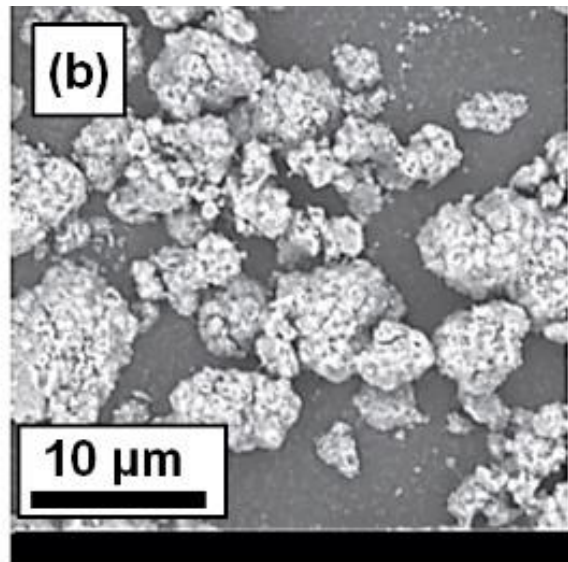
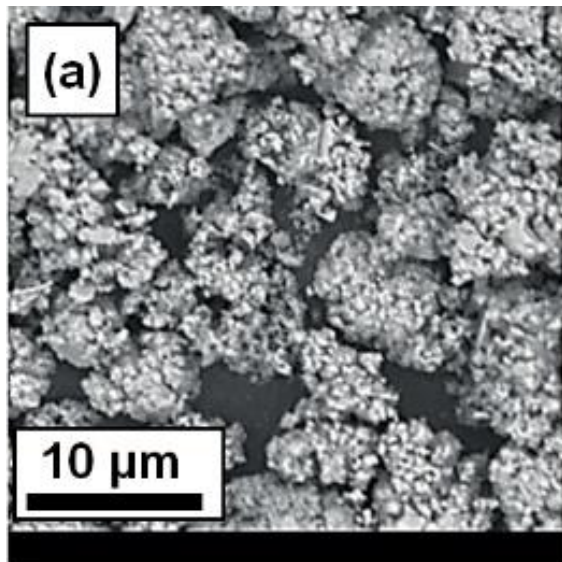


Figure 3.6 Thermogravimetric Analysis (TGA) under N₂ flow (a) and O₂ flow (b) of both supports after washing with DMF, MeOH and drying as described in the methods section.

Bulk composition, crystal morphology and surface composition and oxidation states were studied by elemental analysis (Table 3.1), Scanning Electron Microscopy (SEM) micrographs (Figure 3.7a-b) and X-ray Photoelectron Spectroscopy (XPS) (Figure 3.7c-f). In the case of XPS, the multiplet splitting characteristic of the Fe 2p region significantly increase the complexity of the peak analysis. Here, a simplified deconvolution of the Fe 2p XPS region has been applied (Figure 3.7d, f) and shows that all spectral features possess binding energies higher than 709 eV. This indicates that all iron species detected are Fe³⁺, and the presence of Fe²⁺ under these conditions would be overlapping with the

Fe^{3+} matrix. In spite of the small presence of higher surface oxygen (peak at 533.6 eV), the chemical nature of Fe and O species and the crystal morphology seem to be very similar.



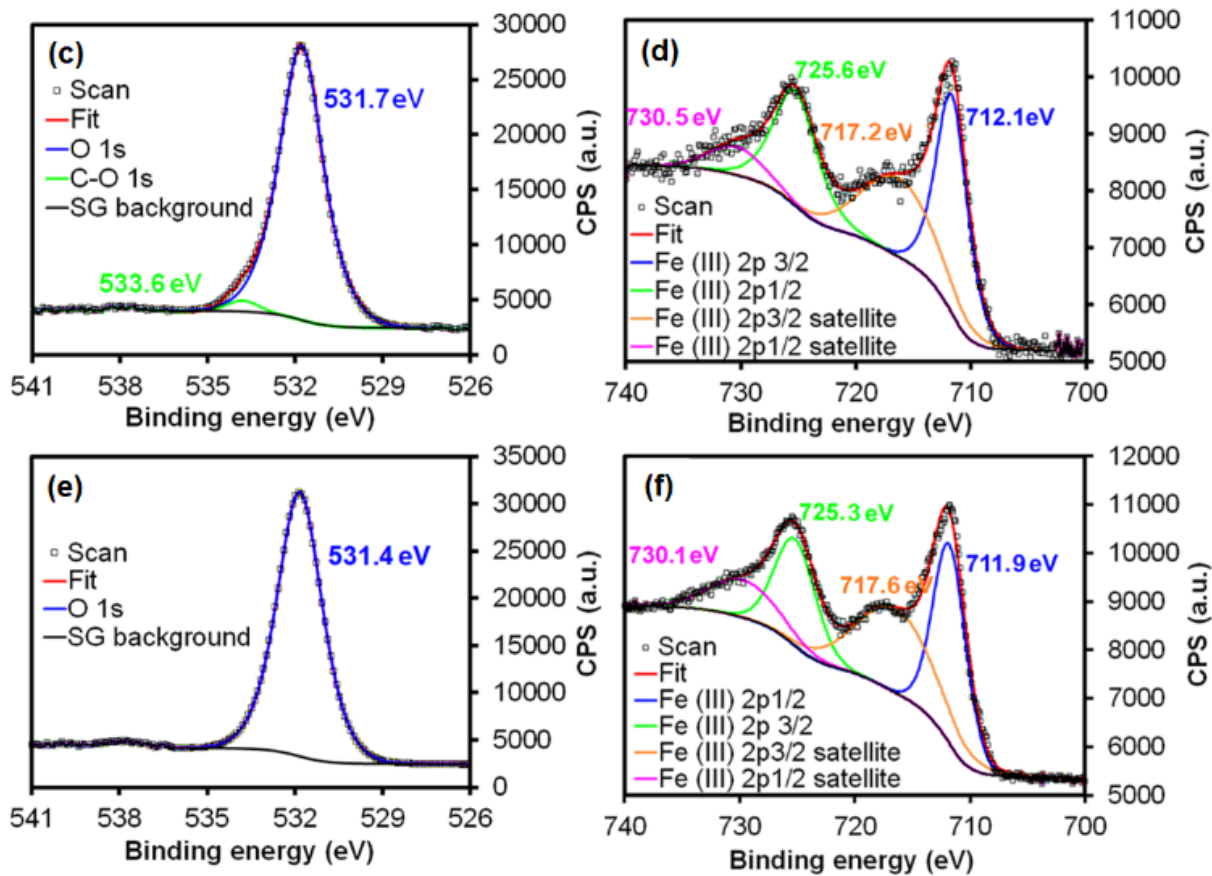


Figure 3.7 Scanning Electron Microscopy (SEM) images at different magnifications of (a) Basolite® F300 and (b) MIL-100(Fe) revealing similar morphology of aggregated nanosized crystallites. The O1s and Fe 2p lines of the X-ray Photoelectron Spectroscopy (XPS) data of (c, d) MIL-100(Fe) and (e, f) Basolite® F300 supports, respectively, revealing mostly Fe^{3+} in an iron oxide environment.

3.3.2. Metal Deposition

When used as a catalyst support, the differing structural and (physico-)chemical properties of MIL-100(Fe) and Basolite® F300 can influence the processes involved in metal NP deposition, including solvent wetting, metal precursor adsorption, nanoparticle formation/activation and stability. In what follows we discuss three archetypal metal deposition methods, i.e., Colloidal Particle Deposition (CPD) (Figures 3.8 and 3.9), Incipient Wetness Impregnation (IWI) (Figures 3.10 and 3.11) and Chemical Vapour Infiltration (CVI) (Figure 3.12) – have been applied to illustrate the potential impact of the MOF support properties on the formation of metal nanoparticle-supported catalyst materials.

a) Colloidal Pd Nanoparticle Deposited on FeBTC Materials. Oleylamine-stabilized Pd nanocrystals with an average particle size of ~5 nm (Figure 3.8) were synthesized and deposited on the external surface of MIL-100(Fe) and Basolite® F300.

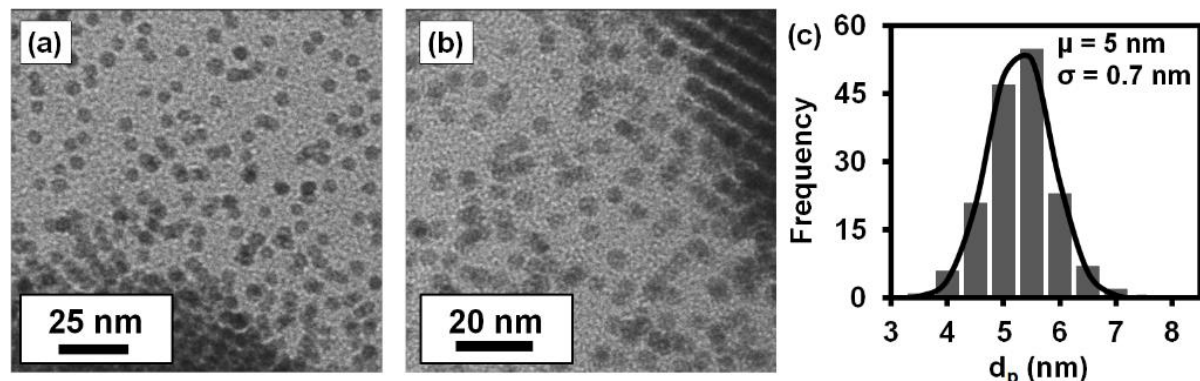


Figure 3.8 (a) and (b) Transmission Electron Microscopy (TEM) images of the monodisperse synthesized colloidal Pd nanocrystals stabilized with oleylamine and tri-octylphosphine and (c) Particle Size Distribution (PSD) of Pd nanoparticles made.

The Pd nanoparticles were readily prepared by mixing $\text{Pd}(\text{acac})_2$ with oleylamine and trioctylphosphine, which acted as a stabilizer and a reducing agent, as described in the Experimental Section. After stirring the colloidal Pd nanoparticles with the MOF support and carefully washing the excess of surfactant with hexane, which partially removed deposited Pd crystals (as indicated by the hexane turning turbid), the metal dispersion on surface was studied by means of Transmission Electron Microscopy (TEM). Some TEM images are shown in Figure 3.9.

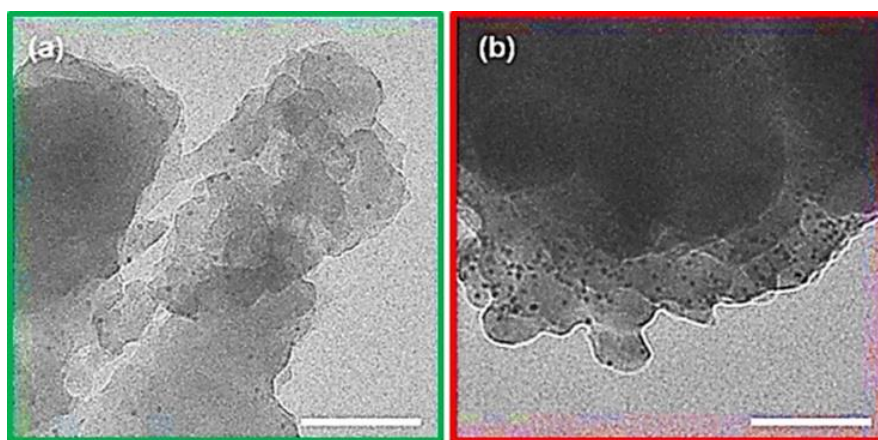
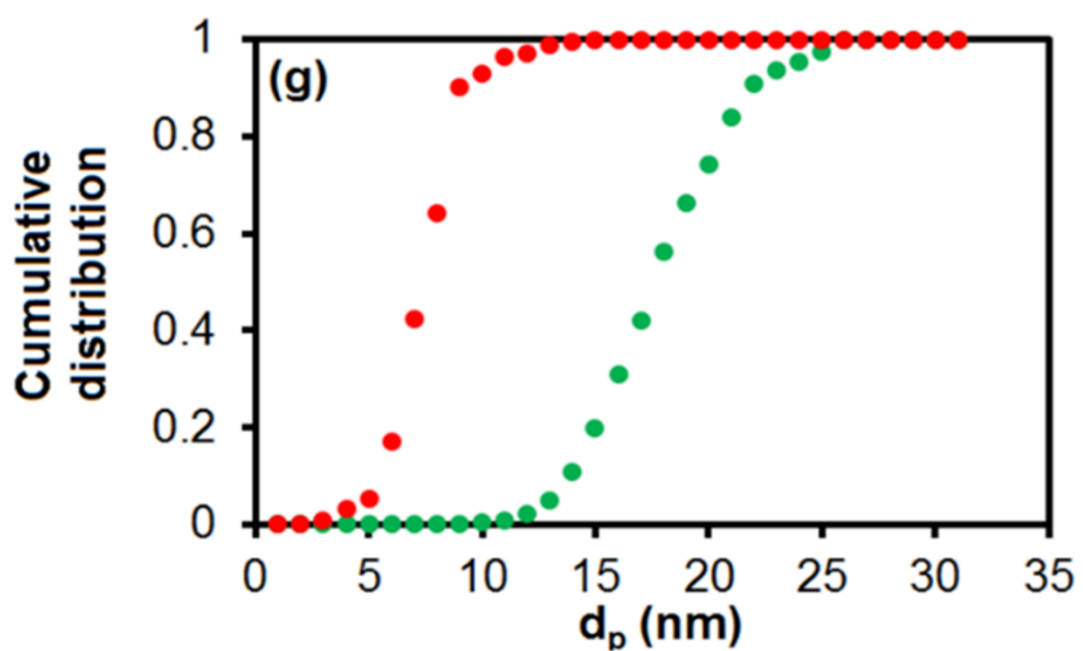
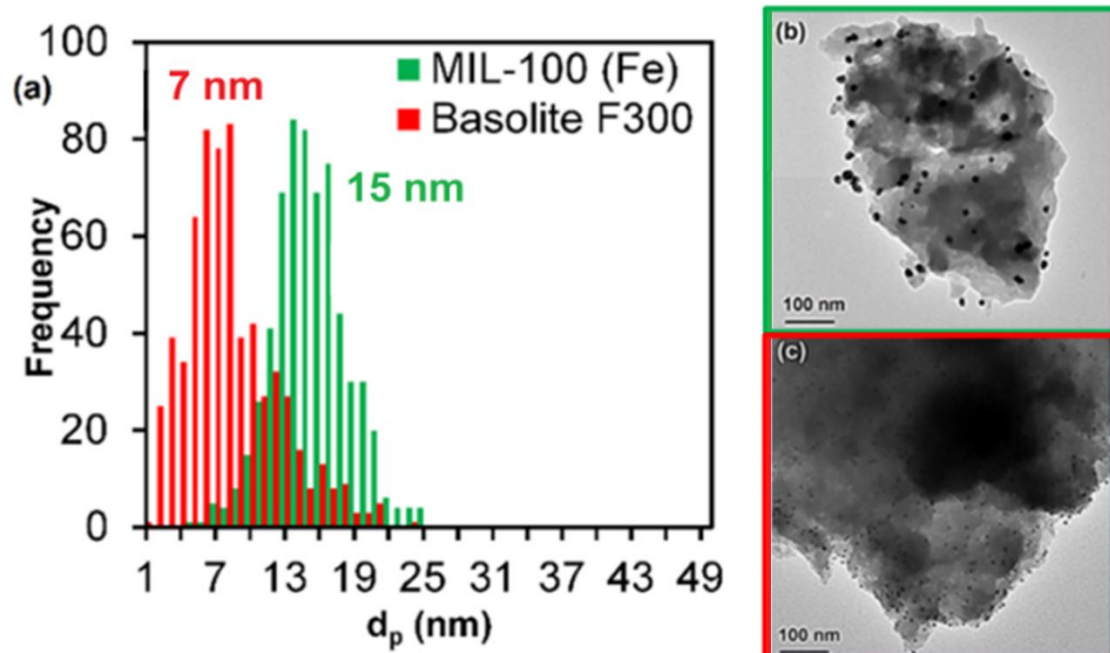


Figure 3.9 Transmission Electron Microscopy (TEM) images of the Pd/MOF composites obtained by depositing colloidal metal nanoparticles on (a) MIL-100(Fe) and (b) Basolite® F300. Scale bar represents 100 nm.

TEM evidences that the Basolite® F300 support surface is decorated with abundant Pd nanoparticles, whereas in the case of MIL-100(Fe) a lower amount of Pd NPs is observed. Indeed, bulk elemental analysis shows a higher colloidal uptake of Pd for the Basolite® F300 support (0.32 wt%) when compared to MIL-100(Fe) (0.2 wt%) (Table 3.2). These results can be rationalized when considering the previously observed support properties: Basolite® F300 is more hydrophobic than MIL-100(Fe) due to its lower Lewis acidity. This hydrophobic nature results in a favourable interaction with apolar oleylamine-capped Pd NPs, leading to attractive forces and consecutive adsorption of the colloidal Pd nanoparticles on the Basolite® F300 support. In contrast, for MIL-100(Fe), the apolar oleylamine capping ligands will establish reduced interactions with the more hydrophilic (polar, Lewis acid) support surface, leading to decreased nanoparticle anchoring. This might eventually result in an increased deposition of paraffin-capped Pd nanoparticles on Basolite® F300 compared to MIL-100(Fe), as observed in Figure 3.9.

b) Pd Nanoparticles Synthesized by Incipient Wetness Impregnation. In the case of Incipient Wetness Impregnation (IWI), two different cases are investigated: IWI of (1) Pd(acac)₂ using (apolar) CHCl₃ as a solvent, and (2) Na₂PdCl₄ using (polar) water on MIL-100(Fe) and Basolite® F300 supports. By calcination and H₂ reduction after impregnation of these Pd precursors, very different Pd nanoparticle size distributions are obtained for MIL-100(Fe) and Basolite® F300 supports, as evidenced by TEM (Figure 3.10). In the case of the Pd(acac)₂-CHCl₃ IWI, well-dispersed Pd nanoparticles with sizes centred ~7-8 nm decorate the Basolite® F300 support. For the more polar MIL-100(Fe) support, larger *ca.* 15 nm were obtained after calcination and H₂ reduction of the Pd precursor (Figure 3.10a-c). In the case of Na₂PdCl₄-water IWI, the situation is reversed, as the larger Pd particles grow on the surface of Basolite® F300, compared to those found on MIL-100(Fe). Furthermore, in addition to those larger Pd particles (> 20 - 50 nm size clusters) found in Basolite® F300, small nanoparticles are also observed for both Basolite® F300 and MIL-100(Fe) supports, as shown in Figure 3.10d-f.



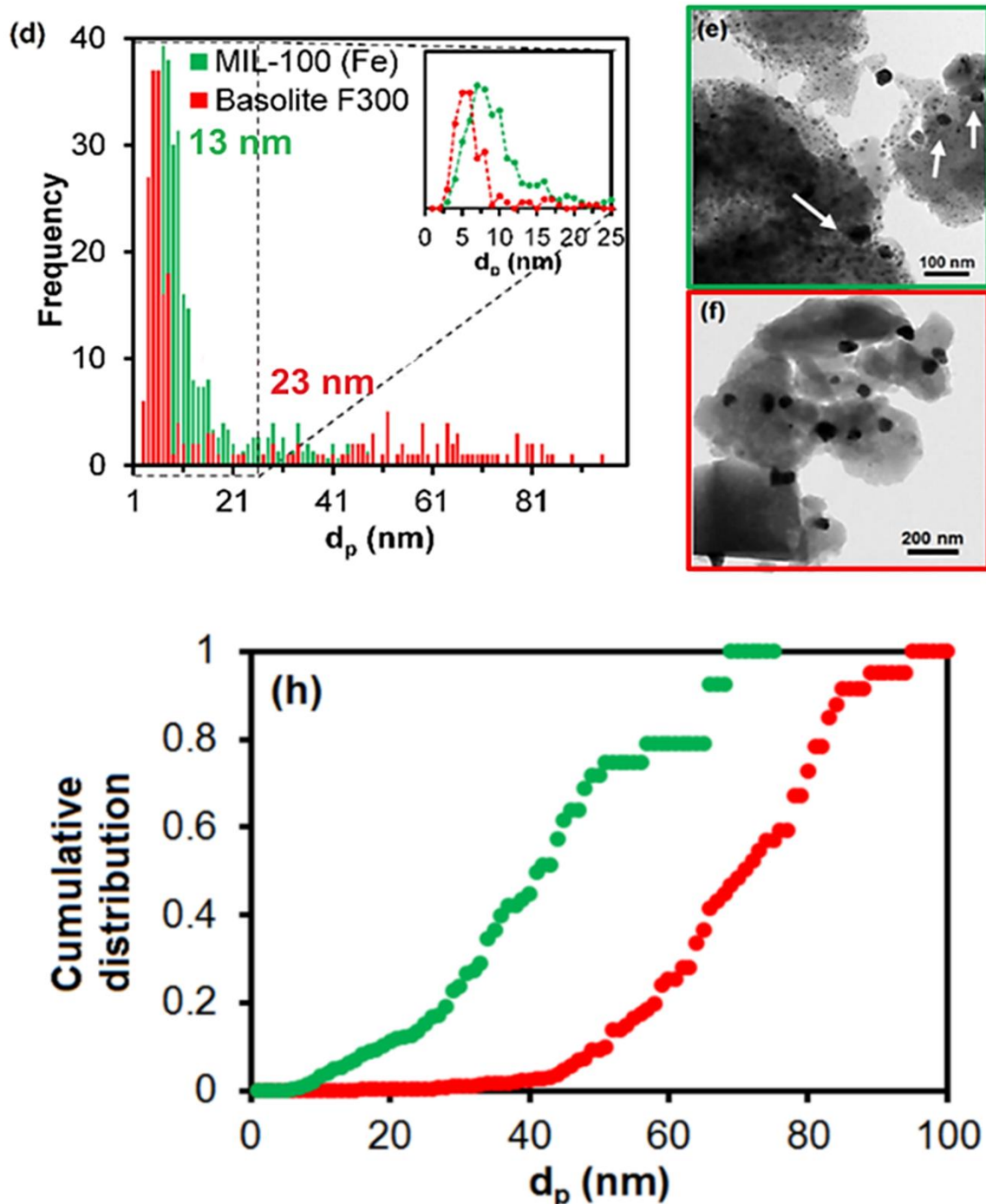


Figure 3.10 (a) Nanoparticle size distribution for both support materials under study. Transmission Electron Microscopy (TEM) images of 1 wt% Pd particles supported on (b) MIL-100(Fe) and (c) Basolite® F300 prepared with $\text{Pd}(\text{acac})_2$ in chloroform. (d) Nanoparticle size distribution of the same supports with 1 wt% Pd using Na_2PdCl_4 in water as a precursor. Inset shows the shape of both distributions for small Pd clusters. TEM images of (e) MIL-100(Fe) and (f) Basolite® F300. The white arrows indicate larger Pd aggregates observed. Nanoparticle size distributions were calculated from at least 150 particles from the TEM images. Cumulative volumetric distribution plots of Pd obtained from (g) $\text{Pd}(\text{acac})_2$ and (h) Na_2PdCl_4 precursors.

In order to better understand the distribution of Pd nanoparticles, the volumetrically weighted cumulative size distribution (Figure 3.10g-h) was calculated, following equation (Eq. 3.1):

$$\sum_i \frac{v_i \cdot f_i}{v_i} \quad (\text{Eq. 3.1})$$

, where v_i is the volume of Pd particles of diameter d_i , and f_i the frequency, assuming spheres. Figure 3.10 (g-h) shows that the majority of the Pd atoms reside in large-sized Pd nanoparticles (> 60 nm) for Basolite® F300 supports, whereas the majority of Pd atoms is included in smaller nanoparticles (< 60 nm) for MIL-100(Fe). XRD corroborate the obtained TEM results, as it shows higher Pd nanoparticle sizes for Basolite® F300 versus MIL-100(Fe) by analysing the Pd (111) and (200) diffractions in the corresponding XRD patterns (Figure 3.11). Even though many parameters play a role in the deposition and formation of Pd nanoparticles, we hypothesize that the described observations can be clarified by favoured polar-polar and apolar-apolar interactions.

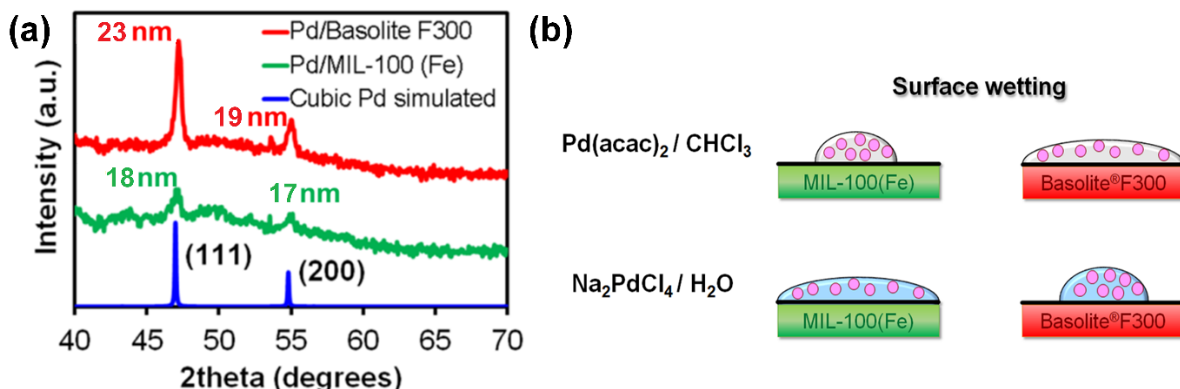


Figure 3.11 (a) X-ray Diffraction (XRD) patterns of MOF-supported Pd particles synthesized from the Na_2PdCl_4 anionic precursor in water, dried and subsequently calcined and reduced. The numbers indicate the estimated crystallite size *via* the Scherrer equation. (b) Surface wetting schematic of MIL-100(Fe) and Basolite® F300 when used as supports with different polar *vs.* apolar combinations of solvent and Pd precursor (depicted as pink circles). Pd precursor aggregates lead to larger particles upon calcination and reduction.

Chloroform is an apolar solvent (dipole moment $\vec{D} = 1.04$), which interacts attractively with the less polar Basolite® F300, and poorly with the more polar MIL-100(Fe). This will induce differences in solvent wetting of the support, which is more favoured on Basolite® F300. Upon sufficient solvent wetting, the acac-ligands undergo apolar-apolar attractive interactions with the Basolite® F300,⁴⁵ resulting in finely dispersed Pd nanoparticles. In

the case of MIL-100(Fe), solvent wetting by chloroform is more limited, which partially prevents intimate interactions between $\text{Pd}(\text{acac})_2$ ligands and the support, causing $\text{Pd}(\text{acac})_2$ precursor molecules to form larger clusters.⁴⁶ In the case of Na_2PdCl_4 -water IWI, the polar solvent will wet the most polar support, namely MIL-100(Fe), and the polar precursor anions (PdCl_4^{2-}) are expected to anchor preferentially on MIL-100(Fe). For more apolar Basolite® F300, solvent wetting will be less favourable, leading to precursor accumulation in the surface and large crystal formation upon calcination and H_2 reduction treatment.

c) Chemical Vapour Infiltration of Allyl Cyclopentadienyl Palladium. Deposition and infiltration of volatile organometallic compounds in MOFs for the formation of metal nanoparticles was pioneered by the group of Fischer.^{7, 47} The main advantage of this method in the particular case of MOFs is the high metal loadings that can be obtained while having a good dispersion and small cluster size (at the expense of complexity and cost of the precursors). Moreover, the formation of Pd nanoparticles is exclusively influenced by diffusion of the volatile compound inside the pores and the interaction with the surface during deposition and reduction.

Thus, we sought in this Chapter to study the differences in using either crystalline or disordered FeBTC supports by infiltrating allyl cyclopentadienyl palladium at low temperature (240 K). After reduction in static H_2 atmosphere, the commercial MOF showed a broad size distribution of the Pd nanoparticles ranging from 1 to 6.5 nm (Figure 3.12), while a narrow size distribution of Pd nanoparticles of *ca.* 2 nm ($\sigma = 1.7$) were observed in MIL-100(Fe). This difference can be explained by the crystalline structure of MIL-100(Fe), in which the precursor is deposited uniformly throughout the pores of the MOF framework structure. In contrast, in the case of the disordered Basolite® F300 this leads to the formation of aggregates of $[\text{Pd}(\eta_3\text{-C}_3\text{H}_5)(\eta_5\text{-C}_5\text{H}_5)]$, which eventually coalesce faster during reduction.

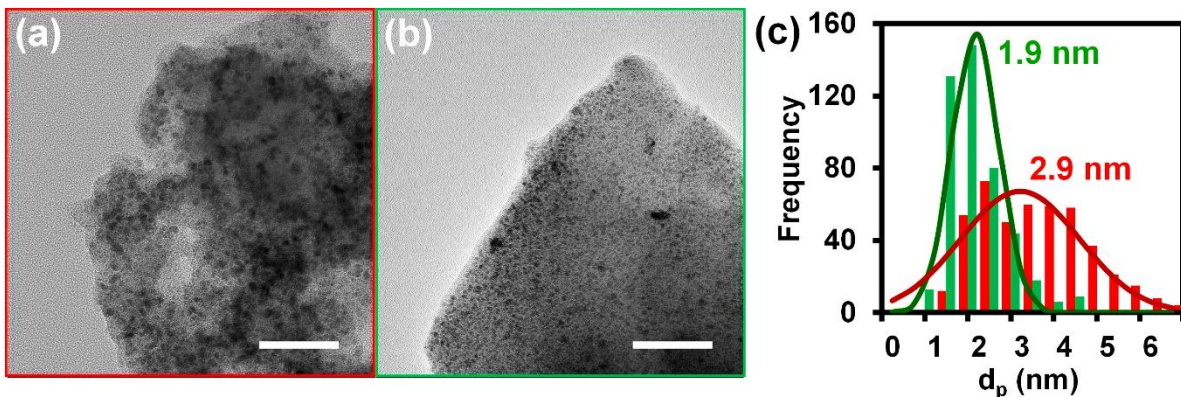


Figure 3.12 Transmission Electron Microscopy (TEM) images of Pd supported on (a) Basolite® F300 and (b) MIL-100(Fe) frameworks obtained by infiltration with the corresponding (c) particle size distributions. Scale bars represent 50 nm in both cases.

In addition, MIL-100(Fe) showed a higher metal loading compared to Basolite® F300 (3.95 wt% *vs.* 1.78%) despite larger Pd particles with a broader size distribution were observed in the latter. This may be ascribed to the differences in particle growth over the surface of Basolite® F300, which lead to such large Pd clusters. Another possible explanation would be the different diffusion within the complex, amorphous pore network of Basolite® F300 as compared with the MIL-100(Fe) material. We clearly show that although both materials have very similar chemical composition, their pore structure and surface properties play a key role in adsorption and formation of metal nanoparticles, which can later affect their catalytic properties.

3.3.3. Catalytic Hydrogenation of Cyclohexene

Hydrogenation reactions are one of the potential fields of application for Pd catalysts supported on MOFs.³ So as to compare the performance of Pd/FeBTC, the solvent-free hydrogenation of cyclohexene in the liquid phase was carried out as a model reaction to assess the properties of the materials made. The Pd-containing catalyst materials prepared from Pd(acac)₂ were used for these tests and the results are summarized in Figure 3.13 and Table 3.3. It was found that there is little influence of the support material on catalyst performance, being the effects more notable at lower temperature, *i.e.* 323 K, and ascribed most probably to diffusional problems inside the intricated pores of Basolite®F300 compared to the well-structured MIL-100(Fe). In fact, the limiting-rate factor

in this type of catalytic hydrogenations when using supported Pd particles in the 1.5 to 15 nm range is the solubility of H₂ gas in cyclohexene.⁴⁹

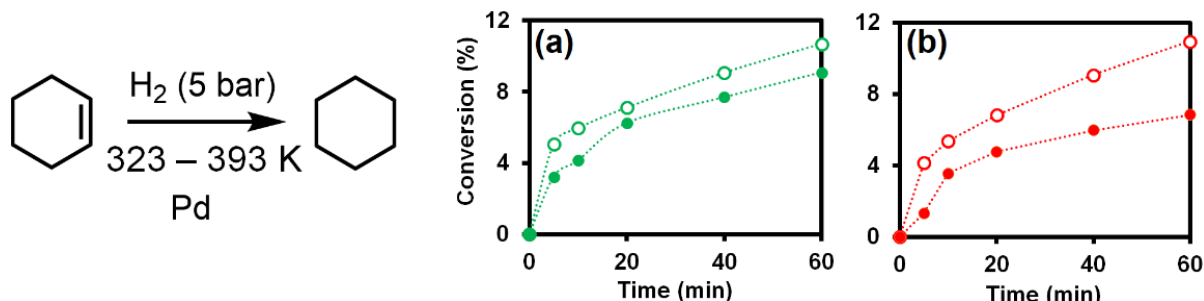


Figure 3.13 Conversion of cyclohexene at 5 bar of H₂ using Pd supported on (a) MIL-100(Fe) and (b) Basolite®F300 over the first hour of reaction conducted at 323 (filled circles) and 343 K (open circles).

Table 3.3. Catalytic performance of different supported nanoparticles for the solvent-free hydrogenation of cyclohexene, including the materials made and characterized in this Chapter.

Catalyst	Pd (%wt)	T (K)	P H ₂ (bar)	TOF (s ⁻¹)	Reference
Pd/Basolite®F300	1.26	323	5	2.16	This work
		393	5	3.47	This work
Pd/MIL-100 (Fe)	1.27	323	5	3.20	This work
		393	5	3.78	This work
Pd/SiO ₂	0.57	283	1	1.42	[49]
Pd/SiO ₂	3.75	283	1	1.36	[49]
Pd/Al ₂ O ₃	4.88	308	1	7.95	[49]
Ni/SiO ₂	3.5	298	10	2.15	[50]
Pt/SiO ₂	3.2	313	0.2	3.6	[51]

Initial turnover frequencies (over the first 60 min of reaction) of supported catalysts in the solvent-free hydrogenation of cyclohexene. Turnover frequency expressed as: TOF = mol_{Cyclohexene}·mol_{Pd}⁻¹·s⁻¹. No reaction products other than cyclohexane were observed in the ¹H NMR spectra.

Based on the results of Figure 3.13 and Table 3.3. we can conclude that the Pd/FeBTC materials prepared are both valuable hydrogenation catalysts. Since no significant

advantages over state-of-the-art materials (e.g. Pd/Al₂O₃) were observed, no further investigations were carried out for the rest of materials prepared. Although in this case, there are no significant differences in the catalytic performance of the Pd particles, this could be of importance when optimizing the preparation method (e.g., Pd size and dispersion) to maximize metal usage and to avoid deactivation by, for instance, metal particle sintering.

3.4 CONCLUSIONS

Industrial Basolite® F300 and lab-synthesized MIL-100(Fe) with a similar iron 1,3,5-benzenetricarboxylate composition show very different behaviour when used as support for the synthesis of Pd metal nanoparticles. XRD and PDF show that MIL-100(Fe) possess long-range order and has a MTN-zeotype crystal structure, while Basolite® F300 lacks long-range order beyond 8 Å. The configurational linker-node disorder responsible for this disordering decreases the number of Lewis acid sites in Basolite® F300 compared to MIL-100(Fe), while the nature of the acid sites remains similar. The decreased Lewis acidity of Basolite® F300 induces a change in the polarity/hydrophilicity of the materials, making Basolite® F300 more hydrophobic compared to hydrophilic MIL-100(Fe). This observation could be confirmed by methanol adsorption experiments. This discrepancy in hydrophilicity strongly alters the wettability of the solvent, depending on its polar nature, and the subsequent precursor anchoring onto the support surface. This has some effect on the hydrogenation catalysis properties of the materials prepared.

3.5. REFERENCES

1. H.-C. Zhou, J. R. Long and O. M. Yaghi, *Chem. Rev.*, 2012, **112**, 673-674.
2. J. Lee, O. K. Farha, J. Roberts, K. A. Scheidt, S. T. Nguyen and J. T. Hupp, *Chem. Soc. Rev.*, 2009, **38**, 1450-1459.
3. A. Corma, H. García and F. X. Llabrés i Xamena, *Chem. Rev.*, 2010, **110**, 4606-4655.
4. M. Muller, A. Devaux, C.-H. Yang, L. De Cola and R. A. Fischer, *Photochem. Photobio. Sci.*, 2010, **9**, 846-853.
5. G. Li, H. Kobayashi, J. M. Taylor, R. Ikeda, Y. Kubota, K. Kato, M. Takata, T. Yamamoto, S. Toh, S. Matsumura and H. Kitagawa, *Nat. Mater.*, 2014, **13**, 802-806.
6. M. Müller, S. Hermes, K. Kähler, M. W. E. van den Berg, M. Muhler and R. A. Fischer, *Chem. Mater.*, 2008, **20**, 4576-4587.
7. C. Rosler and R. A. Fischer, *CrystEngComm*, 2015, **17**, 199-217.
8. M. Meilikhov, K. Yusenko, D. Esken, S. Turner, G. Van Tendeloo and R. A. Fischer, *Eur. J. Inorg. Chem.*, 2010, 3701-3714.

-
9. P. Falcaro, R. Ricco, A. Yazdi, I. Imaz, S. Furukawa, D. MasPOCH, R. Ameloot, J. D. Evans and C. J. Doonan, *Coord. Chem. Rev.*, 2016, **307**, 237-254.
10. Q. Yang, Q. Xu and H.-L. Jiang, *Chem. Soc. Rev.*, 2017, **46**, 4774-4808.
11. A. Dhakshinamoorthy and H. Garcia, *Chem. Soc. Rev.*, 2012, **41**, 5262-5284.
12. H. R. Moon, D.-W. Lim and M. P. Suh, *Chem. Soc. Rev.*, 2013, **42**, 1807-1824.
13. Y. Zhang, Y. Zhou, Y. Zhao and C.-j. Liu, *Catal. Today*, 2016, **263**, 61-68.
14. D. S. Sholl and R. P. Lively, *J. Phys. Chem. Lett.*, 2015, **6**, 3437-3444.
15. L. Yuan, M. Tian, J. Lan, X. Cao, X. Wang, Z. Chai, J. K. Gibson and W. Shi, *Chem. Commun.*, 2018, **54**, 370-373.
16. M. J. Cliffe, W. Wan, X. Zou, P. A. Chater, A. K. Kleppe, M. G. Tucker, H. Wilhelm, N. P. Funnell, F.-X. Coudert and A. L. Goodwin, *Nat. Commun.*, 2014, **5**, 4176.
17. T. D. Bennett and A. K. Cheetham, *Acc. Chem. Res.*, 2014, **47**, 1555-1562.
18. J. Canivet, M. Vandichel and D. Farrusseng, *Dalton Trans.*, 2016, **45**, 4090-4099.
19. Z. Fang, B. Bueken, D. E. De Vos and R. A. Fischer, *Angew. Chem. Int. Ed.*, 2015, **54**, 7234-7254.
20. T. D. Bennett, A. H. Fuchs, A. K. Cheetham and F.-X. Coudert, *Dalton Trans.*, 2016, **45**, 4058-4059.
21. T. D. Bennett, A. K. Cheetham, A. H. Fuchs and F.-X. Coudert, *Nat. Chem.*, 2017, **9**, 11-16.
22. X. Hu, X. Lou, C. Li, Y. Ning, Y. Liao, Q. Chen, E. S. Mananga, M. Shen and B. Hu, *RSC Adv.*, 2016, **6**, 114483-114490.
23. M. Sanchez-Sanchez, I. de Asua, D. Ruano and K. Diaz, *Cryst. Growth Des.*, 2015, **15**, 4498-4506.
24. A. Dhakshinamoorthy, M. Alvaro and H. Garcia, *Chem. Commun.*, 2012, **48**, 11275-11288.
25. N. Yuan, V. Pascanu, Z. Huang, A. Valiente, N. Heidenreich, S. Leubner, A. K. Inge, J. Gaar, N. Stock, I. Persson, B. Martín-Matute, X. Zou, *J. Am. Chem. Soc.*, 2018, **140**, 26, 8206-8217.
26. F. Carson, V. Pascanu, A. Bermejo Gómez, Y. Zhang, E. Platero-Prats Ana, X. Zou and B. Martín-Matute, *Chem. Eur. J.*, 2015, **21**, 10896-10902.
27. F. Zhang, J. Shi, Y. Jin, Y. Fu, Y. Zhong and W. Zhu, *Chem. Eng. J.*, 2015, **259**, 183-190.
28. S.-W. Kim, J. Park, Y. Jang, Y. Chung, S. Hwang, T. Hyeon and Y. W. Kim, *Nano Lett.*, 2003, **3**, 1289-1291.
29. A. K. Soper, *Tech. Rep. RAL-TR-2011-013 Rutherford Appleton Laboratory*, 2011, DOI: 10.1021/cs300345b.
30. D. Keen, *J. Appl. Crystallogr.*, 2001, **34**, 172-177.
31. L. Sciortino, A. Alessi, F. Messina, G. Buscarino and F. M. Gelardi, *J. Phys. Chem. C*, 2015, **119**, 7826-7830.
32. M. Todaro, A. Alessi, L. Sciortino, S. Agnello, M. Cannas, F. M. Gelardi and G. Buscarino, *J. Spectr.*, 2016, 8074297, 7 pages.
33. P. Horcajada, S. Surble, C. Serre, D.-Y. Hong, Y.-K. Seo, J.-S. Chang, J.-M. Grenèche, I. Margiolaki and G. Férey, *Chem. Commun.*, 2007, 2820-2822.
34. J. Shi, S. Hei, H. Liu, Y. Fu, F. Zhang, Y. Zhong and W. Zhu, *J. Chem.*, 2013, 792827, 4 pages.
35. S. Huang, K.-L. Yang, X.-F. Liu, H. Pan, H. Zhang and S. Yang, *RSC Adv.*, 2017, **7**, 5621-5627.
36. F. Tan, M. Liu, K. Li, Y. Wang, J. Wang, X. Guo, G. Zhang and C. Song, *Chem. Eng. J.*, 2015, **281**, 360-367.
37. J. W. Yoon, Y.-K. Seo, Y. K. Hwang, J.-S. Chang, H. Leclerc, S. Wuttke, P. Bazin, A. Vimont, M. Daturi, E. Bloch, P. L. Llewellyn, C. Serre, P. Horcajada, J.-M. Grenèche, A. E. Rodrigues and G. Férey, *Angew. Chem. Int. Ed.*, 2010, **49**, 5949-5952.
38. K. N. Wong and S. D. Colson, *J. Mol. Spectrosc.*, 1984, **104**, 129-151.
39. H. Leclerc, A. Vimont, J.-C. Lavalley, M. Daturi, A. D. Wiersum, P. L. Llewellyn, P. Horcajada, G. Férey and C. Serre, *Phys. Chem. Chem. Phys.*, 2011, **13**, 11748-11756.
40. A. Dhakshinamoorthy, M. Alvaro, P. Horcajada, E. Gibson, M. Vishnuvarthan, A. Vimont, J.-M. Grenèche, C. Serre, M. Daturi and H. Garcia, *ACS Catal.*, 2012, **2**, 2060-2065.
41. J. Canivet, J. Bonnefoy, C. Daniel, A. Legrand, B. Coasne and D. Farrusseng, *New J. Chem.*, 2014, **38**, 3102-3111.
42. S. Dissegna, R. Hardian, K. Epp, G. Kieslich, M.-V. Coulet, P. Llewellyn and R. A. Fischer, *CrystEngComm*, 2017, **19**, 4137-4141.
43. D. Farrusseng, S. Aguado and C. Pinel, *Angew. Chem. Int. Ed.*, 2009, **48**, 7502-7513.
44. Y.-K. Seo, J. W. Yoon, J. S. Lee, U. H. Lee, Y. K. Hwang, C.-H. Jun, P. Horcajada, C. Serre and J.-S. Chang, *Micropor. Mesopor. Mater.*, 2012, **157**, 137-145.
45. D. Esken, X. Zhang, O. I. Lebedev, F. Schroder and R. A. Fischer, *J. Mater. Chem.*, 2009, **19**, 1314-1319.
46. M. L. Toebes, J. A. van Dillen and K. P. de Jong, *J. Mol. Catal. A: Chem.*, 2001, **173**, 75-98.
47. S. Hermes, M.-K. Schröter, R. Schmid, L. Khodeir, M. Muhler, A. Tissler, R. W. Fischer and R. A. Fischer, *Angew. Chem. Int. Ed.*, 2005, **44**, 6237-6241.
-

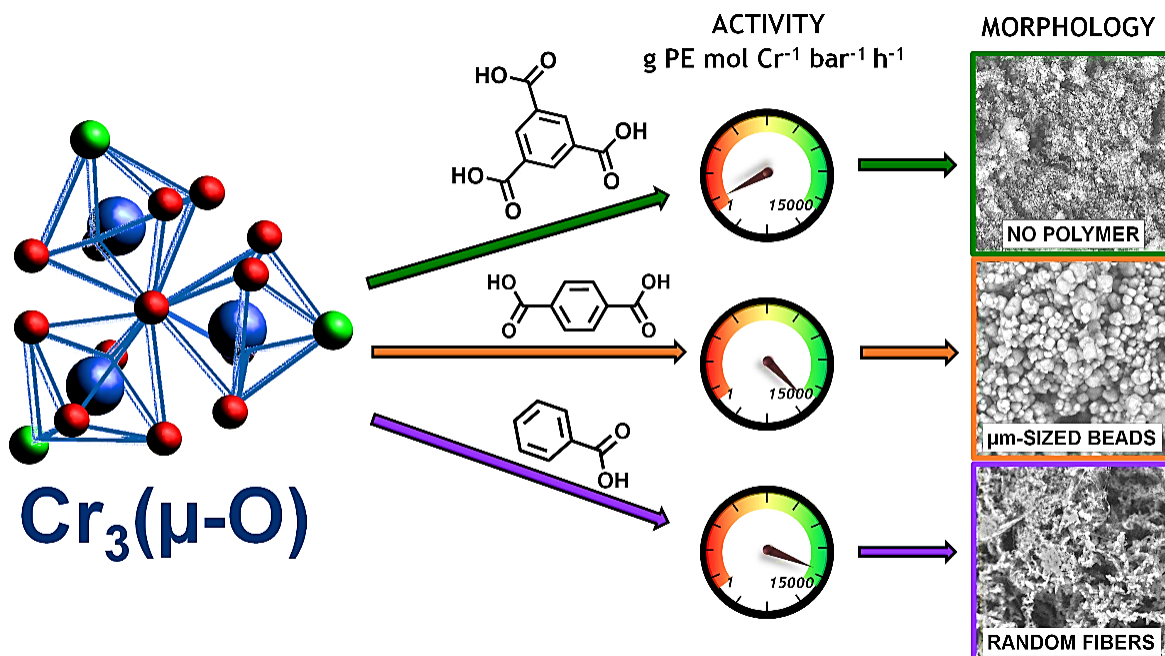
48. P. Munnik, P. E. de Jongh and K. P. de Jong, *Chem. Rev.*, 2015, **115**, 6687-6718.

PART B

Generation of Defects in Metal-Organic Frameworks: Synthesis, Spectroscopy and Catalysis

Chapter 4

Defect Sites in Zeotypic Cr-based Metal-Organic Frameworks: Ethylene Polymerization and *In-situ* Spectroscopy



MIL-100 topology is among the most studied Metal Organic Framework (MOF) structures, due to its combination of mesoporosity, chemical robustness and ease of preparation. In this Chapter, we present the formation of either fibres or micron-sized beads by using the MIL-100(Cr) and MIL-101(Cr) zeotypes. These structures have been used for ethylene polymerization with Diethyl-Aluminium Chloride (DEA) as a co-catalyst, resulting in very different activities and morphologies. *In-situ* Diffuse Reflectance (DR) UV-vis-NIR and FT-IR spectroscopy with CO as probe molecule revealed the formation of different types of Cr species for each material, suggesting that the linker (for the same metal and pore structure) plays a crucial role in the formation of Cr olefin polymerization sites. Activity in ethylene polymerization in toluene at 10 bar and 298 K was related to the observed spectra, corroborating the presence of different types of active sites, by their different activities for the formation of High-Density Poly-Ethylene (HDPE). Scanning Electron

Microscopy (SEM) micrographs revealed that albeit MIL-100 and MIL-101 exhibit identical zeolitic MTN topology, only the latter is able to collapse upon addition of DEA and subsequent ethylene insertion, and to fracture forming polymer beads, thus, show noticeable activity in HDPE formation. We ascribed this effect to the higher pore volume, thus, fragility of MIL-101, which allowed for polymer formation within its larger cages. MOFs were compared to the non-porous chromium (III) benzoate $[Cr_3O(O_2CPh)_6(H_2O)_2](NO_3)_nH_2O$ complex (1), in order to study the effect of the embodiment in the porous framework. The properties of the polymer obtained under identical reaction conditions were comparable to that of MIL-101(Cr) but very different morphologies were observed, indicating that MIL-101(Cr) structure is necessary to impart a certain architecture at the micro-scale. This work shows that for an identical topology and metal in a MOF structure, the linker and the pore structure play crucial role, and has to be carefully considered when designing microporous coordination polymers for catalytic purposes.

The results described in this Chapter are reported in the following manuscript: "Ethylene Polymerization over Metal-Organic Framework Crystallites and the Influence of Linkers on their Fracturing Process", M. Rivera-Torrente, P. D. Pletcher, M. K. Jongkind, N. Nikolopoulos, B. M. Weckhuysen, *ACS Catal.*, 2019, **9**, 3059-3069.

4.1 INTRODUCTION

Polyethylene (PE) production has been estimated to reach 100 million tons per year by 2020, and will continue to be an ubiquitous material for our modern society in the decades to come. A wide variety of reactor configurations (*i.e.* liquid, slurry and gas-phase) and catalyst materials (*i.e.*, (post-) metallocene, Ziegler-Natta and Phillips) are used for its production depending on the required physicochemical properties, such as density, melting point or viscosity, as well as morphology,¹ that need to be conferred onto the polymer for further processing.²⁻⁴ In order to alter the architecture of the polymer at the macroscale, different systems in which the support oxide plays the role of a “cast”, have been used in the past. Examples of such efforts include the so-called extrusion polymerization in which the active olefin polymerization sites have been incorporated in the family of MCM-41 and SBA-15 mesoporous materials, yielding microcrystalline fibres of PE.⁵⁻¹⁰

Their well-defined metal sites have fostered their use as single-site porous catalysts.¹¹⁻¹³ Indeed, a number of Metal-Organic Frameworks (MOFs) have been studied as solid catalysts for the polymerization and oligomerization of short-chain olefins, such as ethylene, propylene and isoprene, due to its industrial relevance and relatively mild conditions required to be operated, together with the necessity of fine tuning its selectivity.¹⁴⁻¹⁸ Due to their porous structure and high metal site density, a number of MOFs have been recently used for polymer templating.¹⁹⁻²⁵ Ethylene oligomerization (both in the liquid²⁶ and the gas phase²⁷⁻³²) and polymerization,³³⁻³⁶ as well as propylene dimerization in the gas phase,³⁷⁻³⁹ or even isoprene polymerization,⁴⁰ can be catalysed by a number of MOFs, being post-synthetic modification necessary in most cases. However, despite its paramount importance in applications, polymer morphology has been often overlooked and most of the MOF-based catalyst materials described often show either poorly or non-shaped materials. Recently, Liu *et al.*⁴¹ reported on the selective oligomerization of ethylene by the chromium nodes of MIL-100(Cr) after activation with organoaluminium species, wherein the activity and selectivity can be tuned by thermal treatments and without the need of modifications of the MOF. Their work has inspired

our efforts in investigating the possibilities of MIL-100(Cr) materials for olefin polymerization. MIL-100(Cr)⁴² and MIL-101(Cr)⁴³ frameworks (where MIL stands for Matériaux de l'Institut Lavoisier), as outlined in Chapter 2, are among the most studied MOFs due to their high porosity ($S_{\text{BET}} \sim 1500 - 3000 \text{ m}^2/\text{g}$), tunability and chemical and hydrothermal stability.

In this Chapter, we have taken advantage of the ability of MIL-101(Cr), in contrast to the more robust MIL-100(Cr) and the homogeneous Cr complex $[\text{Cr}_3\text{O}(\text{O}_2\text{CPh})_6(\text{H}_2\text{O})_3](\text{NO}_3)_3 \cdot n\text{H}_2\text{O}$ (**1**), to fracture upon addition of a strongly oxophilic organoaluminium activator and subsequent ethylene polymerization in the liquid phase. Moreover, we sought to understand the effects of the co-catalysts when used in combination with these MOF materials, as well as the reaction conditions, by means of *in-situ* spectroscopy together with a detailed analysis of the polymer products formed. We will show that even for an identical pore structure and metal in a MOF structure, the organic linker plays a crucial role, and has to be carefully considered when designing microporous coordination polymers for catalytic purposes.

4.2 EXPERIMENTAL SECTION

4.2.1. General Information

For quenching the polymerization experiments, a 0.1 M HCl (37 wt% aq) in methanol (99% tech. VWR International) solution was used. Electrospray Ionization-Mass Spectrometry (ESI-MS) of complex (**1**) dissolved in acetonitrile (HPLC grade, BiosolveTM) was recorded on a Walters LCT Premier XE KE317 Micromass Technologies spectrometer. Diffuse Reflectance Spectroscopy (DRS) in the Ultraviolet-Visible-Near Infrared (UV-vis-NIR) region was recorded with a PerkinElmer Lambda 950 S instrument, equipped with InGaAs and photomultiplier (PMT) detectors; and D₂ and W/halogen lamps, and with Spectralon[®] as a reference, in the 50000-4000 cm^{-1} range with a spectral resolution of 8 cm^{-1} . Fourier Transform-InfraRed (FT-IR) spectroscopy in Attenuated Total Reflectance (ATR) mode was recorded with a Nicolet i5 instrument with a DGTS detector and a diamond indent, with a spectral resolution of 4 cm^{-1} and 32 scans per spectrum.

4.2.1. Materials Preparation

Synthesis of the coordination complex (**1**), MIL-100(Cr) and MIL-101(Cr) was carried out according to previously published procedures.⁴²⁻⁴⁴

a) Synthesis of the oxo-bridged cluster $[\text{Cr}_3\text{O}(\text{O}_2\text{CPh})_6(\text{H}_2\text{O})_3](\text{NO}_3)\cdot\text{H}_2\text{O}$ (1**):** We have followed a previously reported literature protocol [44]: A mixture of 8.0 g of chromium (III) nitrate nonahydrate $\text{Cr}(\text{NO}_3)_3\cdot 9\text{H}_2\text{O}$ (20 mmol (Sigma Aldrich, $\geq 99.99\%$)) and 4.8 g of benzoic acid (40 mmol (Alfa Aesar, 99%)) was stirred in 60 ml of EtOH (VWR International, 96%), refluxed for 3 h, allowed to cool to room temperature and stored overnight at 253 K. The blue-green microcrystalline solid formed was washed copiously with Et_2O (VWR International, 96%) and dried *in vacuo* at room temperature for 24 h. (ESI-MS, CH_3CN): *m/z* calculated for $[(\mathbf{1})\cdot 3\text{CH}_3\text{CN}]^+$, 1021.0703; found, 1021.080233 (100%); $[(\mathbf{1})\cdot 2\text{CH}_3\text{CN}]^+$, 980.0438; found, 980.0552 (38%) and others. The characterization of this material, illustrated in Figure 4.1, shows (UV-Vis-NIR DRS spectroscopy): Ligand-to-Metal Charge Transfer (LMCT) transitions, 33000-50000 cm^{-1} , *d-d* transitions 22470 and 17000 cm^{-1} , NIR bands, 8770, 7060 ($2\nu_1 + 2\delta\text{OH}$ combinations), 6000, 5250 ($\text{Cr}^{3+}\cdots\text{OH}_2$), and 4660 and lower ($\nu_{\text{C-H}}$ overtones);⁴⁵ (FT-IR spectroscopy): 680, 712, 1024, 1069, 1176, 1620, 1492, 1527, 1597, 1620, 3029 and 3061 cm^{-1} .

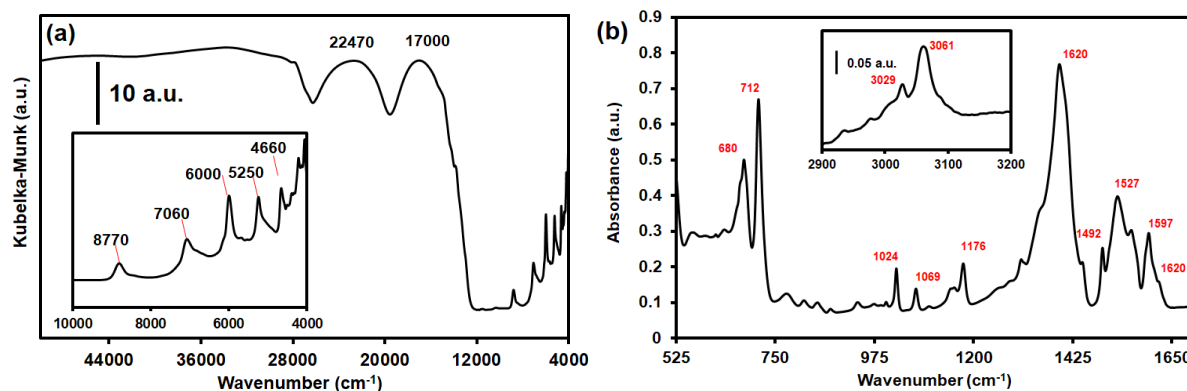


Figure 4.1. (a) UV-Vis-NIR Diffuse Reflectance Spectroscopy (DRS) data and (b) Fourier Transform-Infra-Red (FT-IR) spectrum of coordination complex (**1**).

b) Synthesis of MIL-101(Cr): The synthesis was carried out as described in reference [43]. Briefly, chromium (III) nitrate $\text{Cr}(\text{NO}_3)_3\cdot 9\text{H}_2\text{O}$ (800 mg, 2 mmol (Sigma Aldrich, $\geq 99.99\%$)), 2 mmol of hydrofluoric acid, and 1,4-benzenedicarboxylic acid H_2BDC (164 mg, 2 mmol

(Sigma Aldrich 98%) were added to 8.6 ml H₂O (530 mmol); the mixture is then introduced in a hydrothermal bomb, which is put during 8 h in a 45 mL Teflon-liner sealed in a stainless-steel autoclave held at 493 K. The solution was then cooled to room temperature and the green powder recovered by centrifugation.

c) Synthesis of MIL-100(Cr): The synthesis was done by following a previously reported literature [46]. Chromium (VI) oxide CrO₃ (0.5 g, 6 mmol, (Sigma Aldrich, 99.99%)), 1,3,5-benzenetricarboxylic acid or trimesic acid H₃BTC (1.05 g, 5 mmol, (Sigma Aldrich, 99%)) and 0.3 ml of a 28 M hydrofluoric acid solution (8.4 mmol, (Sigma Aldrich, 48-51%)) were mixed with 24 ml of deionized water and the obtained solution was introduced in a Teflon-liner sealed in a stainless-steel autoclave and heated at 493 K for 4 days. The green powder was recovered by centrifugation and decantation of the supernatant solution.

The activation of the MIL-100 and MIL-101 solids was carried out in an analogous manner in both cases. To remove unreacted species from the pores, the powder was first washed copiously with deionized water and ethanol (VWR International, 96%), and then magnetically stirred for 16 h at 353 K in a round bottom flask with 30 mL of N, N-dimethylformamide DMF (Sigma Aldrich, 99.9%). The supernatant was removed by centrifugation, the solid washed with ethanol two times and dried overnight in air at 393 K.

An anion exchange treatment was carried out as described in reference [47] for both MIL-100 and MIL-101. About 600 mg of the MOF powder was mixed with 5 mL of an aqueous 1 M NaCl solution (Sigma Aldrich, 99.9%) and magnetically stirred for 2 h at 298 K. Thereafter, the supernatant was removed, and the green powder washed extensively with water and acetone. Finally, the solid was dried overnight in air in an oven at 393 K prior to activation.

Activation was carried out the same for all the three samples (*i.e.*, two MILs and the oxo-bridged cluster) by heating the solids at 443 K under dynamic vacuum for 24 h, after which it was stored in a N₂ glovebox (O₂ < 2 ppm, H₂O < 1 ppm) until further use.

4.2.2. Materials Characterization

X-ray Diffraction (XRD) patterns were obtained with a Bruker-AXS D2 Phaser powder X-ray diffractometer in Bragg-Brentano geometry, using Co K_{α1,2} = 1.79026 Å, operated at 30 kV. The XRD measurements were carried out between 2 and 30° using a step size of 0.05° and a scan speed of 1 s, with a 0.1 mm slit for the source. Simulated XRD patterns were obtained by processing the corresponding .cif files with VESTA® (λ = 1.79026 Å, FWHM = 0.2) from references [48] and [42]. *N₂ adsorption isotherms* were measured at 77 K with a Micromeritics TriStar 3000 instrument. Prior to all measurements, samples were dried at 423 K under dynamic vacuum. Specific Surface Areas (SSAs) were calculated using the multi-point Brunauer-Emmett-Teller (BET) method ($0.05 < p/p_0 < 0.25$). Pore volumes (V_p) were calculated by the *t-p/plot* method; and Pore Size Distributions (PSDs) were obtained by Density Functional Theory (DFT) using N₂ and cylindrical pores in the package MicroActive[©]4.06 (Micromeritics). *Fourier-Transform-InfraRed (FT-IR)* spectroscopy measurements at 85 K were recorded with a Perkin Elmer 2000 instrument, in a specially designed cell fitted with CaF₂ windows. The degassed (at 423 K) MOF materials studied were pressed into 3-5 mg wafers inside of a glovebox and fitted into the FT-IR cell. The cell was sealed, connected to the gas/vacuum system, and carefully evacuated to $\sim 10^{-5}$ mbar at 298 K. A 10%CO/He (v/v) mixture was slowly introduced into the cell until the pressure reached 250 mbar and allowed to equilibrate. The sample was then cooled using liquid nitrogen (to 85 K) to allow the CO to saturate and equilibrate on the surface. The cell gas pressure was decreased, and spectral measurements were taken after the pressure stabilized. A final measurement was taken after outgassing the cell for 20 min. To measure the CO FT-IR spectra of the sample activated at 623 K, the cell was slowly allowed to warm to 298 K under vacuum and then heated to 623 K at a rate of 5 K·min⁻¹ and then maintained at 623 K for 1 h. The sample was then allowed to cool to room temperature and the previously described CO FT-IR measurement protocol was used to probe the surface acidity. For the diethylaluminium chloride (DEA, Sigma-Aldrich, 97%) activated samples, *ca.* 20 mg of MOF material was mixed with 100 equivalents of DEA for 20 min in the glovebox. The solvent was decanted and the remaining solid dried under vacuum. Then, *ca.* 5 mg of material was then pressed into a pellet and the CO FT-IR spectroscopy measurements were carried out by following the previously described measurement

protocol. *UV-Vis-NIR Diffuse Reflectance Spectroscopy (DRS)* measurements were performed under *in-situ* conditions making use of a Varian Cary 500 spectrophotometer with a DRS accessory. The measurements were performed in the spectral range of 4000-45000 cm⁻¹ with 33 ms data point scan time and spectral resolutions of 17 cm⁻¹ and 7 cm⁻¹, in the 12500-45000 cm⁻¹ and 4000-12500 cm⁻¹ spectral range, respectively. Two artefacts in the measured spectra were corrected for the detector/grating and light source changeovers at 12500 cm⁻¹ and 28570 cm⁻¹, while the spectral feature appearing at 11250 cm⁻¹ is due to an instrumental artefact. For every measurement, the cell was loaded in a N₂-filled glovebox (< 2 ppm H₂O, O₂), therefore keeping the samples from contact with atmospheric oxygen and water. The samples were measured against a Teflon-white measured in the same cell loaded with the same volume of 30 µm beads of Teflon powder. For measuring the materials, 100 mg of catalyst material was loaded in a home-made cell. Subsequently, the required equivalents of DEA were injected under a N₂ flow of 10 mL·min⁻¹. After injection, the spectra were recorded until no further spectral changes were observed. Subsequently, the gas feed was switched to 10 mL·min⁻¹ C₂H₄ for gas-phase polymerization (Linde, C₂H₄, 99.9 %). Spectra were recorded until no further changes occurred. *Scanning Electron Microscopy (SEM)* micrographs of the MOF crystallites and the MIL-100(Cr) after reaction were recorded on a FEI Helios nanolab 600 Dual Beam instrument, equipped with an Oxford Instruments Silicon Drift Detector X-Max energy-dispersive spectroscope. After depositing the sample onto Al stabs with carbon tape (Electron Microscopy Sciences, Hartfield, PA, USA), the samples were sputtered 22 nm of Pt(-Pd). Thereafter, imaging and Energy Dispersive X-ray (EDX) analysis were carried out at 15kV and 0.1 nA. Micrographs of the polymer samples were recorded on a PhenomPro X microscope (FEI company, USA), equipped with a CsB detector for Back-Scattered Electrons (BSE), operated at 10 kV. The samples were mounted on holey carbon tape supported on Al stubs, not coated prior to measurements. *Differential Scanning Calorimetry (DSC)* analyses were done with ~3-4 mg of polymer for each run were analysed using a Texas Instrument Discovery DSC featuring an automatic sampler and TRIOS software. Each sample was heated from 298 K to 473 K at a rate of 10 K·min⁻¹ and held at 473 K for 2 min to erase the thermal history, then cooled to 313 K at K·min⁻¹ to ensure a slow recrystallization of the polymer. A second heating ramp was used to

determine the melting temperature (T_m) and enthalpy (ΔH_m), in which the sample was heated at $10 \text{ K}\cdot\text{min}^{-1}$ to 473 K, before being cooled back to 298 K. The crystallinity of the polymer samples was determined assuming $\Delta H_m^0 = 293 \text{ J/g}$, for 100% crystalline Ultra-High Molecular Weight Polyethylene (UHMWPE). *Gel Permeation Chromatography (GPC)* was measured with a Polymer Laboratories PL-GPC220 instrument, equipped with a PL BV-400 as refractive index detector. The column set consisted of three Polymer Laboratories 13 μm PLgel Olexis, 300 \times 7.5 mm columns, and the calibration was performed with linear Polyethylene (PE) and Polypropylene (PP) standards. PP molar mass calibration was obtained after conversion from PE to PP using the Mark-Houwink constants.

4.2.3. Materials Testing

The degassed MOFs and complex (**1**) were tested for the polymerization of ethylene in the liquid phase. For the runs, $5 \cdot 10^{-2}$ mmol of the material was introduced into a stainless-steel Parr reactor, together with either Al : Cr = 100, 500, or 1000 eq. of Diethyl-Aluminium Chloride (DEA) (Sigma-Aldrich, 98%) in toluene (Sigma-Aldrich, anhydrous, 99.8%) inside an Ar-filled glovebox ($\text{O}_2, \text{H}_2\text{O} < 2 \text{ ppm}$). The autoclave was connected to an ethylene (Linde AG, 99.9%) line and the system evacuated and flushed with ethylene 3 times before the cell was pressurized to 10 bar at 298 K, and the mixture mechanically stirred at 1000 rpm. The cell was depressurized of ethylene after 1 h of reaction, the autoclave cooled to 195 K using an acetone/dry ice bath and the pyrophoric materials quenched using acidified (37 wt% HCl aq, Merck KGaA) methanol. The solid PE material made was filtered, rinsed with MeOH (98%, VWR International), and dried under high vacuum overnight. Catalytic activity of the materials tested was based on the weighed polymer product.

4.3 RESULTS AND DISCUSSION

MIL-100(Cr) and MIL-101(Cr) Metal-Organic Frameworks (MOFs) are built up with chromium cations in octahedral coordination forming the so-called chromium oxo-bridged trimer units, *i.e.* $[(\text{Cr}_3(\mu_3\text{-O}))]$, bonded to trimesic acid (H₃BTC) or terephthalic acid (H₂BDC) for MIL-100(Cr) or MIL-101(Cr), respectively. Coordinatively Unsaturated Sites (CUS) on the Cr³⁺ cations can be generated by removing the ligand in axial position

(typically nitrate, halide, hydroxy or carboxylate anions arising from the synthesis) upon thermal treatment of the solid under vacuum.⁴⁹ Although the structure exhibits very well-defined Cr³⁺ ions, the nature of the metal active sites upon addition of alkylating agents, such as Diethyl-Aluminium Chloride (DEA), is not well understood. In order to verify that, isoreticular MIL-100(Cr) and MIL-101(Cr) were prepared following standard protocols, and their crystallinity and morphology confirmed by means of X-ray Diffraction (XRD) and Scanning Electron Microscopy (SEM), respectively. The XRD and SEM results are shown in Figure 4.2. Then, the materials were impregnated with DEA and the effect of the activator on their structural integrity were studied by means of XRD.

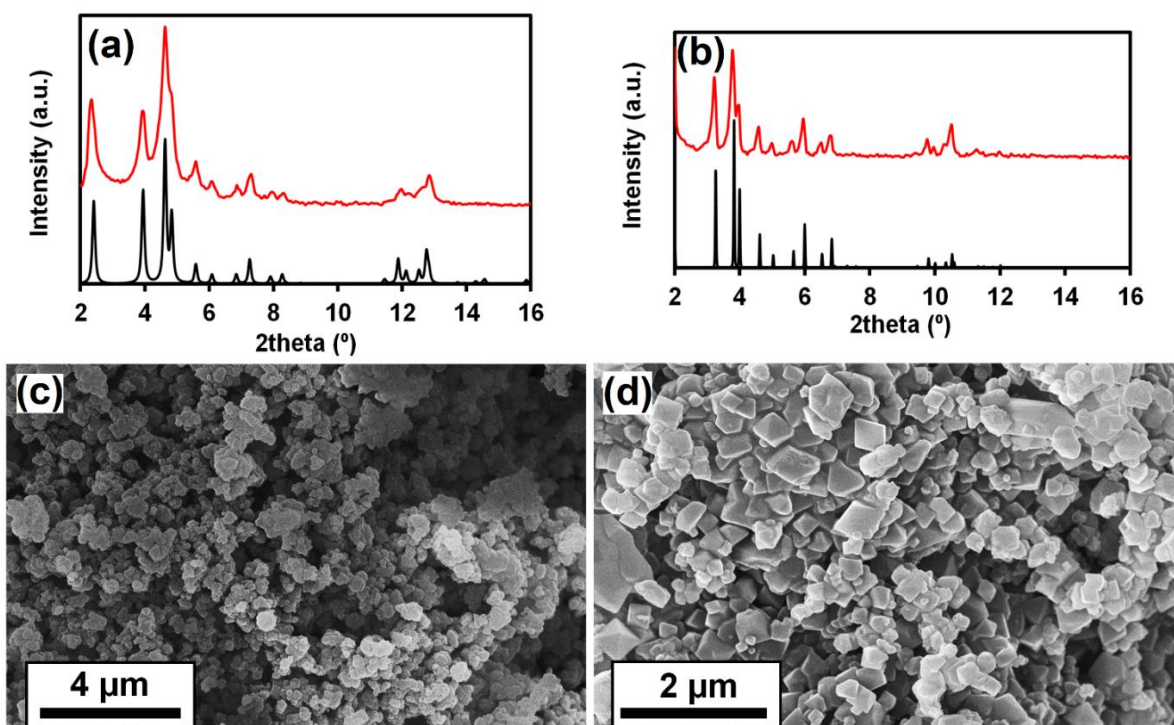


Figure 4.2. X-ray Diffraction (XRD) patterns of the as-synthesized (red) and simulated (black) MIL-100(Cr) (a) and MIL-101(Cr) (b). Scanning Electron Microscopy (SEM) micrographs showing octahedral crystals of (c) MIL-100(Cr) and (d) MIL-101(Cr).

4.3.1. Structural Stability and Catalytically Active Sites

XRD patterns of the materials after reaction with DEA, after having contact with ethylene at 298 K, and subsequent gentle quenching in air, were obtained in order to study the stability of the MOFs upon contact with the co-catalyst. For this purpose, *ca.* 10 mg of activated MIL-100(Cr) and MIL-101(Cr) were mixed with DEA ($\text{Al/Cr} = 100$) in an Ar-filled cell. Then, a $2 \text{ mL}\cdot\text{min}^{-1}$ stream of air was flowed for 30 min at 298 K through the cell to quench any unreacted organoaluminium species. In Figure 4.3a, it can be seen that albeit

the material is diffracting less intensely, the main XRD peaks at 2θ 2.36, 3.97, 4.64, and 4.89°, corresponding to the (220), (311), (222) and (400) reflections, respectively, are still present. This indicates that the crystalline structure is partially retained. Even after flowing ethylene through the cell, the material does not show significant changes, nor the presence of polymeric material. By contrast, the XRD reflections in Figure 4.3b show that reaction of MIL-101(Cr) with DEA resulted in the complete loss of crystalline structure, as none of the main XRD reflections are present and only an amorphous pattern remains. This can be ascribed to a cleavage of the Cr-O bonds by the co-catalyst, resulting in the formation of defects, reduced and alkylated Cr and linker sites; as well as alumina or aluminium oxide-like species. When ethylene was passed through the cell, a white solid, which was confirmed to be traces of HDPE appeared on the surface of the MOF (XRD pattern not shown here). This demonstrated the ability that some of the Cr sites are able to form polymer in the gas-phase, unlike MIL-100(Cr).

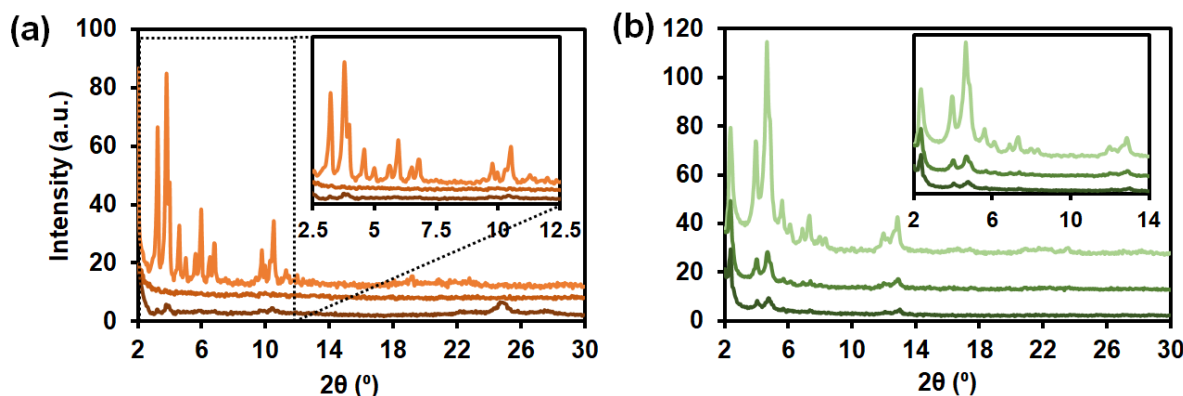


Figure 4.3. X-ray Diffraction (XRD) patterns of (a) MIL-101(Cr) and (b) MIL-100(Cr) as-synthesized (dark) after contacting with 125 eq. of DEA ($\text{Al:Cr} = 100$) (medium) and after flowing ethylene at 298 K for 15 min (light). The asterisk (*) indicates the formation of some High-Density Polyethylene (HDPE). Inset shows the area with the main reflections of the crystalline MOF.

In order to understand if different Cr sites were present in the MOFs after degassing and upon addition of DEA, *in-situ* CO-probe FT-IR spectroscopy experiments were carried out. In line with literature, different types of sites were observed when the material was dried at 423 K or 623 K.⁴⁹ First, in Figure 4.4a-c, the spectra of MIL-100(Cr) dosed with CO show the presence of very few coordinatively unsaturated sites $[\text{Cr}^{3+}\cdots\text{CO}]$ when degassing was done at 423 K (at 2188 cm^{-1}). A very intense band at 2154 cm^{-1} (next to that at 2136 cm^{-1} of physisorbed CO) indicates that most site were still hydroxylated. Interestingly, a small

feature at 2106 cm^{-1} was observed, which may correspond to the formation of extra-framework or defectively coordinated Cr cations during synthesis or degassing. We tentatively ascribe this feature to partially reduced $\text{Cr}^{3/2+}(\text{CO})_x\text{X}_y$ ($\text{X} = \text{Cl}^-$, NO_3^- , OH^- or H_2BTC^-) species, as they are typically present at such low wavenumber regions.⁵⁰⁻⁵⁴ The presence of the main interaction $\text{OC}\cdots\text{Cr}^{3+}(\text{MOF})$ bands at $2200\text{-}2180\text{ cm}^{-1}$ makes impossible to distinguish the presence of Cr^{2+} by using this region. This feature is seen at 2090 cm^{-1} , when the sample is degassed at 623 K , indicating that indeed, the treatment has a certain impact on the coordination environment of this Cr cations. Moreover, the band at 2188 cm^{-1} is shifted towards 2191 cm^{-1} , and is much more intense, indicating a much larger number of Lewis acidic Cr^{3+} sites appear upon degassing at higher temperature.

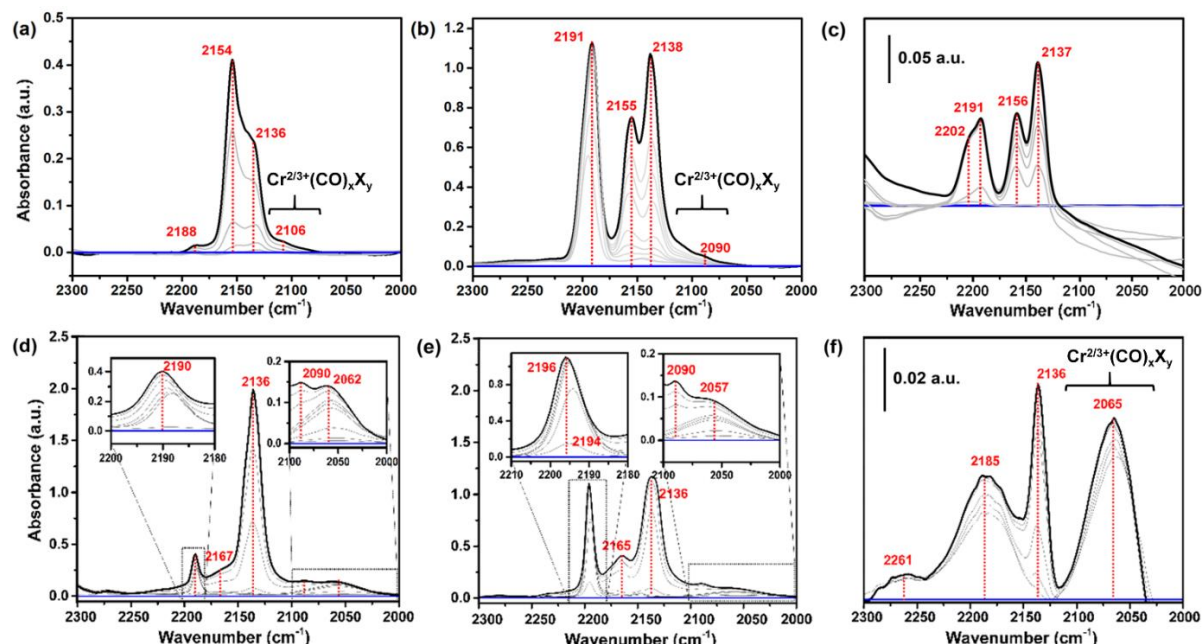


Figure 4.4. *In-situ* CO-probe Fourier Transform Infrared (FT-IR) spectra measured at 85 K of (a-c) MIL-100(Cr) and (d-f) MIL-101(Cr) after activation under vacuum (10^{-5} mbar) for 16 h at 423 K , at 623 K , and after impregnation with DEA (mol Al:Cr ratio of 100) and CO dosage (0 to 1 mbar); at 85 K . Degassed MIL-101(Cr) is subtracted as a reference spectrum in each case.

Addition of the organo-aluminium results in a strong modification of the baseline, as well as the formation of a shoulder at 2200 cm^{-1} , which indicates abstraction of additional counterions from the Cr sites. No further indications of Cr^{2+} sites are present, suggesting that they are alkylated and not available for binding with CO.

When an identical treatment was carried out on MIL-101(Cr), a number of differences was observed. First, when the material was degassed at 423 K, a higher fraction of Lewis Cr³⁺ sites was observed as a band at 2190 cm⁻¹ and a very small amount of hydroxylated Cr sites (seen as a broad shoulder at ca. 2156 cm⁻¹) was probed. Again, a small feature (inset Figure 4.4d) appeared at lower wavenumbers (2090 cm⁻¹) together with another band at 2062 cm⁻¹) after dosing CO, indicating Cr^{2/3+}(CO)_x species. It is important to remark that in this case, two types of Cr carbonyl sites are formed, indicating that not one, but multiple reduced Cr sites appear. When the material was degassed at 623 K, a similar trend as for MIL-100(Cr) was seen, meaning more (and more acidic) Lewis CUS and hydroxylated Cr³⁺ sites present. The small feature at 2090 cm⁻¹ remained unchanged, while the one at 2062 cm⁻¹ became less intense and was shifted to 2057 cm⁻¹, indicating that the thermal treatment results in a higher degree of reduction (*i.e.* red-shift indicates enhanced π -backdonation of the Cr sites).⁵⁵ Addition of DEA to MIL-101(Cr) has a dramatic effect on the spectral features, as shown in Figure 4.5f. The band corresponding to Lewis Cr³⁺ sites broadens significantly, indicating a plethora of different highly acidic Cr³⁺ sites (*e.g.*, extra-framework cations and embedded in the lattice), as they are quickly saturated at low CO pressures. Similarly, the feature at 2065 cm⁻¹, corresponding to the Cr²⁺(CO)_x species, broadens and increases in intensity dramatically. Again, many differently coordinated Cr²⁺ sites are formed upon reaction with the alkylating co-catalyst. It is unclear whether any of the carbonyl adducts are binding atop or bridging at this moment. Decomposition of the MIL-101(Cr) framework by DEA results in another unassigned feature at 2261 cm⁻¹.

Our interpretation of the reduction of Cr is further supported by *in-situ* UV-vis-NIR DR spectra recorded after addition of DEA (Figures 4.5-4.7). The bands observed in the spectrum of activated MIL-100(Cr) (red spectrum, Figure 4.4a) correspond to characteristic bands for Cr³⁺ octahedral (O_h) species with oxide-like ligand environment at 24000 and 16000 cm⁻¹ of the Cr trimers.^{56,57} The t_{2g} → t_{2g}e_g¹ transition, split into the ⁴T_{1g} ← A_{2g} and the ⁴T_{2g} ← ⁴A_{2g} transitions, relate to the higher and lower energy bands, respectively. After addition of DEA (Figure 4.5a, blue spectrum), deconvolution of the spectrum (Figure 4.5b) shows two bands at ~11000-10000 cm⁻¹ indicative for coordinatively unsaturated Cr²⁺ species, suggesting the formation of a few reduced chromium sites, in line with our

previous CO-probe FT-IR spectroscopy results and mentioned literature.⁴¹ Other relevant studies show that metal terephthalate MOFs containing exclusively Cr³⁺, show no absorption below 13000 cm⁻¹ (even for Cr_{Th} geometries), both supported by Time-Dependent Density Functional Theory (TD-DFT) calculations and UV-Vis-NIR DRS experiments, suggesting that indeed, the DEA acts as a reducing agent of Cr cations.⁵⁸ The presence of some [Cr³⁺...OH₂] species even after thermal treatment is verified by the band at ~5220 cm⁻¹ (see Figure 4.5b), which corresponds to the O-H combination band: $\nu_{(OH)} + \delta_{(OH)}$, confirms the presence of few remaining non-dehydroxylated Cr sites (as previously shown with FT-IR).⁴⁹

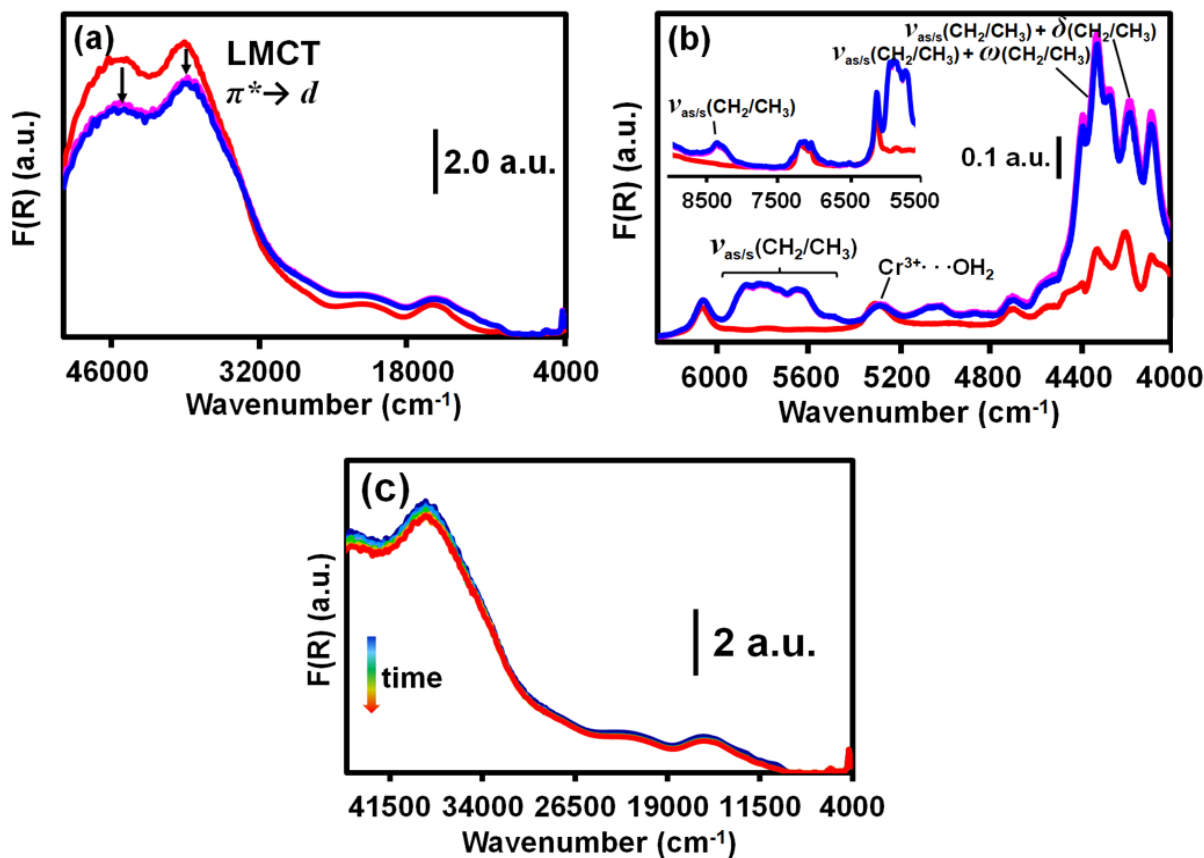


Figure 4.5. Diffuse Reflectance Spectroscopy (DRS) in the UV-Vis-NIR region of MIL-100(Cr) measured under *in-situ* conditions showing details of the spectral regions with (a) the LCMT bands in the region 50000-30000 cm⁻¹, (b) the alkyl C-H vibrations of the alkylated MOF in the region 6500-4000 cm⁻¹, and (c) the spectral evolution in the first 15 min after flowing ethylene over the activated MIL-100(Cr) in the region 50000-4000 cm⁻¹ (an inset is provided in Figure 4.7).

Moreover, we observed a decrease in the Ligand-to-Metal Charge Transfer (LMCT) bands of $\pi^* \rightarrow d$ transitions at 45000-38000 cm⁻¹ (Figure 4.5a). This can be ascribed to a partial degradation of the MOF structure caused by a cleavage of the Cr-O bonds, that react with the organo-aluminium species. Flowing ethylene over the activated MOF results in a decrease of intensity of Cr²⁺ bands (ca. 12000-10000 cm⁻¹) shortly after, although no significant changes are seen in the C-H region, indicating no polyethylene formation.

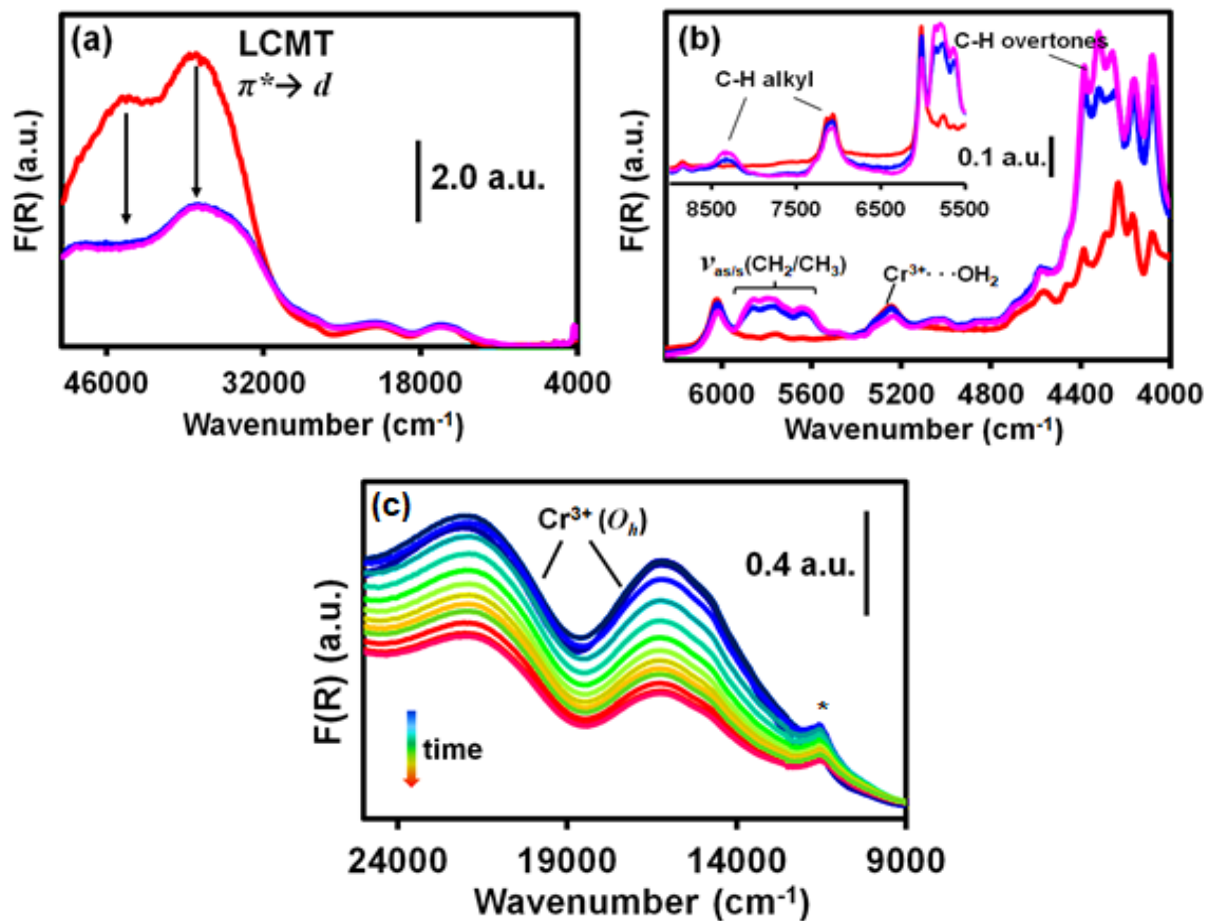


Figure 4.6. Diffuse Reflectance Spectroscopy (DRS) in the UV-Vis-NIR region of MIL-101(Cr) measured under *in-situ* conditions showing the effects of injecting Diethyl Aluminum Chloride (DEA) in (a) the full UV-Vis-NIR range with the drop in LMCT bands and (b) the NIR region with the increase in intensity for alkyl groups. (c) From red to blue showing the DRS spectra after changing the gas feed from N₂ to C₂H₄ at 298 K and 1 bar. The drop-in intensity is due to dilution of the catalyst material with formation of polyethylene within the cell. *Indicates an instrumental artefact.

Again, different species were observed for MIL-101(Cr) both after addition of the co-catalyst and addition of ethylene. A much more pronounced decrease of the LMCT bands occurred (Figure 4.6a), corroborating the structural collapse observed in XRD.

Deconvolution in Figure 4.7e, shows the presence of reduced Cr²⁺ sites, although only octahedral species are formed in this case. Furthermore, the main contribution of the low energy Cr^{3+OH} is shifted towards ca. 15000 cm⁻¹, indicating changes in the nature of the Cr³⁺ sites as well, in agreement with the broad band observed in the FT-IR spectroscopy experiments discussed above.

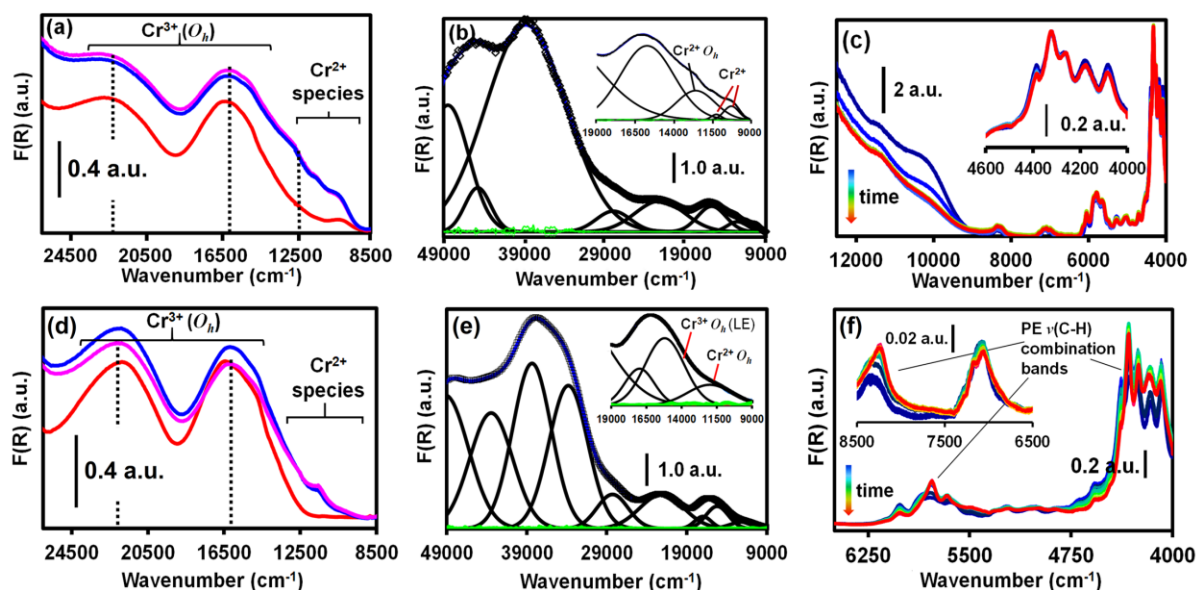


Figure 4.7. (a) UV-Vis range of the diffuse reflectance spectra of activated MIL-100(Cr) (red), after injecting 125 eq of diethyl-aluminium chloride (DEA, blue) and after 15 min (pink). (b) Deconvolution of the spectrum after injecting diethyl-aluminium chloride showing the different Cr species. Inset in (b) shows the presence of small amounts of Cr²⁺ species (both O_h and T_h geometries). Green lines show the residual of the fitting procedure. (c) *In-situ* UV-vis-NIR spectra after switching the gas flow from N₂ to C₂H₄ (10 mL·min⁻¹) at 298 K and 1 bar (from blue, $t = 0$ to red, $t = 60$ min). Inset shows bands where polyethylene should appear if polymerization occurs. (d) UV-vis range of the diffuse reflectance spectra of activated MIL-101(Cr) (red), after injecting 125 eq. of diethyl-aluminium chloride (blue) and after 15 min (pink). (e) Deconvolution of the spectrum after injecting diethyl-aluminium chloride showing the different Cr species. Inset in (b) shows the presence of small amounts of Cr²⁺ species (only O_h geometry). Green lines show the residual of the fitting procedure. (f) *In-situ* near-infrared (NIR) region of the spectra after switching the gas flow from N₂ to C₂H₄ (10 mL·min⁻¹) at 298 K and 1 bar (from blue, $t = 0$, to red, $t = 60$ min), showing the bands of crystalline polyethylene (PE) forming over time. Inset shows additional combination bands of the polymer CH₂ groups.

Peaks at 4180, 4250 and 4325 cm⁻¹, which correspond to C-H combination bands, indicating alkylation of the MOF. When ethylene was introduced in the cell, the formation of HDPE was steadily detected in the sharpening of the C-H combination bands (Figure

4.6e). An increase in the bands at ca. 8400, 5900 and 4500-4000 cm^{-1} over time, corroborates the formation of solid polymer from the gaseous ethylene phase. Indeed, flowing ethylene at slightly higher temperature (313 K) for 1 h into the cell, after activation with 100 eq of DEA, resulted in the formation of significant amounts of HDPE from the gas phase, as confirmed by XRD (Figure 4.8).

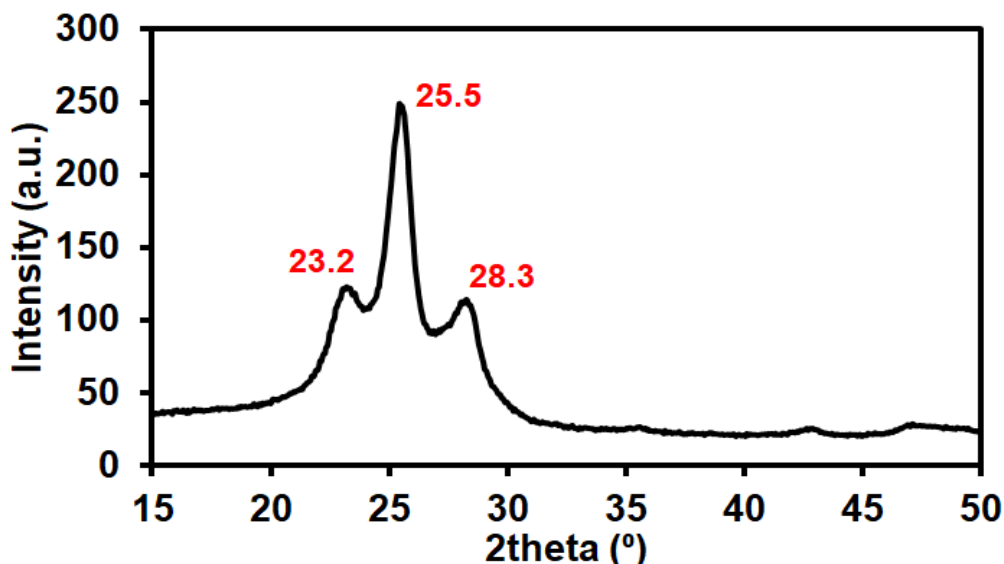


Figure 4.8. X-ray Diffraction (XRD) pattern of the High-Density Polyethylene (HDPE) polymer product obtained after flowing 10 $\text{mL}\cdot\text{min}^{-1}$ of C_2H_4 at 313 K for 1 h after activation of MIL-101(Cr) with diethyl aluminum chloride ($\text{Al/Cr} = 100$).

Summarizing, our *in-situ* UV-vis-NIR DRS analysis shows that, in spite of having the same structural motifs (*i.e.* carboxylates and $\text{Cr}_3(\mu\text{-O})$ trimers, each MOF forms different Cr^{3+} and Cr^{2+} species with similar coordination environments after addition of DEA, and only MIL-101(Cr) is able to produce polymer. Thus, so as to compare both MOFs as active catalysts, polymerization of ethylene in slurry phase (toluene) at 10 bar was carried out. Three different amounts of co-catalyst ($\text{Al:Cr} = 100, 500$, and 1000) were tested, in order to understand the influence of the co-catalyst in the activity and final materials produced. As we hypothesized, Table 4.1 shows that, despite both MOFs possess identical topology, MIL-100(Cr) is practically unable to catalyse the chain-growth of polyethylene, regardless of the Al:Cr ratio used. By contrast, MIL-101(Cr) showed high activity ($15.4 \text{ kg PE}\cdot\text{mol Cr}^{-1}\cdot\text{h}^{-1}\cdot\text{bar}^{-1}$) for a $\text{Al:Cr} = 100$ ratio.

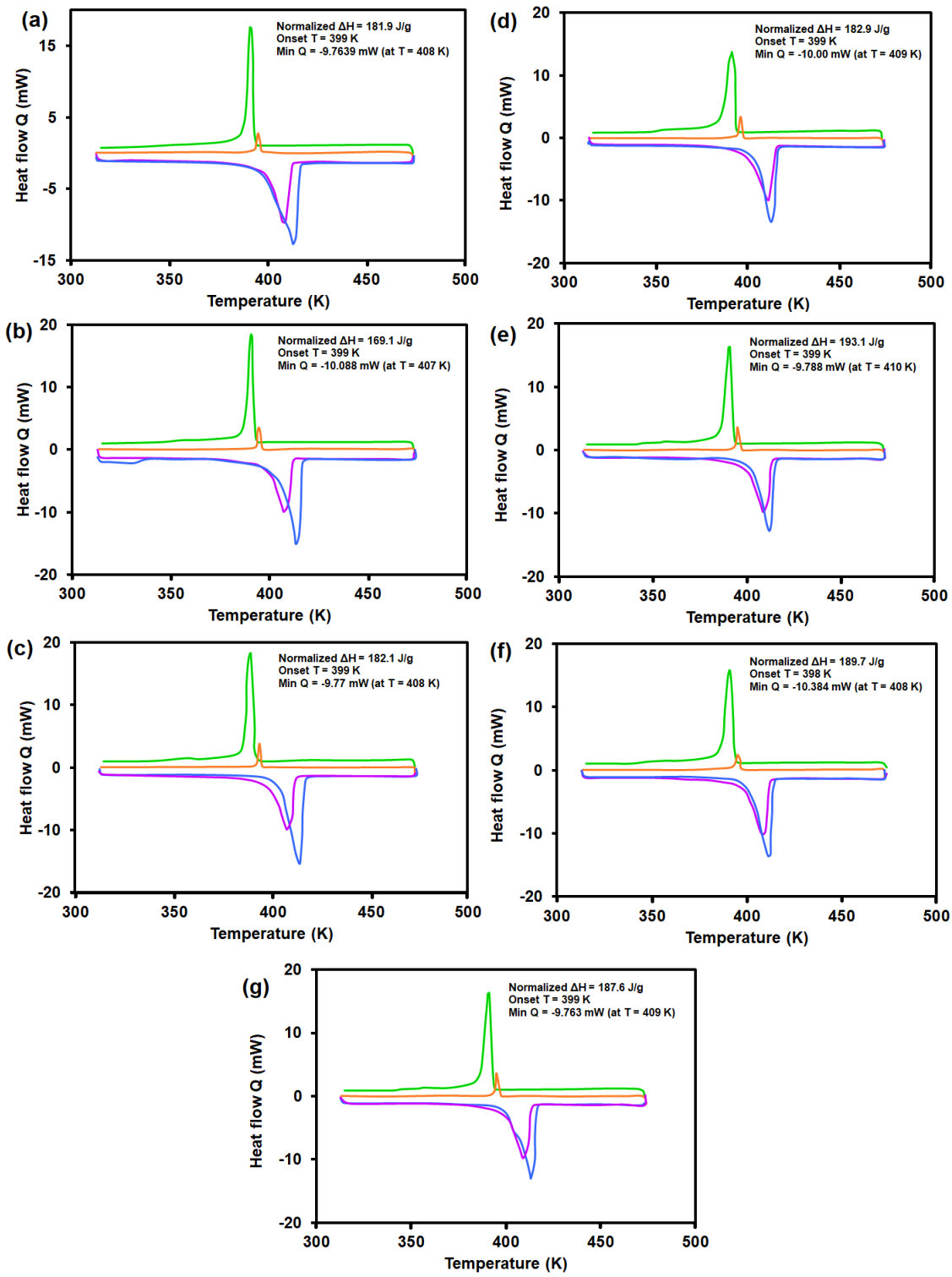


Figure 4.9. Differential Scanning Calorimetry (DSC) of the High-Density Poly-Ethylene (HDPE) obtained with a Al:Cr molar ratio of 1000 (a), 500 (b) and 100 (c) and complex (**1**) catalyst; and a Al:Cr molar ratio of 1000 (d), 500 (e) and 100 (f) and MIL-101(Cr) catalyst. (g) DSC of the polymer obtained from the MIL-101(Cr) filtrate. Blue and purple lines correspond to the heating cycles, while green and orange correspond to the cooling cycles. The melting enthalpy was calculated by integrating the melting peak.

Higher amounts of co-catalyst were detrimental for the performance under the same reaction conditions ($\sim 4\text{-}5 \text{ kg PE}\cdot\text{mol Cr}^{-1}\cdot\text{h}^{-1}\cdot\text{bar}^{-1}$), as previously reported for organo-aluminium alkylated Phillips systems.⁵⁹ In order to further understand if pore confinement and anchoring of the Cr trimer sites had an influence of the active sites, the coordination complex (**1**) (see Section 5.2.) was used as a homogeneous counterpart.

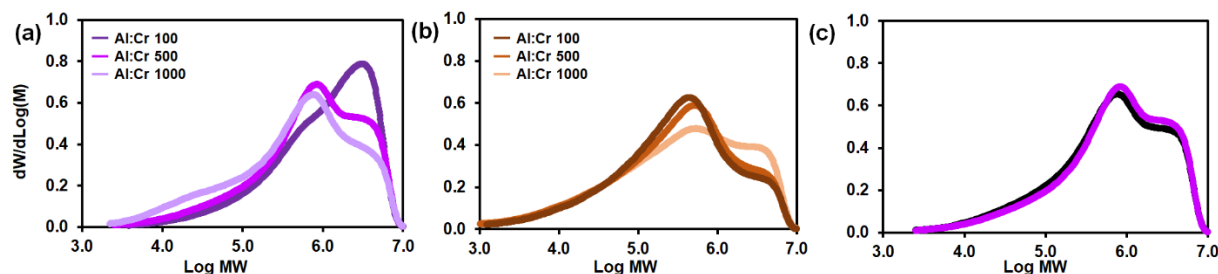


Figure 4.10. Molar Mass Distributions (MMD) of the polyethylene synthesized from (a) MIL-101(Cr) and (b) coordination complex (**1**) with different Al:Cr molar ratios. (c) Molar Mass Distributions (MMD) of the polyethylene synthesized from (black) MIL-101(Cr) (toluene filtered after addition of the organoaluminum) and (purple) coordination complex (**1**) with a Al:Cr molar ratio of 500, performed under identical conditions.

Table 4.1. Catalytic activity and physicochemical properties of the high-density polyethylene products obtained.

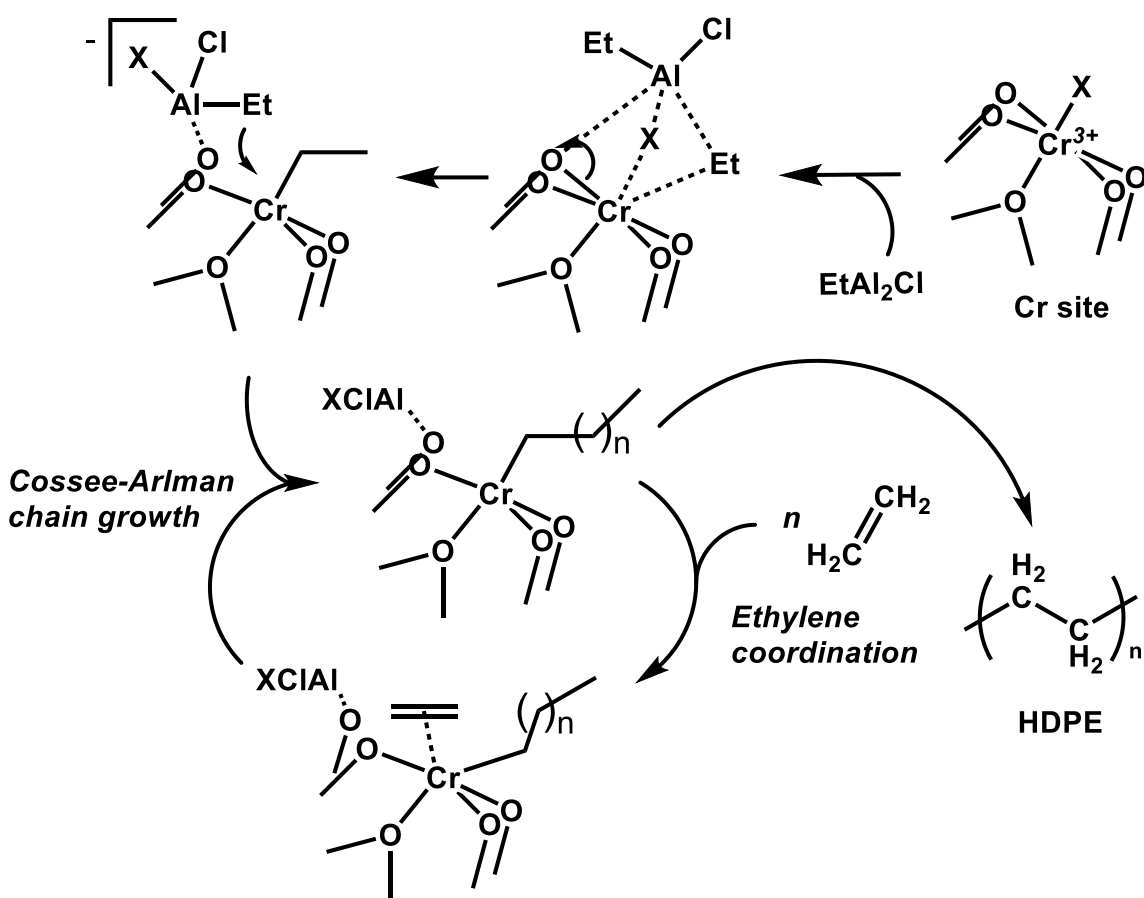
Catalyst	Al:Cr ^b	Activity ^c	T _m (K)	ΔH _m (J/g)	%X ^d	M _w (·10 ³ kDa) ^f	PDI ^f
(1)	100	13.0	408.3	182.1	62.2	1.8	8.3
	500	6.15	407.7	169.1	57.7	1.5	10.6
	1000	4.12	408.2	181.9	62.1	1.2	15.7
MIL-100(Cr) ^e	100	1.3·10 ⁻³	<0.03	-	-	-	-
	500	0.4·10 ⁻³	<0.03	-	-	-	-
	1000	2.1·10 ⁻³	<0.03	-	-	-	-
MIL-101(Cr)	100	15.4	408.5	189.7	64.7	1.1	27.0
	500	4.71	410	193.1	65.9	0.9	22.6
	1000	5.41	410.6	182.9	62.4	0.85	18.0
MIL-101(Cr) ^g	500	0.63	409.3	187.6	64.0	1.4	11.2

^aReaction conditions: 1 h at 10 bar C₂H₄ in 20 ml of toluene at 298 K in a 35 ml Parr-autoclave reactor. ^bMole ratio of Al:Cr. ^cActivity: kg PE·mol Cr⁻¹·h⁻¹·bar⁻¹. ^dAs compared to 293 J/G for 100% crystalline UHMWPE. ^eNot enough polymer product for analysis, experiments at 10, 20, 30 and 40 bar showed no activity. ^fDetermined by GPC calibrated with PE and PP standards. ^gMOF/AlEt₂Cl was stirred together for 30 minutes and filtered into reactor before reaction. Polydispersity Index (PDI) was calculated as PDI = $\overline{M_w}/\overline{M_n}$.

A parallel trend can be observed in activity (Table 4.1), indicating that the active sites present after addition of DEA are rather similar to those of MIL-101(Cr). The physical properties (melting temperature, T_m ; and heat of fusion, ΔH_m) of crystalline HDPE are governed by its molecular structure, which is very much determined by the catalytic sites, DSC analyses (Table 4.1 and Figure 4.9) were carried out to compare the obtained materials. As seen in Table 4.1, both MIL-101(Cr) and complex (**1**) show the typical $\%X$, T_m and ΔH_m ranges for HDPE with low-branching. To elucidate if the co-catalyst led to Cr leaching of MIL-101, the activity of the solution obtained after mixing DEA with MIL-101(Cr) catalyst was evaluated, showing that indeed, some HDPE was formed, with similar properties to those of complex (**1**). This indicates the same active sites for both catalysts, *i.e.* trimers dissolved in toluene. However, to our surprise, MIL-100(Cr) was inactive under the same conditions.

Accordingly, GPC analysis (Figure 4.10 and Table 4.1) shows that $M_w \approx 0.85 - 1.8 \cdot 10^3$ kDa for the polymers produced, *i.e.* lower end to mid-sized HDPE chains, in line with the DSC data. Nevertheless, average molecular weights (M_w) were slightly higher when non-porous complex (**1**) was used instead of the zeotypic MIL-101(Cr), following the activity trend. A correlation between catalyst porosity and high-MW tails has been observed in the past,⁶⁰ explaining this effect of embodiment. In our case, the high-MW shoulder is more prominent for low Al loading and complex (**1**) catalyst. With complex (**1**), there is no need to fracture the active site “embodiment” (*i.e.* the MOF structure), thus, yielding longer chains; while in the case of MIL-101(Cr), the growing chains need the collapse of the MOF crystals to further proceed with monomer insertion. It is clear that the contribution at $\log M_w \sim 6.5$ (see Figure 4.10) decreases with increasing DEA loadings, corroborating a detrimental effect of high co-catalyst amounts for the most active Cr sites. Thus, we hypothesize that the variety of active sites is related not only to MOF-embodiment or solubilization of the Cr trimers, but also to the amount of co-catalyst, which at very high Al:Cr may result in overalkylation, chain termination promotion or simply alumina coverage of the growing chains. Again, Molecular Weight Distributions (MWDs) and Poly-Dispersity Index (PDI) values of the polymer obtained after filtration of the MIL-101(Cr) fully correlate to that of the material obtained with (**1**).

Scheme 4.1. Tentative activation of Cr sites by DEA and subsequent ethylene insertion and polymerization.



This indicates that the active sites consist of alkylated Cr sites derived from the trimers in solution. Recent studies have shown multiple possibilities (*e.g.* metallacycle, Green-Rooney, Cossee-Arlman) for the initiation mechanism of ethylene insertion.⁶¹ However, the agreement is that chain growth in Cr-based Phillips catalysts operates mostly via the Cossee-Arlman mechanism.^{2,62} In the case of MIL-100(Cr) Liu *et al.* described a mechanism involving multiple metal centres acting via metallacycle mechanism yielding short ($\text{C}_6\text{-C}_{12}$) α -olefins.⁴¹ With the results previously described in this work, we propose that the active species for MIL-101(Cr) and **(1)** consist of Cr-alkyl sites formed by partial degradation of the lattice that lead to the formation active sites that can insert ethylene as described in Scheme 4.1. These Cr sites arise from the Cr trimers being most likely Cr^{3+} or Cr^{2+} sites (according to the spectroscopy study) although the oxidation state and coordination geometry remains still elusive. The inability of MIL-100(Cr) to fracture would explain the high activity in the formation of α -olefins.

3.3.2. Polymer Morphology

Control over particle morphology is crucial for the large-scale synthesis of polyethylene.⁶¹⁻⁶⁴ Regardless of the process employed, a number of issues, such as reactor fouling, heat transfer or product properties, have to be taken into account. As already mentioned, Cr-based catalysts are typically supported onto solid oxides (*e.g.* SiO_2) that crumble during ethylene polymerization, allowing chain growth. The above results led us to evaluate the ability of both MIL-100(Cr) and MIL-101(Cr) to generate structured polyethylene upon fragmentation of the MOF catalysts. Surprisingly, Figure 4.11a,b shows that under identical reaction conditions, MIL-101(Cr) generates spherical beads of polyethylene, in contrast to MIL-100(Cr) (Figure 4.11c,d), which produces nanosized (< 1 μm), ill-shaped material. These findings show that not only MIL-101(Cr) is active in ethylene polymerization, but also that its use as catalysts confers the polymer a certain architecture at the macroscale. Experiments with different Al:Cr ratios show that the templating effect is retained in every case, with a minimal effect in the size distribution. Analogously, similar poorly shaped material was covering MIL-100(Cr) crystallites for all the Al:Cr tested, indicating no significant chain growth under these conditions (Figure 4.11).

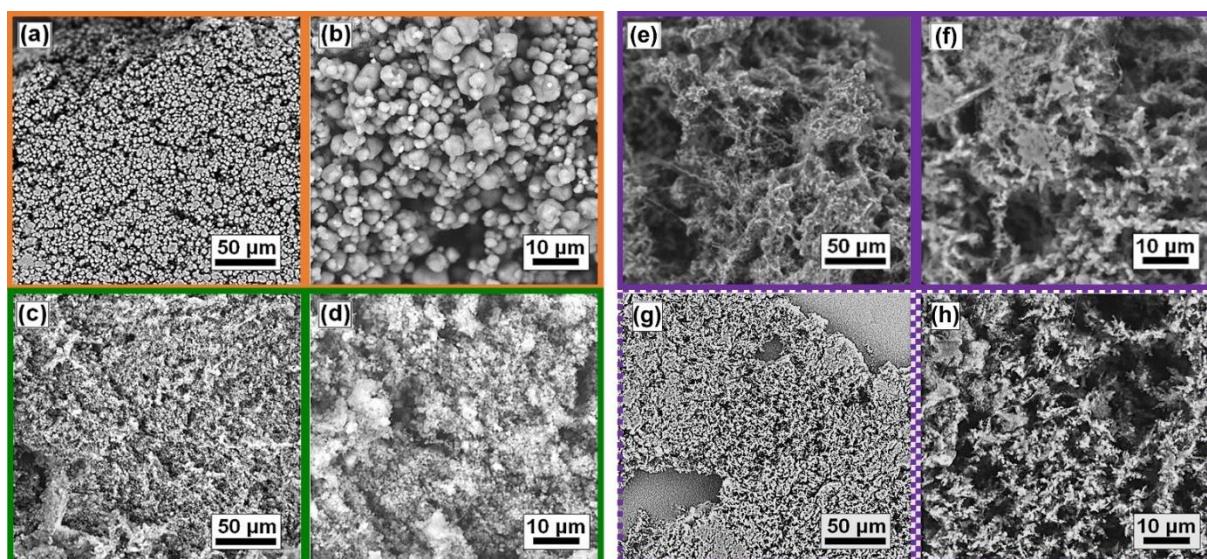


Figure 4.11. Scanning Electron Microscopy (SEM) micrographs of the polymer product obtained with (a,b) MIL-101(Cr), (c,d) MIL-100(Cr) (note that only nanosized crystallites are observed at this magnification), complex (1) (e,f) and the leached Cr from MIL-101(Cr) (g,h). Al:Cr = 100, diethylaluminium chloride (DEA), 298 K, 10 bar C_2H_4 , 1 h. Colour coding relates to Figure 4.14 (below).

We explain this difference based on our previous XRD analysis, which indicated the total collapse of MIL-101(Cr). This enables the Cr active sites to grow polymer chains in the solvent medium, contrary to MIL-100(Cr), which retains its crystalline structure, preventing the crystallites to fracture upon ethylene insertion. Thus, SEM images indicate that MIL-101(Cr) acts as a sacrificial template, in which the catalytically active species reside and that is later covered on polyethylene during reaction, leading to the observed polymer beads. Micrographs of the polymer obtained with catalytic complex **(1)** show randomly oriented, intergrown polymer fibres of *ca.* 3-5 µm thickness (for the same Al:Cr ratios, as shown in Figure 4.11), indicating that, in addition to the Cr trimer units, a solid scaffold is required to control the chain growth. In order to confirm its role as a structural template and discriminate from possible leached species that polymerize in solution, SEM images of the polymer recovered from toluene filtered after suspending DEA-activated MIL-101(Cr) were recorded. Figure 4.11g-h shows very similar fibres to those obtained with complex **(1)**, proving that the sole presence Cr trimers in solution not enough to obtain morphologically controlled polymer (Figure 4.11). SEM images in Figures 3.11 of the recovered MIL-100(Cr) solid after reaction with 500 eq. of DEA co-catalyst corroborate our hypothesis. After filtration from the toluene solvent, most of the MOF crystallites appeared intact (compare to the SEM images shown in Figure 4.12), and only a few polymer fibres arising from the pores were observed. Some species that have leached into solution (the strong alkylating agent causes partial degradation of MIL-100, as shown by XRD) formed polyethylene layers that covered the MOF. However, no evident signs of polymerization around the MOF crystallites, into shaped beads as it is the case for MIL-101(Cr), were observed. In Figure 4.12b, the inset shows a few polymer fibres that emerge from certain MOF crystallites. This is in stark contrast with MIL-101(Cr) and complex **(1)**, and it evidences the inability of MIL-100(Cr) to crumble upon ethylene insertion.

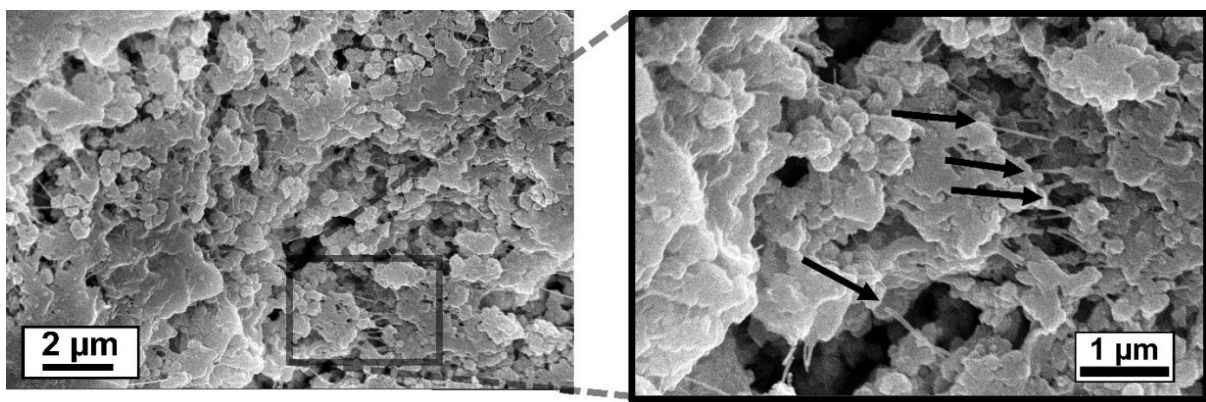


Figure 4.12. Scanning Electron Microscopy (SEM) micrographs of MIL-100(Cr) after reaction (at 10 bar C₂H₄, 298 K, 500 eq. DEA, toluene, 1 h) at high magnification, showing MIL-100(Cr) crystallites still intact. The arrows in the inset image indicate polymer fibres of MOF crystallites that were not able to fracture.

On the other hand, porosity has been shown to greatly impact activity for ethylene polymerization in Cr-based systems. Differences in activity is the porosity of each material. It is well known that support and catalyst porosity have a tremendous effect on polymer production.²

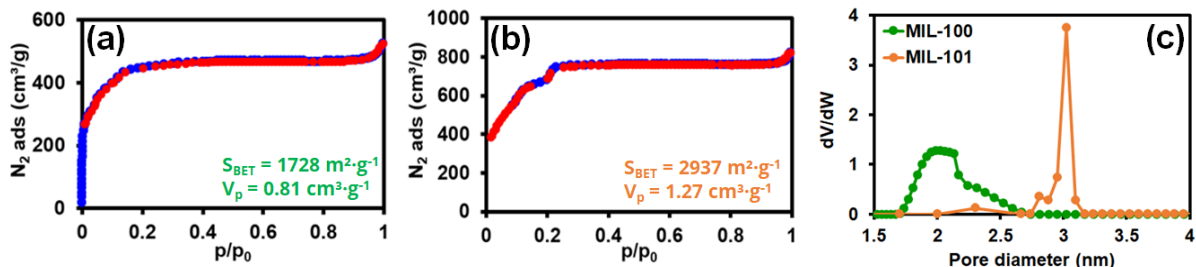


Figure 4.13. N₂ adsorption isotherms at 77 K of (a) MIL-100(Cr) and (b) MIL-101(Cr) (blue points, adsorption; red points, desorption). Density Functional Theory (DFT) pore size distributions of both MOFs calculated from the experimental N₂ adsorption isotherms at 77 K.

It is generally accepted that at least, $V_p \geq 1.0 \text{ cm}^3 \cdot \text{g}^{-1}$ is necessary in a silica support material for the support to crumble upon chain growth. Although of different chemical and physical nature compared to silica, and despite its high porosity, MIL-100 showed a pore volume ($V_p = 0.81 \text{ cm}^3 \cdot \text{g}^{-1}$) below that of the threshold (Figure 4.13). In contrast, MIL-101 ($V_p = 1.27 \text{ cm}^3 \cdot \text{g}^{-1}$) was well above, pointing to a critical effect on polymerization activity. As pointed out by McDaniel, is not the difference in pore volume, but the fragility (which may arise from this difference in pore volume and seems to be the cause for this

difference) what prevents higher polymerization activity. In fact, not only a difference in pore volume, but also a difference in pore diameter and window exists. While MIL-100 has two types of cages, of 25 and 29 Å diameter (with pore windows 5 and 8.6 Å, respectively),⁴³ MIL-101 exhibits diameters of 27 and 34 Å (with 11.6 and 16 Å windows).⁴⁴ This difference in pore diameter, specifically the presence of the larger 34 Å cages, seems to be critical for ethylene polymerization. We argue that chain growth occurring in that specific cage is enough to tear apart MIL-101 crystallites during the process, giving rise to new active sites that further polymerize ethylene. Density Functional Theory (DFT) pore size distributions shown in Figure 4.13 clearly illustrate the difference in pore diameter cages between both MOFs. As for coordination complex **(1)**, it readily dissolves in the reaction medium (toluene), acting as a homogeneous catalyst with no need of fracturing, as observed in the SEM imaged randomly oriented polymer fibres.

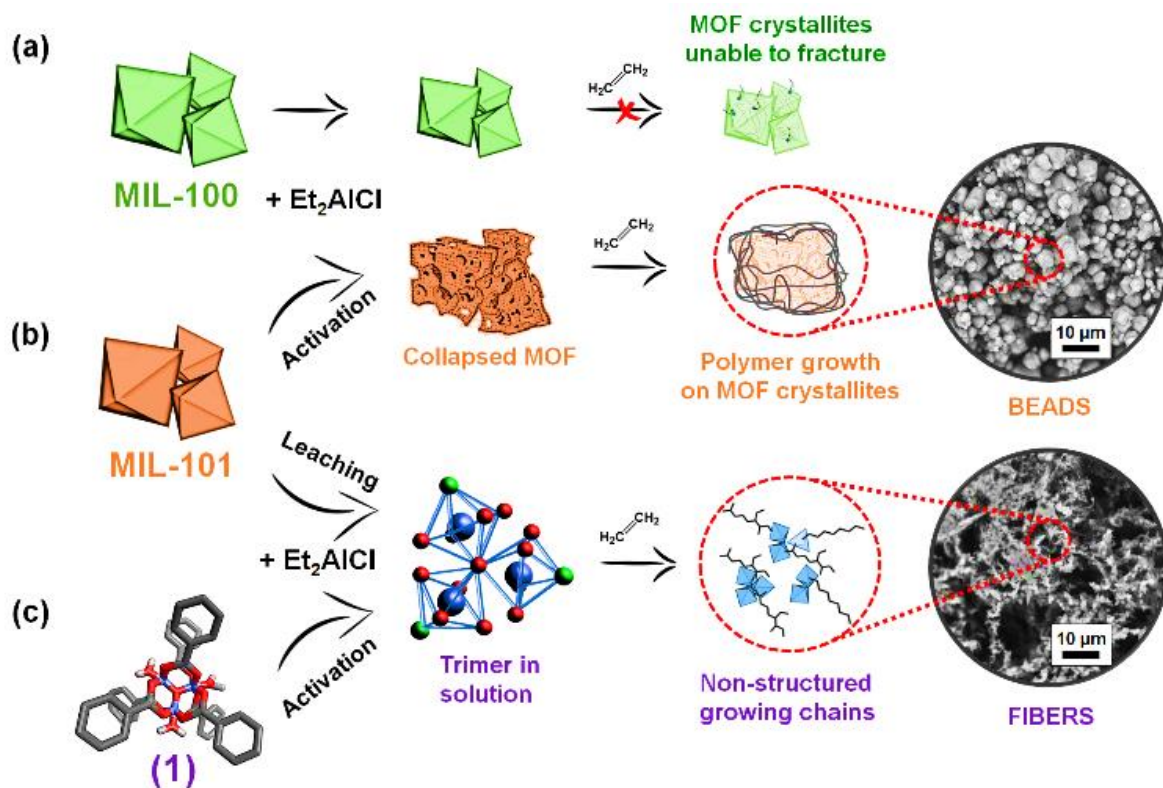


Figure 4.14. (a) MIL-100(Cr) is unable to fracture upon polyethylene formation, resulting in low catalytic activity. (b) MIL-101(Cr) is degraded and partially leaches Cr clusters into the solution upon addition of the co-catalyst, leading to different morphologies. (c) Coordination complex **(1)** in solution generates polymer fibres as the chain growth is not templated by any solid support.

In Figure 4.14, a summary of the different activities and morphologies that are obtained in ethylene polymerization under the studied conditions is presented. MIL-101(Cr) is a valuable catalyst that, although performs below commercial Philips catalyst benchmarks, it can structure the polymer at the microscale, while producing high molecular PE with relatively narrow PDI (orange). In contrast, MIL-100(Cr) (green) is unable to fracture and produce polymer, while complex **(1)** results in non-structured polymer material (purple).

4.4. CONCLUSIONS

We have demonstrated that MIL-101(Cr) can be used as a catalytic morphology template in the polymerization of ethylene. In contrast, the isoreticular MIL-100(Cr) material is unable to reach significant olefin polymerization activities due to the high stability of the Metal-Organic Framework (MOF) crystallites against fragmentation, which has been reported to lead to the formation of short α -olefins. X-ray Diffraction (XRD) studies revealed that, while MIL-100(Cr) is still crystalline after addition of the organoaluminium co-catalyst, MIL-101(Cr) completely collapses, leading to an amorphous solid material. Furthermore, *in-situ* Fourier Transform-Infared (FT-IR) and UV-vis-NIR Diffuse Reflectance (DR) spectroscopies show that different reduced and alkylated Cr sites are formed for each MOF, further indicating different stabilities towards the co-catalyst. The exact nature of the active species (as in the case of the long-term debated Cr/SiO₂ Phillips system) is not fully understood, but experiments with the putative homogeneous coordination complex showed trends in reactivity in the production of High-Density Poly-Ethylene (HDPE) similar to MIL-101(Cr), suggesting alkylated Cr sites as the main catalytic sites. In contrast, MIL-100(Cr) shows very low ethylene polymerization activity, mostly producing gaseous and liquid olefins instead. Scanning Electron Microscopy (SEM) studies revealed that, besides catalysing chain-growth, MIL-101(Cr) can act as a structure modulator for the polymer material obtained, leading to the formation of spherical micron-sized beads. Again, control experiments with the homogeneous complex confirm this hypothesis, as the coordination complex catalyst **(1)** produces interwoven polymer fibres in random orientation. In brief, we have demonstrated the ability of Cr-based MOFs to act as self-sacrificial, catalytic templates for structuring polymer materials.

4.5 REFERENCES

1. Soares, J. B. P.; Leonardo, C. S., in *Handbook of Polymer Reaction Engineering*, 2nd ed., Meyer, T., Keurentjes, J., Eds., Wiley-VCH, Weinheim, 2008, 366–395
2. M. P. McDaniel, *Adv. Catal.*, 2010, **53**, 123-606.
3. J. J. Eisch, *Organometallics*, 2012, **31**, 4917-4932.
4. A. E. Hamielec and J. B. P. Soares, *Prog. Polym. Sci.*, 1996, **21**, 651-706.
5. K. Kageyama, J.-i. Tamazawa and T. Aida, *Science*, 1999, **285**, 2113-2117.
6. F. Cesano, E. Groppo, F. Bonino, A. Damin, C. Lamberti, S. Bordiga and A. Zecchina, *Adv. Mater.*, 2006, **18**, 3111-3114.
7. P. Lehmus and B. Rieger, *Science*, 1999, **285**, 2081-2083.
8. K. Tajima and T. Aida, *Chem. Commun.*, 2000, 2399-2412.
9. B. M. Weckhuysen, R. R. Rao, J. Pelgrims, R. A. Schoonheydt, P. Bodart, G. Debras, O. Collart, P. van der Voort and E. F. Vansant, *Chem. Eur. J.*, 2000, **6**, 2960-2970.
10. R. Ramachandra Rao, B. M. Weckhuysen and R. A. Schoonheydt, *Chem. Commun.*, 1999, 445-446.
11. A. Corma, H. García and F. X. Llabrés i Xamena, *Chem. Rev.*, 2010, **110**, 4606-4655.
12. S. M. J. Rogge, A. Bavykina, J. Hajek, H. Garcia, A. I. Olivos-Suarez, A. Sepulveda-Escribano, A. Vimont, G. Clet, P. Bazin, F. Kapteijn, M. Daturi, E. V. Ramos-Fernandez, F. X. Llabrés i Xamena, V. Van Speybroeck and J. Gascon, *Chem. Soc. Rev.*, 2017, **46**, 3134-3184.
13. S. M. Cohen, Z. Zhang and J. A. Boissonnault, *Inorg. Chem.*, 2016, **55**, 7281-7290.
14. Kissin, Y. V. Polyethylene, linear low density (LLDPE). In *Kirk-Othmer Encyclopedia of Chemical Technology*, 5th ed.; Wiley, New York, 2006, **20**, 179–211.
15. Lappin, G. R.; Nemec, L. H.; Sauer, J. D.; Wagner, J. D. Higher Olefins. In *Kirk-Othmer Encyclopedia of Chemical Technology*, 4th ed., Wiley, New York, 2000; **17**, 709–723.
16. Maraschin, N., Polyethylene, high density (HDPE), in *Kirk-Othmer Encyclopedia of Chemical Technology*, 5th ed., Wiley, New York, 2006, **20**, 211–239.
17. M. P. McDaniel and P. J. DesLauriers, in *Kirk-Othmer Encyclopedia of Chemical Technology*, 5th ed. John Wiley & Sons, Inc., New York, 2000, **20**, 1-40.
18. R. B. Lieberman, M. Dorini, G. Mei, R. Rinaldi, G. Penzo and G. T. Berge, *Kirk-Othmer Encyclopedia of Chemical Technology*, John Wiley & Sons, Inc., New York, 2000, **20**, 523-548.
19. T. Uemura, T. Kaseda, Y. Sasaki, M. Inukai, T. Toriyama, A. Takahara, H. Jinnai and S. Kitagawa, *Nat. Commun.*, 2015, **6**, 7473.
20. T. Uemura, K. Kitagawa, S. Horike, T. Kawamura, S. Kitagawa, M. Mizuno and K. Endo, *Chem. Commun.*, 2005, 5968-5970.
21. T. Uemura, D. Hiramatsu, Y. Kubota, M. Takata and S. Kitagawa, *Angew. Chem.*, 2007, **119**, 5075-5078.
22. T. Uemura, Y. Ono, K. Kitagawa and S. Kitagawa, *Macromol.*, 2008, **41**, 87-94.
23. S. Wang, T. Kitao, N. Guillou, M. Wahiduzzaman, C. Martineau-Corcos, F. Nouar, A. Tissot, L. Binet, N. Ramsahye, S. Devautour-Vinot, S. Kitagawa, S. Seki, Y. Tsutsui, V. Briois, N. Steunou, G. Maurin, T. Uemura and C. Serre, *Nat. Commun.*, 2018, **9**, 1660.
24. M. Takayanagi, S. Pakhira and M. Nagaoka, *J. Phys. Chem. C*, 2015, **119**, 27291-27297.
25. T. Kitao, Y. Zhang, S. Kitagawa, B. Wang and T. Uemura, *Chem. Soc. Rev.*, 2017, **46**, 3108-3133.
26. J. Canivet, S. Aguado, Y. Schuurman and D. Farrusseng, *J. Am. Chem. Soc.*, 2013, **135**, 4195-4198.
27. S. T. Madrahimov, J. R. Gallagher, G. Zhang, Z. Meinhart, S. J. Garibay, M. Delferro, J. T. Miller, O. K. Farha, J. T. Hupp and S. T. Nguyen, *ACS Catal.*, 2015, **5**, 6713-6718.
28. E. D. Metzger, C. K. Brozek, R. J. Comito and M. Dincă, *ACS Centr. Sci.*, 2016, **2**, 148-153.
29. E. D. Metzger, R. J. Comito, C. H. Hendon and M. Dincă, *J. Am. Chem. Soc.*, 2017, **139**, 757-762.
30. S. Pellizzeri, M. Barona, V. Bernales, P. Miró, P. Liao, L. Gagliardi, R. Q. Snurr and R. B. Getman, *Catal. Today*, 2018, **312**, 149-157.
31. J. Ye, L. Gagliardi, C. J. Cramer and D. G. Truhlar, *J. Catal.*, 2017, **354**, 278-286.
32. V. Bernales, A. B. League, Z. Li, N. M. Schweitzer, A. W. Peters, R. K. Carlson, J. T. Hupp, C. J. Cramer, O. K. Farha and L. Gagliardi, *J. Phys. Chem. C*, 2016, **120**, 23576-23583.
33. B. Liu, S. Jie, Z. Bu and B.-G. Li, *J. Mol. Cat. A. Chem.*, 2014, **387**, 63-68.
34. P. Ji, J. B. Solomon, Z. Lin, A. Johnson, R. F. Jordan and W. Lin, *J. Am. Chem. Soc.*, 2017, **139**, 11325-11328.
35. R. J. Comito, K. J. Fritzsching, B. J. Sundell, K. Schmidt-Rohr and M. Dincă, *J. Am. Chem. Soc.*, 2016, **138**, 10232-10237.

-
36. R. C. Klet, S. Tussupbayev, J. Borycz, J. R. Gallagher, M. M. Stalzer, J. T. Miller, L. Gagliardi, J. T. Hupp, T. J. Marks, C. J. Cramer, M. Delferro and O. K. Farha, *J. Am. Chem. Soc.*, 2015, **137**, 15680-15683.
37. R. J. Comito, E. D. Metzger, Z. Wu, G. Zhang, C. H. Hendon, J. T. Miller and M. Dincă, *Organometallics*, 2017, **36**, 1681-1683.
38. A. N. Mlinar, B. K. Keitz, D. Gygi, E. D. Bloch, J. R. Long and A. T. Bell, *ACS Catal.*, 2014, **4**, 717-721.
39. R. J. C. Dubey, R. J. Comito, Z. Wu, G. Zhang, A. J. Rieth, C. H. Hendon, J. T. Miller and M. Dincă, *J. Am. Chem. Soc.*, 2017, **139**, 12664-12669.
40. J. Vitorino Marta, T. Devic, M. Tromp, G. Férey and M. Visseaux, *Macromol. Chem. Phys.*, 2009, **210**, 1923-1932.
41. S. Liu, Y. Zhang, Y. Han, G. Feng, F. Gao, H. Wang and P. Qiu, *Organometallics*, 2017, **36**, 632-638.
42. G. Férey, C. Serre, C. Mellot-Draznieks, F. Millange, S. Surblé, J. Dutour and I. Margiolaki, *Angew. Chem. Int. Ed.*, 2004, **43**, 6296-6301.
43. G. Férey, C. Mellot-Draznieks, C. Serre, F. Millange, J. Dutour, S. Surblé and I. Margiolaki, *Science*, 2005, **309**, 2040-2042.
44. A. Harton, M. K. Nagi, M. M. Glass, P. C. Junk, J. L. Atwood and J. B. Vincent, *Inorg. Chimica Acta*, 1994, **217**, 171-179.
45. L. Lu, J. Cai and R. L. Frost, *Spectros. Lett.*, 2010, **43**, 266-274.
46. M. Latroche, S. Surblé, C. Serre, C. Mellot-Draznieks, P. L. Llewellyn, J.-H. Lee, J.-S. Chang, S. H. Jhung and G. Férey, *Angew. Chem. Int. Ed.*, 2006, **45**, 8227-8231.
47. E. A. Berdonosova, K. A. Kovalenko, E. V. Polyakova, S. N. Klyamkin and V. P. Fedin, *J. Phys. Chem. C*, 2015, **119**, 13098-13104.
48. O. I. Lebedev, F. Millange, C. Serre, G. Van Tendeloo and G. Férey, *Chem. Mater.*, 2005, **17**, 6525-6527.
49. A. Vimont, J.-M. Goupil, J.-C. Lavalle, M. Daturi, S. Surblé, C. Serre, F. Millange, G. Férey and N. Audebrand, *J. Am. Chem. Soc.*, 2006, **128**, 3218-3227.
50. S. L. Shufler, H. W. Sternberg and R. A. Friedel, *J. Am. Chem. Soc.*, 1956, **78**, 2687-2688.
51. E. Groppo, C. Lamberti, S. Bordiga, G. Spoto and A. Zecchina, *Chem. Rev.*, 2005, **105**, 115-184.
52. E. Groppo, C. Lamberti, F. Cesano and A. Zecchina, *Phys. Chem. Chem. Phys.*, 2006, **8**, 2453-2456.
53. S. D. Kohler and J. G. Ekerdt, *J. Phys. Chem.*, 1994, **98**, 4336-4342.
54. C.N. Nenu , E. Groppo, C. Lamberti, M. Beale Andrew , T. Visser, A. Zecchina and B.M. Weckhuysen, *Angew. Chem. Int. Ed.*, 2007, **46**, 1465-1468.
55. K. I. Hadjiivanov and G. N. Vayssilov, *Adv. Catal.*, 2002, **47**, 307-511.
56. B. M. Weckhuysen, A. A. Verberckmoes, A. R. De Baets and R. A. Schoonheydt, *J. Catal.*, 1997, **166**, 160-171.
57. J. J. H. B. Sattler, I. D. Gonzalez-Jimenez, A. M. Mens, M. Arias, T. Visser and B. M. Weckhuysen, *Chem. Commun.*, 2013, **49**, 1518-1520.
58. C. K. Brozek and M. Dincă, *J. Am. Chem. Soc.*, 2013, **135**, 12886-12891.
59. Y. Zeng, P. Channingkwan, R. Baba, T. Taniike and M. Terano, *Macromol. React. Eng.*, 2016, **11**, 1600046.
60. M. P. McDaniel, *ACS Catal.*, 2011, **1**, 1394-1407.
61. D. S. McGuinness, N. W. Davies, J. Horne and I. Ivanov, *Organometallics*, 2010, **29**, 6111-6116.
62. M. F. Delley, C. S. Praveen, A. P. Borosy, F. Núñez-Zarur, A. Comas-Vives and C. Copéret, *J. Catal.*, 2017, **354**, 223-230.

PART C

**Micro-Spectroscopy Studies of
Defect-Engineered and
Functional [Cu₃(BTC)₂] and
Guest@[Cu₃(BTC)₂] Materials**

Chapter 5

Advanced Characterization of Defect-Engineered $[Cu_3(BTC)_{2-x}(CYDC)_x]$ Materials: Origin and Structure of Defects



In the past few years, Defect-Engineered Metal-Organic Frameworks (DEMOFs) have been intensely studied due to the plethora of textural, catalytic or magnetic properties that can be enhanced by carefully introducing defect sites in the crystal lattice. In this Chapter, the spatial distribution of two different non-defective and defective linkers, i.e. 1,3,5-benzenetricarboxylate (BTC) and 5-cyano-1,3-benzenedicarboxylate (CYDC), respectively, in different crystals of the HKUST-1 topology has been studied by utilizing multiple complementary characterization techniques. For example, Raman micro-spectroscopy reveals a non-homogeneous distribution of defect sites over $Cu_3(BTC)_{2-x}(CYDC)_x$ crystals, while other advanced techniques allowed to shed light into the exact nature of the Cu species within the framework as well as the effect of an increasing amount of the defective CYDC linker on crystal size and the formation of mesopores. In other words, this Chapter corroborates the necessity of utilizing microscopy and spectroscopy methods, as well as a whole array of bulk characterization techniques to fully describe multi-component metal-organic frameworks in detail. This work can potentially push the field of crystal

engineering of MOFs to the next level of design and highlights the structural and chemical complexity of DEMOF materials.

The results described in this Chapter are reported in the following manuscript: "Investigation of the Origin and Structure of Defects in Defect-Engineered Metal-Organic Frameworks: The $[Cu_3(BTC)_{2-x}(CYDC)_x]$ showcase, M. Rivera-Torrente, M. Filez, F. Meirer, B. M. Weckhuysen, **2019**, submitted.

5.1 INTRODUCTION

Controlling the structural and chemical composition of functional materials at the nanoscale is critical for altering their physical and chemical properties. The correlation between composition, structure and performance of Metal-Organic Frameworks (MOFs) for different applications has been described in detail in Chapters 1 and 2. One of the advantage of MOFs compared to other porous crystalline materials (*e.g.* zeolites and ordered porous silicas) is the tunability of their building blocks. This makes it often possible to obtain the same topology with functionalized analogues of a given organic linker, the so-called Multi-Variate (MTV)-MOFs.^{1, 2} Moreover, in order to enhance performance of MOFs in fields such as sorption and catalysis, it has been demonstrated that some properties, *e.g.* electronic, textural or magnetic ones, can be tuned by the purposeful introduction of defects within the MOF lattice.³⁻⁶

There are mainly two methods for the preparation of defect-containing MOFs: Post-synthetic treatments (such as partial hydrolysis or pyrolysis of the network) and *de novo* synthesis of defective MOFs. In the latter case, co-crystallization of defects, *i.e.* non- or weakly-coordinating linker molecules,⁷ along with the putative parent linker for the topology of choice, leads to a mixed-linker framework structure with the presence of defect sites.^{8, 9} Thus, the missing carboxylate, imidazolate or phosphonate fragments in the defect-linker, generate more exposed cationic metallic centers, which also become available for *e.g.* reaction. Consequently, the redox properties of the Coordinatively Unsaturated Sites (CUS), if already present, can be altered (*e.g.* reduced oxidation states).¹⁰ Representative examples of this strategy for the HKUST-1 topology have been reported by the groups of Baiker and Fischer,^{7, 11} in which the presence of mixed-valence

paddle-wheel units with Cu²⁺/Cu⁺ centers was observed. Indeed, Fang *et al.* showed that the Cu₃(BTC)₂ material can be doped with different concentrations of low-coordinating linkers,¹² such as 5-cyano-1,3-benzenedicarboxylate (CYDC), which leads to a particular variety of an MTV-MOF, in which additional Cu⁺ sites and mesopores are formed, as compared to the parent, non-doped [Cu₃(BTC)₂]. This way of working has been also shown in the case of the Ru analogue,^{11, 13} with which very active olefin hydrogenation and dimerization catalysts can be synthesized.⁹

An indirect characterization method to address the spatial distribution of linkers was published by Kong *et al.*, who showed that a combination of solid-state Nuclear Magnetic Resonance (NMR) with computational calculations can map differently tagged linkers in the 3-D lattice.¹⁴ In the first example of chemical imaging of MTV-MOFs, Katzenmeyer *et al.* used photothermally-induced infrared (PT-IR) spectroscopy coupled to Atomic Force Microscopy (AFM),¹⁵ to prove that aminoterephthalate and terephthalate linker molecules aggregate in MIL-68(In) crystals. More recently, Schrimpf *et al.*¹⁶ used Fluorescence Lifetime Imaging (FLIM) of tagged UiO-67 crystals to study the distance between these labelled linkers. Moreover, Liu *et al.*¹⁷ have shown by means of High-Resolution Transmission Electron Microscopy (HR-TEM) how ordered defect regions in the UiO-66 crystals form mesopores and change the symmetry of the lattice. However, to the best of our knowledge, a detailed characterization study of the origin and structure of defects in defect-engineered [Cu₃(BTC)₂]_x(CYDC)_x crystals has not yet been presented. In this Chapter, we show how a range of analytical methods, including Raman microscopy,^{18, 19} as well as various bulk characterization techniques, can unravel key features of the linker distribution as well as other relevant physicochemical properties of the [Cu₃(BTC)₂]_x(CYDC)_x materials.

5.2 EXPERIMENTAL SECTION

5.2.1. Materials Synthesis

N,N-dimethylformamide (DMF, HCON(CH₃)₂, ≥99.8%), copper nitrate trihydrate (Cu(NO₃)₂·3H₂O, 99%), trimesic acid (H₃BTC, C₉H₆O₆, 99%), 5-cyano-1,3-benzenedicarboxylic acid (CYDC, C₉H₅NO₄, ≥95%) were all purchased from Sigma-Aldrich.

Ethanol (technical grade, 97%), dichloromethane (CH_2Cl_2 , technical grade, 99%) and acetone ($\geq 99.5\%$) were purchased from BiosolveTM or VWR International. Trifluoroacetic acid (TFA, 99%, HPLC grade, BiosolveTM), dimethyl sulfoxide (DMSO, 98% anhydrous, Sigma-Aldrich), acetonitrile (CH_3CN , HPLC grade, BiosolveTM) and *milli-Q* water (MetrohmLab system, $\Omega = 18 \text{ S}\cdot\text{cm}^{-1}$ at 298 K).

The crystals were synthesized according to the protocol described in the literature.¹² Briefly, $\text{Cu}(\text{NO}_3)_2 \cdot 3\text{H}_2\text{O}$ (0.398 g, 1.61 mmol) were dissolved into 6 mL of deionized (DI) water. Then, L-x moles of H_3BTC and x moles of CYDC (Table 4.1) were dissolved into a mixture of DMF (6 mL) and EtOH (6 mL) by ultrasonication at room temperature for 5 min. Thereafter, the metal and linker solutions were mixed in a sealed glass 25 mL scintillation vial and heated to 343 K in an oven for 12 h. After cooling down to room temperature naturally, the powders were collected by filtration and washed with ethanol (20 mL), acetone (20 mL) and dichloromethane (20 mL) and dried in air at room temperature.

Table 5.1. Mass compositions of the initial mixtures in solution for CYDC-containing HKUST-1.

Sample	$\text{Cu}(\text{NO}_3)_2 \cdot 3\text{H}_2\text{O}$ (g)	H_3BTC (g)	CYDC (g)	$\text{mol}_{\text{BTC}}:\text{mol}_{\text{CYDC}}$
Parent (0%)	0.389	0.210	-	0:100
10%	0.389	0.203	0.021	90:10
30%	0.389	0.156	0.062	70:30
50%	0.389	0.131	0.103	50:50
70%	0.389	0.079	0.144	30:70



Figure 5.1. Image of the different as-synthesized defect-engineered $\text{Cu}_3(\text{BTC})_{2-x}(\text{CYDC})_x$ powders under study in this Chapter. Note that the difference in colour of the materials relates to the presence of different $\text{Cu}^{2+}/\text{Cu}^+$ ratios present, hence already a nice illustration how a different amount of defective CYDC linker can alter the redox properties of the node present in Defect-Engineered Metal-Organic Frameworks (DEMOFs).

5.2.2. Material Characterization

X-ray diffraction (XRD) patterns were obtained by a Bruker-AXS D2 Phaser powder X-ray diffractometer in Bragg-Brentano geometry, using Co K_{α1,2} = 1.79026 Å, operated at 30 kV. Measurements were carried out between 5 and 70° using a step size of 0.05° and a scan speed of 1 s. Simulated patterns were obtained by processing the corresponding .cif files with Mercury 3.7® (λ = 1.79026 Å, FWHM = 0.2). *High-Performance Liquid Chromatography (HPLC)* measurements were carried out in a Waters HPLC machine with an injection volume of 5 µL, a Sunfire C18 column with a pore size of 100 Å, particle sizes of 3.5 µm and a length of 150 mm. Detection took place using a Waters R2451 UV/Vis detector at λ = 254 and 220 nm; under the following eluent gradients: Start with 100% eluent A for 5 min; after that the eluent is changed to 75% B during 15 min; stay at 75% B for 2.5 min; after that the eluent is changed to 100% A during 5 min; stay at 100% A for 2.5 min. (Eluent A: H₂O/CH₃CN/TFA – 95/5/0.1 (% v/v/v), and eluent B: CH₃CN / H₂O/TFA – 95/5/0.1 (% v/v/v)). Prior to measurement, the samples were dissolved in 10% TFA/DMSO (same solvent as the calibration curves with the pure components) and filtered through 45 µm PTFE filters, and the injections ran in duplicate. *N₂ adsorption isotherms* were measured at 77 K on a Micromeritics ASAP 2010 apparatus. Prior to the measurements, samples were activated at 298 K under primary vacuum until the pressure reached 1 mbar and then switched to secondary vacuum at 443 K for 16 h. The measurement temperature was controlled with liquid N₂ at 77 K. Adsorption equilibrium was assumed when the variation of the cell pressure was 5 % for minimum and maximum period of 9 min and 30 min, respectively. *Fourier-transformed infrared (FT-IR)* spectroscopy measurements were recorded on a PerkinElmer System 2000 instrument (16 scans, 4 cm⁻¹ resolution, DTGS detector, cell with KBr windows). The materials were prepared in a press tool by pressing ~10 mg of powder into self-supported pellets (2 cm² area), which were then activated at 448 K for 3 h at p < 10⁻⁵ mbar. After cooling down the cell with liquid N₂ temperature to 85 K, a mixture of 10% NO/He v/v (Linde AG, 99.998% purity) was introduced at the pressures described in the Results and Discussion section (Section 4.3) and was then desorbed under the conditions stated. When pyridine (Py) was used as a probe molecule, similar pellets were placed into a cell as the one described above and the spectra recorded with a ThermoFisher Nicolet iS5 spectrometer (32 scans, 4 cm⁻¹ resolution, DTGS detector). The

pellet was evacuated by heating in a cell at 498 K (ramp of $10\text{ K}\cdot\text{min}^{-1}$) for 24 h at $p < 10^{-5}$ mbar, which was then cooled down to 323 K. At that temperature, pyridine (redistilled, 99.9 %, Sigma-Aldrich) vapour was introduced into the cell and the equilibrium pressure set to 15 mbar. Spectra were recorded in adsorption mode up to 60 min after introduction of the gas. *Raman micro-spectroscopy* measurements were carried out with a Renishaw *InVia*TM microscope with a laser at 532 nm excitation with a power density of $6 \cdot 10^{-3}\text{ W}\cdot\text{cm}^{-2}$, operated at 36 mW total power (power output = 1%), a 1200 lines/mm grating and a detector in reflectance mode. A Si wafer was used as reference and the samples were prepared by dispersing HKUST-1 crystals on dichloromethane (CH_2Cl_2), dropped onto a glass cover and measured after the solvent was dried in air at room temperature. The crystals were then imaged with a 50x objective, and the spectra collected with a pixel size of $1 \times 1\text{ }\mu\text{m}^2$, 1 accumulation and 10 s/acc. Multiple exposures were carried out to ensure that sample damage was not observed. Data processing was done with Wire 3.4[©], TXM Wizard software²⁰ and Matlab R2015a, by generating signal-to-baseline maps of the spectral regions described in the main text (cosmic rays signal and artefacts were manually subtracted). *Scanning Electron Microscopy (SEM)* images were recorded on a PhenomPro X microscope operated at 10 kV equipped with a CsB filament. The powder samples were supported on carbon tape deposited over Al stabs (FEI stabs) and inserted in the microscope vacuum chamber without Au coating. At least 100 crystals were measured to derive the particle size distributions. *Diffuse Reflectance UV-Vis-NIR (DR UV-vis-NIR) spectroscopy measurements* were recorded on PerkinElmer Lambda 950 S equipped with InGaAs and Photo-Multiplier Tube (PMT) detectors; and D₂ and W-halogen lamps ($4\text{ nm}\cdot\text{s}^{-1}$, 2 nm⁻¹ resolution, Halon polymer reference). Powders measured in air were placed in a holder with quartz windows and the spectra recorded right away. In the case of activated materials, the powders were dried at 423 K under primary vacuum ($p < 1\text{ mbar}$) for 15 min, then transferred into a glovebox (BraunTM, O₂ < 1 ppm, H₂O < 1 ppm), placed into a sealed quartz holder and the spectra then recorded. *Electron Paramagnetic Resonance (EPR)* experiments were carried out with a Continuous Wave (CW) Bruker EMX EPR spectrometer working at a frequency of ~ 9.5 GHz (*X*-band). The magnetic-field modulation frequency was 100 kHz. The temperature was set to 100 K by spraying liquid nitrogen to the quartz tubes filled with *ca.* 20 mg of each MOF sample.

5.3 RESULTS AND DISCUSSION

5.3.1 Effect of the Defective CYDC Linker on Crystal Structure, Size and Morphology

The X-ray Diffraction (XRD) patterns of the Defect-Engineered Metal-Organic Frameworks (DEMOFs) under study, namely defect-engineered $\text{Cu}_3(\text{BTC})_{2-x}(\text{CYDC})_x$ materials with $x = 0, 0.2, 0.6, 1.0$ and 1.4 and illustrated in Figure 5.1, are shown in Figure 5.2. The XRD patterns show that the topology (symmetry and space group) is preserved for increasing concentrations of the defective linker CYDC, as was previously reported.¹² Nevertheless, still some unidentified impurities appear when 50 mol% of CYDC is added to the mixture with H_3BTC .

Moreover, it is clear from Figure 5.3 and Table 5.2, that the MOF lattice remains unaffected, in terms of interplanar parameter (d), and unit cell distances, as demonstrated by the constant 2θ and Full-Width at Half Maximum (FWHM) of the main diffraction reflections up to 50 mol% content of CYDC in the mixture, but decreases at higher CYDC concentrations. This indicates a contraction of the lattice compared to the parent HKUST-1. This may be caused by the presence impurities, corresponding to impurities at higher CYDC concentrations, which suggests that an alternative $[\text{Cu}_x(\text{CYDC})_y]$ coordination polymer phase may be formed during crystallization; or that there are inclusions of defects in the lattice (*i.e.* bond contraction and lattice strain for formal charge balance between non-coordinating linkers and metal centres).

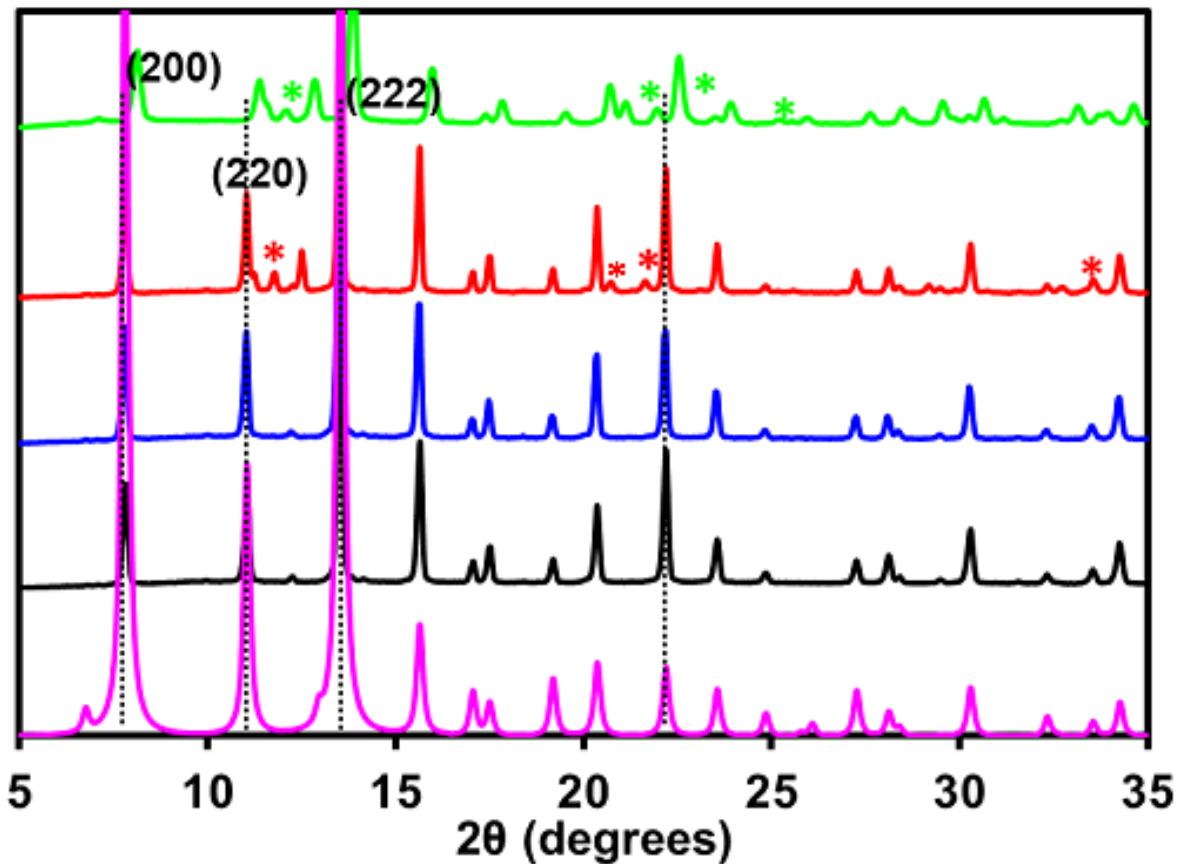


Figure 5.2. X-ray Diffractograms (XRD) of the simulated parent Cu_3BTC_2 (pink) and $\text{Cu}_3(\text{BTC})_{2-x}(\text{CYDC})_x$ materials with $x = 0.2$ (black), 0.6 (blue), 1.0 (red) and 1.4 (green). *The asterisks correspond to different unidentified impurities are present at high CYDC concentrations.

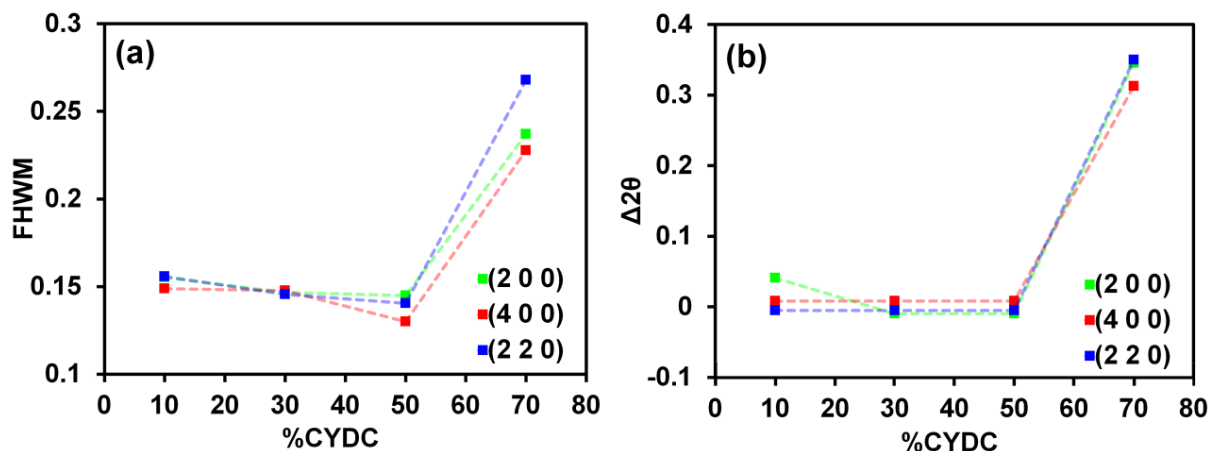


Figure 5.3. (a) Evolution of the Full Width at Half Maximum (FWHM) values with increasing molar concentration of the defective CYDC linker in the $\text{Cu}_3(\text{BTC})_{2-x}(\text{CYDC})_x$ lattices. (b) Shift of the XRD peaks corresponding to the reflections with indexes (2 0 0), (4 0 0) and (2 2 0).

Table 5.2. Lattice parameters calculated for the CYDC-containing HKUST-1 crystals obtained from the Bragg equation ($n\lambda = 2d \cdot \sin \theta$) for different reflections.

$h k l$	2θ (°)	d (Å)			
		x = 0.2	x = 0.6	x = 1.0	x = 1.4
(2 0 0)	7.8	13.15	13.15	13.15	12.60
(2 2 0)	11.1	9.30	9.30	9.30	9.02
(2 2 2)	13.5	7.59	7.59	7.59	7.41

As described in the literature¹¹, quantification of the incorporated defective CYDC linker into the lattice is challenging, given that the solid-state NMR method is hindered by the paramagnetic Cu²⁺ cations in the lattice and the method used for dissolving the lattice results into decomposition of the linker into multiple products.

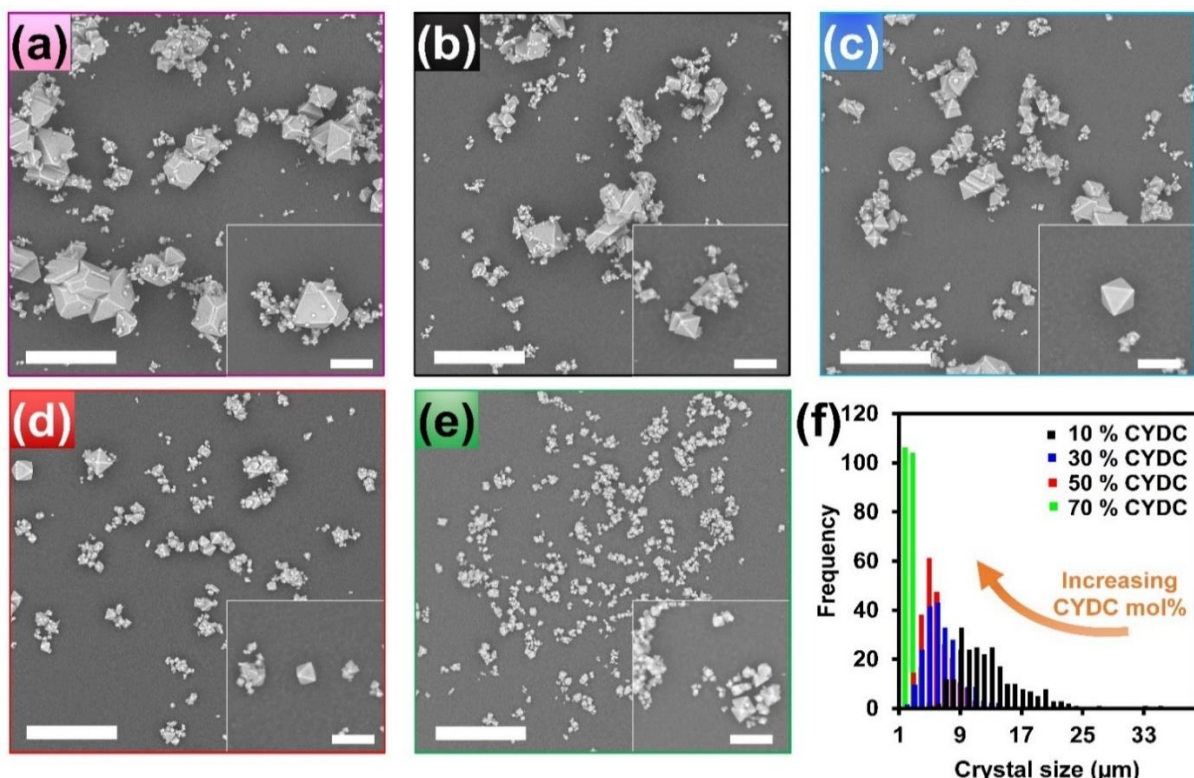


Figure 5.4. Scanning Electron Microscopy (SEM) images of the crystals prepared with the following compositions: (a) $[\text{Cu}_3(\text{BTC})_2]$, (b) $[\text{C}_3(\text{BTC})_{1.8}(\text{CYDC})_{0.2}]$, (c) $[\text{Cu}_3(\text{BTC})_{1.4}(\text{CYDC})_{0.6}]$, (d) $[\text{Cu}_3(\text{BTC})_{1.0}(\text{CYDC})_{1.0}]$ and (e) $[\text{Cu}_3(\text{BTC})_{0.6}(\text{CYDC})_{1.4}]$. Insets show individual crystals with less intergrown domains. Scale bars represent 10 μm (and 5 μm in the insets); (f) crystal size distributions and evolution of the crystal size with the CYDC content in the framework.

This was also observed in our case, where the peak corresponding to CYDC in the samples after digestion split into different eluted compounds. We hypothesize that the decomposition into products *via* hydrolysis of the nitrile group to the amide and the subsequent formation of ammonium salts or oxidation is likely under the digestion conditions (TFA/DMSO and Cu²⁺ ions present).²¹ The results of our quantification are in line with those previously published by the group of Fischer.¹¹ Not only porosity, but also other properties of the MOF materials can be altered by the presence of a different linker, such as the defective CYDC linker. It is indeed well-established that the presence of additional synthetic agents (*e.g.* modulators, surfactants)⁸ in solution greatly affects the properties of a given MOF. In fact, the use of modulators for crystal and defect engineering has been extensively studied in the past. In particular, the group of Kitagawa,²² as well as other groups,²³ revealed how monodentate carboxylic acids, among many other parameters such as the presence of ions^{24, 25} or surfactants^{26, 27} in solution, pH,²⁸ the solvent composition or ultrasounds,²⁹ can steer the kinetics of the growth of {100} or {111} facets in HKUST-1, with the subsequent change in morphology from cube, to cuboctahedra and eventually, octahedra. In order to understand the effects in morphology of co-crystallizing BTC and CYDC under solvothermal conditions, SEM images of the materials with increasing concentration of the defective CYDC linker were obtained. The insets micrographs in Figures 5.4c and 5.4d reveal that for certain concentrations of defective CYDC linker, less secondary nucleation (on the growing crystal surfaces) occurs, leading to well-defined octahedra. It is also clear that the parent [Cu₂(BTC)₃] crystals appear as truncated octahedra, suggesting that the growth rate ν of both faces is similar, *i.e.* $\nu_{\{100\}} \approx \nu_{\{111\}}$. As the concentration of the defective CYDC linker increases, the crystal morphology evolves to well-defined octahedra, as it the case for a much higher rate for the {111} facet, *i.e.* $\nu_{\{100\}} \gg \nu_{\{111\}}$. Thus, we hypothesize that the defective CYDC linker hinders the growth of {100} facet, although more detailed experimental and theoretical studies on the molecular species formed at the first stages would be necessary.

Not only the crystal morphology, but also the crystal size and related crystal size distribution are affected by the presence of the defective CYDC linker. For the parent material (Figure 5.4a), both large crystals of *ca.* 10-20 µm, and very small-size (*ca.* 200-500

nm) crystals in their vicinity are present. In contrast, when CYDC was added (Figure 5.4b-e), the average size of the crystals decreased significantly, as seen in the estimated crystal size distributions, shown in Figure 5.4f. Moreover, the crystal size distribution is narrower for synthesis recipes containing a larger amount of the defective CYDC linker. Indeed, it was found that the presence of CYDC modifies the crystal sizes from 10-20 μm (in the case of 10 %mol CYDC in the synthesis mixture) down to nearly monodisperse crystals of *ca.* 2 μm for the highest concentration of CYDC (in the case of 70% mol CYDC in the synthesis mixture).

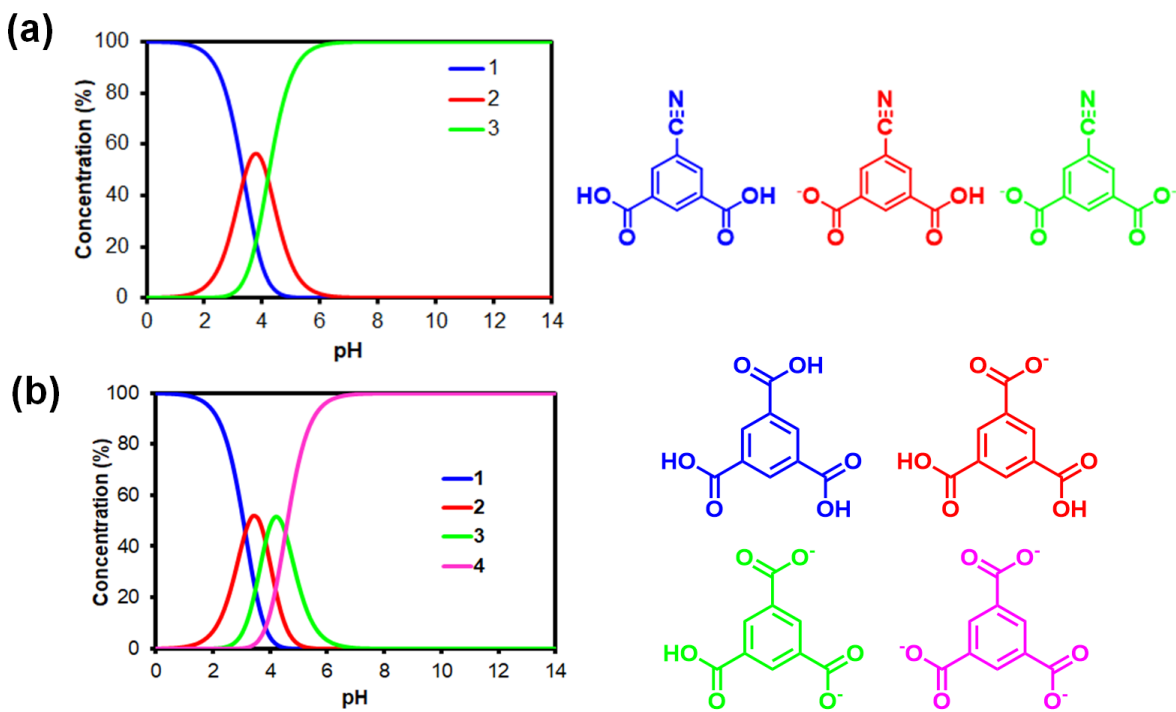


Figure 5.5. Calculated distribution of the different microspecies in aqueous solution at 298 K, 1 bar and ionic strength $\textit{I} = 0$ of (a) 5-cyano-1,3-benzenedicarboxylic acid and (b) 1,3,5-benzenetricarboxylic acid. The distribution was obtained with the Reactor 19.2 package (MarvinView © ChemAxon).

In the case of HKUST-1 crystallization, analyses using the Avrami-Erofe'ev model³⁰ with the Sharp-Hancock³¹ method have previously shown that under preparative synthesis conditions, nucleation continues during growth and it is the rate limiting step.^{32, 33} This leads to polydispersity in the crystallite sizes. However, the defective CYDC linker appears to limit crystal growth and promote nucleation, leading to many small(er) octahedral crystals. In order to rule out the possibility that the CYDC linker alters the pH of the synthesis mixture, we have calculated the microspecies distribution under identical

conditions for BTC and the defect linker. The results are shown in Figure 5.5. It can be noted that similar types of protonated molecules are present at different pH values. This suggests similar reactivity at the molecular level, and thus, the CYDC linker would act as a capping agent hindering growth rather than modify the acidity of the synthesis solution.

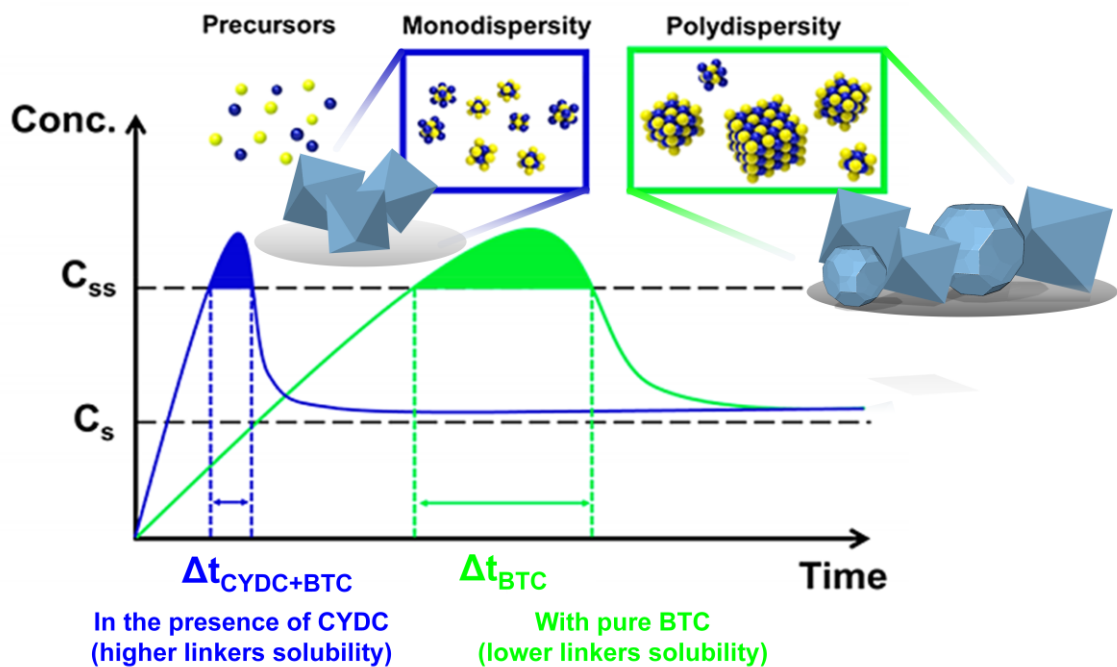


Figure 5.6. LaMer diagram explaining the difference in time evolution of solution concentration during crystallization for the mono- (including CYDC) and poly-dispersed (purely BTC) scenarios. Concentration values c_s and c_{ss} refer to the saturation and the super-saturation concentrations. Adapted and reprinted from reference 34. Copyright © American Chemical Society, 2019.

Another possible scenario may be related to the increased solubility of the CYDC linker in the solvent mixture. In this case, following the LaMer's model,³⁵ a higher solubility of the defective CYDC linker would drive the system faster to supersaturation, and thus, to the nucleation burst before than in the case of BTC. Thus, the mixture would yield more initial nuclei leading to smaller crystallites as a result, as shown in Figure 5.6. Recent examples have shown that by controlling supersaturation of Cu^{2+} and BTC one can, indeed, finely tune the crystallite size,³⁶ or the film thickness.³⁴ Further investigations including *in-situ* spectroscopy and light scattering would be of interest in order to elucidate the different species formed during crystallization.

5.3.2. Effect of the Defective CYDC Linker on Mesopore Formation and Structure

Theoretical studies have predicted that a lattice of $\text{Cu}_3(\text{BTC})_{2-x}(L)_x$, where L is a non-coordinating linker, may have a certain number of mesoporous voids without compromising their mechanical stability.³⁷ Analysis of mesopore formation in MOFs by means of Small-Angle X-ray Scattering (SAXS) has been previously reported by Tsao *et al.*³⁸ In their case, a number of assumptions on pore geometry and dispersion within the MOF matrix made it possible to obtain model-dependent parameters, such as form factor. In this case, the structure of the mesopores remains unknown, so the analysis of the SAXS data was limited to the fitting of Guinier and Porod regions. In this work, we have also performed SAXS measurements and the results are shown in Figure 5.7. The scattering intensity log-plot of $I(q)$ vs. q shows large differences in the region for increasing concentrations of the defective CYDC linker ($0.03 \text{ nm}^{-1} < q$). By extrapolating the SAXS data to $q=0$ using an approximation for single particle scattering yields Equation (5.1):³⁹

$$I(q) = I(0) \cdot e^{-\left[\frac{(q \cdot R_g)^2}{3}\right]} \quad (\text{Equation 5.1})$$

, where $I(0)$ represents a contrast parameter, the excess of electrons of the scatterer relative to its surroundings, and R_g is the radius of gyration, which is indicative for the size of the scatterer. As can be seen in Figure 5.7 as well as in Table 5.3, the higher values of $I(q)$ in that region can be correlated to less dense materials, *i.e.* more scattered X-rays, due to the presence of more (or larger) mesopores.

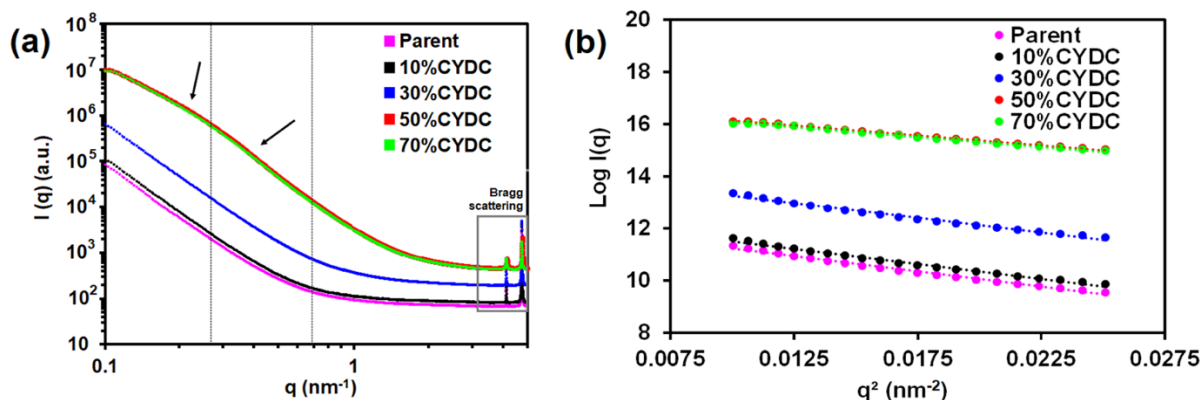


Figure 5.7. (a) Small-Angle X-ray Scattering (SAXS) curves of the defect-engineered $[\text{Cu}_3(\text{BTC})_{2-x}(\text{CYDC})_x]$ powders. Dashed lines indicate the two distinct Porod regions for the materials with 50 and 70% CYDC defective linker. (b) $\log I(q)$ vs. q^2 plot used showing the linear fit used to calculate the Guinier parameters.

Table 5.3. Values of the different parameters obtained by fitting the Guinier-Porod regions of the Small-Angle X-ray Scattering (SAXS) data of the defect-engineered $[\text{Cu}_3(\text{BTC})_{2-x}(\text{CYDC})_x]$ powders.

CYDC (%mol) ^[a]	$I(0) \times 10^6$ ^[a]	R_g (nm) ^{[a][b]}	D_1 ^[c]	D_2 ^[d]
0	0.311	20.2 (± 0.4)	4.5	-
10	0.354	19.5 (± 0.4)	4.04	-
30	2.15	19.3 (± 0.4)	4.03	-
50	24.2	15.14 (± 0.2)	2.75	4.18
70	23.9	15.6 (± 0.2)	2.86	4.14

[a] Calculated using the Guinier equation in the $0.01 < q < 0.02 \text{ nm}^{-2}$ region. [b] Values in brackets indicate the relative error in the R_g value. [c] Calculated using the Porod equation in the $0.14 < q < 0.2 \text{ nm}^{-1}$ [d] Calculated using Porod equation in the $0.27 < q < 0.7 \text{ nm}^{-1}$.

The presence of mesopores in the $[\text{Cu}_3(\text{BTC})_{2-x}(\text{CYDC})_x]$ powders is corroborated by the two distinct regions at higher q values ($0.2 \text{ nm}^{-1} < q$) for the materials with high loadings of the defective CYDC linker, *i.e.* 50 and 70 %mol. Porod's law describes the scattering at higher q values as shown in Equation (5.2):

$$I(q) = K \cdot q^{-D} \quad (\text{Equation 5.2})$$

, where K is a constant and the scattering depends on the exponential value D . In line with literature,³⁸ fitting of the scattering measured for the MOFs with 50 and 70% CYDC in the $0.14 < q < 0.2 \text{ nm}^{-1}$ region, yielded exponential values of *ca.* -2.8. At higher q , this value approached the typical $D = 4$, as it did for the materials with lower concentrations of the defective CYDC linker, corroborating the absence of mesopores within these materials. The differences in slope are typically associated with the presence of higher polydispersity of the scatterer volumes and confirms the presence of pores with different *radii*, *i.e.* apart from the micropores of 13.2, 11.1 and 5 Å diameter. Thus, mainly, three types of defect-engineered MOFs can be distinguished from the SAXS data: i) materials with no defects or a negligible effect in the pore structure (which is the case for materials containing 0 and

10 %mol of CYDC), ii) materials with intermediate mesopores (which is the case for materials containing 30 %mol of CYDC), and iii) materials with large cavities within the MOF (which is the case for materials containing 50 and 70 %mol of CYDC).

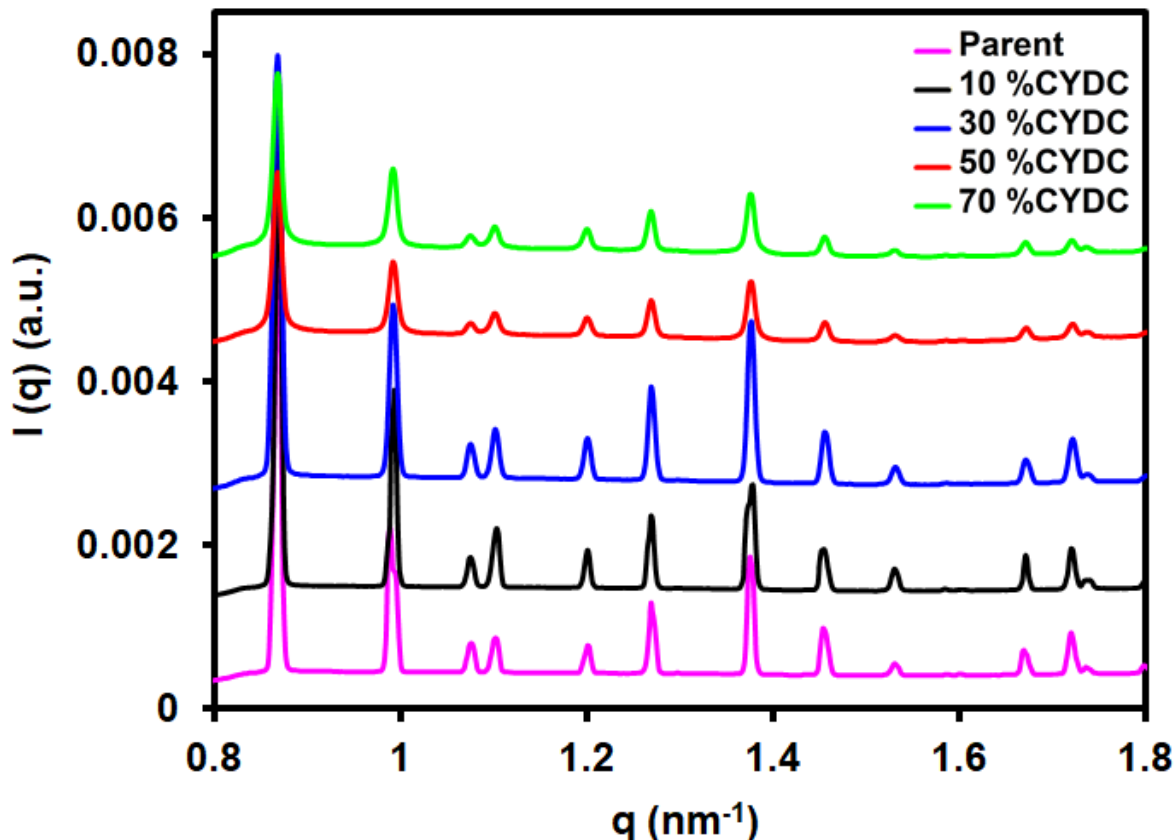


Figure 5.8. (a) Wide-Angle X-ray Scattering (WAXS) profiles of the defect-engineered $[Cu_3(BTC)_{2-x}(CYDC)_x]$ powders with increasing concentration of CYDC: parent with 0 %mol (pink), 10 %mol (black), 30 %mol (blue), 50 %mol (red) and 70 %mol (green); showing the Bragg reflections indicative of $[Cu_3(BTC)_2]$ for all concentrations. Note that the intensity of the scattered radiation drops at higher CYDC %mol loadings, indicating either smaller crystallites or less crystalline materials.

The crystallinity at the long-range, as shown by XRD, was further corroborated by collecting Wide-Angle X-ray Scattering (WAXS) patterns of the defect-engineered $[Cu_3(BTC)_{2-x}(CYDC)_x]$ powders with increasing concentration of CYDC. The results are shown in Figure 5.8, which indeed showed that the intensity of the Bragg reflections decreases for increasing CYDC concentrations. In line, with the SAXS and WAXS data, the nitrogen adsorption isotherms of Figure 5.9 reveal hysteresis loops of type H4 according to IUPAC classification, often associated with narrow pore slits.⁴⁰ Non-Local Density

Functional Theory (NLDFT) pore size distributions with slit geometry for an oxidic surface showed the presence of mesopores of *ca.* 13 nm when 30 %mol of CYDC was present in the mixture (Figure 5.9). Larger mesopores in the range of 15 to 25 nm were found when larger fractions of CYDC (50 and 70 %mol of CYDC) were added to the mixture. However, no clear trends in terms of specific surface area and pore volumes were observed for the defect-engineered HKUST-1 materials (Table 5.4).

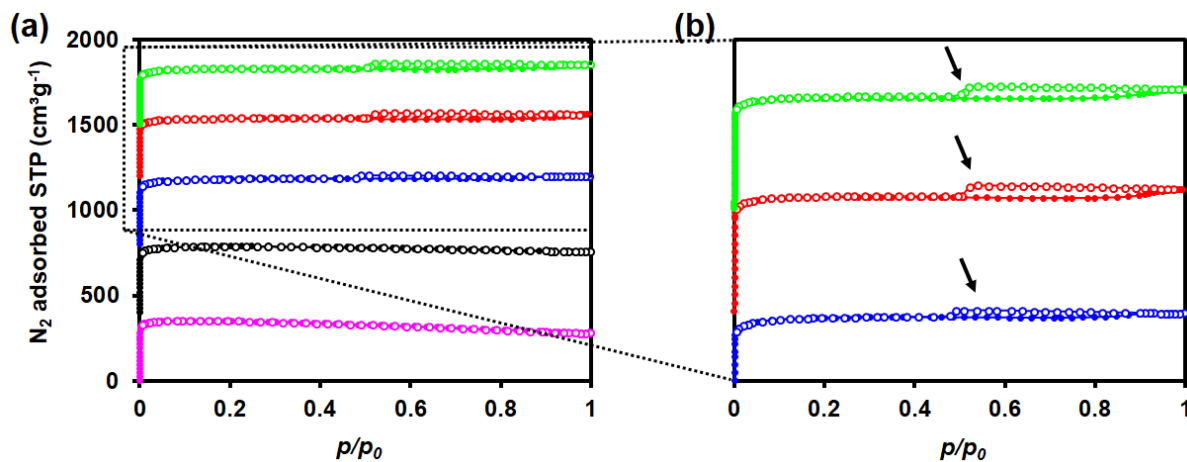


Figure 5.9. (a) Nitrogen adsorption isotherms at 77 K of the the defect-engineered [Cu₃(BTC)_{2-x}(CYDC)_x] powders with increasing concentration of CYDC: parent with 0 %mol (pink), 10 %mol (black), 30 %mol (blue), 50 %mol (red) and 70 %mol (green); in the mixture and (b) hysteresis loops type H4 with the arrows indicating the limit of each loop. The lack of hysteresis loops in the samples with 0 and 10 %mol CYDC indicates the presence of only micropores.

Table 5.4. Specific surface areas; total, micro- and mesopore volumes of the defect-engineered [Cu₃(BTC)_{2-x}(CYDC)_x] powders with increasing concentration of CYDC (expressed in mol%), as obtained from N₂ adsorption isotherms at 77 K.

CYDC (mol%)	Specific Surface Area BET (m ² ·g ⁻¹)	Total V _p at p/p ₀ = 0.99 (cm ³ ·g ⁻¹)	t-plot micropore volume (cm ³ ·g ⁻¹)	Mesopore volume (% of total V _p)
0	1470	0.57	0.57	0
10	1592	0.58	0.58	0
30	1550	0.61	0.55	10
50	1372	0.56	0.49	12.5
70	1331	0.55	0.47	14.5

Interestingly, and in agreement with the SAXS data, the volume fraction of mesopores increased proportionally with CYDC concentration in the material. As observed before, three regimes of mesopore voids were observed: i) none to few mesopores in the lattice (for the materials with 0 and 10 %mol CYDC), ii) intermediate amount of mesopores (for the material with 30 %mol CYDC); and iii) a higher fraction of mesopores (for the materials with 50 and 70 %mol CYDC). Not only the amount of mesopores, but also their size changes, from a narrow distribution around 12-13 nm to larger ill-defined pores between 10-30 nm in diameter (Figure 5.10).

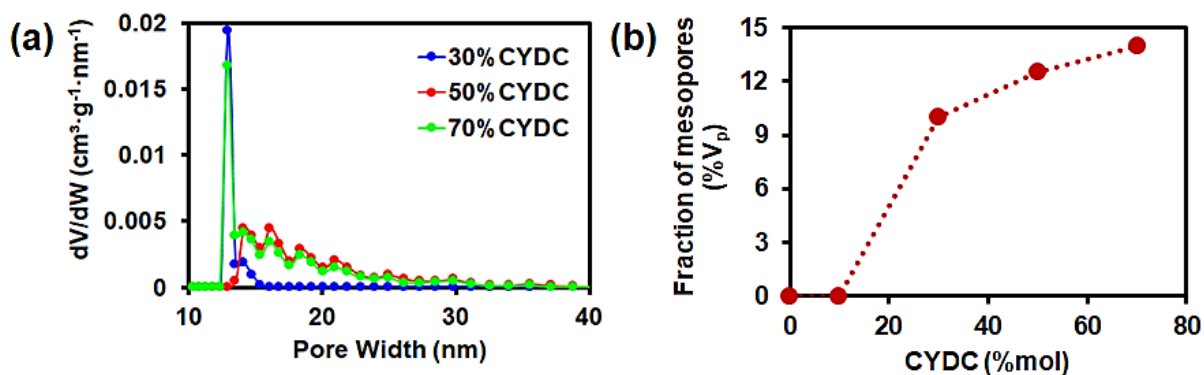


Figure 5.10. Non-Local Density Functional Theory (NLDFT) pore size distribution at 77 K with slit pore geometry obtained from the nitrogen adsorption isotherms of the defect-engineered $[\text{Cu}_3(\text{BTC})_{2-x}(\text{CYDC})_x]$ powders with 30 (blue), 50 (red) and 70 (green) %mol CYDC in the mixture. Only the $p/p_0 > 0.3$ region was fitted with NLDFT for calculating the mesopores. *NLDFT with oxidic surfaces and slit pores has been suggested to fit with this type of surfaces. (b) Evolution of the mesopore fraction of the total pore volume with CYDC concentration in the lattice.

5.3.3. Effect of the Defective CYDC Linker on the Redox Properties of Copper

As already suggested by the images of the powdered samples, as shown in Figure 5.1, the introduction of the defective CYDC linker results in a change of colour from blue to green, suggesting a higher tendency towards the reduction from Cu^{2+} to Cu^+ in the paddlewheel units with increasing CYDC linker amount. In order to verify this hypothesis, we have performed Diffuse Reflectance (DR) UV-Vis-NIR spectroscopy. The results of this analysis are summarized in Figure 5.12. The different spectra show that the band at *ca.* 14200 cm^{-1} , corresponding to Cu^{2+} with O_h distorted symmetry and oxygen or OH-like ligands, *i.e.* the metal sites, decreases with increasing CYDC-concentration in the $[\text{Cu}_3(\text{BTC})_{2-x}(\text{CYDC})_x]$ materials, as expected for Cu^+ . Accordingly, the Ligand-to-Metal Charge Transfer (LMCT) band at $\sim 33333\text{ cm}^{-1}$, shows a lower intensity for increasing CYDC content, which relates

to the spectrum of pure 5-cyano-1,3-benzenedicarboxylic acid, which is given in Figure 5.11, that shows a sharper $\pi \rightarrow \pi^*$ excitation band compared to that of trimesic acid.⁴¹

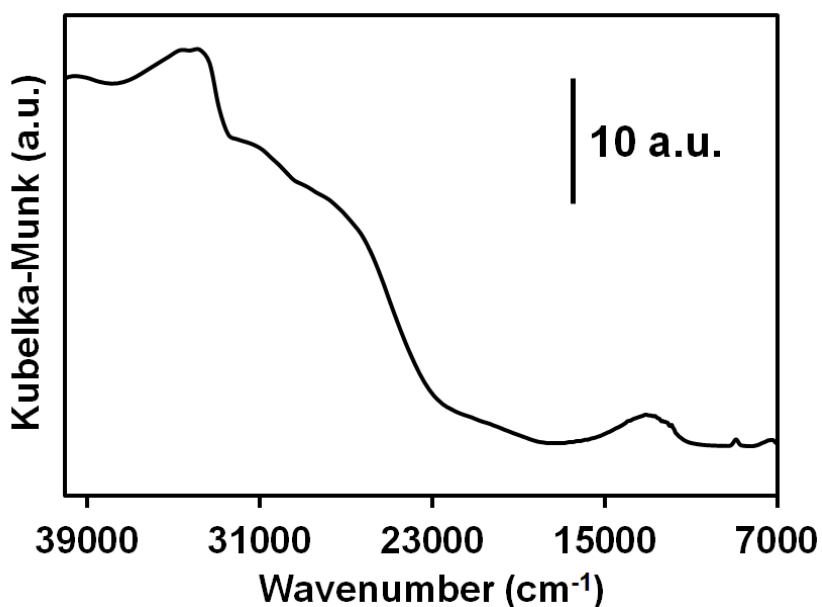


Figure 5.11. Diffuse Reflectance (DR) UV-Vis-NIR spectroscopy of the pure 5-cyano-1,3-benzenedicarboxylic acid (CYDC). The sharp band at around 34000 cm^{-1} corresponds to the $\pi \rightarrow \pi^*$ transition.

To exclude the effects of solvent in the pores, degassing under vacuum of the materials was carried out at 423 K for a short period of time (only 5 min, to avoid the Cu²⁺ auto-reduction as much as possible).⁴²⁻⁴⁶ The corresponding DR UV-vis-NIR spectra show a shoulder at $\sim 25000\text{ cm}^{-1}$ corresponding to the change in symmetry of the Cu centres upon loss of axial water. The intensity of this shoulder decreases for increasing concentration of the defective CYDC linker in the [Cu₃(BTC)_{2-x}(CYDC)_x] crystals. At higher concentrations of the defective CYDC linker (*i.e.*, for $x = 1.4$), both spectral features, *i.e.* the Cu²⁺ *d-d* transition and the high energy shoulder at 25000 cm^{-1} , are distinguishable as different bands. This indicates two effects when CYDC is introduced: *i*) even before activation, a certain fraction of Cu is already in the Cu⁺ state; and *ii*) degassing leads to large fractions of Cu⁺ in the framework.

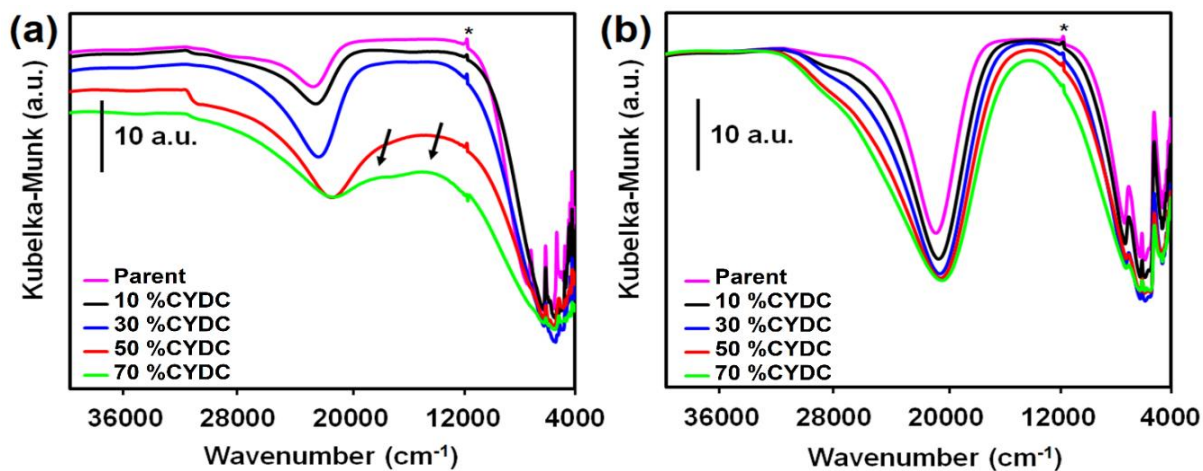


Figure 5.12. Diffuse Reflectance (DR) UV-Vis-NIR spectroscopy of the defect-engineered $[\text{Cu}_3(\text{BTC})_{2-x}(\text{CYDC})_x]$ powders with increasing concentration of CYDC (x): $x = 0$ (pink), 0.2 (black), 0.6 (blue), 1.0 (red) and 1.4 (pink) fraction of CYDC-linker (a) after and (b) before degassing under vacuum ($p < 1$ mbar) at 423 K for 15 min. *Peak corresponding to the monochromator switch at 860 nm. Arrows in (a) indicate the presence of two distinct types of d - d transitions of Cu^{2+} ions in the lattice.

To further study the nature of the Cu species, Continuous Wave (CW) Electron Paramagnetic Resonance (EPR) measurements were performed at X-band and recorded at 100 K. Pöppel et al. have previously shown the plethora of Cu species within $[\text{Cu}_3(\text{BTC})_2]$ (including the Cu^{2+} dimers, i.e. paddle-wheels; extra-framework monomeric $[\text{Cu}(\text{H}_2\text{O})_6]^{2+}$ complexes;⁴⁷⁻⁴⁹ as well as the presence of Cu^+ sites present before activation in defect-engineered $[\text{Cu}_3(\text{BTC})_2]$ samples). Moreover, Todaro et al.^{44,50} reported on the presence of different types of Cu sites in $[\text{Cu}_3(\text{BTC})_2]$, formed by the activity of water in the air in the paddlewheels that yields Cu^{2+} and Cu^+ centres. These authors showed how the typical antiferromagnetic coupling arising from the overlapping wavefunctions of both d^9 cations in $\text{Cu}_2(\text{OR})_4$ carboxylate paddlewheel dimers with $S = \frac{1}{2}$ is not kept when one of the cations is reduced to Cu^+ . As it is the case for the DR UV-Vis-NIR spectroscopy measurements, the HKUST-1 frameworks with revealed a higher amount of Cu^+ with increasing amount of the defective CYDC linker, confirming the trends we have observed (see Figure 5.12 and Table 5.5). This can be seen in the less-defined lines corresponding to the hyperfine quadruplet ($S = \frac{1}{2}$) in g_{\parallel} , as well as the for increasing %mol loadings of the CYDC linker. It is interesting to highlight that the highest concentration of Cu^+ appears to be in the case of 50 %mol loading of CYDC, rather than when the most CYDC is present. This may be ascribed to the

formation of a $[\text{Cu}_x(\text{CYDC})_y]$ coordination polymer or extra-framework Cu^{2+} cations when higher concentrations of defect-linker are used, rather than co-crystallizing in the MOF lattice as defects. Another reason is that one should be careful in using this characterization method in a too quantitative manner as other materials and instrumentation effects can play a role in the overall quantification of both Cu^{2+} and Cu^{2+} cations in the $[\text{Cu}_3(\text{BTC})_{2-x}(\text{CYDC})_x]$ crystals.

Table 5.5. Values of the Hamiltonian parameters in Gauss and g -factor for defect-engineered $[\text{Cu}_3(\text{BTC})_{2-x}(\text{CYDC})_x]$ powders with increasing concentration of CYDC as determined by Continuous Wave (CW) Electron Paramagnetic Resonance (EPR), as measured at 100 K and recorded in X-band.

CYDC (% mol)	B_0 (G)	ΔB_{pp} (G)	g_{\parallel}	g^{\perp}
10	3260.9	105.6	2.35	2.070
30	3255.1	146.7	2.39	2.066
50	3243.4	240.5	2.38	2.070
70	3259.2	164.6	2.38	2.074

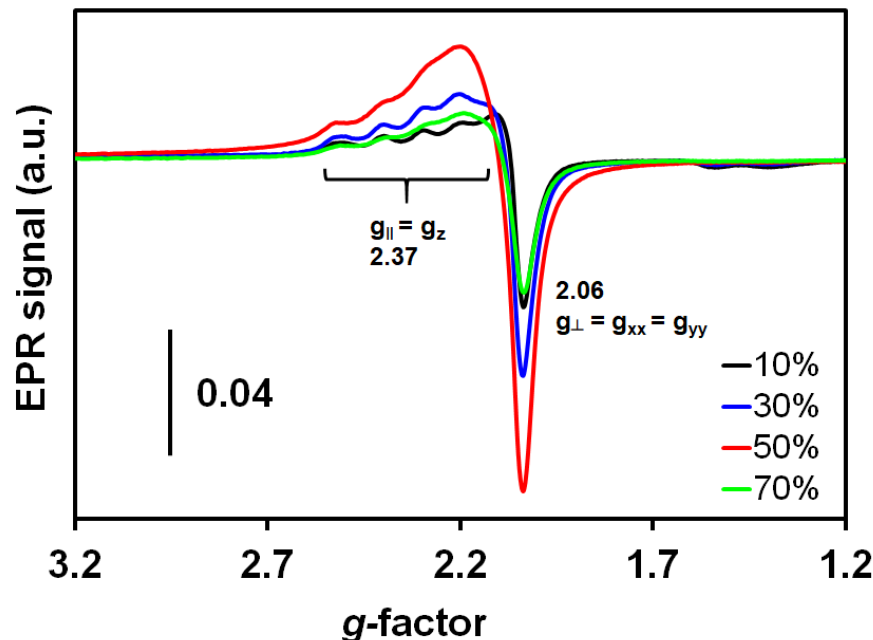


Figure 5.13. Continuous Wave (CW) Electron Paramagnetic Resonance (EPR) spectra of the defect-engineered $[\text{Cu}_3(\text{BTC})_{2-x}(\text{CYDC})_x]$ powders with increasing concentration of CYDC: 10 %mol (black), 30 %mol (blue), 50 %mol (red) and 70 %mol (green). Full-width sweep showing the hyperfine coupling lines of Cu^{2+} with $S = \frac{1}{2}$ and its nuclear spin $I_{\text{Cu}} = \frac{3}{2}$ gets diluted as the concentration of CYDC increases.

In order to better understand the properties of the Cu⁺²⁺ sites as Lewis acids in the defect-engineered [Cu₃(BTC)_{2-x}(CYDC)_x] powders, we made use of pyridine (Py) as a molecular probe in combination with FT-IR spectroscopy.

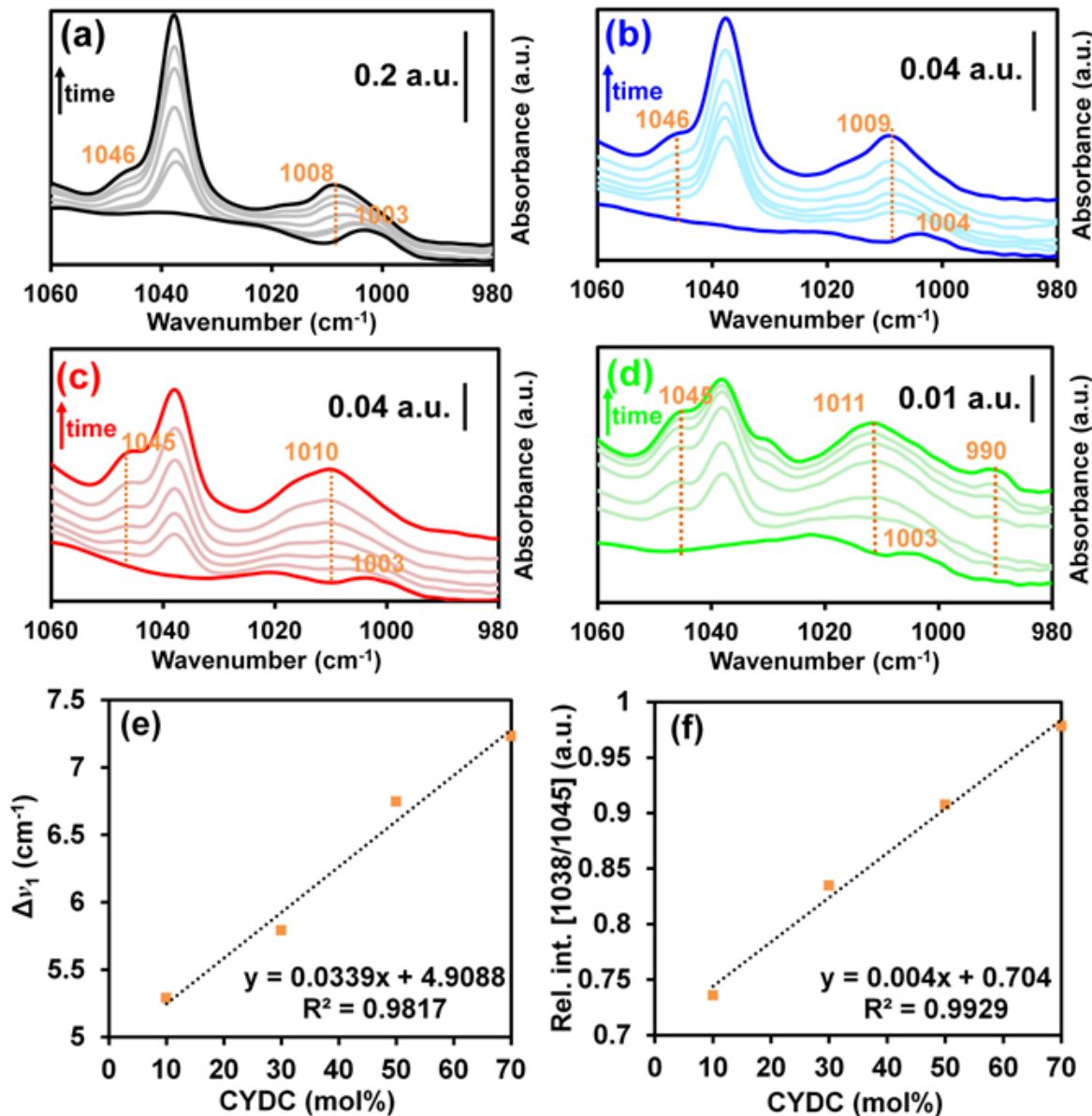


Figure 5.14. Pyridine (Py)-probe FT-IR spectra of the defect-engineered [Cu₃(BTC)_{2-x}(CYDC)_x] powders with increasing concentration of CYDC: (a) 10, (b) 30, (c) 50 and (d) 70 mol% CYDC showing the FT-IR bands corresponding to the ν_{12} and ν_1 (~1038 and ~1008 cm⁻¹) asymmetrical ring stretching modes. (e) Evolution of the shift of the ν_1 mode (band at ~1008 cm⁻¹) with increasing CYDC-concentration. (f) Increase of the relative intensity of the shoulder at ~1046 cm⁻¹ with increasing CYDC-concentration.

The results are summarized in Figure 5.14. It can be seen that in addition to the ν_{12} vibrational mode of Py adsorbed onto the Lewis Cu²⁺ sites at 1038 cm⁻¹,⁵¹ a shoulder at

around 1046 cm^{-1} , assigned to the interaction of the σ -donating N pair of Py with the defect Cu^+ sites,⁵² in contrast to previous reports,⁵³ appeared. The intensity of this shoulder gradually increased with increasing concentration of the defective CYDC linker in the lattice, further corroborating our hypothesis. Pyridine-probe FT-IR spectroscopy has been previously used for the characterization of the acid and redox metal sites in MOF materials.⁵⁴⁻⁵⁶ However, up to now and to the best of our knowledge, no characterization studies have been carried out with defective HKUST-1 systems, in which redox-active $\text{Cu}^{2+}/\text{Cu}^+$ sites are also present. In line with what has been previously reported for MIL-100(Fe) systems, in which $\text{Fe}^{2+}/\text{Fe}^{3+}$ sites were present, after contacting the MOF with 10 mbar of pyridine vapor, a series of FT-IR bands in the $1060\text{-}980\text{ cm}^{-1}$ region develop over a period of 2 h. In every case, a band appeared at $\sim 1037\text{ cm}^{-1}$, corresponding to the ν_{12} complex ring bending,⁵¹ and evolved by steadily increasing over the first 60 min, reaching a plateau thereafter (Figure 5.15).

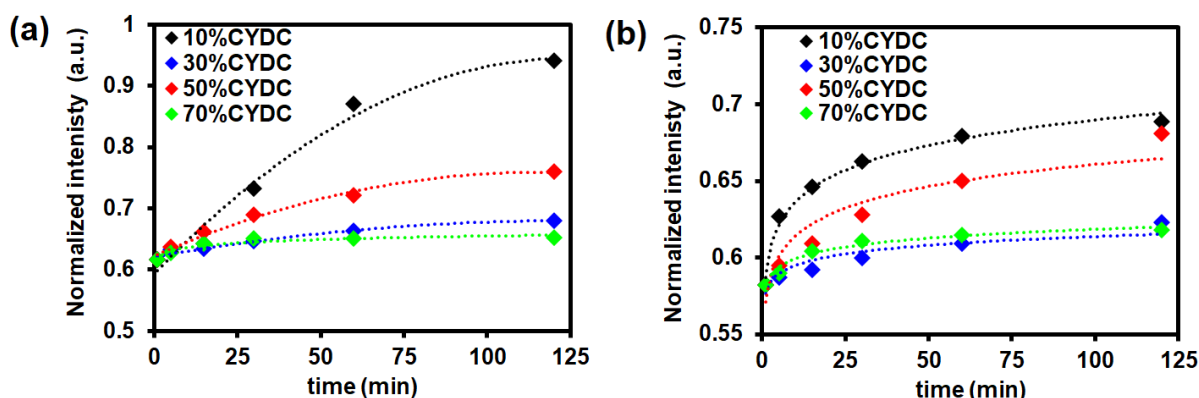


Figure 5.15. Evolution of the normalized intensity of the FT-IR bands at (a) 1037 and (b) 1008 cm^{-1} over 2 h time at constant pyridine pressure during adsorption onto defect-engineered $[\text{Cu}_3(\text{BTC})_{2-x}(\text{CYDC})_x]$ powders with increasing concentration of CYDC. The lines are included as eye-guides.

This suggests that most of Cu available sites readily interact with pyridine gas after 1 h, which can be approximated to a Langmuir model of the form:



$$\theta_A = \frac{V}{V_m} = \frac{K_{eq}^{Py} \cdot p_{Py}}{1 + K_{eq}^{Py} \cdot p_{Py}} \quad (\text{Equation 5.4})$$

, where θ_A is the fraction of occupied sites, V_m is the volume of a monolayer on the surface, K_{eq}^{Py} is the equilibrium constant for the adsorption of pyridine on a surface site, and p_{Py} is the pyridine pressure. This finding is surprising, given the pore structure, surface heterogeneity and polar nature (thus, lateral interactions and non-ideality) of HKUST-1 and pyridine; which renders this system far from ideal. Note that typically the occupancy is a function of pressure rather than time. However, if a constant pressure and temperature condition is defined according to the kinetic theory describing Brownian motion by Smoluchowski and Einstein, it can be related to the number density of the gas. This is in term, related a flow through an area element dA , which depends on the velocity of the Brownian gas particles (Knudsen diffusion inside the pores). We can then define the effusive flow $\Phi_{effusion}$ through the porous volume with Equation 5.5:

$$\Phi_{effusion} = \frac{P \cdot A}{\sqrt{2\pi m k_B T}} \quad (\text{Equation 5.5})$$

this finding is further corroborated by evaluation the intensity evolution of other FT-IR bands, such as the one at $\sim 1008 \text{ cm}^{-1}$, corresponding to the ν_1 mode of pyridine bonded to dehydrated Cu^{2+} centers, which follow the same trend, as shown in Figure 5.13. Interestingly, this FT-IR band is slightly shifted with increasing concentration of CYDC, showing a maximum at 1008 and 1011 cm^{-1} for the 10 and 70 mol% defect-engineered $[\text{Cu}_3(\text{BTC})_{2-x}(\text{CYDC})_x]$ materials, respectively. Moreover, a shoulder at $\sim 1014 \text{ cm}^{-1}$ develops for the 50 and 70 mol% CYDC-containing crystals. This has been previously ascribed to the interaction of pyridine with reduced $\text{Fe}^{2+}/\text{Fe}^{3+}$ for MIL-100(Fe) systems.⁵⁶ Simultaneously, a shoulder next to the ν_{12} band, at $\sim 1045 \text{ cm}^{-1}$ develops over time for every sample, and its relative intensity (compared to the FT-IR band at 1037 cm^{-1}) increases with increasing amount of CYDC in the defect-engineered $[\text{Cu}_3(\text{BTC})_{2-x}(\text{CYDC})_x]$ powders. Fischer *et al.* demonstrated by means of CO-probed FT-IR spectroscopy and X-ray Photoelectron Spectroscopy (XPS) (see also Chapter 1), that a higher amount of reduced Cu^+ sites is present with increasing CYDC concentrations.¹² Thus, this shoulder can be correlated with pyridine interacting with the less acidic Cu^+ sites, since the ring bending appears at higher energy. This result stems from a weaker N-Cu⁺ interaction (less σ -donation than for Cu²⁺) which allows for higher energetic flexing of the C-C and C-H bonds. In the case of the 70 mol% CYDC-containing material, two additional spectral features, a shoulder at ~ 1031

cm^{-1} and a band at $\sim 990 \text{ cm}^{-1}$, appear after 60 min of exposure to pyridine gas. These FT-IR bands correspond to non-coordinated pyridine gas (to the ν_1 and ν_{12} modes, respectively),⁵¹ indicating that all the Cu^{x+} sites are saturated with pyridine.

To compare the behavior of the defective $\text{Cu}^{+/2+}$ sites towards other reactive probes than pyridine, FT-IR spectroscopy was used in combination with NO as a molecular probe. The results of these experiments are summarized in Figure 5.16 and Figure 5.17 for the parent $[\text{Cu}_3(\text{BTC})_2]$ and defect-engineered $[\text{Cu}_3(\text{BTC})_{1.0}(\text{CYDC})_{1.0}]$ powders, respectively. It can be seen that for both materials two large sets of FT-IR bands at $\sim 1720\text{-}1800$ and $\sim 1840\text{-}1920 \text{ cm}^{-1}$ develop with increasing NO pressures.

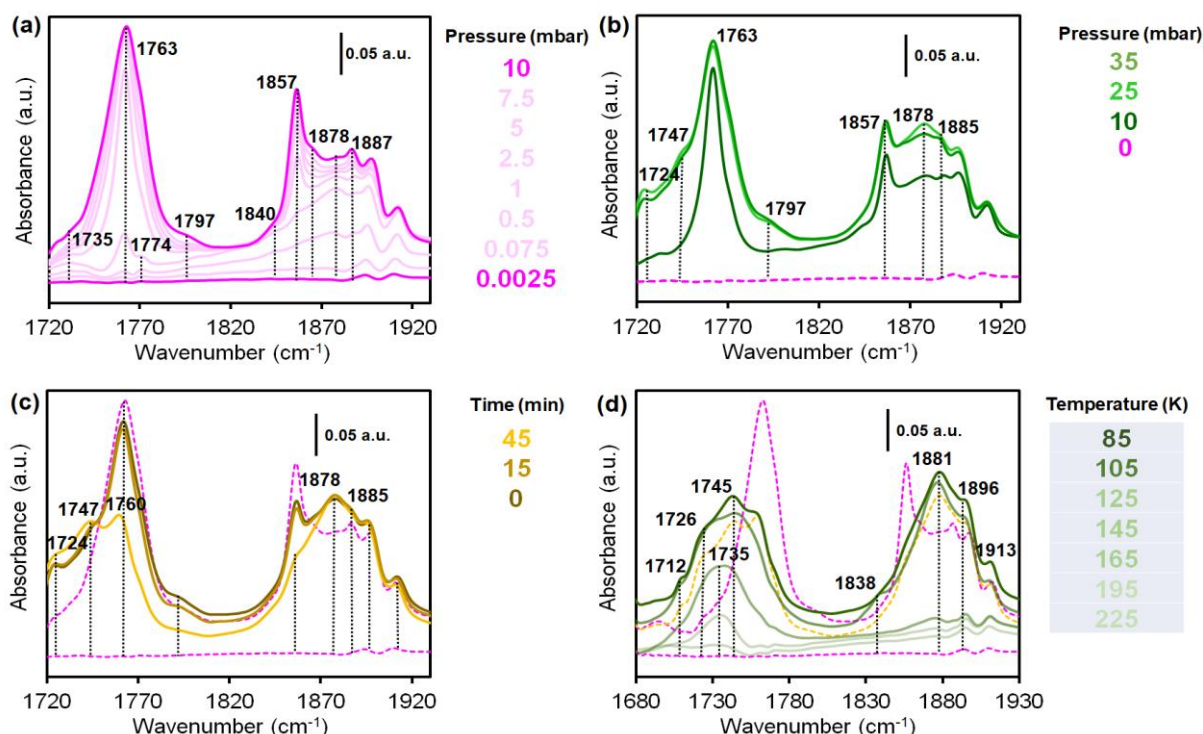


Figure 5.16. FT-IR spectra of the parent $[\text{Cu}_3(\text{BTC})_2]$ material: (a) after dosing NO pressures at 85 K; (b) at high NO pressures, up to 35 mbar (dashed line represents clean cell); (c) desorption of NO at constant temperature at $p < 10^{-5}$ mbar over time; and (d) increasing temperature (dashed pink lines correspond to the previous spectra recorded at 0 and 10 mbar). The pellet was activated under $p < 10^{-5}$ mbar, at 298 K for 24 h and further at 423 K ($5 \text{ K}\cdot\text{min}^{-1}$) for 5 min (to avoid heat induced reduction).

This is in contrast with previous reports, in which only one strong band is observed, although different evacuation procedures have been used.⁴² However, the FT-IR spectra

similar to those described here have been previously observed for Cu-exchanged zeolites.⁵⁸ Furthermore, a very intense, broad band centered at 1763 cm⁻¹, ascribed to Cu⁺···(NO)₂ dimers formed at low temperature and that becomes more intense at $p_{NO} > 1$ mbar, appears, and shows a similar behavior as the one at 1857 cm⁻¹, is observed. A low intensity band at 1774 cm⁻¹ may correspond to either the *trans*-isomers of Cu⁺···(NO)₂ species, or to (NO)Cu⁺(NO) species.⁵⁹

Despite its high intensity, suggesting a large number of Cu⁺ sites, it has been reported the high molar extinction coefficient of adsorbates interacting with Cu⁺ sites.⁶⁰ A small at 1735 cm⁻¹ appears at low pressures, as well as one shoulder at 1797 cm⁻¹. These bands are assigned to different reduced Cu⁺ species with a slightly different chemical nature to that of the paddlewheel metal atoms, *e.g.* defects, extra-framework Cu cations. On the other hand, the band at 1882-1887 cm⁻¹ has been previously assigned to Cu²⁺···NO species, remaining strongly adsorbed after desorption over time and decreasing in intensity only at T > 200 K. An overlapping FT-IR band at 1787 cm⁻¹, which shows a very similar behavior, is assigned to slightly different Cu²⁺ sites. It has been previously reported that up to ~ 40 % of Cu can be reduced,⁶¹ due to the presence of different types of paddlewheel (Cu²⁺/Cu⁺ or Cu²⁺/Cu²⁺) units, and might explain the presence of this band. Two small spectral features at ~ 1896 and ~ 1913 cm⁻¹ are present before the introduction of NO, and have been previously assigned to combination bands of the aromatic backbone.^{42, 62} As seen in the FT-IR spectra, the presence of NO strongly enhances the absorbance of those bands, indicating an interaction not only with the metal sites, but also with the organic linkers.

In contrast to Figure 5.16 for the parent [Cu₃(BTC)₂] material, Figure 5.17a-c shows that, although a similar profile with two sets of FT-IR bands is observed for the [Cu₃(BTC)_{1.0}(CYDC)_{1.0}] material, several differences are evident. First, the material activated under similar conditions to the parent material (vacuum at 298 K for 16 h, then 5 min at 423 K), showed that the FT-IR band corresponding to the $\nu_{as}(N-O)$ mode of the Cu⁺···(NO)₂ dimer, is red-shifted of 17 cm⁻¹. This is not observed for the symmetric mode $\nu_s(N-O)$, which appears at 1857 cm⁻¹, as for the parent material. Moreover, the shape of the band

looks rather asymmetric, suggesting that another band of less intensity at *ca.* 1758 cm⁻¹, corresponding to Cu⁺…NO adsorbates in different types of Cu, may be overlapping.

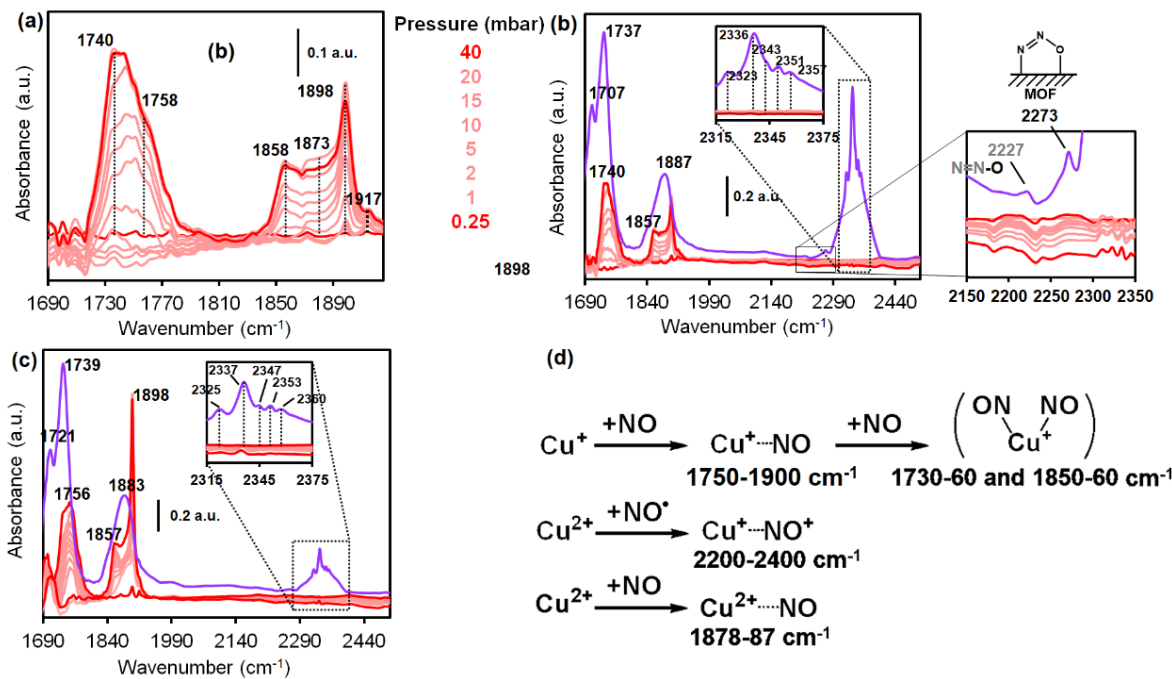


Figure 5.17. FT-IR spectra of the [Cu₃(BTC)_{1.0}(CYDC)_{1.0}] material at 85 K. (a) Dosing of NO stepwise to the equilibrium pressures noted. (b) Saturation of the cell with NO after 5 min. (c) Identical pressures and experiments with a heating pretreatment of 16 h. *For (a) and (b), the pellet was activated under $p < 10^{-5}$ mbar, at 298 K for 24 h and further at 423 K ($5\text{ K}\cdot\text{min}^{-1}$) for 5 min (to avoid heat induced reduction). For (c), the second treatment was carried out for 16 h instead of 5 min. (d) Scheme of the adsorption of NO onto the metal Cu sites onto Cu sites.⁶³

At 1898 and 1917 cm⁻¹, the FT-IR bands corresponding to the framework are strongly affected by NO dosing, specifically the former one. The intensity of this band is much higher after the longer thermal pretreatment, indicating that the activation procedure affects not only the metal CUS sites, but also the organic backbone. At higher energies, *ca.* 2200-2400 cm⁻¹, a set of bands, that are typically assigned to N₂, NO₂, N₂O are visible, indicating that similar pretreatments affect the fraction of reduced Cu⁺ sites, as well as their reactivity in a different manner. This clearly shows that depending on the pretreatment, the intensity of the different surface N_xO_y species that are formed varies. Although the spectral profile is similar, the maximum of the band corresponding to Cu⁺…NO adducts are slightly blue-shifted from ~ 1740 to ~ 1756 cm⁻¹ suggesting that the

species present after pretreatment for 5 min are dissimilar to those formed after 16 h of heating at 423 K.

5.3.4. Raman Imaging of the Spatial Distribution of Defects

As earlier mentioned in this Chapter, the distribution of defective linkers in Defect-Engineered Metal-Organic Frameworks (DEMOFs) remains elusive, mainly due to the lack of spatially resolved characterization studies.⁶⁴⁻⁶⁷ In order to study the spatial distribution of the defective CYDC linker throughout the HKUST-1 lattice, a set of $[\text{Cu}_3(\text{BTC})_2]$ and $[\text{Cu}_3(\text{BTC})_{2-x}(\text{CYDC})_x]$ crystals was deposited on a glass cover and chemical mapping by means of Raman micro-spectroscopy was carried out.

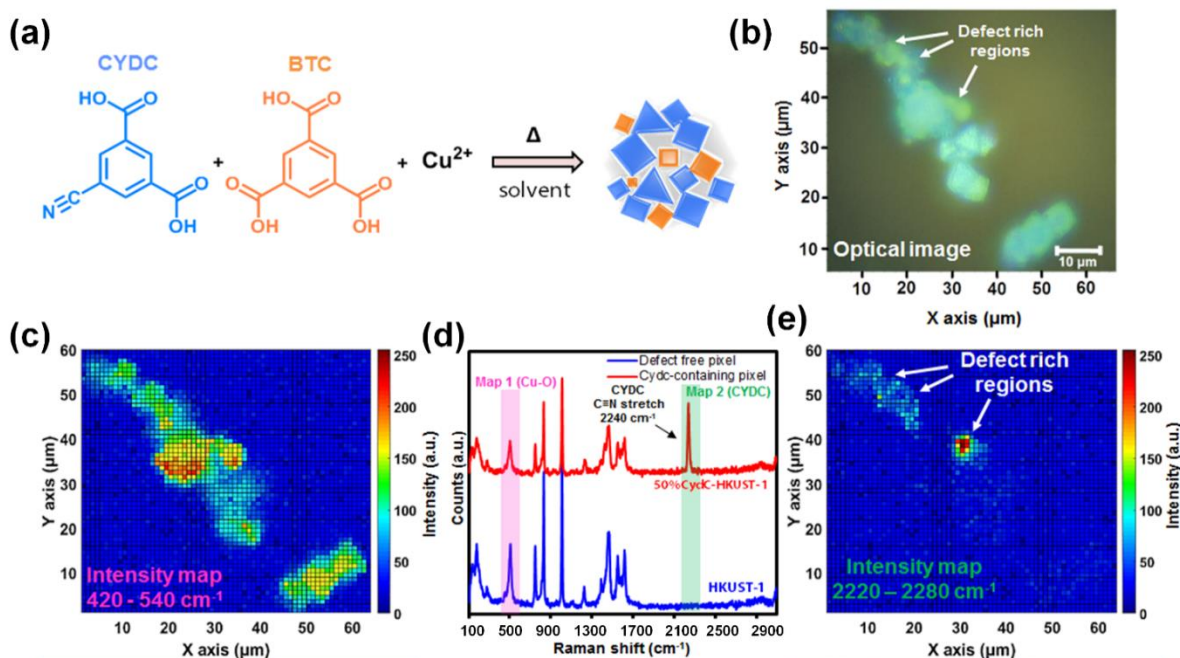


Figure 5.18. (a) Schematic of the obtained crystals when mixing CYDC and BTC for the crystallization of defect-engineered $[\text{Cu}_3(\text{BTC})_2]$. (b) The optical image shows a randomly selected group of crystals; below, the maps corresponding to the (c) signal-to-baseline of the $\nu_{(\text{Cu}-\text{O})}$ stretching at 505 cm^{-1} (present in any HKUST-1 crystal) and the areas where (e) the $\nu_{(\text{C}\equiv\text{N})}$ stretch at 2240 cm^{-1} (only in areas containing CYDC linker) is detected, corresponding to partially defective crystals. (d) Raman spectra of exemplary pixels with no linker present (blue spectrum) and with CYDC defect linkers (red spectrum).

Given the fact that this microscopy method is a local technique and restricted to only small amounts of crystals per scan, extensive areas (ca. $60 \times 60 \mu\text{m}$) containing large sets of multiple crystals had to be visualized. Figure 5.18 shows two sets of exemplary Raman spectra recorded for: i) a pixel in which the bands corresponding to the stretching mode

of the C≡N bond at ~ 2241 cm⁻¹, thus, the defective-linker (green) is visible; and ii) a pixel in which this Raman band is not present (orange), and only the Raman bands, associated to the parent Cu₃(BTC)₂ crystal composition, are observable.

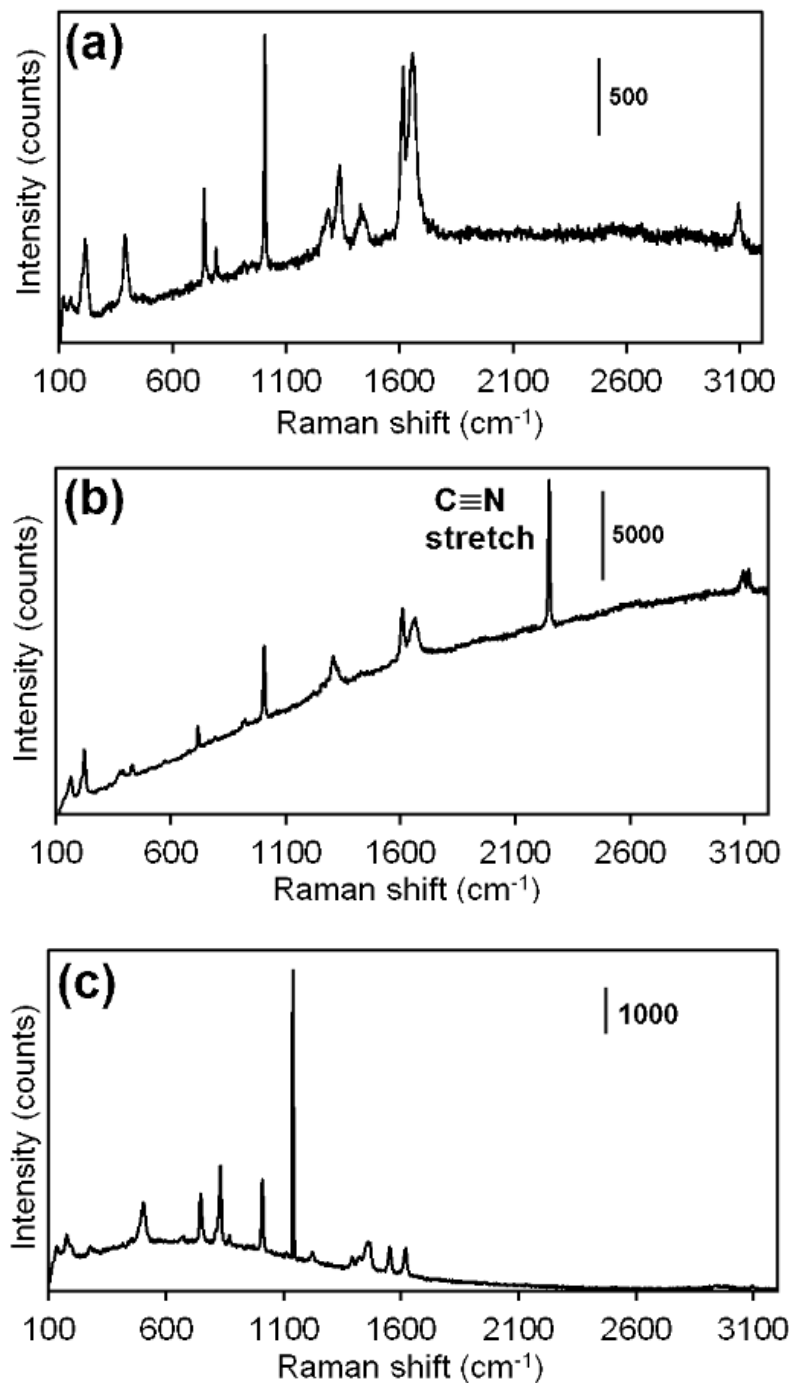


Figure 5.19. Raman spectra of the pure linker compounds: (a) trimesic acid (BTC), (b) 5-cyano-1,3-benzenedicarboxylic acid (CYDC) and (c) parent Cu₃BTC₂. Note the Raman peak at ~ 2247 cm⁻¹ corresponding to the C≡N stretch of the CYDC linker in spectrum (b).

The Raman $\nu(\text{C}\equiv\text{N})$ band was observed at $\sim 2247 \text{ cm}^{-1}$ (Figure 5.19) in pure CYDC, which means a red shift of $\Delta\nu$ of 6 cm^{-1} compared to the CYDC embedded in the MOF lattice. This may be ascribed to partial donation of the N atom in the $-\text{C}\equiv\text{N}$ group to the Cu cations in the paddlewheel, or to the vibrational restrictions imposed by the lattice itself.

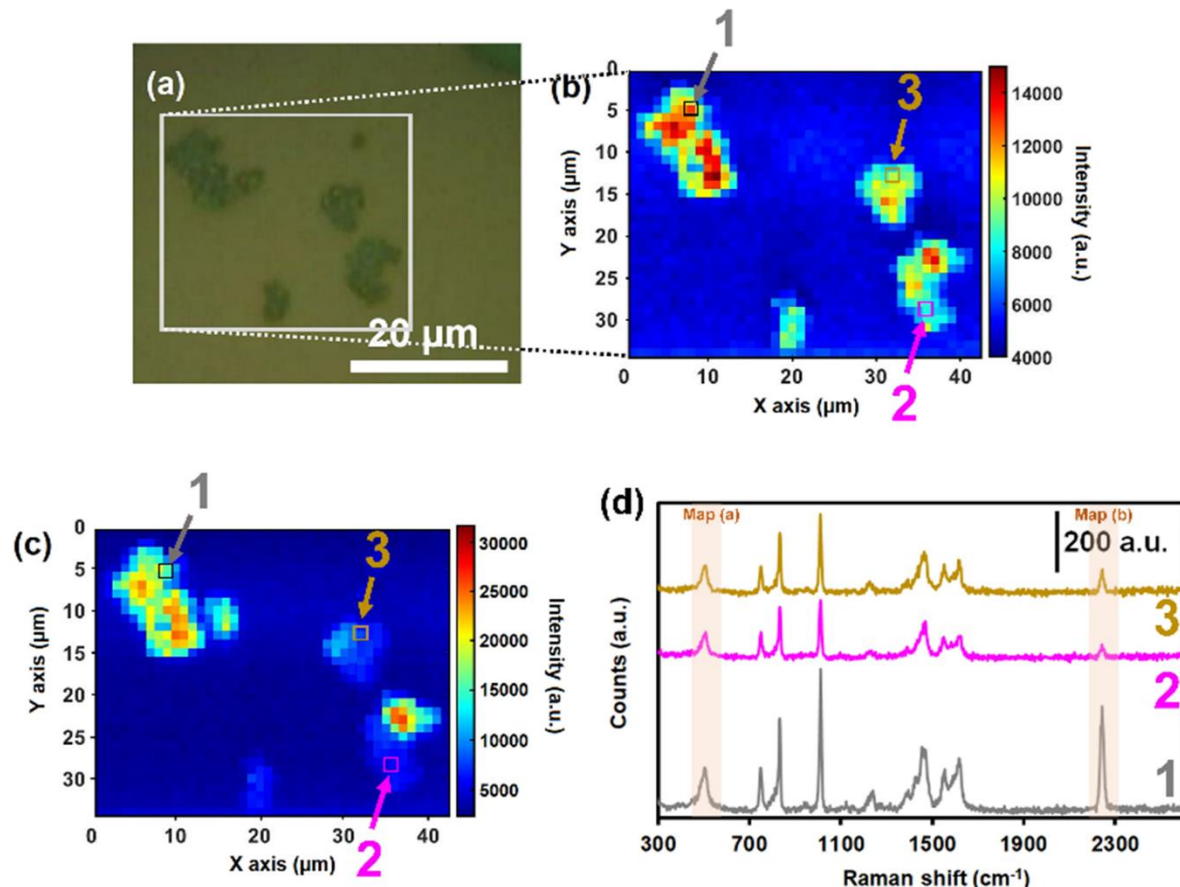


Figure 5.20. (a) Optical image of $[\text{Cu}_3(\text{BTC})_{1.0}(\text{CYDC})_{1.0}]$ crystals with the corresponding Raman maps of the (b) $480\text{-}520 \text{ cm}^{-1}$ and the (c) $2220\text{-}2260 \text{ cm}^{-1}$ spectral regions. (d) Raman spectra of selected, exemplary pixels in (b) and (c) showing different contents of the defective CYDC linker and Cu_3BTC_2 material. Note that the different areas show low intensity $\nu_{(\text{C}\equiv\text{N})}$ stretching mode at 2240 cm^{-1} corresponding to heterogeneous distribution on the defect CYDC linker. The intensity of the maps corresponds to normalized signal-to-baseline.

However, the nature of the defects themselves (*e.g.* defective paddlewheels and mesopores) within the lattice is still under debate,³⁷ rendering their study a complicated task. Representative signal-to-baseline ratio maps of the region corresponding to the $\nu_{(\text{Cu}-\text{O})}$ stretching mode at 505 cm^{-1} (Figure 5.20c, map 1), and that of the stretching mode of the $\nu_{(\text{C}\equiv\text{N})}$ band at $\sim 2241 \text{ cm}^{-1}$ of the CYDC linker (Fig. 5.20e, map 2) were obtained.

Raman spectral maps of $[Cu_3(BTC)_{0.6}(CYDC)_{1.4}]$ exhibited a similar phenomenon, with a higher number of pixels where the Raman $\nu_{(C\equiv N)}$ band was observable (Figure 5.20). Three locations have been selected to showcase the differences observed in the Raman spectra. Pixel 1 (grey colour) shows a high intensity of both the fingerprint Raman bands, corresponding to $[Cu_3(BTC)_2]$,⁶⁸ and the Raman $\nu_{(C\equiv N)}$ band. The count ratio of the $\nu_{(C\equiv N)}$ to the $\nu_{(Cu-O)}$ stretch bands was $I_{C\equiv N}/I_{Cu-O} = 1.66$ for the Raman spectrum measured in pixel 1, indicating the presence of a large amount of C≡N bonds, and thus, of the defective CYDC linker. In contrast, this ratio was $I_{C\equiv N}/I_{Cu-O} = 0.75$ and 0.99 for the spectra collected in pixels 2 and 3, respectively. It is worth mentioning that the differences in Raman intensity may appear when using a laser, given that the probed objects might be at different focal z planes. Moreover, spherical aberration and scattered light vary as a function of the depth to which the incident beam is focused. For the experimental configuration employed here, Everall has described how these phenomena become relevant only at probing distances $d \geq 3 - 5 \mu m$,⁶⁹⁻⁷¹ which are larger than the average size of the crystals measured in this work, and suggesting that the differences in Raman intensity are not associated to spectral artefacts. The Raman maps of the $[Cu_3(BTC)_{2-x}(CYDC)_x]$ crystals with a lower concentration of the defective CYDC linker (*i.e.*, 30 %mol in the initial mixture) were collected to evaluate if there is any effect of this parameter. As seen in Figure 5.19, a set of crystals of the $[Cu_3(BTC)_{1.4}(CYDC)_{0.6}]$ crystals deposited on a glass cover was mapped and the signal-to-baseline maps of the $480-520 \text{ cm}^{-1}$ (Figure 5.21b) and the $2220-2260 \text{ cm}^{-1}$ (Figure 5.21c) plotted. Surprisingly, no signs of defect linker could be observed in this material, although theoretically 30% of the pixels containing crystal material should exhibit at least partially the band at 2240 cm^{-1} of the C≡N stretch. It is worth mentioning that larger sets of crystals were mapped in addition to those in Figure 5.21 (not shown here for brevity) but giving similar results. One possibility might be a higher degree of dispersion of the defect linker at lower concentrations; preventing us from effectively detecting them at lower concentrations. Alternatively, we therefore ascribe this absence of defects to the fact that Raman micro-spectroscopy is a local technique, and the probability of mapping defects depends on selecting the appropriate crystals. It further corroborates the hypothesis of a heterogeneous distribution of the CYDC linker throughout the defect-engineered HKUST-1 crystals.

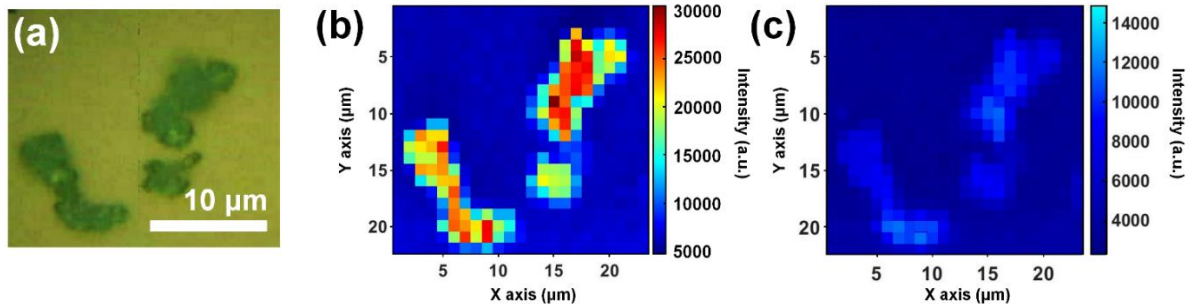


Figure 5.21. (a) Optical image of $[\text{Cu}_3(\text{BTC})_{1.4}(\text{CYDC})_{0.6}]$ crystals with the corresponding signal-to-baseline Raman maps of the (b) $480\text{-}520\text{ cm}^{-1}$ and the (c) $2220\text{-}2260\text{ cm}^{-1}$ spectral regions. (d) Raman spectra of selected, exemplary pixels in (b) and (c) showing different contents of CYDC linker and Cu_3BTC_2 material. Note that the different areas show low intensity $\nu_{(\text{C}\equiv\text{N})}$ stretching mode at 2240 cm^{-1} corresponding to heterogeneous distribution on the defect linker. Intensity of the maps corresponds to normalized signal-to-baseline. Note that the colour intensity bar has been adjusted so that similar colour shades match for both maps.

5.4 CONCLUSIONS

In this Chapter we have studied the spatial distribution of two different non-defective and defective linkers, namely 1,3,5-benzenetricarboxylate (BTC) and 5-cyano-1,3-benzenedicarboxylate (CYDC), respectively, in different Metal-Organic Frameworks (MOFs) crystals of the HKUST-1 topology. We could show that the defective linkers (CYDC), heterogeneously disperse throughout the $[\text{Cu}_3(\text{BTC})_{2-x}(\text{CYDC})_x]$ MOF crystals and aggregate in relatively small clusters rich in defective linkers. These small clusters result in the formation of mesopores that are also heterogeneous in size and geometry, as demonstrated by the SAXS profile of the materials. Furthermore, the introduction of these defective linkers results in a decrease of the crystallite size in a quantitative manner; due to different supersaturation regimes during the crystallization process (according to LaMer's theory).

Additionally, we have demonstrated the presence of a higher fraction of Cu^+ sites within the pores. These sites have different reactivities towards molecular probes, such as NO. Further experiments with pyridine as probe may lead to differentiating between the defect Cu sites on the outer surface and those within the pores of the crystals. Our work highlights the importance of using a wide variety of advanced characterization tools, such as vibrational spectroscopy (Raman micro-spectroscopy and FT-IR spectroscopy with

probe molecules), electronic spectroscopy (DRS UV-vis-NIR spectroscopy), magnetic resonance spectroscopy (EPR), X-ray scattering and diffraction (SAXS, WAXS, XRD) and electron microscopy (SEM) for understanding the underlying chemistry of complex, multi-component porous materials, including MOF materials and therefore provides guidelines for the improved design of defect-engineered frameworks. This may have a profound impact on the catalytic or gas sorption properties of these materials, by enhancing mass transport properties towards the pores and metal active sites.

5.5 REFERENCES

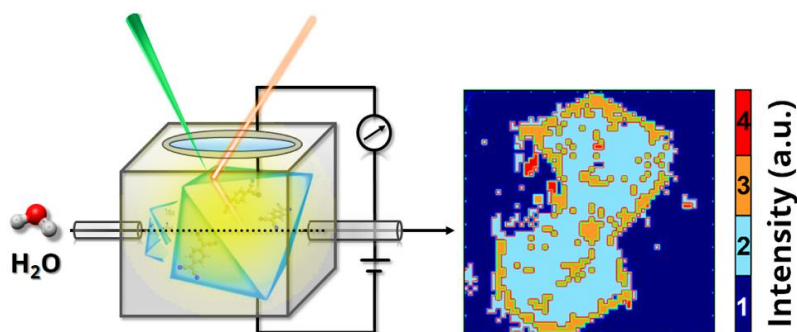
1. H. Deng, C. J. Doonan, H. Furukawa, R. B. Ferreira, J. Towne, C. B. Knobler, B. Wang and O. M. Yaghi, *Science*, 2010, **327**, 846-850.
2. M. Lammert, S. Bernt, F. Vermoortele, D. E. De Vos and N. Stock, *Inorg. Chem.*, 2013, **52**, 8521-8528.
3. J. Jiang and O. M. Yaghi, *Chem. Rev.*, 2015, **115**, 6966-6997.
4. H. Furukawa, U. Müller and O. M. Yaghi, *Angew. Chem. Int. Ed.*, 2015, **54**, 3417-3430.
5. K. M. Choi, H. J. Jeon, J. K. Kang and O. M. Yaghi, *J. Am. Chem. Soc.*, 2011, **133**, 11920-11923.
6. Z. Fang, B. Bueken, D. E. De Vos and R. A. Fischer, *Angew. Chem. Int. Ed.*, 2015, **54**, 7234-7254.
7. S. Marx, W. Kleist and A. Baiker, *J. Catal.*, 2011, **281**, 76-87.
8. N. Stock and S. Biswas, *Chem. Rev.*, 2012, **112**, 933-969.
9. I. Agirrezabal-Telleria, I. Luz, M. A. Ortuño, M. Oregui-Bengoechea, I. Gandarias, N. López, M. A. Lail and M. Soukri, *Nat. Commun.*, 2019, **10**, 2076.
10. W. Zhang, M. Kauer, O. Halbherr, K. Epp, P. Guo, M. I. Gonzalez, D. J. Xiao, C. Wiktor, F. X. Liabrés i Xamena, C. Wöll, Y. Wang, M. Muhler and R. A. Fischer, *Chem. Eur. J.* 2016, **22**, 14297-14307.
11. H. Noei, O. Kozachuk, S. Amirjalayer, S. Bureekaew, M. Kauer, R. Schmid, B. Marler, M. Muhler, R. A. Fischer and Y. Wang, *J. Phys. Chem. C*, 2013, **117**, 5658-5666.
12. Z. Fang, J. P. Dürholt, M. Kauer, W. Zhang, C. Lochenie, B. Jee, B. Albada, N. Metzler-Nolte, A. Pöppl, B. Weber, M. Muhler, Y. Wang, R. Schmid and R. A. Fischer, *J. Am. Chem. Soc.*, 2014, **136**, 9627-9636.
13. O. Kozachuk, I. Luz, F. X. Llabrés i Xamena, H. Noei, M. Kauer, H. B. Albada, E. D. Bloch, B. Marler, Y. Wang, M. Muhler and R. A. Fischer, *Angew. Chem. Int. Ed.*, 2014, **53**, 7058-7062.
14. X. Kong, H. Deng, F. Yan, J. Kim, J. A. Swisher, B. Smit, O. M. Yaghi and J. A. Reimer, *Science*, 2013, **341**, 882-885.
15. A. M. Katzenmeyer, J. Canivet, G. Holland, D. Farrusseng and A. Centrone, *Angew. Chem. Int. Ed.*, 2014, **53**, 2852-2856.
16. W. Schrimpf, J. Jiang, Z. Ji, P. Hirschle, D. C. Lamb, O. M. Yaghi and S. Wuttke, *Nat. Commun.*, 2018, **9**, 1647.
17. L. Liu, Z. Chen, J. Wang, D. Zhang, Y. Zhu, S. Ling, K.-W. Huang, Y. Belmabkhout, K. Adil, Y. Zhang, B. Slater, M. Eddaudi and Y. Han, *Nat. Chem.*, 2019, **11**, 622-628.
18. M. G. O'Brien, A. M. Beale and B. M. Weckhuysen, *Chem. Soc. Rev.*, 2010, **39**, 4767-4782.
19. B. M. Weckhuysen, *Chem. Soc. Rev.*, 2010, **39**, 4557-4559.
20. Y. Liu, F. Meirer, P. A. Williams, J. Wang, J. C. Andrews and P. Pianetta, *J. Synchrotron Rad.*, 2012, **19**, 281-287.
21. K. Omura and D. Swern, *Tetrahedron*, 1978, **34**, 1651-1660.
22. A. Umemura, S. Diring, S. Furukawa, H. Uehara, T. Tsuruoka and S. Kitagawa, *J. Am. Chem. Soc.*, 2011, **133**, 15506-15513.
23. M. J. Van Vleet, T. Weng, X. Li and J. R. Schmidt, *Chem. Rev.*, 2018, **118**, 3681-3721.
24. Q. Liu, J.-M. Yang, L.-N. Jin and W.-Y. Sun, *CrystEngComm*, 2016, **18**, 4127-4132.
25. Q. Liu, J.-M. Yang, L.-N. Jin and W.-Y. Sun, *Chem. Eur. J.*, 2014, **20**, 14783-14789.
26. Q. Liu, L.-N. Jin and W.-Y. Sun, *Chem. Commun.*, 2012, **48**, 8814-8816.
27. S. Diring, S. Furukawa, Y. Takashima, T. Tsuruoka and S. Kitagawa, *Chem. Mater.*, 2010, **22**, 4531-4538.
28. F. Wang, H. Guo, Y. Chai, Y. Li and C. Liu, *Micropor. Mesopor. Mater.*, 2013, **173**, 181-188.

-
29. M. R. Armstrong, S. Senthilnathan, C. J. Balzer, B. Shan, L. Chen and B. Mu, *Ultra. Sonochem.*, 2017, **34**, 365-370.
30. M. P. Attfield and P. Cubillas, *Dalton Trans.*, 2012, **41**, 3869-3878.
31. J. D. Hancock and J. H. Sharp, *J. Am. Ceram. Soc.*, 1972, **55**, 74-77.
32. D. Zacher, J. Liu, K. Huber and R. A. Fischer, *Chem. Commun.*, 2009, 1031-1033.
33. F. Millange, R. El Osta, M. E. Medina and R. I. Walton, *CrystEngComm*, 2011, **13**, 103-108.
34. J.-C. Lee, J.-O. Kim, H.-J. Lee, B. Shin and S. Park, *Chem. Mater.*, 2019, **31**, 7377-7385.
35. V. K. LaMer and R. H. Dinegar, *J. Am. Chem. Soc.*, 1950, **72**, 4847-4854.
36. X.-G. Wang, Q. Cheng, Y. Yu and X.-Z. Zhang, *Angew. Chem. Int. Ed.*, 2018, **57**, 7836-7840.
37. J. P. Dürholt, J. Keupp, Schmid and Rochus, *Eur. J. Inorg. Chem.*, 2016, **2016**, 4517-4523.
38. C.-S. Tsao, M.-S. Yu, T.-Y. Chung, H.-C. Wu, C.-Y. Wang, K.-S. Chang and H.-L. Chen, *J. Am. Chem. Soc.*, 2007, **129**, 15997-16004.
39. A. Guinier and G. Fournet, *Small angle scattering of X-rays*, John Wiley & Sons, Ltd, Hoboken, 1955.
40. S. Lowell, J. E. Shields, M. A. Thomas and M. Thommes, in *Characterization of Porous Solids and Powders: Surface Area, Pore Size and Density*, eds. S. Lowell, J. E. Shields, M. A. Thomas and M. Thommes, Springer, Dordrecht, 2004, 15-57.
41. G. Mahalakshmi and V. Balachandran, *Spectr. Acta: Mol. Biomol. Spect.*, 2014, **124**, 535-547.
42. J. Szanyi, M. Daturi, G. Clet, D. R. Baer and C. H. F. Peden, *Phys. Chem. Chem. Phys.*, 2012, **14**, 4383-4390.
43. L. Alaerts, E. Séguin, H. Poelman, F. Thibault-Starzyk, P. A. Jacobs and D. E. De Vos, *Chem. Eur. J.*, 2006, **12**, 7353-7363.
44. M. Todaro, L. Sciortino, F. M. Gelardi and G. Buscarino, *J. Phys. Chem. C*, 2017, **121**, 24853-24860.
45. V. L. Sushkevich, A. V. Smirnov and J. A. van Bokhoven, *J. Phys. Chem. C*, 2019, **123**, 9926-9934.
46. V. L. Sushkevich and J. A. van Bokhoven, *Chem. Commun.*, 2018, **54**, 7447-7450.
47. B. Jee, M. Hartmann and A. Pöppl, *Mol. Phys.*, 2013, **111**, 2950-2966.
48. F. Gul-E-Noor, M. Mendt, D. Michel, A. Pöppl, H. Krautscheid, J. Haase and M. Bertmer, *J. Phys. Chem. C*, 2013, **117**, 7703-7712.
49. A. Pöppl, S. Kunz, D. Himsl and M. Hartmann, *J. Phys. Chem. C*, 2008, **112**, 2678-2684.
50. M. Todaro, A. Alessi, L. Sciortino, S. Agnello, M. Cannas, F. M. Gelardi and G. Buscarino, *J. Spectr.*, 2016, 54 8074297.
51. K. N. Wong and S. D. Colson, *J. Mol. Spectrosc.*, 1984, **104**, 129-151.
52. D.-Y. Wu, B. Ren, Y.-X. Jiang, X. Xu and Z.-Q. Tian, *J. Phys. Chem. A*, 2002, **106**, 9042-9052.
53. E. Pérez-Mayoral, Z. Musilová, B. Gil, B. Marszalek, M. Položij, P. Nachtigall and J. Čejka, *Dalton Trans.*, 2012, **41**, 4036-4044.
54. C. Volkinger, H. Leclerc, J.-C. Lavalle, T. Loiseau, G. Férey, M. Daturi and A. Vimont, *J. Phys. Chem. C*, 2012, **116**, 5710-5719.
55. A. Dhakshinamoorthy, M. Alvaro, P. Horcajada, E. Gibson, M. Vishnuvarthan, A. Vimont, J.-M. Grenèche, C. Serre, M. Daturi and H. Garcia, *ACS Catal.*, 2012, **2**, 2060-2065.
56. H. Leclerc, A. Vimont, J.-C. Lavalle, M. Daturi, A. D. Wiersum, P. L. Llwendlyn, P. Horcajada, G. Ferey and C. Serre, *Phys. Chem. Chem. Phys.*, 2011, **13**, 11748-11756.
57. M. S. Holm, S. Svelle, F. Joensen, P. Beato, C. H. Christensen, S. Bordiga and M. Bjørgen, *Appl. Catal. A*, 2009, **356**, 23-30.
58. H. Kwak Ja, H. Lee Jong, D. Burton Sarah, S. Lipton Andrew, H. F. Peden Charles and J. Szanyi, *Angew. Chem. Int. Ed.*, 2013, **52**, 9985-9989.
59. K. I. Hadjiivanov, *Catal. Rev.*, 2000, **42**, 71-144.
60. K. I. Hadjiivanov and G. N. Vayssilov, in *Adv. Catal.*, Academic Press, 2002, **47**, 307-511.
61. P. St. Petkov, G. N. Vayssilov, J. Liu, O. Shekhah, Y. Wang, C. Wöll and T. Heine, *ChemPhysChem*, 2012, **13**, 2025-2029.
62. N. Drenchev, E. Ivanova, M. Mihaylov and K. Hadjiivanov, *Phys. Chem. Chem. Phys.*, 2010, **12**, 6423-6427.
63. T. Cheung, S. K. Bhargava, M. Hobday and K. Fogar, *J. Catal.*, 1996, **158**, 301-310.
64. S. Abednatanzai, P. Gohari Derakhshan, H. Depauw, F.-X. Coudert, H. Vrielinck, P. Van Der Voort and K. Leus, *Chem. Soc. Rev.*, 2019, **48**, 2535-2565.
65. L. Liu, Z. Chen, J. Wang, D. Zhang, Y. Zhu, S. Ling, K.-W. Huang, Y. Belmabkhout, K. Adil, Y. Zhang, B. Slater, M. Eddaoudi and Y. Han, *Nat. Chem.*, 2019, **11**, 622-628.
66. C. Wiktor, M. Meledina, S. Turner, O. I. Lebedev and R. A. Fischer, *J. Mater. Chem. A*, 2017, **5**, 14969-14989.
-

-
- 67. A. Mayoral, M. Sanchez-Sanchez, A. Alfayate, J. Perez-Pariente and I. Diaz, *ChemCatChem*, 2015, **7**, 3719-3724.
 - 68. C. Prestipino, L. Regli, J. G. Vitillo, F. Bonino, A. Damin, C. Lamberti, A. Zecchina, P. L. Solari, K. O. Kongshaug and S. Bordiga, *Chem. Mater.*, 2006, **18**, 1337-1346.
 - 69. N. J. Everall, *Analyst*, 2010, **135**, 2512-2522.
 - 70. N. J. Everall, *App. Spectrosc.*, 2009, **63**, 245A-262A.
 - 71. N. J. Everall, *App. Spectrosc.*, 2000, **54**, 773-782.

Chapter 6

HKUST-1 Metal-Organic Framework Crystals Loaded with Tetracyanoquinodimethane: Effects of Water on Host-Guest Chemistry and Electroconductivity



Composite materials, constituting of a Metal-Organic Framework (MOF) and a guest molecule, further denoted as Guest@MOF composites, gained lately strong interest due to the guest-induced tunability of the host properties, for example in sensing or electroconductivity applications. However, decoding the complexity of these Guest@MOF composites and extracting structure-performance relationships is far from trivial and requires the use of a gamut of characterization tools. In this Chapter, we use various micro-spectroscopic tools both under static (*ex-situ*) and dynamic (*in-situ*) conditions to map the properties and diffusion behavior of TCNQ (*7,7,8,8-tetracyano-quinodimethane*) as guest molecule in single HKUST-1 crystals as host. Raman micro-spectroscopy allowed to map the spatial distribution of TCNQ within HKUST-1 single crystals, thereby revealing a heterogeneous distribution of TCNQ after initial TCNQ-infiltration, concentrated at the crystal edges, and a homogeneous redistribution upon water vapor treatment. These insights are correlated to Electrochemical Impedance Spectroscopy (EIS), showing changes in the electric conductivity after several cycles of water adsorption/desorption

possibly related to the TCNQ-redistribution. During water vapor treatment, FT-IR micro-spectroscopy suggests lower transient diffusion rates for water inside TCNQ@HKUST-1 relative to bare HKUST-1, likely due to steric obstruction of the pore-filling TCNQ molecules in the HKUST-1 framework.

The results described in this Chapter are reported in the following manuscript: "HKUST-1 Metal-Organic Frameworks Crystals Loaded with 7,7,8,8-Tetracyanoquinodimethane: Effects of Water on Host-Guest Chemistry and Electro-Conductivity", M. Rivera-Torrente, M. Filez, C. Schneider, E. C. van der Feltz, K. Wolkersdörfer, D. H. Taffa, M. Wark, R. A. Fischer, B. M. Weckhuysen, *Phys. Chem. Chem. Phys.*, **2019**, 21, 25678-25689.

6.1 INTRODUCTION

Metal-Organic Frameworks (MOFs) have emerged as a class of porous crystalline materials with high potential to act as host materials for guest entities, such as metal nanoparticles, organic molecules as well as enzymes. The performance of these functionalized host-guest materials, further denoted as guest@MOFs, critically depends on the precise location of these guest species within the host material (*i.e.*, the MOF crystal). More particularly, microscopic heterogeneities in the intracrystal distribution of guest molecules might affect both the bulk properties as well as of the performance of the guest@MOFs materials made. Thus, it is of utmost importance to use spatially resolved techniques to shed light on the precise location of guest molecules within guest@MOF systems; under both *ex-situ* and *in-situ* conditions.

In contrast to other classes of porous functional materials, such as zeolites (*e.g.* zeolite materials with the framework structures FAU, BEA and MOR), mesoporous structured materials (*e.g.* MCM-41 and SBA-15) and (pillared) clay minerals,¹⁻⁵ the number of studies using spatially-resolved spectroscopies are very limited in the field of MOFs. Notable examples include the linker distribution mapping in multivariate MTV-MOFs or defect imaging in HKUST-1, as recently addressed by vibrational and fluorescence micro-spectroscopies.⁶⁻¹⁰ In addition, infrared micro-spectroscopy has been applied by the Kärger group to extract the transient diffusion behaviour of probe molecules within ZIF-8 crystals.¹¹⁻¹⁵ However, to the best of our knowledge, micro-spectroscopic studies reporting on charting the spatial location, distribution and chemical properties of functional guest molecules in MOFs does not exist. Typically, for example, mapping nanoparticle distributions in MOFs is achieved by Transmission Electron Microscopy (TEM).¹⁶ However, the probing volume of TEM is limited to the nm³-range, which typically hinders imaging of the distribution of guest entities over the entire MOF crystal. Also, TEM (unless coupled to Energy Dispersive X-ray (EDX) analysis, which usually requires high voltages and intense electron beams; and therefore, could result in beam damage) does not provide chemical information, but rather structural properties of the

sample. The application of micro-spectroscopic tools to locate and speciate guest molecules in MOFs can thus offer chemical information with spatial resolution across micrometer-sized MOF crystals in a non-destructive way under both *ex-situ* and *in-situ* conditions. Among the guest@MOF materials, HKUST-1 loaded with TCNQ (TCNQ = 7,7,8,8-tetracyano-quinodimethane) has been one of the most interesting yet challenging systems to be studied. Initially introduced by Allendorf *et al.*,¹⁷ this guest@MOF composite material has attracted the interest of many researchers for its strong increase in electronic conductivity upon infiltration with TCNQ as guest molecule.¹⁸⁻²⁰ TCNQ is a very well-known unsaturated polynitrile, strong π -acceptor molecule with an electron affinity of *ca.* 3 eV that can easily undergo reduction to a radical species ($\text{TCNQ}^{\cdot-}$), and to an anionic species (TCNQ^{2-}). As shown in Figure 6.1, not only reduction but also π -stacking or dimerization can happen to the anionic molecular species, rendering a difficult task to elucidate which is the state within the MOF material.

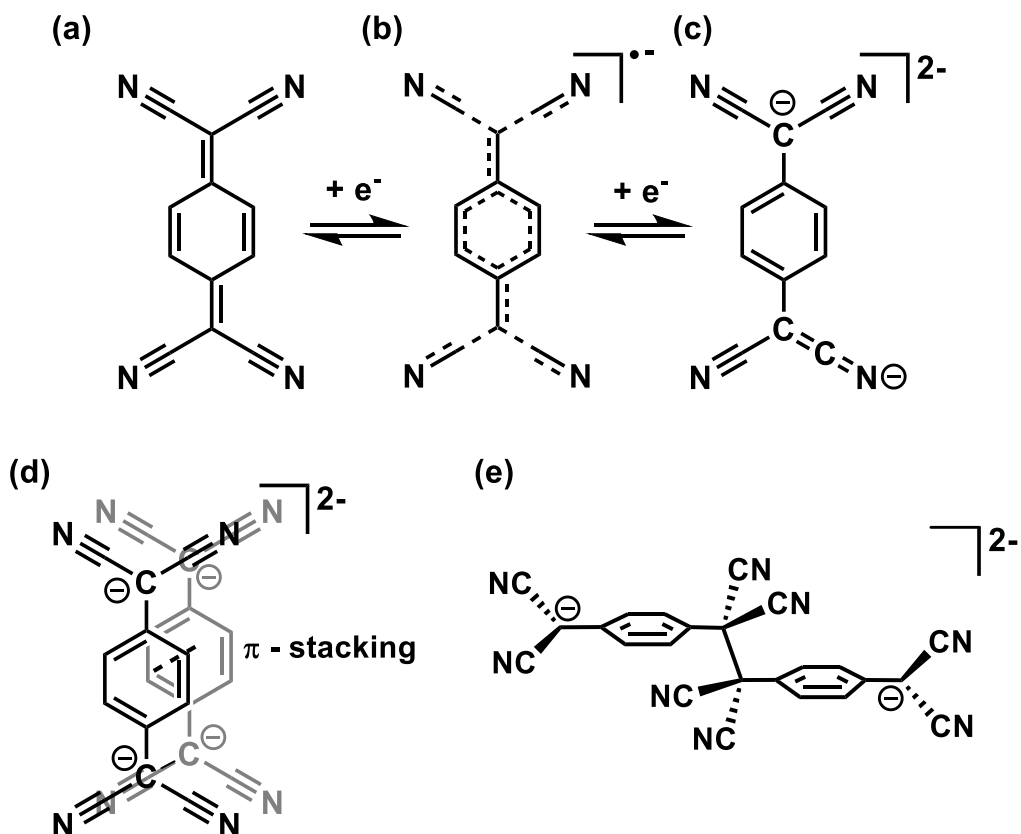


Figure 6.1. Different species of 7,7,8,8-tetracyanoquinodimethane (TCNQ) that can be formed upon reacting with another substrate: (a) neutral, (b) radical ion and (c) anion. The anion depicted in (c) may (d) stack or (e) dimerize forming other species.

Electrically conductive MOFs have been intensively researched in recent years,^{21 22} and in this context the post-synthetic introduction of redox-active species into intrinsically insulating MOF materials represents a promising strategy to combine porosity and electrical conductivity in one material. For a precise elucidation of the underlying electrical conductivity mechanism, structural information of the guest molecule is of utmost important. While theory predicted the coordination of TCNQ to two adjacent metal nodes of HKUST-1,¹⁷ just recently some of us found crystallographic evidence for this preferential adsorption, when TCNQ was introduced via the vapor phase.²³ However, an ordering was not observed when TCNQ was introduced via Vapor Phase Infiltration (VPI) to yield highly ordered TCNQ guest molecules within the pores of Cu₃BTC₂. Given the complexity of the system, elaborate characterization techniques are necessary to identify the necessary structure-property relationships and to study how moisture affects the spatial distribution of TCNQ as guest molecule within the host MOF material and how this spatial distribution impacts the electroconductivity of the host-guest material.

In this Chapter, we have used Raman microspectroscopy to map the spatial distribution of TCNQ as guest molecule within large HKUST-1 crystals before and after dosing water vapour. Spectral mapping was done under controlled conditions within a sealed chamber, avoiding contact with air, water therein or contaminants. Advanced data processing, by means of Principal Component Analysis (PCA), was used to improve data quality and related spectral interpretation. In addition, *in-situ* FT-IR micro-spectroscopy has been used to compare the diffusion behaviour of TCNQ-loaded and pristine HKUST-1 crystals upon water vapor dosing in the chamber. The obtained results are compared to water uptake isotherms, X-ray Photoelectron Spectroscopy (XPS) data and current (I)-voltage (V) curves, as obtained from Electrochemical Impedance Spectroscopy (EIS). By doing so, we show that the multi-technique approach taken allows to further shed light in the complex host-guest chemistry of the TCNQ@HKUST-1 system.

6.2 EXPERIMENTAL SECTION

6.2.2. Synthesis of Cu₃TBC₂ and TCNQ@Cu₃TBC₂ Large Crystals

HKUST-1 large crystals were prepared by following a procedure of Tovar *et al.*²⁴ In brief, Cu(NO₃)₂·3H₂O (0.49 g, 2.0 mmol, 99%, Acros Organics) was dissolved in 3 mL of deionized water in a glass vial. In another vial, benzene-1,3,5-tricarboxylic acid (H₃TBC, 0.24 g, 1.1 mmol, 98%, Sigma-Aldrich) was dissolved in 3 mL of ethanol (VWR International, 96%). Then, the Cu solution was mixed with 3 mL of N,N-dimethylformamide (DMF, anhydrous, 99.8%, Sigma-Aldrich) in a 20 mL glass vial. The linker solution and 12 mL of glacial acetic acid (99%, Sigma-Aldrich) were added to the mixture and the vial placed in a preheated oven at 328 K for 72 h. The crystals were collected and immersed in fresh ethanol and CH₂Cl₂ (99%, Sigma-Aldrich) for 1 week, respectively, before activation at $p \sim 10^{-3}$ mbar and 453 K for 24 h. Activated HKUST-1 was stored into an Ar BraunTM glovebox (O₂ < 1 ppm, H₂O < 1 ppm) until further use. 7,7,8,8-tetracyanoquinodimethane (TCNQ, 98%, acbr GmbH, Germany) was recrystallized three times from acetonitrile (anhydrous, 99%, Sigma-Aldrich) under inert conditions to yield molecular, crystalline TCNQ in high purity. Dry HKUST-1 single crystals were loaded into a glass ampoule with recrystallized TCNQ (TCNQ, approx. 2 eq. of TCNQ per HKUST-1) following the protocol reported in reference [23].

6.2.3. Materials Characterization

Ex-situ X-ray Diffraction (XRD) was collected in a 2θ range of 5–50° in steps of 0.0016413° (2θ) with a PANalytical Empyrean instrument equipped with a Cu source ($\lambda_{K\alpha}=1.54184$ Å) at 45 kV and 40 mA. The samples were loaded in borosilicate capillaries of 0.7 mm diameter. The radiation was focused onto the sample through a focusing X-ray beam mirror equipped with a 1/8° divergence slit and 0.02 radian Soller slits. The diffracted X-ray beam was detected by a PIXcel1D detector in receiving slit mode equipped with a 1/8° anti-scatter slit and 0.02 radian Soller slits. *In-situ X-ray Diffraction (XRD)* measurements were carried out in a 2θ range of 5–30 ° in steps of 0.05 ° (2θ), and 1 s/step time, on a Bruker Advance D8 diffractometer in Bragg-Brentano geometry equipped with a Co K_{1,2} source ($\lambda=1.79026$ Å), a VANTEC-1 detector and 1/8° divergence slits. *Scanning Electron Microscopy (SEM)* micrographs were recorded with a FEI Helios nanolab 600 DualBeam

microscope operated at 2.00 kV voltage and 25 pA current. All images were formed by secondary electrons with a 3 μ s dwell time. Images of the large HKUST-1 crystals were recorded on a PhenomPro X microscope, equipped with a CsB detector and operated at 10 kV voltage. The single-crystals were supported on C tape deposited over Al stabs (FEI stabs) and inserted in the vacuum chamber without any Au or Pt coatings. *X-ray Photoelectron Spectroscopy* (XPS) measurements were performed using a Thermo Fischer Scientific ESCALAB 250Xi (UK) instrument equipped with a monochromatic Al Ka radiation source (1486.6 eV). The powder samples were placed into an aluminium sample holder and pressed using a custom-made steel presser and degassed until the base pressure reaches $\sim 5 \times 10^{-7}$ bar. Core level XPS spectra of Cu 2p, N 1s, O 1s and C 1s were recorded with 10 eV pass energy and 0.01 eV step size and 5 spectra were averaged. The XPS spectra were deconvoluted and fitted with smart background employing mixed Gaussian-Lorentzian line shapes using the Avantage software (Version 5.986).

6.2.4. Conductivity and Water Uptake Isotherms

Water sorption isotherms were collected with a Quantachrome Hydrosorb 1000 instrument controlled with the software HydroWin v5. In a N₂-filled glovebox, *ca.* 50 mg of pre-activated 1.0TCNQ@HKUST-1 were transferred to a sample cell. Five adsorption-desorption cycles were performed at 298 K. Before every cycle the sample was evacuated at 298 K until constant pressure was achieved. The temperature of the sample cell was controlled by a water bath set at 298 K. *Electrical conductivity* measurements were conducted on compressed powder pellets. After the sample preparation in a glove box the previously described custom-made measuring cell was connected to a ZahnerZennium electrochemical workstation.²⁵ *Electrochemical Impedance Spectroscopy* (*EIS*) measurements were performed an alternating voltage of 10 mV was employed in the frequency range from 1 Hz to 1 MHz at 0 V DC voltage. Ion current (I)- Voltage (V)-curves were collected in the voltage range from -1 to 1 V with a slew rate of 100 mV.

6.2.5. Micro-spectroscopy and Data Analysis

Raman micro-spectroscopy was performed with a RenishawTM *InVia* microscope, using a 532 nm diode excitation laser with a 20x magnification objective, a 1200 lines \cdot mm⁻¹

grating and a Charge Coupled Device (CCD) with a pixel size of $3.33 \times 3.33 \mu\text{m}^2$ under the conditions described below. The objective has a Numerical Aperture (NA) of 0.4 and the calculated theoretical laser spot size is $1.62 \mu\text{m}$ diameter. All measurements were performed with a total 0.44 mW power output (power density of $1.27 \cdot 10^{-5} \text{ W} \cdot \text{cm}^{-2}$) in the $1500\text{-}2300 \text{ cm}^{-1}$ range and a spectral resolution of 1 cm^{-1} . In a glovebox, the samples were transferred to a sealed Linkam cell equipped with CaF_2 windows and filled with 1 bar of Ar (99.999% Linde AG). Data analysis of the Raman microscopy maps was performed using WiRE 3.4[©] (Renishaw) and TXM Wizard²⁶ software packages. Principal Components Analysis (PCA) of the signal-to-baseline or single wavelength intensity maps were obtained with Matlab R2018a (Mathworks). PCA was done by *K*-means clustering of pixels with similar spectral features, resulting into Voronoi cells grouped in four different clusters. In order to define the representative components (eigenvectors) of the PCA analysis, the Scree test and Cumulative Variance Explained (CVE) tests are shown (Figure 6.2). It is clear that with three to four components, a representative part of the data set can be analysed without losing relevant information. Deconvolution of the bands of the average spectra obtained from cluster analysis was carried out with the Fityk 1.3.1[©] package (Nedler-Mead simplex).

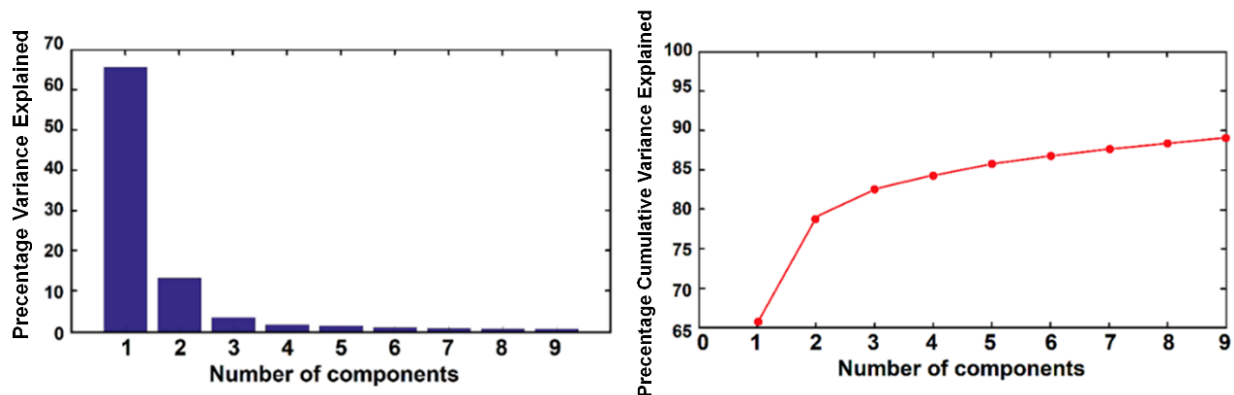


Figure 6.2. Scree tests and Cumulative Variance Explained (CVE) of each principal component of the Principal Component Analysis (PCA) used for the Raman microscopy analysis.

In Figure 6.3, the first nine principal components of the PCA analysis carried out for the maps, depicted in Figures 6.5 and 6.7, are shown. As it can be noted, most of the spectral information is present in the first few components. This was due to the high intensity of

cosmic ray noise that occurs during the spectral acquisition, thus rendering PCA as an extremely useful tool for our purpose.

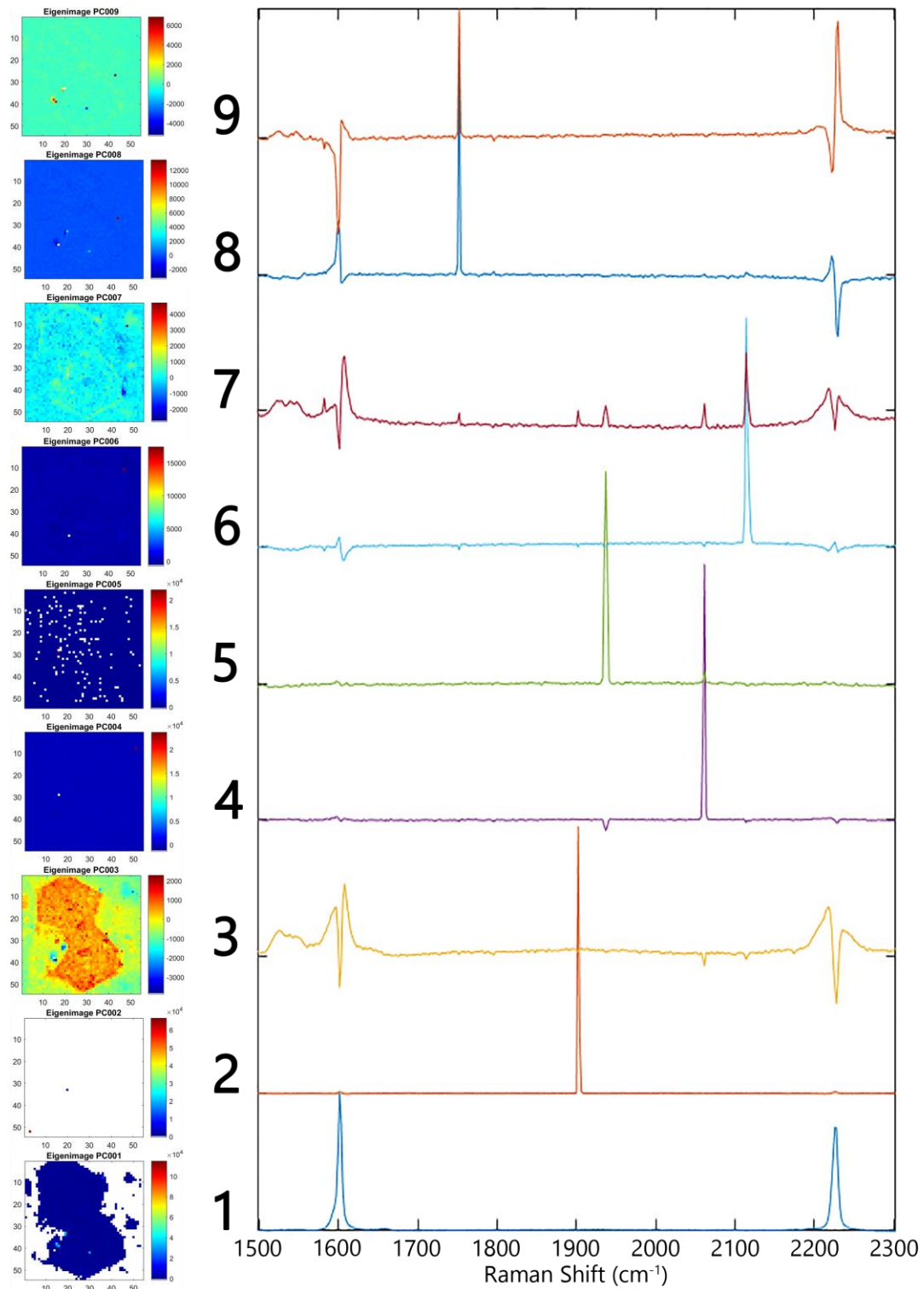


Figure 6.3. Eigen-images and associated spectra for each component of the Principal Component Analysis (PCA) applied on the Raman micro-spectroscopy maps obtained for the second crystal, as shown in Figures 6.5 and 6.7.

Fourier-Transform Infra-Red (FT-IR) micro-spectroscopy was carried out with a Perkin Elmer Frontier MIR/FIR spectrometer coupled to a Perkin Elmer Spotlight 400 FT-IR microscope, with Mercury-Cadmium-Telluride (MCT) detector cooled with liquid N₂, in a 16x16 array of 6.25 x 6.25 μm pixels. The samples were kept in sealed cells equipped with CaF₂ windows, under inert conditions. Then, a flow of 60 mL·min⁻¹ of nitrogen gas (99.99%, Linde AG) saturated with demineralized water (at 298 K) was introduced into the sample cell for 5 min, stopping every 30 s to collect FT-IR microscopy maps of the HKUST-1 crystals.

6.3 RESULTS AND DISCUSSION

The two Metal-Organic Framework (MOF) materials under study, namely large crystals of HKUST-1 and TCNQ@HKUST-1, were obtained as described in a previous report by Schneider *et al.*²³, in which their phase purity, crystallinity, morphology and porosity are reported. TCNQ was introduced by vapour phase infiltration in an evacuated glass ampoule. During this treatment, TCNQ sublimes and diffuses into the large pores of HKUST-1, in which only half contain uncoordinated Cu sites pointing to the centre of the pore. As shown by Schneider *et al.*, TCNQ chemically binds via its two terminal nitrile groups to two neighbouring metal nodes as evidenced by the increasing intensity of the (111) reflection in the X-ray diffraction data.²³ In addition, physisorbed TCNQ fills the remaining pore space and weakly interact with the MOF framework. This leads to loadings reaching up to two TCNQ molecules per large pore, while maintaining pore space accessible for small molecules, as shown by sorption experiments with N₂ and H₂O.

To study the spatial distribution of TCNQ molecules within a HKUST-1 crystal after vapour phase infiltration, Raman micro-spectroscopy is used as characterization method, as illustrated in Figure 6.4. Raman spectroscopy has been extensively used for characterizing TCNQ and Cu-TCNQ compounds, due to the fact that the Raman intensity is highly sensitive to charge transfer processes, such as the binding to metal substrates or electrical switching.²⁷⁻²⁹ By applying Raman spectroscopy in a spatially resolved manner with a resolution of ~1 μm, chemical 3-D imaging of the HKUST-1 crystals can be achieved by focussing an incident laser beam on the sample, in combination with pinhole filtering

of out-of-plane contributions and signal detection using a Charge Coupled Device (CCD) array detector. If an objective with a long working distance is used, a sealed Linkam cell with CaF_2 windows can be placed in the focal point of the beam, which allows to monitor the dynamics of the MOF material under *in-situ* conditions.^{30, 31} After data collection, Principal Component Analysis (PCA) and Cluster Analysis (CA) can be used to extract the variance of the dataset and to classify the Raman spectra into different groups with similar spectral features.^{32, 33}

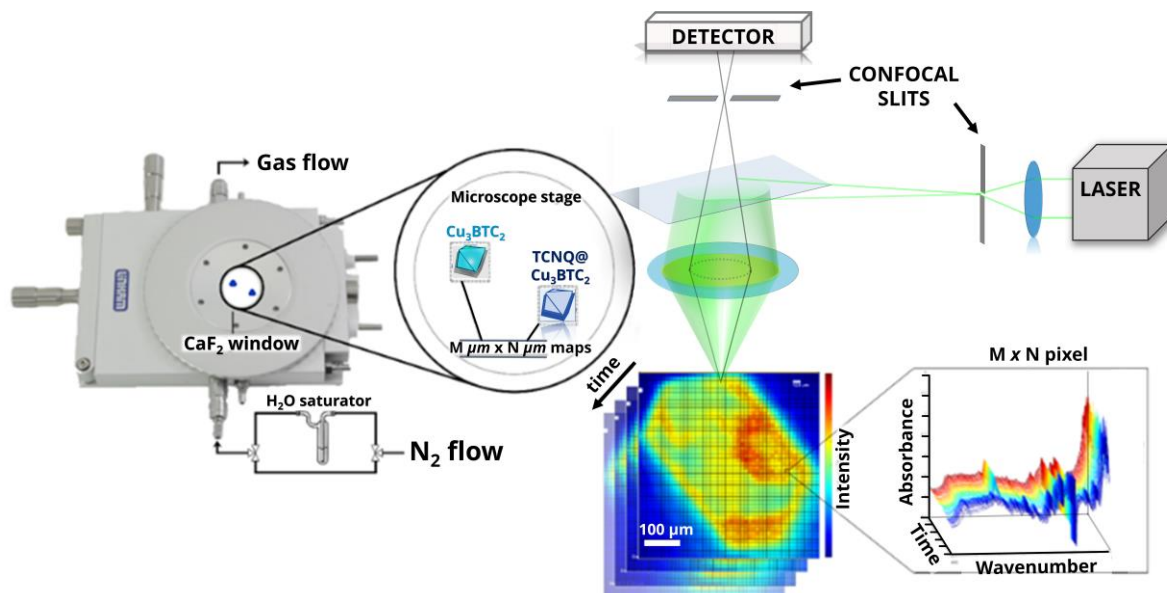


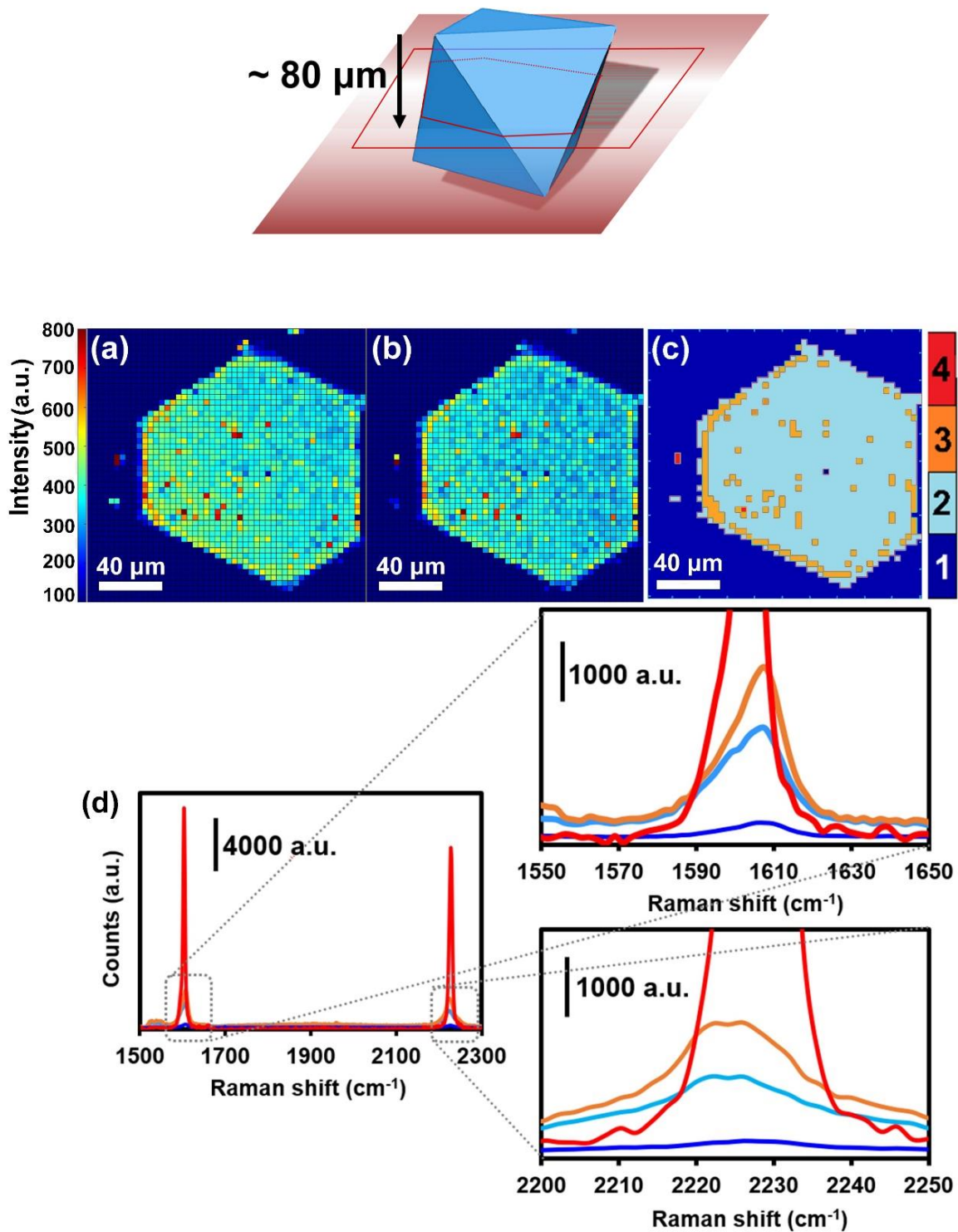
Figure 6.4. Micro-spectroscopic approach used to investigate the influence of H_2O in large crystals of HKUST-1 and TCNQ@HKUST-1 materials. Confocal Raman micro-spectroscopy allows 3-D *in-situ* chemical imaging of MOF crystals under dynamic conditions by focussing the laser beam into selected (X,Y) areas of the crystal. A saturator can be connected to an air-sealed cell in order to dose water vapour.

Raman micro-spectroscopy maps of a HKUST-1 crystal, loaded with TCNQ, is given in Figure 6.5a-b. The Raman intensity map in Figure 6.5a displays the aromatic C=C stretching band ($\nu_{\text{C}=\text{C}}$) at 1605 cm^{-1} and visually shows where the HKUST-1 crystal and TCNQ are relatively located, since this Raman band is present in the BTC linker of the host material as well as TCNQ as guest molecule. In Figure 6.5b, the Raman map of the 2226 cm^{-1} band, associated with stretching of TCNQ C≡N nitrile groups ($\nu_{\text{C}\equiv\text{N}}$) alone, is also shown. In order to identify and group the Raman spectra within the maps into different classes, PCA and CA have been performed using all the recorded Raman spectra within the map. Aside from extracting the variance of the dataset, the analysis minimizes the influence of scattering, out-of-focus contributions, cosmic rays or impurities that may

affect the signal and obscure the interpretation. In the current case, four different clusters are obtained, which exhibit fingerprint spectra, and which mainly differ in their 1605 ($\nu_{C=C}$) and 2226 cm^{-1} ($\nu_{C\equiv N}$) band intensity and thus their abundance in TCNQ. The results are shown in Figure 6.5c-d.

Cluster 1 represents the spectra containing limited TCNQ Raman intensity and are located outside the TCNQ@HKUST-1 crystal in regions where no TCNQ is present. Cluster 2 contains fingerprint spectra, which exhibit moderate TCNQ abundance, and are mostly populating the crystal interior. Cluster 3 contains spectra, which expose increased TCNQ intensity relative to the moderately intense spectra in cluster 2. Pixels classified in cluster 3 mainly situate at the crystal edges, implying that the TCNQ abundance increases radially toward the outside of the HKUST-1 crystal and therefore resembles a core-shell structure. In addition, small, non-uniformly dispersed islands of cluster 3 are observed across the HKUST-1 crystal, implying fluctuations in the TCNQ concentration after initial infiltration. Finally, cluster 4 groups spectra with TCNQ concentrations an order of magnitude higher compared to clusters 2 and 3. Cluster 4 pixels are only observed on a spatially remote location outside TCNQ@HKUST-1, suggesting that this area is caused by TCNQ condensates. Figure 6.6 shows the micrographs of the crystals of pristine HKUST-1 and the TCNQ@HKUST-1 host-guest composite material. It was found that needle-like Cu-TCNQ coordination polymer²³ are found at the surface of the TCNQ@HKUST-1 host-guest composite material. The bands corresponding to both materials were present after deconvolution of the average Raman spectra of each cluster (see Figure 6.5e): one contribution arising from physically deposited TCNQ, at 2224 cm^{-1} and a smaller component at 2210-2214 cm^{-1} , assigned to TCNQ coordinated to the Cu paddlewheels. In contrast, no signs clear signs of Cu-TCNQ coordination polymer, that typically shows the $C\equiv N$ stretch at 2205 cm^{-1} were observed.^{29, 34, 35} It is important to bear in mind that the average spectra contain the spectral contribution of different pixels located at the edge of the crystal and other areas. Further, the pixel size of $1\times 1 \mu\text{m}^2$ is enough to probe nanometric needles of Cu-TCNQ and TCNQ@HKUST-1, preventing us from a clear distinction of species, yet corroborating different compounds within the TCNQ@HKUST-1 crystals. The focal point of the laser was set to a depth of $z \sim 80 \mu\text{m}$ from the top edge,

allowing us to obtain chemical maps of the cross-sections, rather than the top crystal surfaces of the TCNQ@HKUST-1 host-guest composite material.



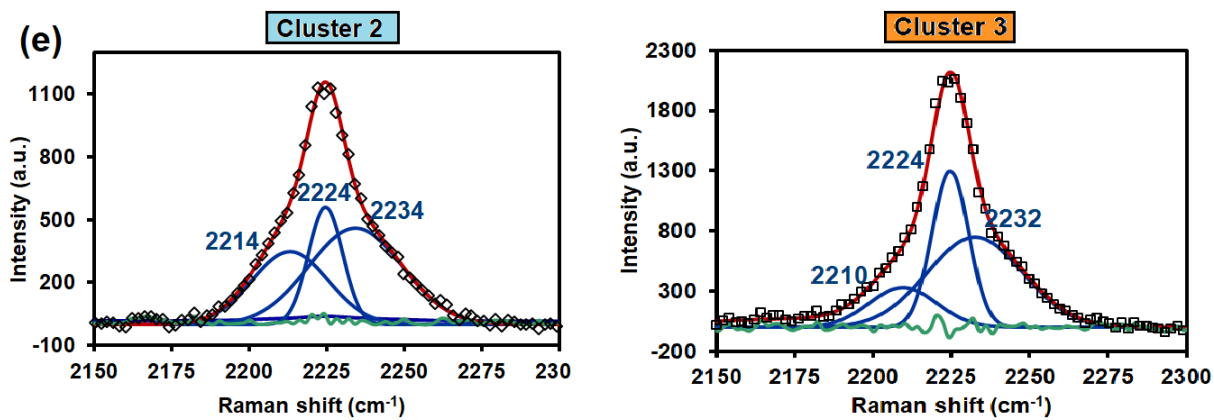


Figure 6.5. (Top) Scheme showing the cross-section of two intertwined, octahedral HKUST-1 crystals, loaded with TCNQ, and probed with the Raman laser at a depth of $Z \sim 80 \mu\text{m}$. Signal-to-baseline ratio maps of the Raman bands at (a) 1605 cm^{-1} (corresponding to the C=C aromatic stretching vibration); and at (b) 2226 cm^{-1} (corresponding to the C≡N stretching vibration) of a HKUST-1 crystal, loaded with TCNQ. (c) Different spectral clusters obtained from Principal Component Analysis (PCA) of the $1500\text{-}2300 \text{ cm}^{-1}$ region, showing different intensities throughout the TCNQ@HKUST-1 crystals. (d) Raman spectra corresponding to each cluster of the map in (c). Scale bars indicate $40 \mu\text{m}$ in all cases. (e) Deconvolution of the nitrile stretch band in the average spectra of cluster 2 and 3 seen in (d). The green line corresponds to the residual of the Nedler-Mead simplex algorithm used.

The formation of aggregates on the edges is due to diffusion barriers that occur during the vapour-phase deposition process, in which the TCNQ molecules that enter the pores first, coordinate strongly to the Cu^{2+} Lewis sites and block these pores as diffusion pathways, preventing other TCNQ molecules from entering the MOF crystal. Not only coordination within the pores, but formation of a thin, nanometric layer of Cu-TCNQ coordination polymer on the surface of the HKUST-1 crystals. The coordinatively unsaturated Cu sites on surface react with the diffusing TCNQ molecules at high temperature, forming this layer observed by SEM (Figure 6.6). Additional TCNQ entering the MOF material is only physically deposited within the pores, as the Raman band at 2225 cm^{-1} corresponds to neutral, non-reduced (*i.e.* non-coordinated to the Cu centres).³⁶ This layer of condensed TCNQ has a thickness of *ca.* $5 \mu\text{m}$, *i.e.* 1-2 pixels in the Raman maps, in contrast to the typical nanometric films of Cu-TCNQ coordination polymer formed on the surface.³⁷ Important to mention here is that despite the formation of these aggregates, no signs of dimeric TCNQ radicals^{38,39} were present in the Raman spectra.

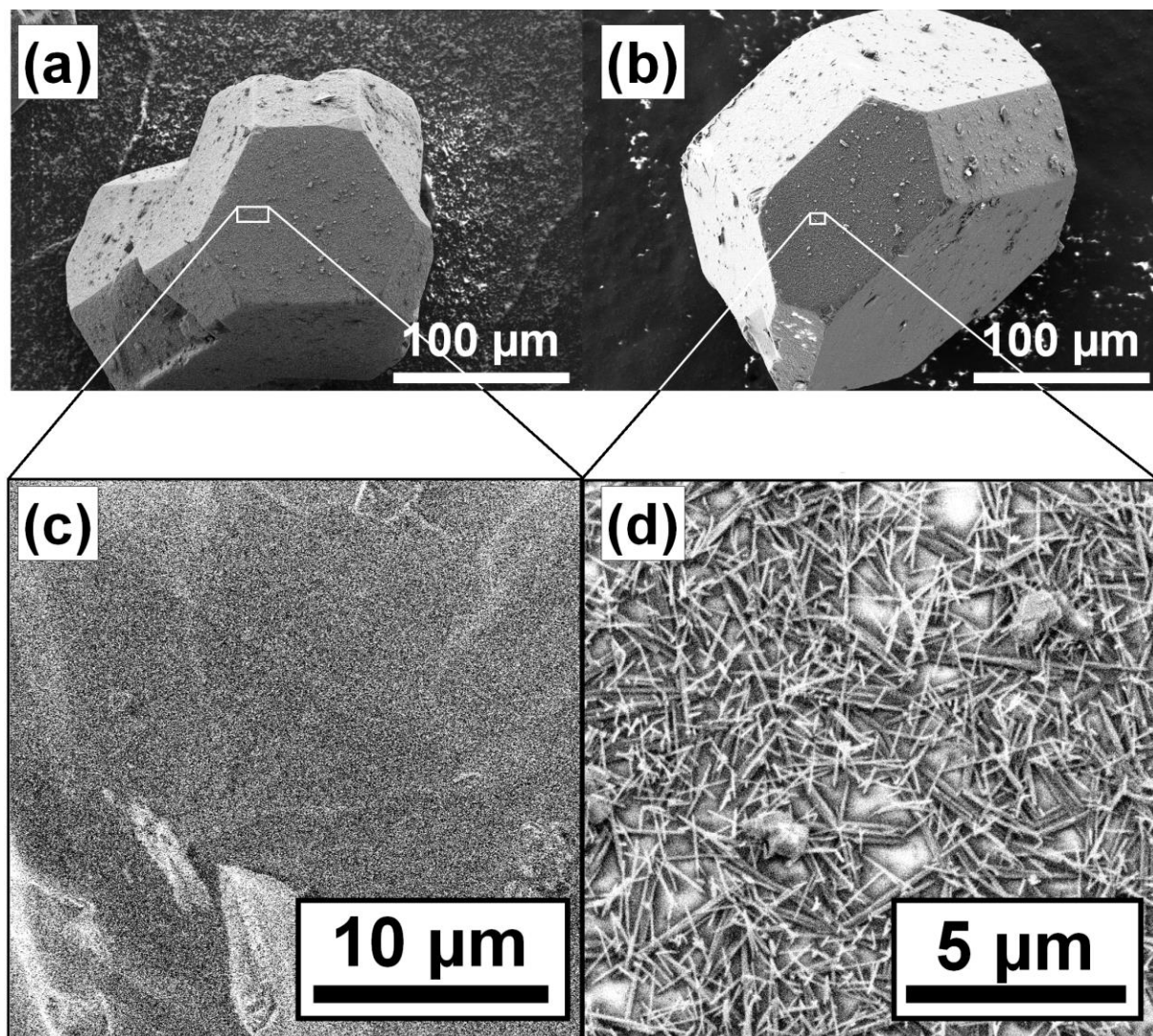
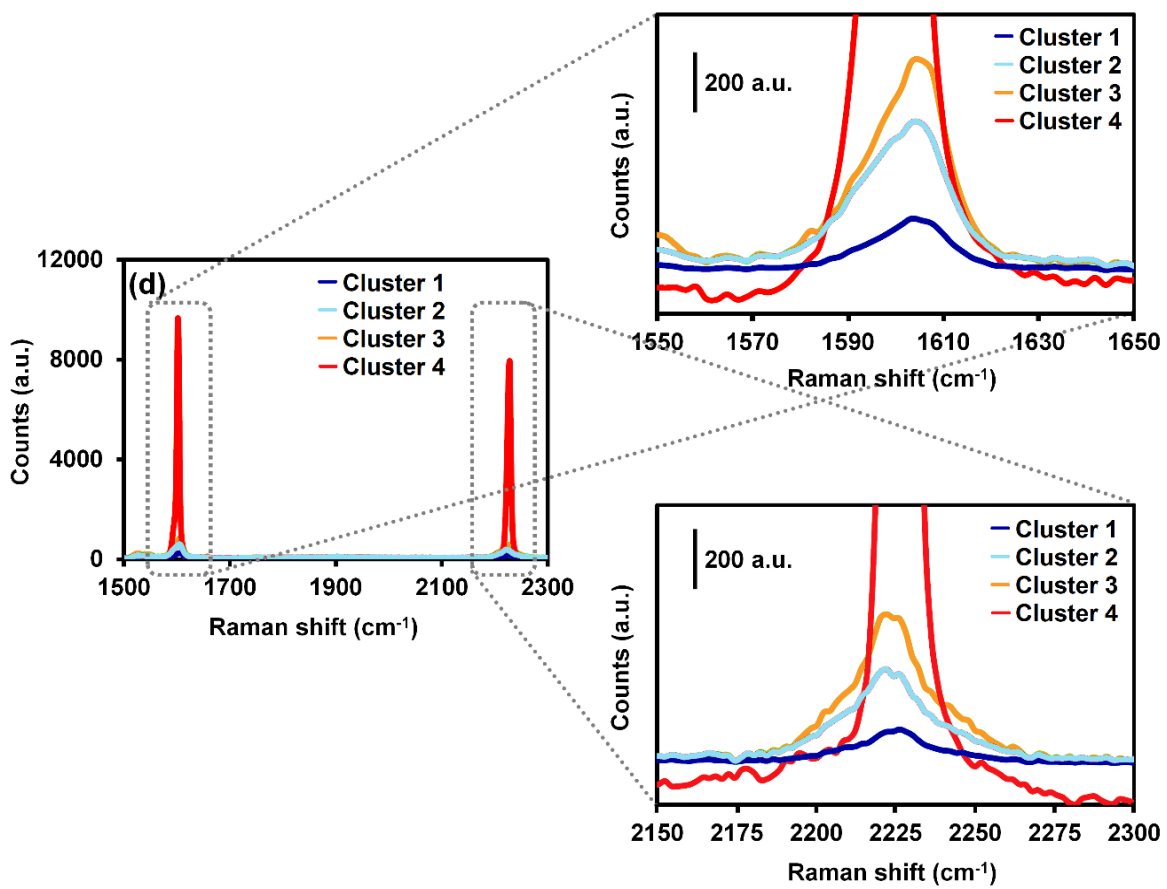
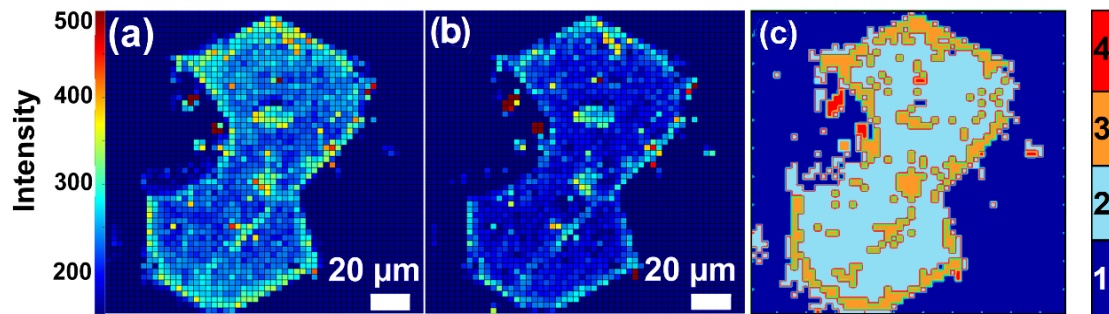
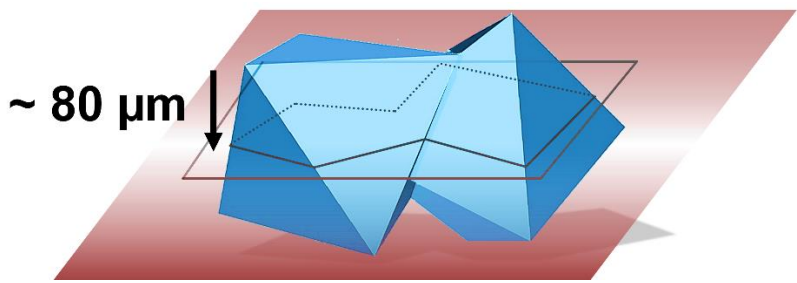


Figure 6.6. Scanning Electron Microscopy (SEM) micrographs of the crystals of (a) pristine HKUST-1 and (b) the TCNQ@HKUST-1 host-guest composite material. Cu-TCNQ needles covering the surface of the crystal are clearly visible at higher magnifications in (d), in comparison to the neat surface observed in (c).

To verify that this finding is consistent, two intertwined, octahedral HKUST-1 crystals were mapped and analysed following the same procedure. The maps and cluster analysis are presented in Figure 6.7, and also show the characteristic aggregation of TCNQ in the inner edges of the HKUST-1 crystals. Some zones in proximity to the surface also showed a few aggregates of TCNQ. Thus, we could corroborate that the formation of this layer of TCNQ is widespread throughout the HKUST-1 sample probed.



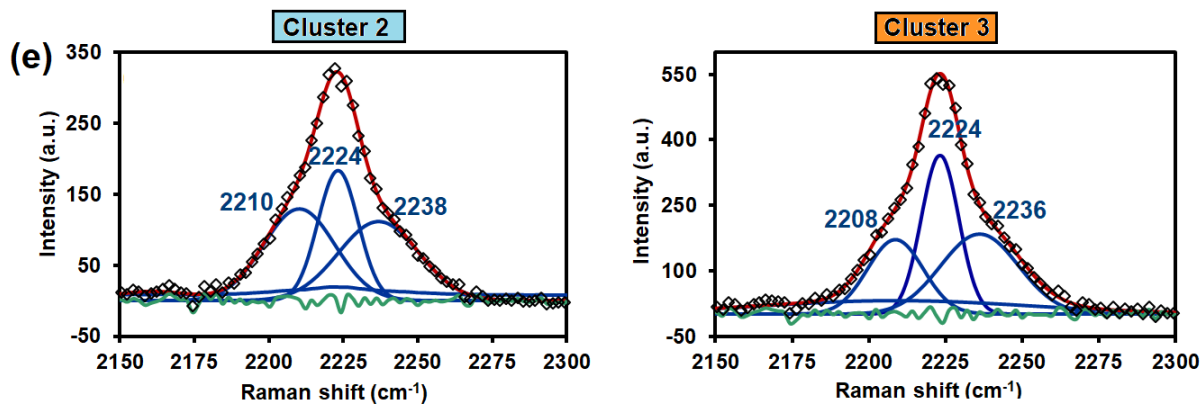


Figure 6.7. (Top) Scheme showing the cross-section of two intertwined, octahedral HKUST-1 crystals, loaded with TCNQ, and probed with the Raman laser at a depth of $Z \sim 80 \mu\text{m}$. (Bottom) Raman maps of a second crystal showing a similar trend with aggregates around the crystal edges. Signal-to-baseline ratio maps of the Raman bands at (a) 1605 cm^{-1} (corresponding to the C=C aromatic stretching vibration); and at (b) 2226 cm^{-1} (corresponding to the C≡N stretching vibration) of TCNQ. (c) Different spectral clusters obtained from Principal Component Analysis (PCA) of the $1500\text{-}2300 \text{ cm}^{-1}$ region showing different intensities throughout the two adjacent $\text{TCNQ@Cu}_3\text{BTC}_2$ crystals. (d) Raman spectra corresponding to each cluster of the map in (c). (e) Deconvolution of the band corresponding to the nitrile stretch in clusters 2 and 3 of the average spectra shown in (d). The green line corresponds to the residual of the Nedler-Mead simplex algorithm used.

It is known that HKUST-1 crystals have a limited stability to moisture and water, having potential consequences ranging from Cu reduction to pore collapse depending on the exposure time and water vapor pressure.⁴⁰⁻⁴⁵ To ensure that no such effects occur during the hydration experiments in this work, *in-situ* X-ray Diffraction (XRD) experiments were performed by recording XRD patterns during a temperature-programmed experiment with dosing of water-saturated He gas ($60 \text{ mL}\cdot\text{min}^{-1}$ He flow through a bubbler filled with demineralized H_2O following the temperature program depicted in Figure 6.8a, at a heating rate of $5 \text{ K}\cdot\text{min}^{-1}$). The results are summarized in Figure 6.8.

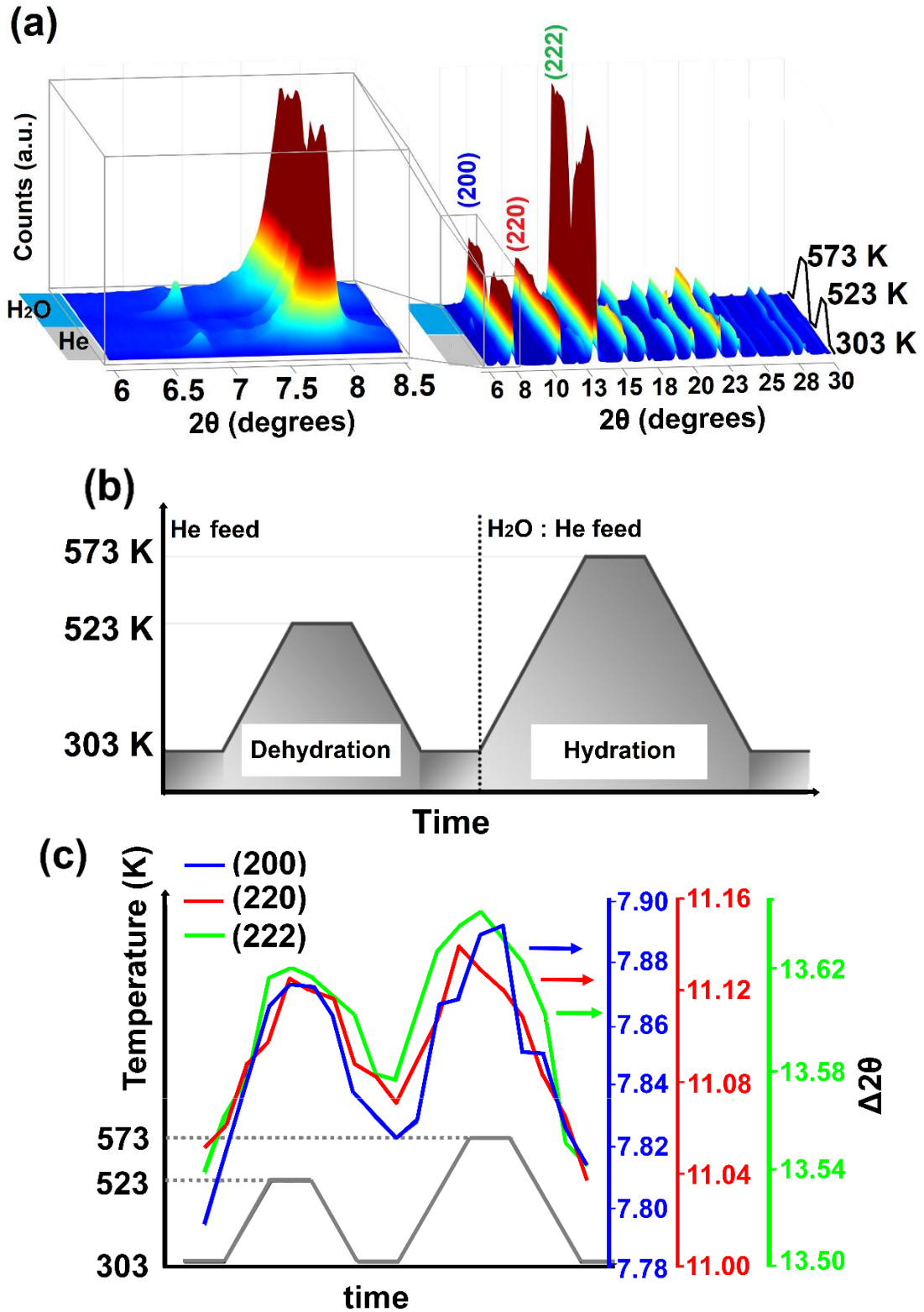


Figure 6.8. (a) Evolution of the intensities of the X-Ray Diffraction (XRD) peaks of the TCNQ@HKUST-1 host-guest composite material over time under dynamic conditions, as shown in the scheme (b). Dehydration of the crystals results in higher lattice parameter d of the (200), (220) and (222) plane reflections, as evidenced by the shift shown in (c). Dosing of water vapor at higher temperatures does not significantly affect the HKUST-1 lattice.

An increase in the lattice parameter a was observed for the HKUST-1 Bragg reflections at temperatures up to 573 K, as a result of temperature-induced lattice expansion. However, no signs of framework decomposition were detected, as the XRD peaks showed the same intensity before and after high temperature vapor dosing. These findings are in line with Giovine *et al.*⁴⁶, where decomposition of HKUST-1 in air or moisture does not occur on short timescales, comparable to exposure times in our experiments. This confirms that the HKUST-1 framework is stable under the described experimental conditions and allows for its *in-situ* micro-spectroscopic study from room temperature up to 573 K in H₂O-saturated He or N₂ flows.

To further study the effect of pore blockage on the HKUST-1 crystal edges, caused by TCNQ aggregates, *in-situ* FT-IR microscopy of the materials under study was performed. More specifically, we have studied the process of hydration by monitoring the evolution of the FT-IR band at 3400 cm⁻¹, which corresponds to the O-H stretching mode of water, of both pristine HKUST-1 and TCNQ@HKUST-1 crystals.

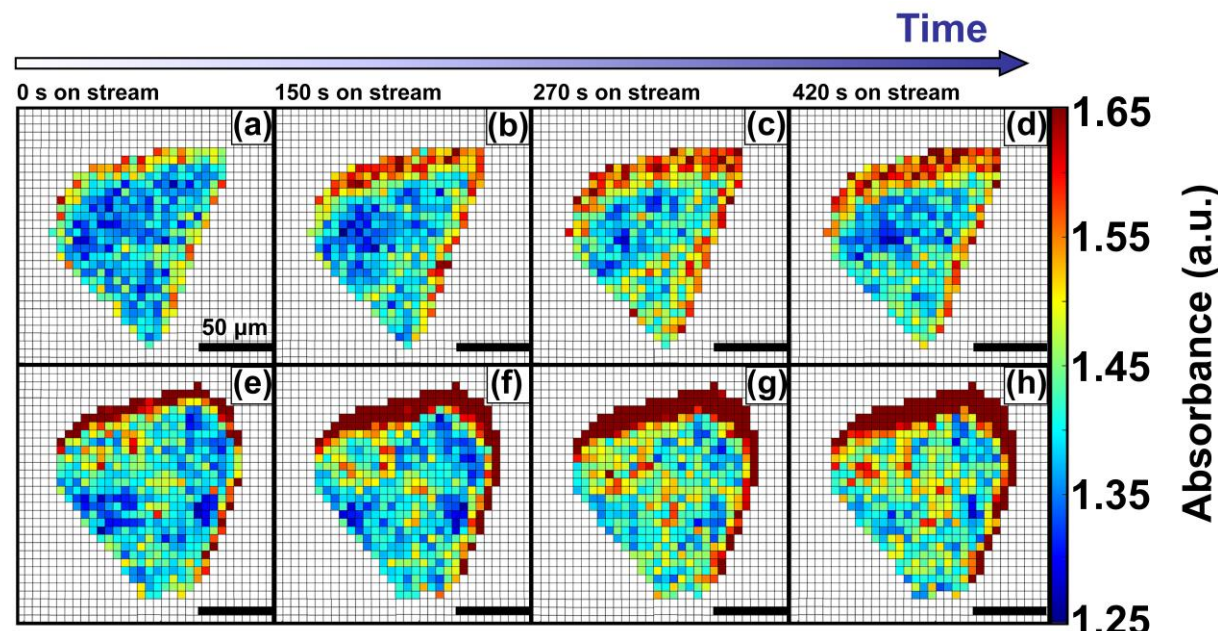


Figure 6.9. *In-situ* FT-IR microscopy maps of the intensity of the band at 3400 cm⁻¹ of (top; a-d) pristine HKUST-1 and (bottom; e-h) TCNQ@HKUST-1 after hydration by water vapor at room temperature for 0, 150, 270 and 420 s. Note that the preferential uptake on the right side is due to the incoming flow from that side of the spectroscopic cell. All scale bars represent 50 μm.

The results are shown in Figure 6.9, where the evolution of two different crystals (parent HKUST-1, on top; and TCNQ@HKUST-1, below) under a stream of N₂ saturated with water for 5 min at 298 K. The maps show the absorbance of IR band at 3400 cm⁻¹ over time for each pixel present in the crystal, where water penetrates the pores from the right side (incoming flow in the cell). At different time steps, from t = 0 to t = 420 s, the absorbance increases steadily on different parts of both crystals: first edges, and then, the core of the MOF, indicating that unlike TCNQ, it can flow through the pores with lower diffusional barriers.

To obtain more quantitative information we have plotted the evolution of the absorbance of the 3400 cm⁻¹ band over the entire HKUST-1 crystal, in the absence and presence of TCNQ. The increase in the absorbance of the 3400 cm⁻¹ band, averaged for all the pixels corresponding to the materials, shows a gradual saturation after *ca.* 5 min (300 s). This indicates that the pores are filled with water vapor very shortly after the dosing starts, in line with previous experiments showing the high capacity and kinetics of HKUST-1 for that purpose.^{47, 48} Indeed, water molecules rapidly fill the pores and coordinate to any remaining coordinatively unsaturated Cu²⁺ sites that may not be occupied by TCNQ. The similar profiles suggest that TCNQ does not play a significant role in hindering the maximum water uptake of HKUST-1 crystals at the bulk scale (Figure 6.10).

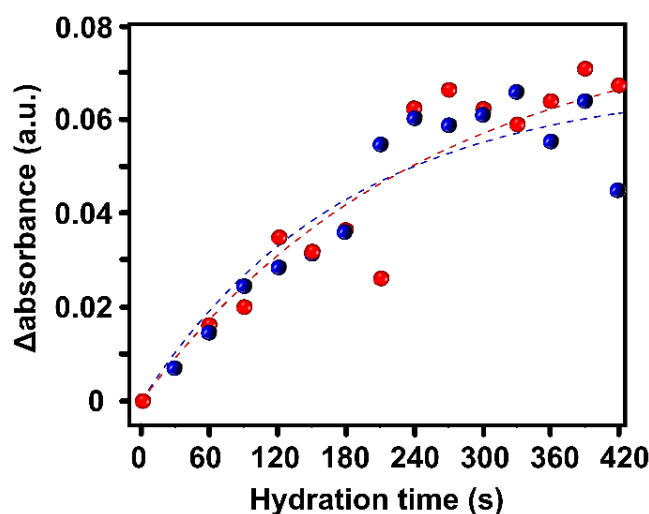


Figure 6.10. Evolution of the average change in absorbance of all the pixels for each crystal: pristine (blue) and TCNQ@HKUST-1 (red) during adsorption of water. Note that there is not a significant difference at the bulk scale.

As mentioned above, the FT-IR micro-spectroscopy maps, shown in Figure 6.9, reveal spatial differences in the water uptake depending on the distance to the centre of the HKUST-1 crystal. In order to better understand the kinetic behaviour of hydration, we have analysed the evolution of the band at 3400 cm^{-1} with respect to the distance to the centre of the crystal. An algorithm, applied to the FT-IR microscopy maps, recorded during the hydration experiments was used to analyse the average absorbance of the band with an increasing radial distance. The results are given in Figure 6.10a, where the red area represents pixels further away to the centre of the HKUST-1 crystal (blue area). The HKUST-1 crystal was divided into 11 different areas from crystal surface to centre, as described in the related schematic.

In Figure 6.11b and c, the plots show that the average absorbance of the 3400 cm^{-1} band progressively decays from outer areas of the HKUST-1 crystal, *i.e.* surface (pixel 1), to inner zones (pixel 11). This observation holds for both the pristine HKUST-1 and TCNQ@HKUST-1 crystals. It is important to note that Figure 6.10c shows that the decay observed between pixels 1 to 3 (a total radius of around $18.75\text{ }\mu\text{m}$, with pixel size of $6.25\text{ }\mu\text{m}$) is more pronounced in the case of the TCNQ-loaded crystals. This indicates that, indeed, although the guest molecule aggregates do not decrease the total uptake significantly, they do hinder to some extent diffusion within the surface pores towards the inner areas of the HKUST-1 crystal. These different diffusional behaviours can be better seen in Figure 6.11d where the apparent rate constant of hydration over time for pixels of increasing distance to the centre of the HKUST-1 crystal were calculated.

The apparent rate constant of increase in absorbance was fitted to a function of the type: $\Delta Abs = A(1 - e^{-kt})$, where A represents the maximum Δ absorbance, t the hydration time and k the rate constant of hydration. It is clear that in the pristine HKUST-1 material hydration occurs at a similar rate throughout the entire MOF crystal. However, the TCNQ-loaded material shows decreasing rates for increasing distance to the surface, indicating that the areas on the outer cores hydrate at similar rates as the pristine HKUST-1, but the areas closer to the centre of the crystal need longer times to hydrate.

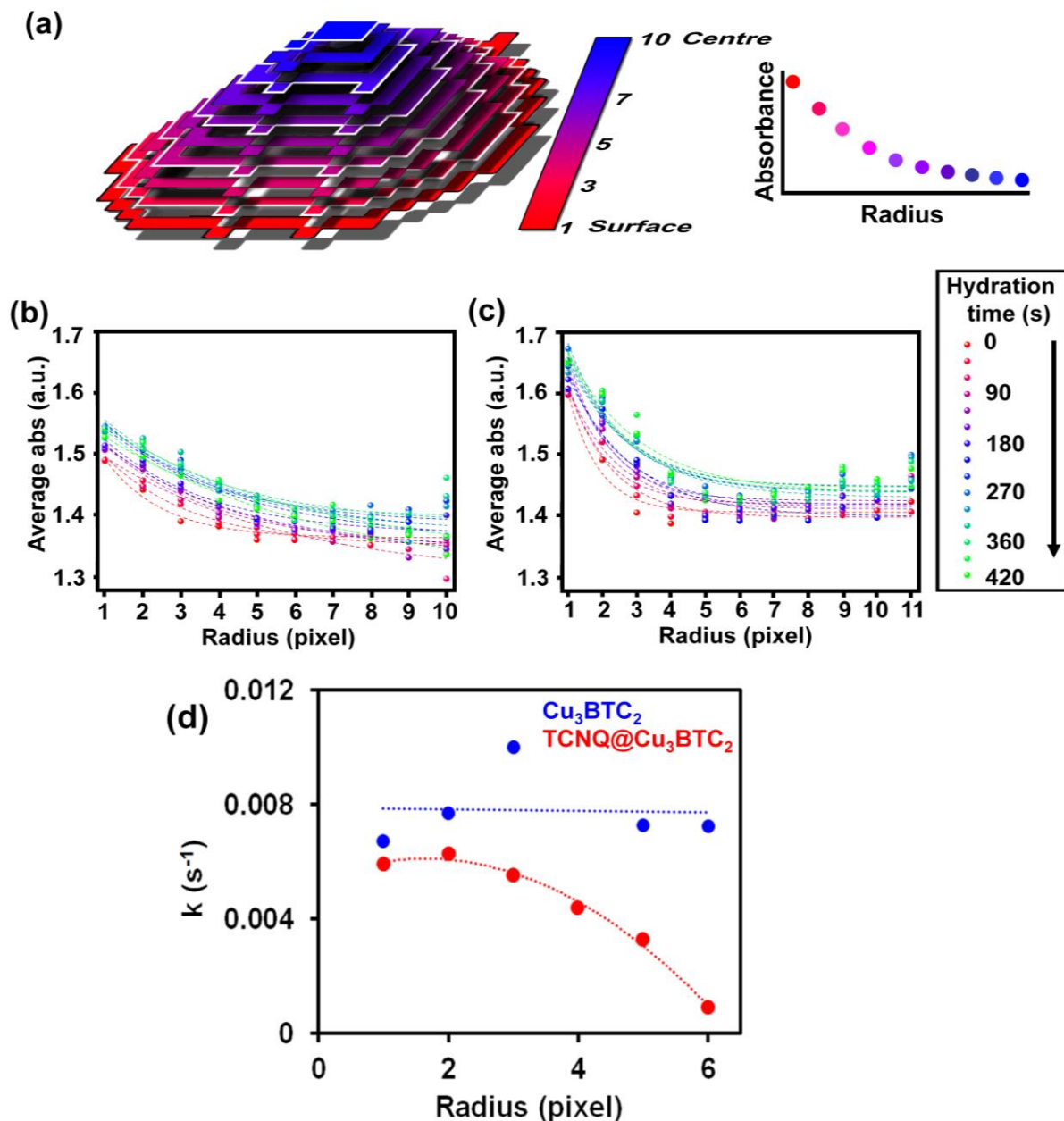


Figure 6.11. (a) Scheme of the algorithm applied to understand water uptake with respect to the centre of the HKUST-1 crystal. Average absorbance of the water band at 3400 cm^{-1} for different pixels at increasing distances from the central part of the (a) pristine HKUST-1 and (b) $\text{TCNQ}@\text{HKUST-1}$ host-guest composite material. (d) Rate constant (k) for the hydration *vs.* radius describing the diffusion barrier created by TCNQ at the edges of the HKUST-1 crystals.

In other words, water molecules need longer time to reach the pores of HKUST-1 and interact with the Cu^{2+} sites, if the interaction with the MOF occurs much faster than diffusion.

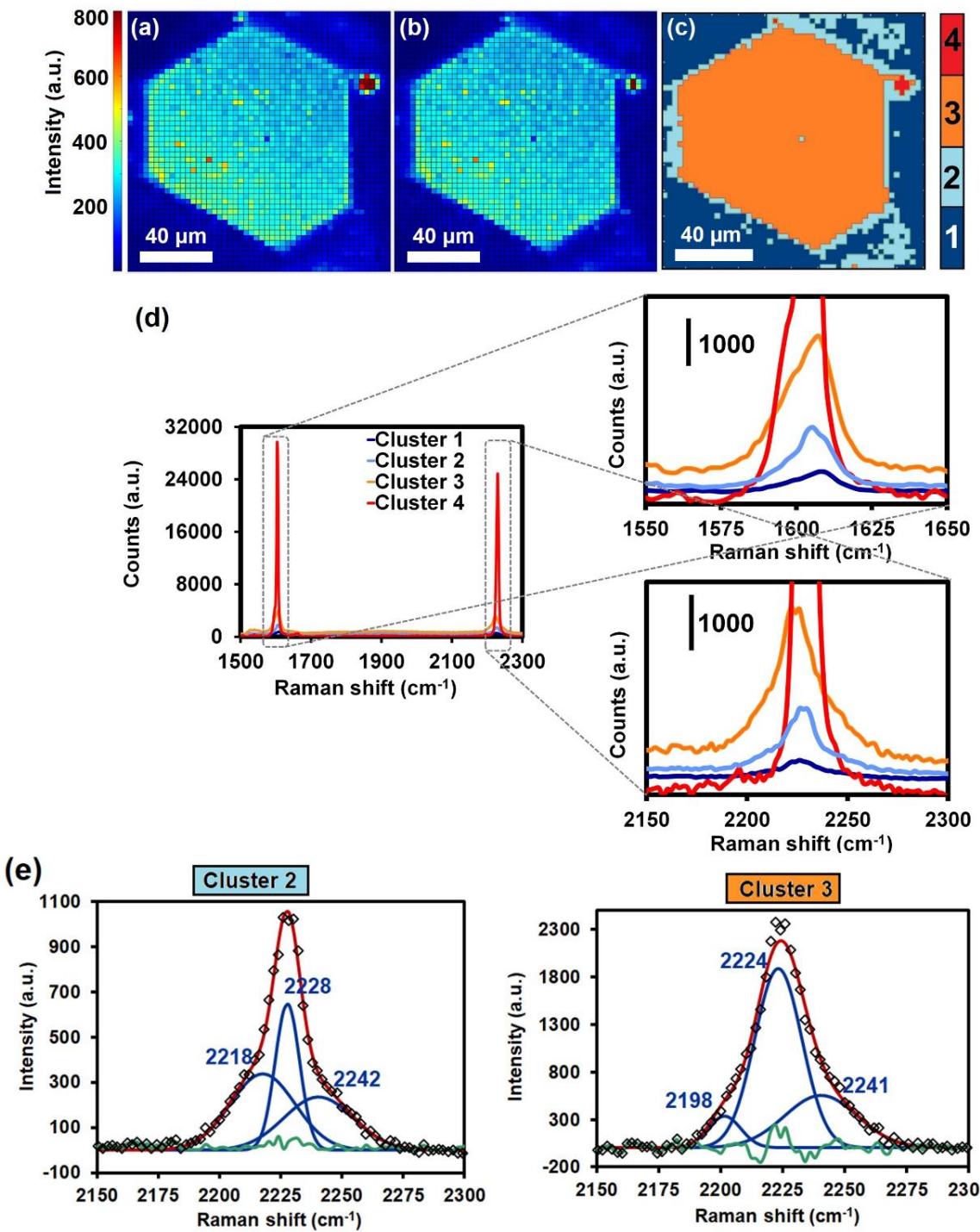


Figure 6.12. Raman maps of the crystal shown in Figure 6.5 after bubbling N₂ saturated with deionized water through the sealed cell for 5 min at 298 K. Signal-to-baseline ratio maps of the Raman bands at (a) 1605 cm⁻¹ (corresponding to the C=C aromatic stretching vibration); and at (b) 2226 cm⁻¹ (corresponding to the C≡N stretching vibration) of TCNQ. (c) Different spectral clusters obtained from Principal Component Analysis (PCA) of the 1500-2300 cm⁻¹ region showing different intensities throughout the two adjacent TCNQ@Cu₃BTC₂ crystals. (d) Raman spectra corresponding to each cluster of the map in (c). (e) Deconvolution of the band corresponding to the nitrile stretch in clusters 2 and 3 of the average spectra shown in (d). The green line corresponds to the residual of the Nelder-Mead simplex algorithm used.

In order to investigate if the inclusion of water had an impact on the spatial distribution of TCNQ, Raman micro-spectroscopy maps of the band corresponding to the nitrile stretch of TCNQ@HKUST-1 (located at 2226 cm^{-1}) after the hydration experiments were recorded. As shown in Figure 5.12, PCA of the Raman spectra obtained reveals that the spatial heterogeneities within the HKUST-1 crystals are not present anymore and consequently a very different picture is observed. Cluster 2 (light blue), with lower average intensity than Cluster 3 (orange), is present on the crystal edges and outer sections, *i.e.* the intensity on the surfaces is now lower than in the crystal core and no signs of heterogeneities are observed.

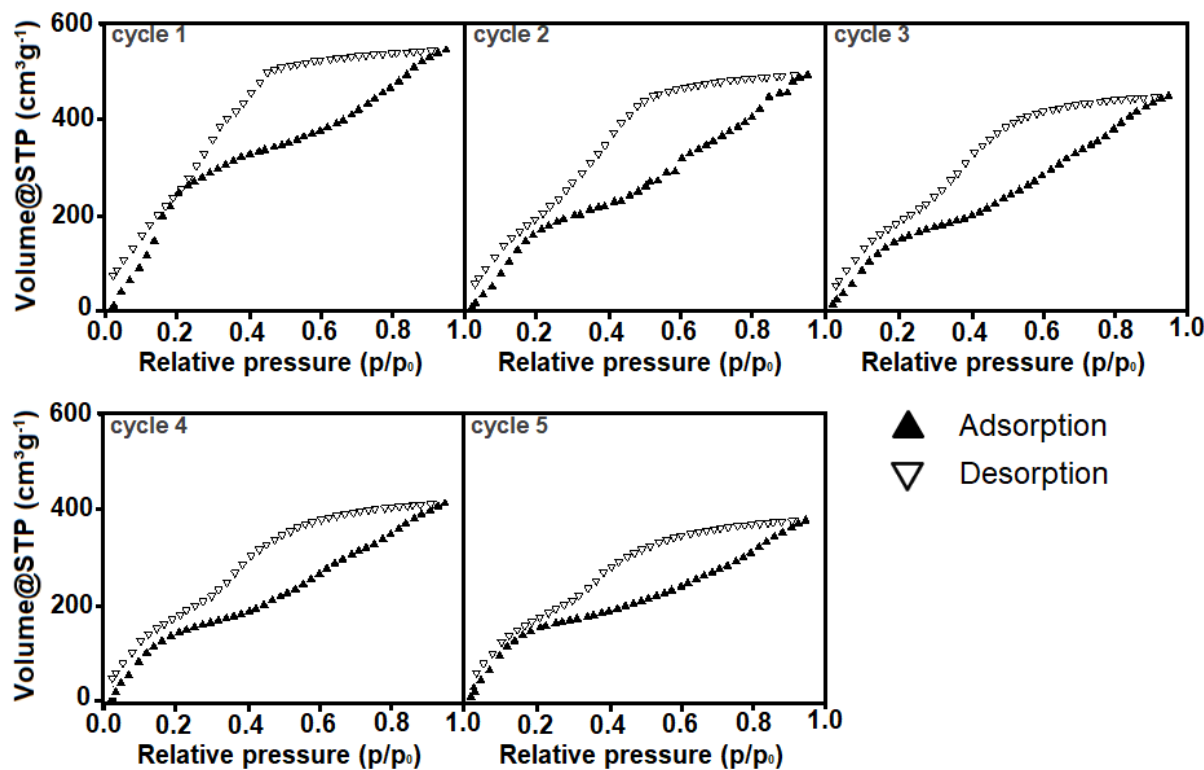


Figure 6.13. Water adsorption-desorption cycles of the TCNQ@HKUST-1 host-guest composite material measured at 298 K. STP stands for standard pressure and temperature (273.15 K, 1 atm).

This indicates that TCNQ, in contrast to the Raman micro-spectroscopy maps of Figures 6.5 and 6.7, is homogeneously distributed throughout the HKUST-1 crystal. This suggests that flowing water vapour through the HKUST-1 crystals results in a redispersion of the TCNQ guest molecules, filling the pore cavities of the MOF material in a more homogeneous manner. Water adsorption-desorption cycles at 298 K were measured to

study if any losses in capacity are observable upon dosing water into the materials under study. The results are summarized in Figure 6.13. It was found that there is a slight decrease for every sorption cycle, revealing that water cycling may influence the distribution of TCNQ.

To study the effect of this TCNQ redispersion in the electrical conductivity of the TCNQ@HKUST-1 material, we have measured Electrochemical Impedance Spectroscopy (EIS) of the materials before and after the hydration-dehydration cycles was obtained. It is worth mentioning that the conductivity measurements were carried out with μm -sized Cu_3BTC_2 powders (10-20 μm octahedra) infiltrated with TCNQ, as previously described in the literature.²³ However, we believe that the redispersion phenomenon may be present also in the case of those powder samples. Previous studies have suggested that TCNQ, aligned within the pores of HKUST-1, lead to a percolation system through which electrons can hop from one pore to the next one. Thus, it may be hypothesized that water vapour flowing into the pores induces the redispersion of the TCNQ molecules.

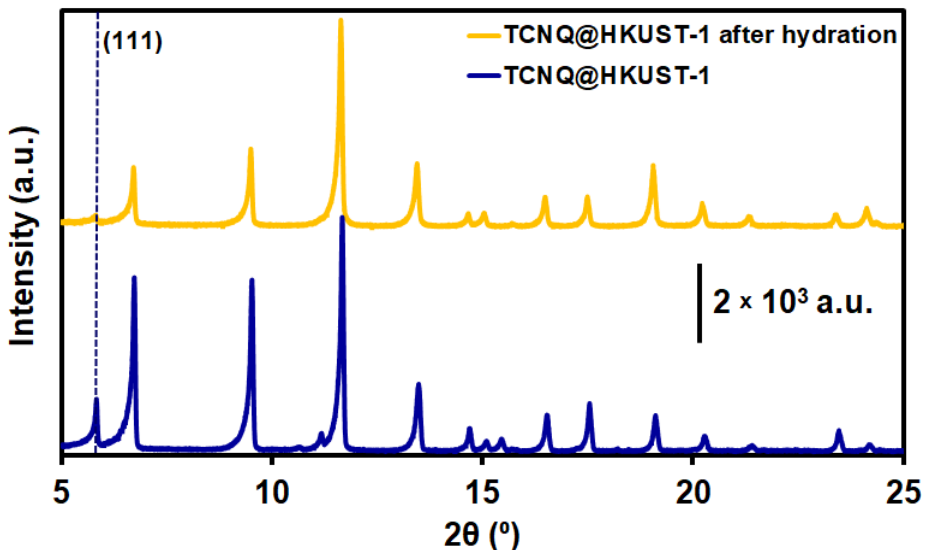


Figure 6.14. X-ray Diffraction (XRD) patterns of the TCNQ@HKUST-1 host-guest composite material before (blue) and after (yellow) exposure to air atmosphere. Dashed line at 5.8 ° indicates the (111) reflection originating from TCNQ ordered within the pores.

Competitive adsorption of H_2O to the Cu cations would then lead to a loss in the long-range ordering of the TCNQ molecules aligned in the pores. This should be observable via the (111) reflection in the corresponding XRD patterns. In Figure 6.14, it can be seen how

the intensity of the (111) reflection at 5.8 ° strongly decreases in intensity upon exposure of the TCNQ@HKUST-1 material to air. This suggests that moisture indeed affects the percolation network through which electrons are mobile, rendering the material less conductive. Indeed, using the so-called Current-Voltage (I-V) graphs of the material at different temperatures, as shown in Figure 6.15, the activation energy for electron conduction was obtained. The Arrhenius plot of the charge transfer of TCNQ@HKUST-1 before hydration reveals a temperature activated conductivity mechanism with an activation energy of 0.18 eV. The exposure of the sample to a low level of relative humidity, *i.e.* ambient atmosphere at 298 K, results in a slight decrease of the conductivity.

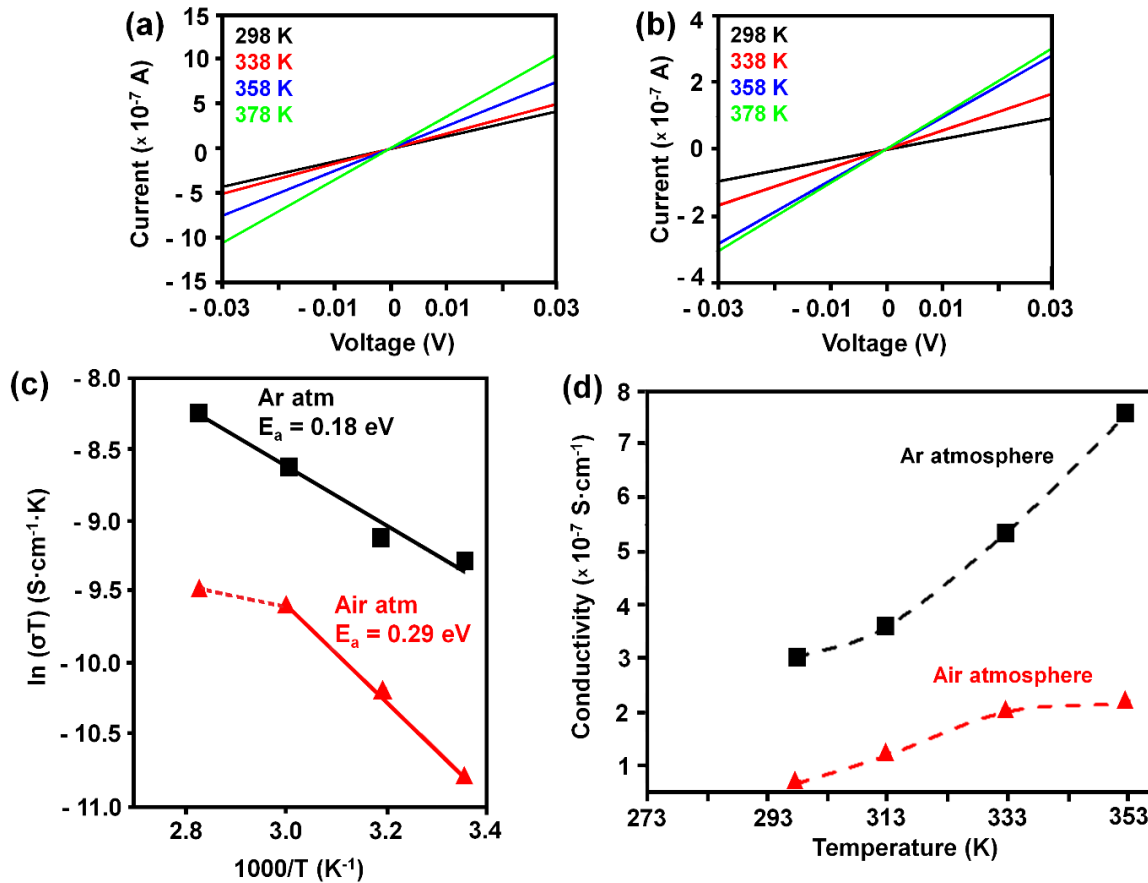


Figure 6.15. I-V graphs of the TCNQ@HKUST-1 host-guest composite material under (a) Ar and (b) ambient atmospheres at different temperatures: 298 (black), 318 (red), 338 (blue) and 358 K (green). Note the different y-axis scales when comparing conductivity. (c) Arrhenius plot $\ln K$ vs. $1/T$ of the conductivity measurements and (d) evolution of the conductivity at different temperatures under Ar (black squares) and ambient (red triangles) atmospheres showing a higher activation energy for the material exposed to air.

It was found that a high level of relative humidity does not induce a fast and pronounced response of the TCNQ@HKUST-1 material. However, after prolonged exposure (*ca.* 68 h) to a humidified atmosphere, different unknown electrochemical processes lead to a slight increase in electron conductivity, as illustrated in Figure 6.16. In a compressed powder pellet, the interaction between MOF particles plays an important role for the charge transfer. In this manner, it can be assumed that a high loading of TCNQ molecules in the outer shell of the HKUST-1 material is beneficial for the charge transfer. An alternative explanation for electrical conductivity has been the presence of the Cu-TCNQ coordination polymer on the crystal surfaces, which would act as a conductive coating over the crystals.³⁷ The lower intensity of the C≡N vibrational band around the crystal edges in the Raman micro-spectroscopy cluster maps, shown in Figures 6.5 and 6.7, suggests that this layer is affected by the presence of moisture. This may be an alternative explanation for the drop-in conductivity after exposure to water. The absence of a pronounced tail in the EIS measurements of the humidified samples indicates a low mobility of H₂O in the framework. If any, there is just a minor ionic contribution to the overall conductivity of the system.

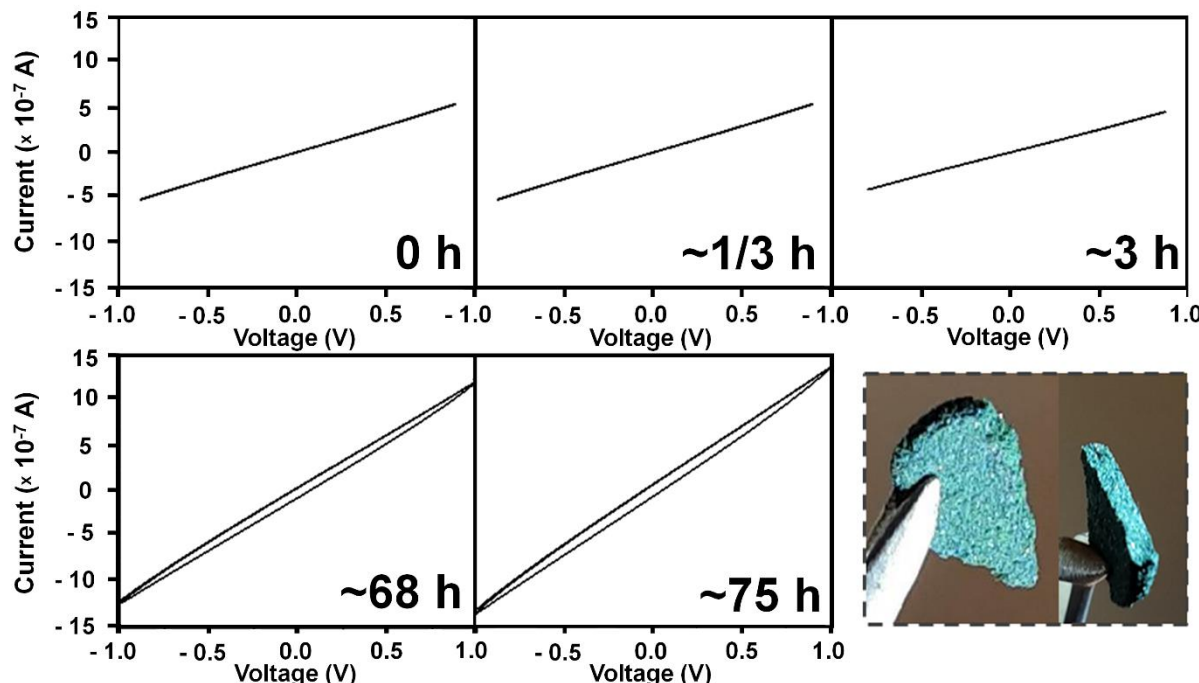


Figure 6.16. I-V graphs of the TCNQ@HKUST-1 host-guest composite material after different times of exposure to air atmosphere. Image in the inset shows the powdered pellets used for conductivity measurements.

In order to understand the nature of the species on the HKUST-1 surface, X-ray Photoelectron Spectroscopy (XPS) measurements before and after measuring electrochemical impedance, as well as after the water sorption experiments, were performed. The results are summarized in Figure 6.17. It can be noted that the N 1s spectra of the pristine TCNQ@Cu₃BTC₂ material are characterized by two prominent XPS peaks centred at ~ 398.91 eV and ~ 399.98 eV as well as by a XPS shake-up at ~ 401.59eV. The two main XPS peaks can be assigned to the coordinated and uncoordinated C≡N groups respectively, and these peak positions are consistent with literature reports.^{23, 49} Upon exposure to moisture (and also after conductivity measurement) only one prominent XPS peak at ~ 399.5 (and ~ 399.2 eV, respectively) with a XPS shake-up feature at slightly higher energy is clearly observed.

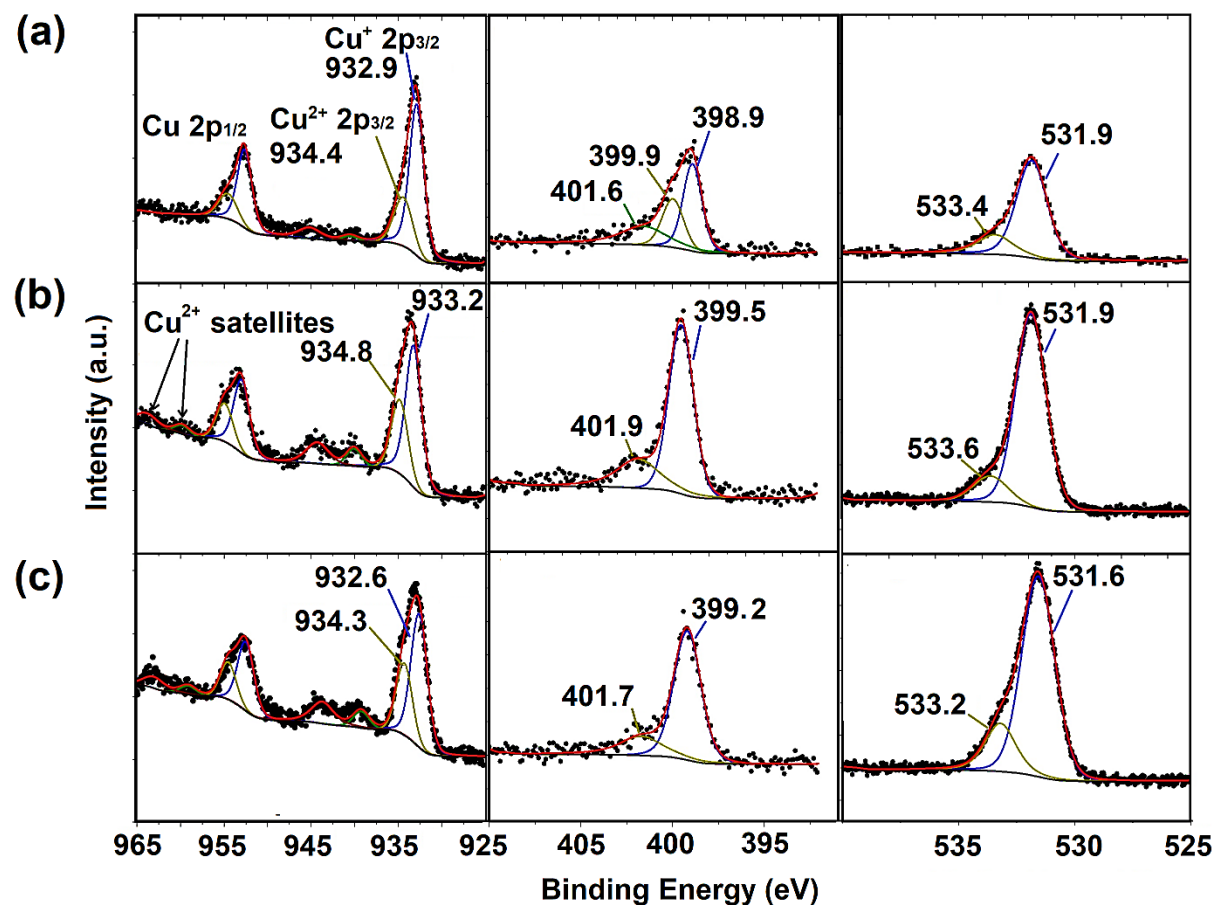


Figure 6.17. X-ray Photoelectron Spectroscopy (XPS) data of the Cu 2p (left), N 1s (middle) and O 1s (right) edges for TCNQ@HKUST-1 host-guest composite material (a) before, (b) after measuring electrochemical impedance and (c) after water sorption experiments.

This finding corroborates that water affects the coordination of TCNQ molecules to the Cu centres. Moreover, the Cu 2p_{3/2} XPS peak can be decomposed into two contributions, assigned to Cu⁺ and Cu²⁺ species. The XPS satellite features become more pronounced upon water vapor exposure and the conductivity measurement under humidified atmosphere, which suggests a slow oxidation of Cu⁺ to Cu²⁺. From literature Cu²⁺ species are characterized by strong XPS satellite peaks.⁵⁰ The ratios of Cu⁺/Cu²⁺ were estimated from the integrals of the XPS peak areas resulting in a value of 2.64 for the pristine sample and values of 1.97 and 1.94 after water vapor adsorption and conductivity measurements, respectively, for the TCNQ@HKUST-1 host-guest composite material. The values obtained for the pristine HKUST-1 sample is in a good agreement with previously reported data.²³ Furthermore, the O 1s XPS spectra show two main peaks originating from adsorbed water (531.5-531.9 eV) and from the organic linker BTC molecules (> 533 eV). These changes confirm that different processes affect the TCNQ@HKUST-1 host-guest composite material upon dosage of water vapour.

6.4 CONCLUSIONS

By taking large HKUST-1 Metal Organic Framework (MOF) crystals as host material and TCNQ (7,7,8,8-tetracyano-quinodimethane) as guest molecule, we have shown that new physicochemical insights can be obtained into the underlying processes of guest@MOF composites when employing a set of characterization methods. These methods include amongst others Raman micro-spectroscopy, FT-IR micro-spectroscopy, X-ray Photoelectron Spectroscopy (XPS) and Scanning Electron Microscopy (SEM). For example, Raman micro-spectroscopy and subsequent Principal Component Analysis (PCA) of the data obtained showed that large agglomerates of TNCQ are formed on the inner surface of the MOF crystals. In addition to Cu-TCNQ coordination polymer needles visible by SEM, these agglomerates were present within a few microns of the surface.

Moreover, *in-situ* FT-IR micro-spectroscopy experiments of the degassed crystals under dynamic hydration conditions showed that the observed TCNQ agglomerates lead to the formation of diffusional barriers, in comparison with pristine HKUST-1 crystals, in which hydration is less hindered by diffusion. Not only hydration is affected, but also the spatial

distribution of TCNQ was modified upon flowing nitrogen saturated with water vapour within the crystals, re-dispersing the guest TCNQ molecules within the host HKUST-1 crystals. Electrical conductivity measurements showed that hydration of the TCNQ@HKUST-1 guest-host composite material results in a slight decrease of conductivity. This study highlights the importance of using a multi-technique approach to tackle the lack of understanding in the functioning of MOFs as functional materials for different applications. The use of this ensemble of characterization tools paves the way for more advanced, spatially resolved studies of MOF crystals.

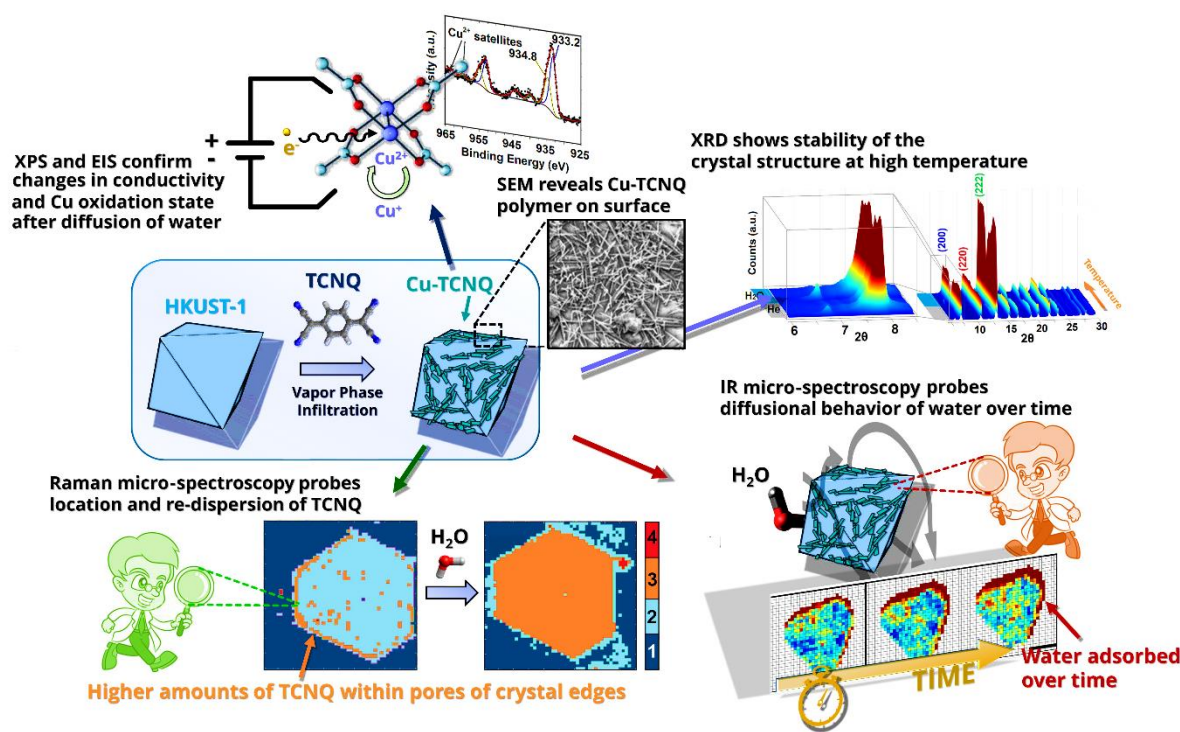


Figure 6.18. TCNQ@HKUST-1 crystal, as studied by a combination of Raman micro-spectroscopy and Principal Component Analysis (PCA), reveal the presence of aggregates on the edges (besides the well-known formation of a Cu-TCNQ coordination polymer on surface, as shown by Scanning Electron Microscopy (SEM)). Water molecules, moving through the pores, lead to a redispersion of TCNQ molecules; and the presence of these guest molecules hinder the transport of gases within the pores, as revealed by *in-situ* FT-IR micro-spectroscopy. Stability at high temperature in the presence of water was corroborated by *in-situ* X-ray Diffraction (XRD); while X-ray Photoelectron Spectroscopy (XPS) and electrical conductivity measurements showed that diffusion of water and electron flows lead to changes in the Cu⁺ to Cu²⁺ ratio. The ensemble of characterization techniques provided a detailed picture of the different molecular and structural aspects of this complex material.

6.5 REFERENCES

1. F. Meirer, D. T. Morris, S. Kalirai, Y. Liu, J. C. Andrews and B. M. Weckhuysen, *J. Am. Chem. Soc.*, 2015, **137**, 102-105.
2. D. E. Perea, I. Arslan, J. Liu, Z. Ristanovic, L. Kovarik, B. W. Arey, J. A. Lercher, S. R. Bare and B. M. Weckhuysen, *Nat. Commun.*, 2015, **6**, 7589.
3. C. E. Harvey, I. E. I. Petterson, B. M. Weckhuysen, C. Gooijer, F. Ariese and A. J. G. Mank, *App. Spectrosc.*, 2012, **66**, 1179-1185.
4. I. L. C. Buurmans and B. M. Weckhuysen, *Nat. Chem.*, 2012, **4**, 873-886.
5. A. M. Beale, S. D. M. Jacques and B. M. Weckhuysen, *Chem. Soc. Rev.*, 2010, **39**, 4656-4672.
6. A. M. Katzenmeyer, J. Canivet, G. Holland, D. Farrusseng and A. Centrone, *Angew. Chem. Int. Ed.*, 2014, **53**, 2852-2856.
7. R. Ameloot, F. Vermoortele, J. Hofkens, F. C. De Schryver, D. E. De Vos and M. B. J. Roeffaers, *Angew. Chem. Int. Ed.*, 2013, **52**, 401-405.
8. W. Schrimpf, J. Jiang, Z. Ji, P. Hirschle, D. C. Lamb, O. M. Yaghi and S. Wuttke, *Nat. Commun.*, 2018, **9**, 1647.
9. K. C. Jayachandrababu, D. S. Sholl and S. Nair, *J. Am. Chem. Soc.*, 2017, **139**, 5906-5915.
10. A. Ghosh, P. Mukherjee, S. Deb and R. Bhargava, *J. Phys. Chem. Lett.*, 2017, **8**, 5325-5330.
11. C. Chmelik, H. Bux, J. Caro, L. Heinke, F. Hibbe, T. Titze and J. Kärger, *Phys. Rev. Lett.*, 2010, **104**, 085902-085905.
12. C. Chmelik, F. Hibbe, D. Tzoulaki, L. Heinke, J. Caro, J. Li and J. Kärger, *Micro. Meso. Mater.*, 2010, **129**, 340-344.
13. C. Chmelik, J. Kärger, M. Wiebcke, J. Caro, J. M. van Baten and R. Krishna, *Micro. Meso. Mater.*, 2009, **117**, 22-32.
14. D. Tzoulaki, L. Heinke, H. Lim, J. Li, D. Olson, J. Caro, R. Krishna, C. Chmelik and J. Kärger, *Angew. Chem. Int. Ed.*, 2009, **48**, 3525-3528.
15. F. Hibbe, C. Chmelik, L. Heinke, S. Pramanik, J. Li, D. M. Ruthven, D. Tzoulaki and J. Kärger, *J. Am. Chem. Soc.*, 2011, **133**, 2804-2807.
16. C. Wiktor, M. Meledina, S. Turner, O. I. Lebedev and R. A. Fischer, *J. Mater. Chem. A*, 2017, **5**, 14969-14989.
17. A. A. Talin, A. Centrone, A. C. Ford, M. E. Foster, V. Stavila, P. Haney, R. A. Kinney, V. Szalai, F. El Gabaly, H. P. Yoon, F. Léonard and M. D. Allendorf, *Science*, 2014, **343**, 66-69.
18. K. J. Erickson, F. Léonard, V. Stavila, M. E. Foster, C. D. Spataru, R. E. Jones, B. M. Foley, P. E. Hopkins, M. D. Allendorf and A. A. Talin, *Adv. Mater.*, 2015, **27**, 3453-3459.
19. T. Neumann, J. Liu, T. Wächter, P. Friederich, F. Symalla, A. Welle, V. Mugnaini, V. Meded, M. Zharnikov, C. Wöll and W. Wenzel, *ACS Nano*, 2016, **10**, 7085-7093.
20. X. Chen, Z. Wang, P. Lin, K. Zhang, H. Baumgart, E. Redel and C. Wöll, *ECS Trans.*, 2016, **75**, 119-126.
21. L. Sun, G. Campbell Michael and M. Dincă, *Angew. Chem. Int. Ed.*, 2016, **55**, 3566-3579.
22. I. Stassen, N. Burtch, A. Talin, P. Falcaro, M. Allendorf and R. Ameloot, *Chem. Soc. Rev.*, 2017, **46**, 3185-3241.
23. C. Schneider, D. Ukaj, R. Koerver, A. A. Talin, G. Kieslich, S. P. Pujari, H. Zuilhof, J. Janek, M. D. Allendorf and R. A. Fischer, *Chem. Sci.*, 2018, **9**, 7405-7412.
24. T. M. Tovar, J. Zhao, W. T. Nunn, H. F. Barton, G. W. Peterson, G. N. Parsons and M. D. LeVan, *J. Am. Chem. Soc.*, 2016, **138**, 11449-11452.
25. M. Feyand, C. F. Seidler, C. Deiter, A. Rothkirch, A. Lieb, M. Wark and N. Stock, *Dalton Trans.*, 2013, **42**, 8761-8770.
26. Y. Liu, F. Meirer, P. A. Williams, J. Wang, J. C. Andrews and P. Pianetta, *J. Synchrotron Rad.*, 2012, **19**, 281-287.
27. G. R. Anderson and J. P. Devlin, *J. Phys. Chem.*, 1975, **79**, 1100-1102.
28. S. Matsuzaki, R. Kuwata and K. Toyoda, *Solid. State Commun.*, 1980, **33**, 403-405.
29. E. I. Kamitsos and W. M. Risen, *J. Chem. Phys.*, 1983, **79**, 5808-5819.
30. B. M. Weckhuysen, *Chem. Soc. Rev.*, 2010, **39**, 4557-4559.
31. E. Stavitski and B. M. Weckhuysen, *Chem. Soc. Rev.*, 2010, **39**, 4615-4625.
32. L. Zhang, M. J. Henson and S. S. Sekulic, *Anal. Chimica Acta*, 2005, **545**, 262-278.
33. O. A. Maslova, G. Guimbretière, M. R. Ammar, L. Desgranges, C. Jégou, A. Canizarès and P. Simon, *Mater. Charact.*, 2017, **129**, 260-269.

-
34. P. G. Gucciardi, S. Trusso, C. Vasi, S. Patanè and M. Allegrini, *Phys. Chem. Chem. Phys.*, 2002, **4**, 2747-2753.
35. P. M. Usov, H. Jiang, H. Chevreau, V. K. Peterson, C. F. Leong and D. M. D'Alessandro, *J. Phys. Chem. C*, 2017, **121**, 26330-26339.
36. J. S. Chappell, A. N. Bloch, W. A. Bryden, M. Maxfield, T. O. Poehler and D. O. Cowan, *J. Am. Chem. Soc.*, 1981, **103**, 2442-2443.
37. K. Thürmer, C. Schneider, V. Stavila, R. W. Friddle, F. Léonard, R. A. Fischer, M. D. Allendorf and A. A. Talin, *ACS Appl. Mater. Interfaces*, 2018, **10**, 39400-39410.
38. S.-i. Terashita, K. Nakatsu, Y. Ozaki and S. Takagi, *J. Phys. Chem.*, 1995, **99**, 3618-3628.
39. R. Bozio, A. Girlando and C. Pecile, *J. Chem. Soc., Faraday Trans.: Mol. Chem. Phys.*, 1975, **71**, 1237-1254.
40. M. Todaro, L. Sciortino, F. M. Gelardi and G. Buscarino, *J. Phys. Chem. C*, 2017, **121**, 24853-24860.
41. M. Todaro, A. Alessi, L. Sciortino, S. Agnello, M. Cannas, F. M. Gelardi and G. Buscarino, *J. Spectr.*, **2016**, **7**, 8074297.
42. M. Todaro, G. Buscarino, L. Sciortino, A. Alessi, F. Messina, M. Taddei, M. Ranocchiari, M. Cannas and F. M. Gelardi, *J. Phys. Chem. C*, 2016, **120**, 12879-12889.
43. N. Drenchev, E. Ivanova, M. Mihaylov and K. Hadjiivanov, *Phys. Chem. Chem. Phys.*, 2010, **12**, 6423-6427.
44. L. Alaerts, E. Séguin, H. Poelman, F. Thibault-Starzyk, P. A. Jacobs and D. E. De Vos, *Chem. Eur. J.*, 2006, **12**, 7353-7363.
45. P. St. Petkov, G. N. Vayssilov, J. Liu, O. Shekhah, Y. Wang, C. Wöll and T. Heine, *ChemPhysChem*, 2012, **13**, 2025-2029.
46. R. Giovine, F. Pourpoint, S. Duval, O. Lafon, J.-P. Amoureaux, T. Loiseau and C. Volkringer, *Cryst. Growth Des.*, 2018, **18**, 6681-6693.
47. D. Kim and H. Lee, *RSC Adv.*, 2015, **5**, 2749-2755.
48. J. M. Castillo, T. J. H. Vlugt and S. Calero, *J. Phys. Chem. C*, 2008, **112**, 15934-15939.
49. J. M. Lindquist and J. C. Hemminger, *Chem. Mater.*, 1989, **1**, 72-78.
50. M. C. Biesinger, L. W. M. Lau, A. R. Gerson and R. S. C. Smart, *Appl. Surf. Sci.*, 2010, **257**, 887-898.

Chapter 7

Summary, Concluding Remarks and Future Perspectives

In this Chapter, a summary of the PhD thesis and the research described herein is presented. A critical discussion of the possibilities and future lines of research will be given, including the extent to which the different aspects of Metal-Organic Framework (MOF) defect chemistry can be investigated at the different length scales of importance. We will emphasize how different properties of MOFs can be tuned via lattice disorder and how this could influence functional properties, such as catalysis. Moreover, we will propose additional experiments to elucidate the nature of Cr-based MOF catalysts for ethylene polymerization, besides suggesting potential strategies to their activity in ethylene polymerization. Finally, a section is provided describing the various challenges in characterizing redox active MOF materials and ways to assess their different oxidation states under dynamic reaction environment conditions.

7.1 SUMMARY AND CONCLUDING REMARKS

In this PhD thesis we have studied the chemistry of defects within Metal-Organic Frameworks (MOFs) as well as the properties of the related Defect-Engineered Metal-Organic Frameworks (DEMOFs). We also have investigated the potential roles of MOF and DEMOF materials as new solid catalysts or porous hosts for functional guests, being it metal nanoparticles or electroactive organic molecules.

Given the complexity of MOF materials, the wide variety of building blocks (*i.e.*, linker and nodes), topologies, morphologies, dynamic nature and broad potential applications (with a special focus on catalysis) must be rationalized in terms of general (physical) chemistry concepts. This is the topic of **Chapter 1**, which presents the core concepts behind MOF and DEMOF chemistry. A brief introduction on coordination chemistry, spectroscopy and an outline on what MOFs are and how they may be involved as solid catalysis is included. MOFs consist of multiple molecular units that assemble into porous materials (often crystalline, although that is not necessarily the case). Whether this occurs due to kinetic or thermodynamic reasons is still a matter of debate and depends on the framework structure, although it has been established that dense phases are energetically (mostly entropically) favoured.¹⁻³ In any case, given their multicomponent nature, studying MOF and DEMOF materials is a formidable challenge for both the spectroscopist and material scientist.

A literature survey of the various analytical methods used to study the relevant properties of MOF and DEMOF materials is presented in **Chapter 2**. This Chapter covers the techniques that are relevant for the bespoke applications, *i.e.* gas sorption; heterogeneous catalysis and redox/electroactive components. It was concluded that, in general, defects in the form of lattice disorders, cleaved metal-oxygen bonds or non-coordinating linkers affect the properties of MOFs. A broad toolkit of characterization techniques allowed us to assess and evaluate which properties are mostly affected in each case (*e.g.* surface polarity, metal oxidation state and porosity) when a change is induced in a MOF material. It is important to highlight here that the use of spatially resolved

spectroscopy is still limitedly used in the MOF field, which indicates that there are many opportunities for further research.

In **Chapter 3**, we have compared two MOF materials with the same building blocks, namely MIL-100(Fe) and Basolite®F300 (which has the same, or probably a very similar chemical composition), and different degrees of crystallinity, *i.e.* highly crystalline *vs.* amorphous. X-ray Diffraction (XRD) and Pair Distribution Function (PDF) demonstrated, respectively, that the long-range order is only present in the MIL-100(Fe) material, but that the bond distances for the first three coordination spheres are very similar when comparing MIL-100 and Basolite®F300, indicating that there are similar iron (III) trimers within both materials. Pyridine-probe FT-IR spectroscopy, X-ray Photoelectron Spectroscopy (XPS) and methanol sorption experiments revealed that the crystalline material is more polar (*i.e.*, acidic), probably due to better dispersed metal sites thanks to the high lattice order. This also affects how Pd molecular precursors are deposited onto the surface of these MOF materials and subsequently agglomerate into metal nanoparticles by using different synthesis methods. We have explored three synthesis methods, namely Incipient Wetness Impregnation (IWI), Colloidal Particle Deposition (CPD) and Chemical Vapor Infiltration (CVI). For instance, during the IWI preparation, and depending on the solvent used (*e.g.* water or chloroform) and the charge of the precursor (neutral or anionic), different materials can be obtained. When an aqueous solution of sodium chloropalladate was used, there is a broad distribution of the metal nanoparticle sizes for both type of materials, but a smaller nanoparticle size was found for MIL-100(Fe) (which is more hydrophilic). In contrast, when the pores were filled with a chloroform solution of palladium (II) acetylacetone, a narrower metal nanoparticle distribution was obtained, with *ca.* 7 nm for Basolite®F300, while it was *ca.* 14 nm for MIL-100(Fe), strengthening our hypothesis on surface polarity. Deposition of colloidally stabilized Pd particles with a hydrophobic capping agent further corroborated our hypothesis and showed less uptake and worse dispersion for the crystalline material (MIL-100(Fe)), suggesting a more hydrophilic surface. Finally, metal deposition from the gas phase with CVI showed a larger average size and a broader metal nanoparticle distribution for the less polar MOF material. Thus, we have shown that lattice order is an important feature

for affecting the properties of MOF materials. This conclusion is in line with what the group of Bennett has shown some years ago,⁴⁻¹⁰ *i.e.* amorphous (disordered) metal-organic frameworks may become of practical use upon careful design of their physicochemical properties.

The concept of disorder is also central to the theme covered in **Chapter 4**. In this Chapter, the effects of mixing MIL-100(Cr) and MIL-101(Cr) with a strong alkylating co-catalyst, namely Diethyl-Aluminium Chloride (DEA), for the polymerization of ethylene has been studied. Upon the addition of DEA to the MOF material, different structural changes were observed by X-ray Diffraction (XRD), indicating that the lattice was maintained for MIL-100(Cr), while it collapsed and became amorphous (disordered) in the case of MIL-101(Cr). Not only structural changes, but also the coordination and geometry of the Cr sites was modified, as revealed by UV-Vis and CO-probe FT-IR spectroscopies. These differences, together with the larger pore volume in the case of MIL-101(Cr), resulted in a strong contrast in activity for ethylene polymerization in the liquid phase for the different materials under study. Control experiments with the molecular analogue of the Secondary Building Unit (SBU) (*i.e.*, the Cr oxo-trimer unit), showed that this discrete compound is likely responsible for ethylene polymerization. This observation is further corroborated by the fact that the physical and molecular properties of the polyethylene produced by the complex and MIL-101(Cr) are almost identical. MIL-100(Cr) yielded virtually no polymer, a finding that was associated to the lower pore volume than that of MIL-101(Cr) (or the trimer compound, which is soluble in the liquid-phase). Finally, Scanning Electron Microscopy (SEM) imaging showed that although similar HDPE in terms of physical properties may be obtained by the discrete chromium (III) oxo-benzoate, the polymer morphology is optimal if MIL-101(Cr) is used as a catalyst. In this case, the product obtained consists of spherical beads of regular shapes and sizes, which seem not to be affected by the amount of co-catalyst added to the Cr-MOF material.

In **Chapter 5**, single-site defects in a HKUST-1 material, as created by the introduction of non-coordinating linkers into the solvothermal mixture,^{11, 12} are investigated. Following previous research, the aim was to better understand how defect linkers influence the

properties of a MOF material. We have studied the following aspects of DEMOF materials: i) the location of defective linkers at the inter- and intra-crystal level, ii) the effect of the defective linkers on the crystal size (and size distribution) and morphology, iii) the effect of defective linkers on the formation of mesopore structures; and iv) the effect of defective linkers on the nature of the Cu sites on the paddlewheels. We have shown by means of Raman micro-spectroscopy that defects aggregate in certain crystals as well as in defect-rich areas of a single crystal. Furthermore, the crystallite size decreases strongly with increasing amounts of the defective CYDC linker in the mixture, probably due to the coordination-modulation mechanism described in the literature.¹³⁻¹⁶ Another observation was that the presence of the defective CYDC linker leads to different mesopore regimes, ranging from 0 to *ca.* 14% volume of mesopores relative to total pore volume. The mesopores formed seem heterogeneous in shape and size, according to Small-angle X-ray Scattering (SAXS) measurements, suggesting a random distribution within defect-rich crystals. Lastly, experiments with Electron Paramagnetic Resonance (EPR), Diffuse Reflectance (DRS) UV-Vis spectroscopy and Py-probe FT-IR spectroscopies confirmed that increasing amounts of Cu⁺ sites are present when higher amounts of CYDC are present in the DEMOF material. Furthermore, NO-probe FT-IR spectroscopy showed that under similar conditions, nitrous oxide disproportionates differently for the 50 %mol CYDC material, compared to the parent HKUST-1 material. This confirms different reactivity patterns of the Cu sites embedded with the parent MOF and DEMOF material. This shows that single-site defect-linkers have a wide variety of effects on MOF materials at different levels of scale (*i.e.*, the atom-, meso-scale and inter-crystal scale). In order to obtain a complete understanding, more studies, including other analytical techniques and a more systematic approach towards different type of materials would be of great use.

Chapter 6 focuses on the same structure, namely HKUST-1, as **Chapter 5**. However, in this Chapter, HKUST-1 is used as a host for an electroactive molecule, namely TCNQ. We have studied the location of the TNCQ within large single crystals of HKUST-1 and have evaluated what the effect of water is in creating defects as well as on accommodating electron conduction pathways. First, by means of Raman micro-spectroscopy and Principal Component Analysis (PCA), we have pinpointed the regions with higher signal

(and thus concentration) of TCNQ within the HKUST-1 crystals, which are the edges. This was explained in terms of the formation of a layer of extraneous Cu-TCNQ coordination polymer on the surface (as shown by SEM), and of the initial TCNQ diffusion and later on coordination to the areas close to the crystal edge. The materials were measured again after a flow of water-saturated N₂, which seem to evenly spread the TCNQ molecules throughout the HKUST-1 crystals. Furthermore, the diffusion and hydration kinetics of the TCNQ-loaded and parent HKUST-1 crystals were compared with FT-IR spectroscopy, in order to conclude that TCNQ partially hinders the diffusion of molecules (even small ones, such as water). A set of analytical techniques further corroborated the effects observed. However, the mechanism by which electrons hop within crystals still merits further research, as well further research is needed to determine the nature of the charge transfer between TCNQ (radical, anionic, neutral) and the Cu²⁺ sites within HKUST-1 crystals.

7.3. OUTLOOK AND FUTURE PERSPECTIVES

In **Chapter 1**, we have described the fundamental concepts that need to be considered for the chemistry of DEMOF materials. One of the first measures that should be taken, not only in the frame of this PhD thesis, but in general in the field of MOFs, is to consistently develop a nomenclature for this kind of compounds. Although challenging (due to their modular nature and the, potentially, millions of possible molecular combinations), it would be important to select and assign names that better explain the compound (even if this is just an abbreviation of the linker and the metal the nodes are built of). For the non-experienced MOF researcher, understanding and studying each different structure already somewhat presents a burden of remembering the various codenames, that usually do not reflect the structure.¹⁷

Following the (potential) changes in the mindset of the members of the MOF community, which should address specific reactions in which MOFs can show their advantages, it would be very interesting to consistently develop new or better MOF catalysts. They should offer superior activities and selectivities than their zeolite, acidic resins, porous silicates or metal supported counterparts, as highlighted by Corma and others by means

of their special pore environments.^{18, 19} Given the fact that MOF and DEMOF materials will remain expensive compared to traditional porous silica (or other chemical composition) materials, carbon fibres or zeolite catalysts; one should first think of *niche* applications for MOFs and DEMOFs. For instance, many examples of asymmetric catalysts or separations may be found in the literature, and are potentially interesting lines for the future.²⁰⁻²⁵ For instance, one may introduce metal nanoparticles for different reactions, such as borylation (Ir), C-C or A³ couplings (Au, Pd) or hydrogenations (Pt, Rh) within the bespoke chiral MOF scaffolds.²⁶ Examples of this strategy have been already reported for COFs.²⁷ Other interesting strategy to create new solid catalysts may be to use defects as anchoring points for reactive species with enhanced diffusion properties and accessibility. For instance, Korzyński *et al.*,²⁸ deposited Methyl Tri-Oxorhenium (MTO) onto the Zr₆ dehydroxylated nodes of the NU-1000 MOF material. It could be interesting to prepare modulated UiO-66²⁹ or MOF-808³⁰ and deposit MTO in a similar fashion. These frameworks are less expensive than NU-1000, and may benefit from different reactivity for olefin metathesis (potentially including ring-opening polymerization or ring-closing metathesis).^{31, 32}

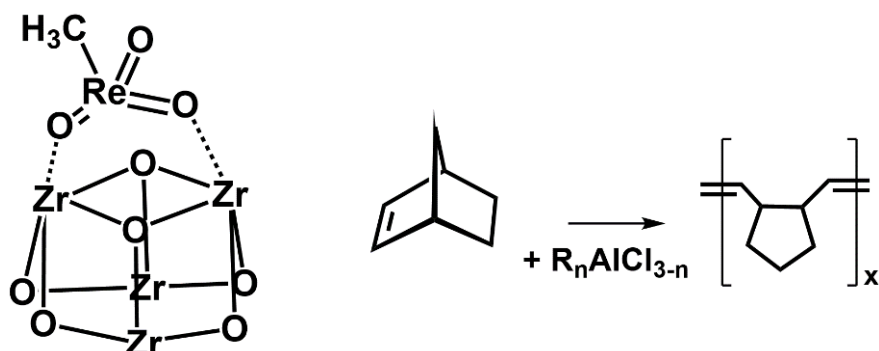


Figure 7.1. Methyl-Tri-Oxorhenium (MTO) grafted onto the Zr₆ nodes of UiO-66, MOF-808 or NU-1000. This may result, along with organo-aluminium as co-catalysts, in metathesis catalysts with enhanced or unique reactivity.

On the other hand, and as mentioned in the main text of this PhD thesis, the special coordination environments and porous confinement of metal sites in MOFs and DEMOFs require some further attention. As an example, one could combine the exciting, unique chemistry of stabilized cobalt (III) carbenes that are stabilized within Co(TTP) (TTP = tetraphenylporphyrins),³³⁻³⁵ with already existing frameworks (*e.g.* PCN-222(Co)) that contain the exact same linker [Co²⁺(pyrrole)₄] units, as described in Figure 7.2.³⁶

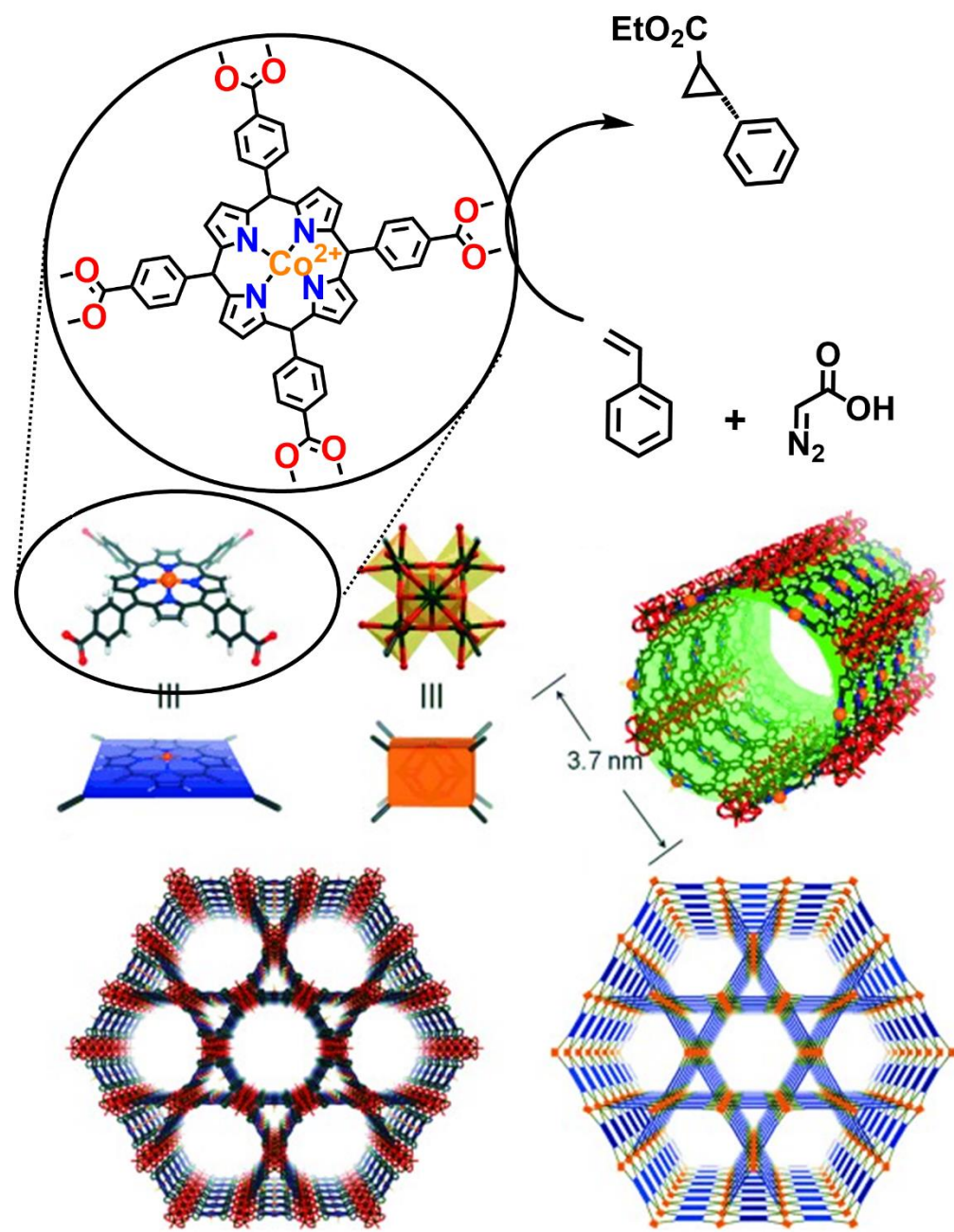


Figure 7.2. Possible combination of the PCN-222(Co) network (below) with radical chemistry for stereoselective cyclopropanations mediated by cobalt (III) carbenes stabilized within the porphyrin rings. Adapted and reprinted from reference [36]. Copyright © John Wiley & Sons, 2012.

In **Chapter 2**, we have presented an overview of the different analytical tools used for studying the linkers and metal nodes, as well as the different structural features during gas sorption or catalysis for the two specific topologies, described in this PhD thesis. Studying metal sites may be best done by selective-probe techniques, such as CO, NO, CD_3CN , pyridine, ... -probe FT-IR spectroscopy. However, in the case of defect sites, which

may be present in very low concentrations, more sensitive tools, such as EPR could be used. Such studies remain very necessary given the fact that their role in catalysis or electroconductivity could be important.^{37, 38}

As shown throughout the PhD thesis, we have demonstrated that bulk techniques are invaluable for the characterization of MOF and DEMOF materials. However, this research field also requires, in analogy to for example the field of zeolite-based catalyst materials, a more widespread use of microscopy and micro-spectroscopy tools, in order to unravel the effects of proximity, core-shell configurations or location of the active or defect phases within the pores. In this sense, the use of X-ray based techniques (rather than using electron-based beams, which are usually more damaging towards MOF and DEMOF materials), would be of high interest. For instance, imaging of pore cavities, crystallization defects, oxidation states and coordination of the metal nodes by tomographic tools (*e.g.* Transmission X-ray Microscopy (TXM) or tomography, X-ray holography or X-ray ptychography) are interesting lines of research. This is illustrated in Figure 7.3.^{39, 40}

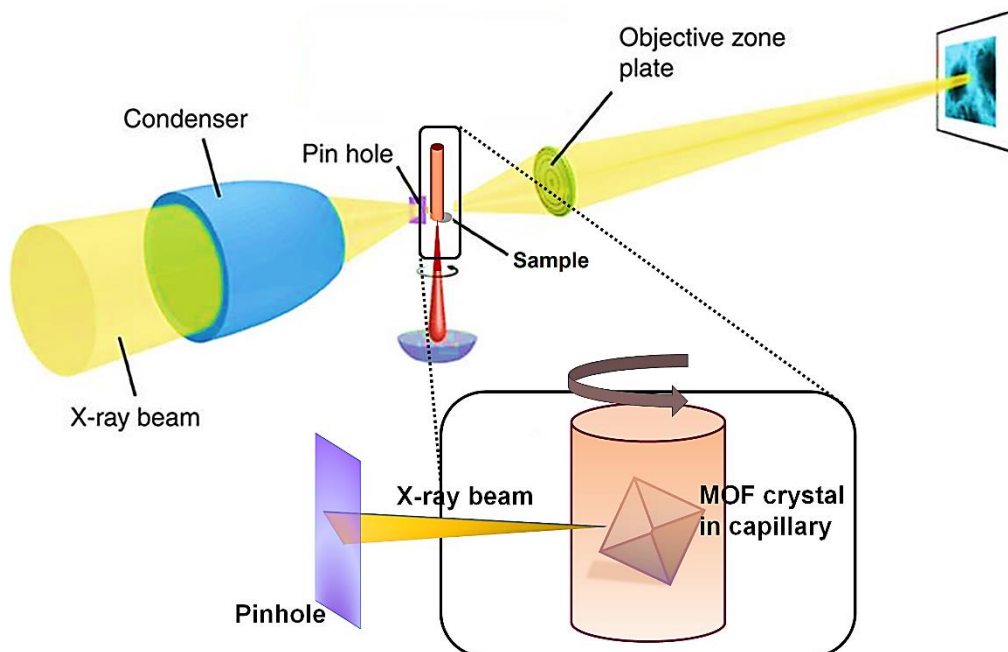


Figure 7.3. Scheme of an X-ray tomography experimental set-up with which 3-D reconstructions of a MOF material can be obtained when using Kapton® capillaries.

In **Chapter 3**, we have probed the effect of lattice disorder on the deposition and formation of Pd metal nanoparticles. Several questions remain open as for the surface properties of the materials. First, additional measurements on the structural differences,

including X-ray Absorption Near Edge Spectroscopy (XANES) and Extended X-ray Absorption Fine Structure (EXAFS), to study any different Fe species in terms of oxidation state and coordination geometry could be of great help. Furthermore, it would be necessary to quantitatively assess the number of acid sites (*i.e.*, both Brønsted and Lewis acid sites) in each material by using *e.g.* zeta potential measurements. Within this context, it is important to mention the Weitkamp hydrophobicity index or quantification of the Py-adsorbed FT-IR spectra *via* the Lambert-Beer law (after the appropriate determination of the molar absorption coefficient values).

Although this may help to obtain further information on the properties of the MOF surfaces, it may be of more interest to understand the Pd species after deposition and during growth in the case of impregnation. Although the IWI method is a process governed by solvent wetting and pore filling, the nature of the Pd species adsorbed after drying is still unknown. In this case, it would be very interesting to obtain X-ray absorption, UV-Vis and CO-probe FT-IR spectra after impregnation of the various Pd precursors, since there exist multiple possibilities of coordination (Figure 7.4).

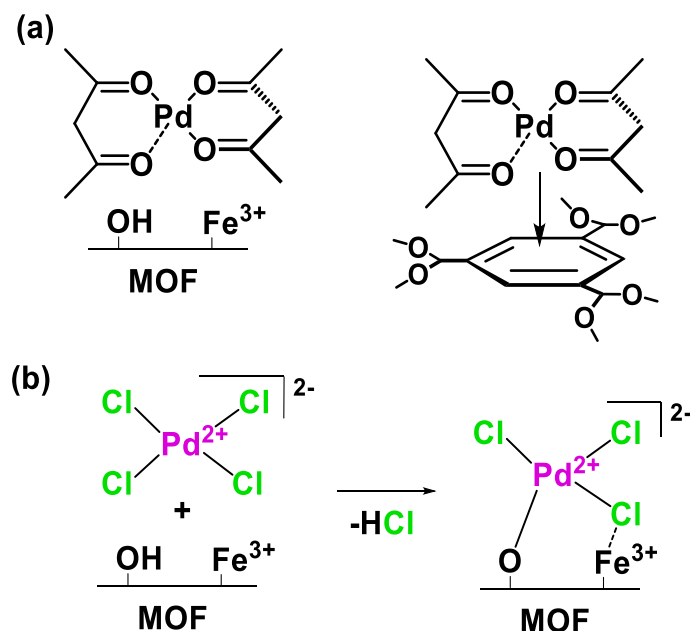


Figure 7.4. (a) Coordination of $\text{Pd}(\text{acac})_2$ with either acid sites or organic linker fragments of the MOF structure. (b) Interaction of Na_2PdCl_4 in aqueous solution at $\text{pH} = 6$, the precursor dissociates into 2Na^+ and PdCl_4^{2-} anions that likely interact with the positively charged surface of the MOF ($\text{IEP} \sim 4 - 4.5$).

It would also be beneficial to study the agglomeration of the dispersed metal nanoparticles during reduction under hydrogen atmosphere. For instance, newly developed characterization methods, such as *in-situ* TEM (although there is a risk of inducing beam damage), or *in-situ* X-ray Absorption Spectroscopy (XAS) experiments,⁴¹ may shed light on the agglomeration mechanism (Ostwald ripening *vs.* sintering) and the coordination and oxidation state of Pd during reduction, respectively.

When colloidally stabilized particles were used, the synthesis is carried out in trioctylphosphine, which is an apolar molecule. Thus, methanol provokes a certain agglomeration of the particles during deposition, which may not lead to optimal dispersion on the surface. Optimization of the conditions (*i.e.*, solvent, time, temperature and MOF:Pd ratio) may be of interest to further observe differences between crystalline and amorphous MOF.

In **Chapter 4**, we have investigated the potential of MIL-101(Cr) as a catalyst for the polymerization of ethylene in the liquid phase and have elucidated the active sites that are formed upon mixing with the co-catalyst. It is well-known that Cr-based catalysts are greatly affected by almost every parameter in ethylene polymerization and oligomerization.^{42, 43} Thus, there is plenty of room for modifying the polymer obtained by means of optimization:

- Reactor configuration, (slurry or even gas-phase after using different activation procedures), stirring speed or blade geometry may affect geometry of the polymer and viscosity of the medium during catalysis.
- Reaction solvent (aliphatics, such as methylcyclopentane or cyclohexane) are typically better than aromatics, due to enhanced interaction of the π-system with the Cr centres that leads to poisoning or decrease in the insertion rate).⁴⁴
- Different co-catalysts, *e.g.* borate Lewis pairs such as $[(C_nH_{2n+2})_2NHMe]^+[B(C_6F_5)_4]^-$,⁴⁵ or triethyl aluminium, Methyl-Aluminoxane (MAO), Modified-Methyl-Aluminoxane (MMAO);⁴² which have a direct impact on activity.
- The introduction of ligands in solution (*e.g.*, pincer phosphines, scorpionates or thiolates) may drive the selectivity towards different olefin products.

- Use of different metals (*i.e.*, Ti and Fe)⁴⁶ introduced by post-synthetic modification to *in-situ* generate lower olefins, thus, change branching and morphology of the polymer formed.

The modification of these parameters stirs the metallacycle *vs.* Cossee-Arlmann insertion ratio, giving rise to either gaseous or liquid light olefins instead of a polymeric product. Investigation of these products by means of gas chromatography could shed more light onto the active sites and explain the differences observed between the MIL-100 and MIL-101 materials. Furthermore, in order to better understand the different active sites, X-ray absorption and photoelectron spectroscopies of the materials after reaction with the co-catalyst (*i.e.*, short timespans due to the short lifetime of the alkylated sites) could be used. They could be coupled to periodic calculations to assign the different spectroscopic features observed. Another interesting way of tuning catalyst activity and selectivity, maybe to tailor the functional groups on the MOF linker (MIL-101) to study the effects on polymerization activity and selectivity. Not only functional groups, but also different Cr-based MOFs with different topologies could be used as solid catalysts too, with a study of its own necessary for each topology.

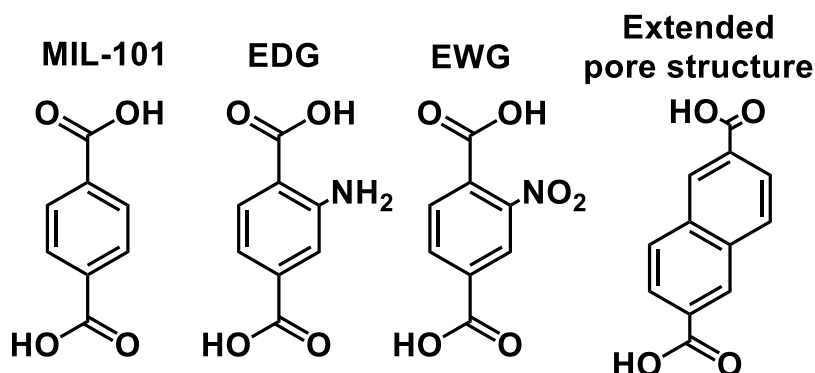


Figure 7.4. Different linkers that may be used for tuning activity, molecular architecture and morphology of polyethylene by using MIL-101(Cr) analogues for ethylene polymerization. Terephthalic acid corresponds to the parent MIL-101 framework, while the R = -NH₂ group would act as an Electron Donating Group (EDG) and the R = -NO₂ would act as an Electron Withdrawing Group (EDG). Finally, by using 2,6-naphthalenedicarboxylic acid, the pore size can be increased, which may lead to different activity too.

Moreover, a more detailed study of the polymer materials made, including ¹³C NMR, Melt Flow Index (MFI) and dynamic viscosity and moduli, may provide information on branching and physical properties, that can, in term, be related to different active sites.

In **Chapter 5**, defect-engineered HKUST-1 crystals were prepared in order to study the spatial distribution of defect-linkers, the structure of mesopores, the crystal size and morphology and the nature of the Cu defective paddlewheels. One of the important questions that remains unanswered, is the defect-linker distribution at the single-crystal level. It may be of interest to select here HKUST-1 crystals with high and lower content of CYDC linker and chemically image them by means of Photothermally Induced IR (PT-IR) microscopy, Atomic Force Microscopy combined with Infrared Spectroscopy (AFM-IR), Tip-Enhanced Raman Spectroscopy (TERS) or μ -XRD techniques so as to determine if the linkers are actually incorporated (and how) into the DEMOF lattice, or if Cu(CYDC) coordination polymers are embedded or interpenetrated in those HKUST-1 crystallites. Furthermore, it would be interesting to study if the effect of the heterogeneous distribution of defect-linker ('zoning') occurs with other non-coordinating linkers as well, such as those used in the literature.^{37,47} Not only the linkers, but also in other metal nodes could be studied. In other words, it would be worthwhile to validate the zoning concepts also for Ru-, Rh-, Co- or Ni-containing DEMOF materials.⁴⁷⁻⁴⁹.

In order to better understand the X-ray scattering data obtained, modelling the pore geometry and fitting it (if possible) to the experimental values may help in understanding the agglomeration of defects into mesoporous voids. Other than mesopores, *in-situ* spectroscopies (*e.g.*, Raman, UV-Vis and X-ray absorption)^{50, 51} and scattering (SAXS);⁵²⁻⁵⁴ and particle size determination by means of dynamic light scattering during crystallization may shed light on the mechanisms by which the linker modulates crystal size. Lastly, the precise nature of the Cu sites remains an open question (as it does for the case of the parent HKUST-1 framework), in the sense that FT-IR spectroscopy with probe molecules (*e.g.* NO) would need to be applied more systematically to all the series of CYDC concentrations of importance. Moreover, different heat treatments (*e.g.*, temperature, time and ramp) for the activation protocol have shown to greatly affect the Cu⁺ content in MOF materials, implying the need to systematically address this issue too for the different CYDC concentrations in DEMOF materials.⁵⁵⁻⁵⁹ Modelling with Density Functional Theory (DFT) methods of the NO binding modes to plausible defective Cu⁺ paddlewheels may be of interest to (better) assign every band present in the spectra. Finally, experiments with

alkylpyridines may help in locating defect sites within the DEMOF materials. If the metal density allows for it, mapping of the different Cu oxidation states may be done by means of Scanning Transmission X-ray Microscopy (STXM), or with different cyanide probes.

Finally, in **Chapter 6**, we have studied the location of TCNQ as guest molecule within HKUST-1 crystals as host. This was done by deposition from the gas phase and these guest-host materials have been investigated before and after exposure to water vapor. More specifically, we have probed the kinetics of water diffusion by means of *in-situ* FT-IR microscopy and correlated these findings to conductivity measurements. The next step would now be to obtain quantitative measures of the water introduced within the high-temperature cell used for *in-situ* XRD since in this case only a bubbler was used to introduce N₂ saturated with water at 298 K. Furthermore, it would be interesting to measure conductivity and Electrochemical Impedance Spectroscopy (EIS) after this exposure, rather than just exposure to air and moisture, in order to systematically compare the hydration conditions. By using PCA, we have located TCNQ species within large HKUST-1 crystals and assigned the signals under the broad bands at *ca.* 2225 cm⁻¹ to different TCNQ (radical, bonded, ...) species. As mentioned above, the charge transfer situation that likely goes *via* σ -donation from the N atoms to the Cu²⁺ centres is not completely understood (to which extent reduction or radical formation occurs). On the other hand, the role of Cu⁺ defects that maybe present (as shown in the literature as well as in **Chapter 2** and **Chapter 5**) play, is also an interesting line of research, since these defects may affect the percolation network that allows electron hopping. It is well-known that Cu(TCNQ) is a conductive material, and its formation on the outer layer of the surface may contribute to the overall conductivity of the guest-host composite material.

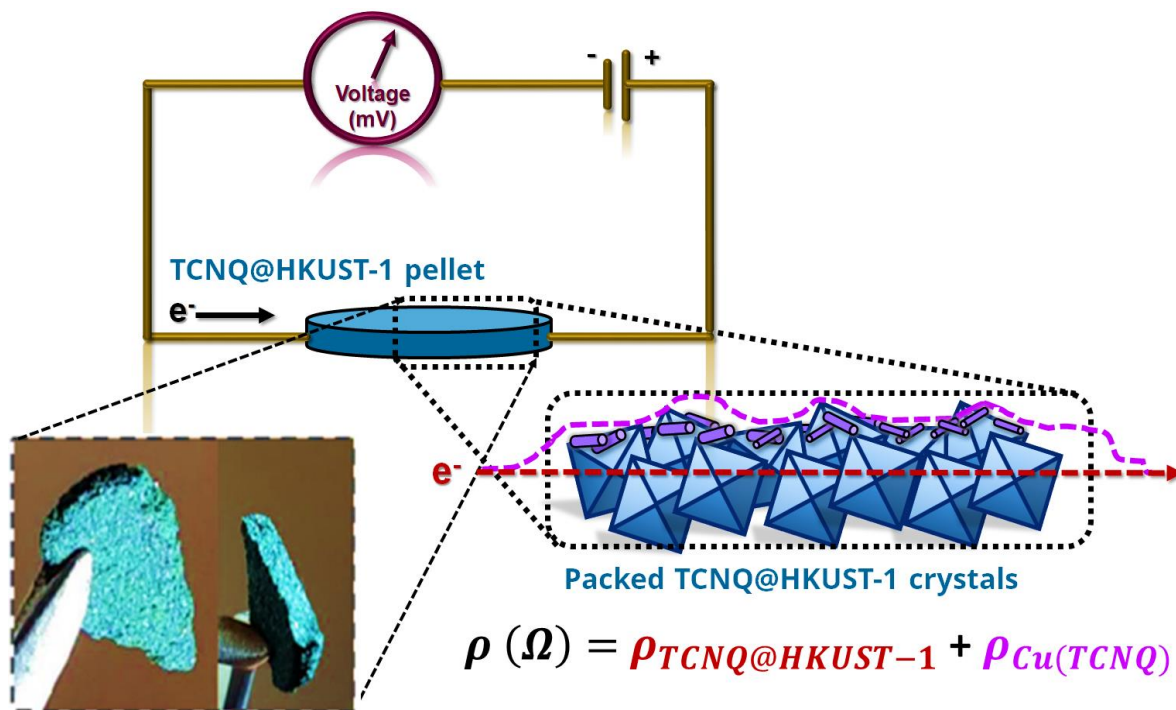


Figure 7.5. Different parts of the pellet made out of TCNQ@HKUST-1 material may have different resistivities (or conductivities) that contribute to the total resistivity, given the fact that electrons may flow through the loaded TCNQ@HKUST-1 crystals or *via* the Cu(TCNQ) coordination polymer on the surface.

As demonstrated by Schneider *et al.*,⁶⁰ it is possible to obtain a clean surface for TCNQ-loaded HKUST-1. Thus, a potential set of experiments may be to use Kelvin-probe Force Microscopy (KPFM), to measure the surface potential of local areas where Cu(TCNQ) may be found, and compare this to that of a clean HKUST-1. Moreover, as mentioned above, it may be interesting to determine the different oxidation states of the metal nodes (*i.e.*, Cu) throughout a single MOF crystal by means of *e.g.* STXM. As a general outlook remark, it could be of interest to relate the results obtained for single MOF and DEMOF crystals to those obtained for micrometric powders (10-20 μm), which are the typical sizes for commercial HKUST-1 and are likely to be used as conductive devices in case these materials would reach commercial application.

7.4. REFERENCES

1. A. J. Rieth, A. M. Wright and M. Dincă, *Nat. Rev. Mater.*, 2019, **4**, 708-725.
2. A. K. Cheetham, G. Kieslich and H. H. M. Yeung, *Acc. Chem. Res.*, 2018, **51**, 659-667.
3. J. Xing, L. Schweighauser, S. Okada, K. Harano and E. Nakamura, *Nat. Commun.*, 2019, **10**, 3608.

-
4. J. Hou, C. W. Ashling, S. M. Collins, A. Krajnc, C. Zhou, L. Longley, D. N. Johnstone, P. A. Chater, S. Li, M.-V. Coulet, P. L. Llewellyn, F.-X. Coudert, D. A. Keen, P. A. Midgley, G. Mali, V. Chen and T. D. Bennett, *Nat. Commun.*, 2019, **10**, 2580.
5. T. D. Bennett, A. K. Cheetham, A. H. Fuchs and F.-X. Coudert, *Nat. Chem.*, 2017, **9**, 11-16.
6. T. D. Bennett, T. K. Todorova, E. F. Baxter, D. G. Reid, C. Gervais, B. Bueken, B. Van de Voorde, D. De Vos, D. A. Keen and C. Mellot-Draznieks, *Phys. Chem. Chem. Phys.*, 2016, **18**, 2192-2201.
7. T. D. Bennett, A. H. Fuchs, A. K. Cheetham and F.-X. Coudert, *Dalton Trans.*, 2016, **45**, 4058-4059.
8. T. Tian, J. Velazquez-Garcia, T. D. Bennett and D. Fairn-jimenez, *J. Mater. Chem. A*, 2015, **3**, 2999-3005.
9. T. D. Bennett and A. K. Cheetham, *Acc. Chem. Res.*, 2014, **47**, 1555-1562.
10. T. D. Bennett, S. Cao, J. C. Tan, D. A. Keen, E. G. Bithell, P. J. Beldon, T. Friscic and A. K. Cheetham, *J. Am. Chem. Soc.*, 2011, **133**, 14546-14549.
11. S. Marx, W. Kleist and A. Baiker, *J. Catal.*, 2011, **281**, 76-87.
12. Z. Fang, J. P. Dürholt, M. Kauer, W. Zhang, C. Lochenie, B. Jee, B. Albada, N. Metzler-Nolte, A. Pöppl, B. Weber, M. Muhler, Y. Wang, R. Schmid and R. A. Fischer, *J. Am. Chem. Soc.*, 2014, **136**, 9627-9636.
13. R. J. Marshall, C. L. Hobday, C. F. Murphie, S. L. Griffin, C. A. Morrison, S. A. Moggach and R. S. Forgan, *J. Mater. Chem. A*, 2016, **4**, 6955-6963.
14. B. Seoane, S. Castellanos, A. Dikhtierenko, F. Kapteijn and J. Gascon, *Coord. Chem. Rev.*, 2016, **307**, Part 2, 147-187.
15. P. Cubillas, M. W. Anderson and M. P. Attfield, *Chem. Eur. J.*, 2012, **18**, 15406-15415.
16. A. Umemura, S. Diring, S. Furukawa, H. Uehara, T. Tsuruoka and S. Kitagawa, *J. Am. Chem. Soc.*, 2011, **133**, 15506-15513.
17. S. R. Batten, N. R. Champness, X.-M. Chen, J. Garcia-Martinez, S. Kitagawa, L. Ohrstrom, M. O'Keeffe, M. P. Suh and J. Reedijk, *CrystEngComm*, 2012, **14**, 3001-3004.
18. J. Gascon, A. Corma, F. Kapteijn and F. X. Llabrés i Xamena, *ACS Catal.*, 2014, **4**, 361-378.
19. A. Corma, H. García and F. X. Llabrés i Xamena, *Chem. Rev.*, 2010, **110**, 4606-4655.
20. T. Sawano, N. C. Thacker, Z. Lin, A. R. McIsaac and W. Lin, *J. Am. Chem. Soc.*, 2015, **137**, 12241-12248.
21. M. Yoon, R. Srirambalaji and K. Kim, *Chem. Rev.*, 2012, **112**, 1196-1231.
22. L. Ma, C. Abney and W. Lin, *Chem. Soc. Rev.*, 2009, **38**, 1248-1256.
23. S.-H. Cho, B. Ma, S. T. Nguyen, J. T. Hupp and T. E. Albrecht-Schmitt, *Chem. Commun.*, 2006, 2563-2565.
24. C.-D. Wu, A. Hu, L. Zhang and W. Lin, *J. Am. Chem. Soc.*, 2005, **127**, 8940-8941.
25. S. M. J. Rogge, A. Bavykina, J. Hajek, H. Garcia, A. I. Olivos-Suarez, A. Sepulveda-Escribano, A. Vimont, G. Clet, P. Bazin, F. Kapteijn, M. Daturi, E. V. Ramos-Fernandez, F. X. Llabres i Xamena, V. Van Speybroeck and J. Gascon, *Chem. Soc. Rev.*, 2017, **46**, 3134-3184.
26. S. Bhattacharjee, I. M. Khan, X. Li, Q.-L. Zhu and X.-T. Wu, *Catalysts*, 2018, **8**, 3, 120.
27. H.-C. Ma, C.-C. Zhao, G.-J. Chen and Y.-B. Dong, *Nat. Commun.*, 2019, **10**, 3368.
28. M. D. Korzyński, D. F. Consoli, S. Zhang, Y. Román-Leshkov and M. Dincă, *J. Am. Chem. Soc.*, 2018, **140**, 6956-6960.
29. G. C. Shearer, S. Chavan, S. Bordiga, S. Svelle, U. Olsbye and K. P. Lillerud, *Chem. Mater.*, 2016, **28**, 3749-3761.
30. H. H. Mautschke, F. Drache, I. Senkovska, S. Kaskel and F. X. Llabrés i Xamena, *Catal. Sci. Technol.*, 2018, **8**, 3610-3616.
31. T. Bein, C. Huber, K. Moller, C.-G. Wu and L. Xu, *Chem. Mater.*, 1997, **9**, 2252-2254.
32. W. A. Herrmann, W. Wagner, U. N. Flessner, U. Volkhardt and H. Komber, *Angew. Chem. Int. Ed.*, 1991, **30**, 1636-1638.
33. M. Otte, P. F. Kuijpers, O. Troeppner, I. Ivanović-Burmazović, J. N. H. Reek and B. de Bruin, *Chem. Eur. J.*, 2014, **20**, 4880-4884.
34. C. te Grotenhuis, N. van den Heuvel, J. I. van der Vlugt and B. de Bruin, *Angew. Chem. Int. Ed.*, 2018, **57**, 140-145.
35. A. S. Karns, M. Goswami and B. de Bruin, *Chem. Eur. J.*, 2018, **24**, 5253-5258.
36. D. Feng, Z.-Y. Gu, J.-R. Li, H.-L. Jiang, Z. Wei and H.-C. Zhou, *Angew. Chem. Int. Ed.*, 2012, **51**, 10307-10310.
37. Z. Fang, B. Bueken, D. E. De Vos and R. A. Fischer, *Angew. Chem. Int. Ed.*, 2015, **54**, 7234-7254.
38. D. S. Sholl and R. P. Lively, *J. Phys. Chem. Lett.*, 2015, **6**, 3437-3444.
39. F. C. Hendriks, S. Mohammadian, Z. Ristanović, S. Kalirai, F. Meirer, E. T. C. Vogt, P. C. A. Bruijnincx, H. C. Gerritsen and B. M. Weckhuysen, *Angew. Chem. Int. Ed.*, 2018, **57**, 257-261.
-

-
40. F. Meirer, D. T. Morris, S. Kalirai, Y. Liu, J. C. Andrews and B. M. Weckhuysen, *J. Am. Chem. Soc.*, 2015, **137**, 102-105.
41. N. Yuan, V. Pascanu, Z. Huang, A. Valiente, N. Heidenreich, S. Leubner, A. K. Inge, J. Gaar, N. Stock, I. Persson, B. Martín-Matute and X. Zou, *J. Am. Chem. Soc.*, 2018, **140**, 8206-8217.
42. M. P. McDaniel, *Adv. Catal.*, 2010, **53**, 123-606.
43. O. L. Sydora, *Organometallics*, 2019, **38**, 997-1010.
44. K. Albahily, Y. Shaikh, Z. Ahmed, I. Korobkov, S. Gambarotta and R. Duchateau, *Organometallics*, 2011, **30**, 4159-4164.
45. Y. Gao, J. Chen, Y. Wang, D. B. Pickens, A. Motta, Q. J. Wang, Y.-W. Chung, T. L. Lohr and T. J. Marks, *Nat. Catal.*, 2019, **2**, 236-242.
46. J. Castells-Gil, N. M. Padial, N. Almora-Barrios, I. da Silva, D. Mateo, J. Albero, H. García and C. Martí-Gastaldo, *Chem. Sci.*, 2019, **10**, 4313-4321.
47. O. Kozachuk, I. Luz, F. X. Llabrés i Xamena, H. Noei, M. Kauer, H. B. Albada, E. D. Bloch, B. Marler, Y. Wang, M. Muhler and R. A. Fischer, *Angew. Chem. Int. Ed.*, 2014, **53**, 7058-7062.
48. W. R. Heinz, T. Kratky, M. Drees, A. Wimmer, O. Tomanec, S. Günther, M. Schuster and R. A. Fischer, *Dalton Trans.*, 2019, **48**, 12031-12039.
49. D. M. Shakya, O. A. Ejegbawo, T. Rajeshkumar, S. D. Senanayake, A. J. Brandt, S. Farzandh, N. Acharya, A. M. Ebrahim, A. I. Frenkel, N. Rui, G. L. Tate, J. R. Monnier, K. D. Vogiatzis, N. B. Shustova and D. A. Chen, *Angew. Chem. Int. Ed.*, 2019, **58**, 16533-16537.
50. Y. Wu and D. Qin, *J. Am. Chem. Soc.*, 2018, **140**, 8340-8349.
51. M. J. Van Vleet, T. Weng, X. Li and J. R. Schmidt, *Chem. Rev.*, 2018, **118**, 3681-3721.
52. M. G. Goesten, E. Stavitski, J. Juan-Alcañiz, A. Martínez-Joaristi, A. V. Petukhov, F. Kapteijn and J. Gascon, *Catal. Today*, 2013, **205**, 120-127.
53. J. Juan-Alcaniz, M. Goesten, A. Martinez-Joaristi, E. Stavitski, A. V. Petukhov, J. Gascon and F. Kapteijn, *Chem. Commun.*, 2011, **47**, 8578-8580.
54. E. Stavitski, M. Goesten, J. Juan-Alcañiz, A. Martínez-Joaristi, P. Serra-Crespo, A. V. Petukhov, J. Gascon and F. Kapteijn, *Angew. Chem. Int. Ed.*, 2011, **50**, 9624-9628.
55. L. Alaerts, E. Séguin, H. Poelman, F. Thibault-Starzyk, P. A. Jacobs and D. E. De Vos, *Chem. Eur. J.*, 2006, **12**, 7353-7363.
56. J. Szanyi, M. Daturi, G. Clet, D. R. Baer and C. H. F. Peden, *Phys. Chem. Chem. Phys.*, 2012, **14**, 4383-4390.
57. S. Bordiga, L. Regli, F. Bonino, E. Groppo, C. Lamberti, B. Xiao, P. S. Wheatley, R. E. Morris and A. Zecchina, *Phys. Chem. Chem. Phys.*, 2007, **9**, 2676-2685.
58. C. Prestipino, L. Regli, J. G. Vitillo, F. Bonino, A. Damin, C. Lamberti, A. Zecchina, P. L. Solari, K. O. Kongshaug and S. Bordiga, *Chem. Mater.*, 2006, **18**, 1337-1346.
59. N. Drenchev, M. H. Rosnes, P. D. C. Dietzel, A. Albinati, K. Hadjiivanov and P. A. Georgiev, *J. Phys. Chem. C*, 2018, **122**, 17238-17249.
60. C. Schneider, D. Ukaj, R. Koerver, A. A. Talin, G. Kieslich, S. P. Pujari, H. Zuilhof, J. Janek, M. D. Allendorf and R. A. Fischer, *Chem. Sci.*, 2018, **9**, 7405-7412.

NEDERLANDSE SAMENVATTING

Metal-Organic Framework (MOF) materialen bestaan uit metaalionen of clusters (meestal overgangsmetaalionen en aardalkali ionen) gebonden aan multidentaat organische liganden die op regelmatige wijze 3-D-netwerken met micro- (of meso-) poreuze holtes creëren. Dit betekent dat ze vaak kristallijn zijn, hoewel zeer recentelijk ook ongeordende en amorf MOF-materialen de aandacht hebben getrokken. MOF-materialen zijn het onderwerp van uitgebreid onderzoek gedurende de afgelopen 30 jaar. Het veld kent zijn begin in de belangrijke ontdekkingen van onder meer Robson, Kitagawa en Yaghi. Het feit dat MOF-materialen zo poreus zijn, heeft onderzoek op veel toepassingsgebieden gestimuleerd, waaronder (selectieve) adsorptie en scheidingen (zowel van vloeistoffen als gassen), medicijnafgifte of elektrisch geleiding. Afgezien van deze praktische toepassingen is een van de andere mogelijke toepassingsgebieden katalyse.

Zoals vele andere materialen in de natuur, zijn MOF-materialen verre van ideale structuren en bevatten ze vaak onregelmatigheden op de schaal van micrometers en nanometers en zelfs op het niveau van atomen. Naast natuurlijk voorkomende defecten hebben onderzoekers aangetoond dat defecten ook expres kunnen worden geïntroduceerd om bepaalde chemische bindingen te splitsen of andere nieuwe chemische bindingen te creëren. Omdat hun structuur bovendien wiskundig kan worden beschreven als een rooster volgens de grondslagen van de groepentheorie; andere soorten defecten kunnen ook bestaan, zoals gebieden waar de atomen niet op periodieke wijze zijn gerangschikt. Afhankelijk van de aanwezige defecten in MOF-materialen, kan men verschillende fysische en chemische eigenschappen van deze materialen wijzigen en ze dus voor bepaalde toepassingen selectief aanpassen. Van daar ook de naam *Defect-Engineered* MOF (DEMOF) materialen. In dit proefschrift hebben we bijzondere aandacht besteed aan deze DEMOF-materialen als zodanig, evenals hun vermogen om moleculen (bv. een geleidend molecule) of andere structuren (bv. clusters van metaalatomen) in hun poriën te plaatsen. Daarnaast hebben we ook de mogelijkheid onderzocht om defecten te creëren door ze te mengen met een reactief molecule dat actieve locaties voor polymerisatiereacties creëert. Kortom, we hebben een breed scala aan spectroscopische,

microscopische en verstrooiingsmethodes, naast andere meettechnieken, gebruikt om MOF- en DEMOF-materialen in detail te bestuderen en daardoor beter te begrijpen.

In **Hoofdstuk 1** hebben we de fundamentele gebieden van de chemie beschreven waarmee deze MOF-materialen kunnen begrepen: i) coördinatiechemie, d.w.z. de chemie van verbindingen die coördinatieverbindingen bevatten (meestal overgangsmetaalionen met organische moleculen) waarin de d orbitalen (van het metaal) interactie aangaat met de s of p orbitalen (van de organische liganden); ii) kristaltheorie en hoe materialen periodiek worden samengevoegd tot macrostructuren, evenals de defecten die ze kunnen bevatten; iii) de begrippen en thermodynamica van chemische kinetiek en katalyse, en hoe chemische reacties optreden; en ten slotte iv) de elektronische en atomaire structuur van materie en hoe spectroscopische technieken gebruikt kunnen worden om ze in detail te bestuderen. Bovendien wordt een beschrijving van de *state-of-the-art* onderzoek naar MOF-materialen en hun potentieel als katalysatoren beschreven. Hierbij is er aandacht voor de praktische uitdagingen en interessante kansen, die MOF- en DEMOF-materialen bieden.

Naar aanleiding van deze concepten hebben we in **Hoofdstuk 2** twee chemische kristalstructuren geïntroduceerd met een specifieke rangschikking (dit zijn topologieën) die in dit proefschrift uitvoerig worden onderzocht. Het gaat hier om MOF-199 (ook bekend als HKUST-1, CuBTC of $[Cu_3(BTC)_2]$) en MIL-100 en 101 (twee structuren die isoreticulair zijn, wat dezelfde topologie met verschillende bouwstenen betekent). In dit hoofdstuk wordt een uitgebreid overzicht gegeven van de verschillende analytische technieken, die door andere onderzoeksgroepen worden gebruikt, om deze twee verschillende materialen te karakteriseren en daardoor beter te begrijpen. We hebben specifiek gewezen op de mogelijkheden van *in-situ* en *operando* technieken, die het mogelijk maken om de dynamiek van chemische bindingen en ruimtelijke structuur te bestuderen, terwijl de MOF-materialen zich onder reactieve omstandigheden bevinden (d.w.z. bij hoge druk en temperatuur en/of in de aanwezigheid van andere (reactieve) moleculen). In deze zin zijn *Fourier-Transform Infrared* (FT-IR) spectroscopie, evenals röntgenabsorptie- en emissietechnieken (bijvoorbeeld XPS, XANES of EXAFS) van enorm

belang geweest om de zogenaamde coördinatief onverzadigde sites (CUS) in MOF-materialen te begrijpen. Deze CUS-plaatsen zijn metaalatomen die zich kunnen binden aan moleculen in de poriën vanwege de vrije posities eromheen. Met deze kennis in de hand probeerden we de eigenschappen van een selectie van de op maat gemaakte MOF-materialen beter te begrijpen, die bekend zijn vanwege hun chemische en thermische stabiliteit.

In **Hoofdstuk 3** hebben we de structuur van MIL-100 (Fe), die een zeer poreus en kristallijn materiaal heeft, vergeleken met een commercieel materiaal met identieke bouwstenen bekend als Basolite®F300. Ze zijn beide samengesteld uit Fe-atomen en 1,3,5-benzentricarboxylaateenheden; met zeer vergelijkbare stoichiometrieën. Ons onderzoek, inclusief de metingen met röntgendiffractie en verstrooiing, stikstofadsorptie bij lage temperaturen en methanolsorptie, evenals koolmonoxide- en pyridinesonde FT-IR-spectroscopie, tonen aan dat beide materialen heel sterk verschillen in hun eigenschappen. Verder konden we aantonen dat MIL-100 (Fe) iets zuurder, in tegenstelling tot eerdere studies, is dan de amorfde analoge Basolite®F300. Dit heeft invloed op hun oppervlakte-energieën wanneer Pd-nanokristallen, atomen of moleculaire complexen erop en in de poriën worden verspreid. Dit is van belang omdat dit een typische methode is om katalysatormaterialen te verkrijgen met grote metaaloppervlakken (die nodig zijn om chemische reacties uit te voeren), terwijl ze aan grotere dragermaterialen gehecht blijven die voorkomen dat ze opnieuw agglomereren. We hebben dus aangetoond dat zelfs voor een identieke MOF chemische samenstelling, de lange afstand organisatie in 3-D van de bouwstenen van een MOF-materiaal sterk kan verschillen. Hierdoor ontstaan er ook andere eigenschappen, die van belang kunnen zijn in bijvoorbeeld de katalyse.

In **Hoofdstuk 4** hebben we beschreven hoe dezelfde MIL-101 topologie, maar nu bestaande uit Cr-atomen (in tegenstelling tot de Fe-atomen in **Hoofdstuk 3**); kan worden gebruikt voor het maken van materialen die ethyleen kunnen omzetten in polyethyleen. We hebben onderzocht hoe deze structuur en de isoreticulaire MIL-100 reageren op een sterk alkylenderende verbinding, meer in het bijzonder, diethylaluminiumchloride.

Röntgendiffractie en koolmonoxide in combinatie met FT-IR spectroscopie, evenals UV-Vis spectroscopie, hebben ons geholpen om te begrijpen wat het proces is dat plaatsvindt voor beide materialen na het mengen met hogergenoemde verbinding. Ten slotte hebben we de morfologieën van het polyethyleen onderzocht, dat ontstaat wanneer de polymerisatiereactie van ethyleen wordt uitgevoerd met de verschillende materialen die we onderzochten. De verschillen in reactiviteit kunnen geraationaliseerd worden op basis van de poriestructuur en holtes van elk materiaal (die vergelijkbaar zijn, maar verschillen in volume). Onze hypothese was dat het MIL-101 materiaal voldoende polymeer kan maken om te blijven reageren, terwijl MIL-100 onvoldoende volume heeft om verder op te breken tijdens de polymerisatie van ethyleen, waardoor de verdere polymerisatie wordt voorkomen. Over het algemeen hebben we laten zien hoe men MOF-materialen defecten kunnen maken door een reactieve verbinding toe te voegen om het materiaal katalytisch actief te maken.

In **Hoofdstuk 5** hebben we een welbekende strategie gebruikt om DEMOF-materialen met de HKUST-1 structuur te maken. Hiertoe hebben we de organische linker, die werd gebruikt om de ideale MOF-structuur te synthetiseren, gemengd met een organische linker, die gedeeltelijk is afgekapt en specifieke puntdefecten creëert in het MOF-materiaal. Deze introductie van defecten beïnvloedt de eigenschappen van het metaal in de omgeving, Cu in dit geval, en leidt tot belangrijke veranderingen in de oxidatietoestand, geometrie en coördinatie van het metaalion. Deze observaties kunnen gemaakt worden op basis van onder meer door UV-Vis, EPR en FT-IR spectroscopische metingen. Bovendien hebben we laten zien hoe de aanwezigheid van een stijgende hoeveelheid van defect-inducerende linker moleculen grotere poriën introduceert in het MOF-materiaal. Een ander gevolg is dat de kristalgrootte afneemt en deze linker ingrijpt op de thermodynamica en kinetiek van het kristallisatie- en assemblageproces. De meest opvallende bevinding kwam echter voort uit Raman-microscopie-karteringsexperimenten, die aangaven dat sommige kristallen grote hoeveelheden defecten bevatten, terwijl andere kristallen het ideale raamwerk lijken te zijn (en dus geen defecten bezitten). Dit is eerder gemeld voor andere materialen (bijvoorbeeld

aluminiumzonering in zeolieten) en kan interessant zijn voor s onderzoekers om nieuwe strategieën te ontwikkelen om MOF-materialen te modificeren.

Met hetzelfde MOF-materiaal, namelijk HKUST-1, hebben we in **Hoofdstuk 6** een gastmolecuul geïntroduceerd voor het genereren van wat bekend staat als een *gast@MOF*-composiet. Het molecuul, bekend als 7,7,8,8-tetracyanoquinodimethaan (TCNQ), kan de geleidbaarheid van elektrische stroom door de poriën van dit MOF-materiaal met verschillende grootte-ordes verhogen. Het is dus belangrijk om de positie van dit molecule in de poriën van afzonderlijke HKUST-1 kristallen te bepalen. Hiertoe hebben we Raman-microscopie-experimenten uitgevoerd en gebruik gemaakt van geavanceerde gegevensverwerking, waaronder principale componentenanalyse (PCA). Deze methodiek toonde aan dat de TCNQ-moleculen zich meestal aan de randen van de poriën bevinden en bevestigden wat andere onderzoeksgroepen al meldden (dat het onzuiverheden van een $Cu_x(TCNQ)_y$ coördinatiepolymeer vormt). Vervolgens hebben we het effect van water op het *gast@MOF*-composiet materiaal onderzocht. Eerst hebben we onderzocht of TCNQ in de poriën deze kan blokkeren en de diffusie van waterdamp door het MOF-materiaal kan beïnvloeden. Hiervoor hebben we *in-situ* FT-IR-microscopie gebruikt. Daarnaast hebben we de locatie van TCNQ in het MOF-materiaal na het behandelen met waterdamp geanalyseerd. We konden aantonen dat er een herverdeling van de moleculen over de kristallen plaatsgrijpt. Ten slotte hebben we de effecten van herverdeling en water op de elektrische geleidbaarheid van het *gast@MOF*-composiet materiaal onderzocht.

Tot slot hebben we in **Hoofdstuk 7** de belangrijkste wetenschappelijke bevindingen van dit Proefschrift samengevat. Dit hebben we gedaan door voor elk van de hoofdstukken de hoofdobservaties en bijhorende conclusies te formuleren. Ook worden mogelijke onderzoekslijnen voor de toekomst beschreven, inclusief de ontwikkeling van hulpmiddelen, meettechnieken of MOF-materialen als nieuwe katalysatoren.

ACKNOWLEDGEMENTS

The completion of this PhD thesis has been only possible thanks to many people who have contributed in different ways, not only with experiments or scientific talks. A famous Castilian proverb says: "... es de bien nacido, el ser agradecido"; so, I would like to express my gratitude to all those people.

First, I would like to thank my supervisor Prof. Bert Weckhuysen for giving me the opportunity to carry out this research in his group. The courses, conferences, seminars, workshops and lectures in catalysis, kinetics and spectroscopy to which I had the chance of attending thanks to the funding (in- and outside the ICC) throughout the PhD have been invaluable.

Moreover, I would like to thank the reading committee: **Prof. Pascal van der Voort** (U. Gent), **Prof. Bert Klein Gebbink** (UU), **Prof. Monique van der Veen** (TU Delft), **Prof. Maarten Roeffaers** (KU Leuven) and **Prof. Pieter Bruijnincx** (UU) for taking the time to evaluate my thesis and oppose me at the defence ceremony.

The journey to complete this PhD thesis starts much earlier than May 2015, since much of the chemistry involved comes from people who encouraged me with inspiring lectures (and effort that is less appreciated than research very often) to follow this pathway. If I continued my chemistry studies, it was thanks to **Prof. Rafael López Fernández** (Química-Física, Universidad Autónoma de Madrid – UAM), **Prof. Pilar Ocón Esteban** (Química-Física Aplicada, UAM), **Prof. Vicente Fernández Herrero** (Dpto. Química Inorgánica, UAM), **Prof. José Antonio Pérez López** (Dpto. Química Analítica y Análisis Instrumental, UAM) and **Dr. Juan Rubio** (ICV-CSIC) whose efforts and interest in transmitting their knowledge in chemistry. Also **Prof. Yves Holl** (ECPM – ICS) in Strasbourg, with his lessons on polymer physics. They are the people who sparked my curiosity and fascination for chemistry and physics. I also want to mention people who were involved in my formation in one or another way, such as **Olivier Fleischel, Lucía Jiménez García** and **Matthias Schwab**, who have been always there offering support.

Chapters 3 and 5 of this PhD thesis are the direct result of the collaboration with the **Prof. Roland A. Fischer** (Technische Universität München, TUM), and the excellent researchers of his group. I would like to thank him for hosting me during 5 months at his group where I learnt a great deal of synthesis and organometallic chemistry. The help and support given by **Konstantin (you are my modern-everyday-BvB hero)**, **Christian, Stefano, Pia, Werner, David, Julius, Katy, Dardan, Lisa** (and others that I probably forgot), as well as the amazing beers, parties in München and the trips to New Zealand and Raitenhaslach (including **Romy Ett!**).

Apart from Germany, I traveled to many other places I never thought I would have the chance to, and got a great deal of support in MOF science by the whole DEFNET (and friends) crew, specially **Paul, Carlos, Chiara, Julianna, Collin** (great trip to Singapore), **Emily and Rifan** (whose help resulted in part of Chapter 3). I would also like to thank **Prof. Philip Lewellyn** and **Dr. Vanessa Coulet** (both from Uni. Aix Marseille, for their help with gas sorption), **Prof. Dirk de Vos** (for hosting me at KU Leuven) and **Dr. Xesc Llabrés i Xamena** (ITQ, Valencia, for the great talks) and everyone who carried forward the DEFNET program.

Other people who directly contributed to this PhD thesis are my 'daily' supervisors, **Dr. Florian Meirer** and **Dr. Matthias Filez**, who were always willing to share their scientific knowledge and moved forward many of the experiments, data or writing involved in this PhD thesis. I wish you both all the best in your future that I am sure will lead to great spectroscopy in the future. I would also like to include **Prof. Krijn de Jong**, that allowed me to collaborate in experiments not reflected in this PhD thesis, but that surely helped me in better understanding MOFs (as well as the catalyst synthesis course, that I could attend), chemistry and more importantly - kindness; **Prof. Pieter Bruijnincx**, who was always willing to help out and share some knowledge.

Obviously, the list of people from the ICC group who contributed one way, or another is nearly endless, so I would like to thank every past or present member who helped me with chemicals, experiments, scientific discussions or just chatting with a coffee. Among all, I want to specially thank **Ilse, Koen** and Beatriz Seoane for their help during the beamtrip to Stanford (and other parts of MOF research in the case of Bea); **Paul Pletcher**

and **Maarten Jongkind**, you own Chapter 4 of this thesis; **Ewout van der Feltz**, you mostly own Chapter 6; and **Laurens Atteveld, Charles Fabrie, Youri Huijzer** and **Danny Kroon, Robby van der Pluijm, Philipp Dolata, Nicolette Maaskant and Guido de Reijer**, your help with experiments during your bachelor and master projects was very needed. **Gareth**, I am still trying to measure gas sorption on those extrudates so we can publish it! I would like to particularly mention the technical and the support staff (**Fouad, Ad VdE, Ad Mens, Oscar, Pascal, Jan Willen, Dennie, Herrick, Marjan, Iris, Dymph, Belén and Monique Lamers** - I will never forget your help with the DEFNET workshop).

As they always say, a PhD thesis resembles a roller-coaster, and in my case, it was not different. If I finished it, it was also thanks to the support of many friends to whom I would like to express my gratitude (please excuse me if I forget someone, but I think you all know how grateful I am to you guys!).

All the people I met through this entire journey: **Dimitrije, Joe Stewart, Zoran, Jovana, Baira, Martin Oschatz, Zafer, Peter Ngene, Roy, Gang, Peter Bramwell, Tom Van Deelen, Yann LeBrech, Jessi Van der Hoeven, Ramon, Özgun, Joel, Nazila, Marisol, Charlotte, Micha Roelofs, Chris Lancefield, Ana, Ara, Hector, Dani del Monte, Sara García, Jeroen, Lisette, Katinka, Abhishek, Jogchum, Thomas Gaudisson, Bas, Romy, Remco, Petra, Iris, Anna-Eva, Fabianne, Wirawan, Sam, Robin, Hongyu (thanks for the photos!), Khaled, Romy, Jo(g)ch(u/e)m**, and so many other people that I hope will forgive me for forgetting to mention them, but for sure did a lot!

Por supuesto, hay mucha otra gente que me han hecho sentir más cerca de casa durante este tiempo. **Vero, Cristina, Laura, Nerea**, ¡espero que podamos seguir viéndonos estemos donde estemos!; **José, Gonzalo y Alex**, me hicisteis buena persona y mejor químico en Estrasburgo; **Fede, Yus, Alba, Mars Bello**, seguid siendo como sois y cuidando de Tres Cantos (o Dresden, o Friedreichshafen, o Livermore) para cuando vuelva. Gracias a la banda de **La Cosa Nostra** y la de **Los Que Solían Salir**; que siempre encontráis tiempo para verme, aunque vaya a España sin avisar.

Inés González y Laurens it was great to meet you and hope you will have a great life here in Utrecht! To **Ina, Sang-Ho, Pasi, Lee, Fang Liu, Max, Kordula, Christia, Pierre, Rozbeh, Francesco, Michael, Rafael, Joris K., Savannah, Giorgio, Laura Barberis, Laura de Kort, Robert Geitner**: Thank you all for the great discussions, parties, games, beers and nights out; you literally changed my life some of those nights.

Thomas Hartman, thanks so much for the amazing cover and good times!

Rolf, Lennart, Katerina, Stano, José, Xinwei, Justine, thank you for dealing with me on a daily basis and teaching me a lot of chemistry, catalysis, spectroscopy (and so much more); **Laurens MdK**, keep the MOF banner flying high, thanks for the scientific chats!, you rocked my world.

Claudine, le Chapitre 4 est dédié à toi et comme je te l'ai déjà dit s'est basé sur tes publis. Tu es sûrement une des personnes les plus gentilles, affectueuses et loyales que je n'ai jamais rencontré. Tu sais bien que rien de ça n'aurait pas été possible sans toi, sans ton support et ton aide, et une grosse partie de cette thèse t'appartient.

Juanjo, ya sabes que me has mantenido cuerdo una gran parte de la tesis, y que de mayor quiero ser como tú.

Mr. Fu, we have been to war together and survived to tell everyone about it! **Kang**, every Chinese person should be like you! the **Dutchbasilio** gang, I hope you guys will always stay here (but wherever you are you will never get rid of me), thank you for taking care of me all this time; **Carlos**, nunca habría entendido bien este país de no ser por ti;

Bea, ya sabes cuánto te admiro y todo lo que te debo; gracias por todo durante estos cuatro años.

Y sobre todo gracias a **mi familia**, que me quieren, me apoyan y me ayudan allí donde voy y con cualquier cosa que hago. A vosotros os corresponde también una parte muy grande de la tesis. Probablemente, dos de las frases que más me han marcado en la vida las han dicho, mi padre - ¡Hijo, no seas membrillo, saber por saber es algo bueno!; y mi madre - Hijo, tu haz lo que quieras que te vamos a querer igual -.

Appendix A. Scientific Publications and Presentations at Conferences

A.1. Scientific Publications

- 1. "Metal-Organic Frameworks as Catalyst Supports: Influence of Lattice Disorder on Metal Nanoparticle Formation"**, M. Rivera-Torrente, M. Filez, R. Hardian, E. Reynolds, B. Seoane, M. -V. Coulet, F. E. Oropeza Palacio, J. P. Hofmann, R.A. Fischer, A. L. Goodwin, P. L. Llewellyn, B. M. Weckhuysen, *Chem. Eur. J.* **2018**, 24, 7498-7506.
- 2. "Ethylene Polymerization over Metal-Organic Framework Crystallites and the Influence of Linkers on their Fracturing Process"** M. Rivera-Torrente, P. D. Pletcher, M. K. Jongkind, N. Nikolopoulos, B. M. Weckhuysen, *ACS Catal.* **2019**, 9, 3059–3069.
- 3. "HKUST-1 Metal-Organic Framework Crystals Loaded with Tetracyanoquinodimethane: Effects of Water on Host-Guest Chemistry and Electrical Conductivity"**, M. Rivera-Torrente, M. Filez, C. Schneider, E. C. van der Feltz, K. Wolkersdörfer, D. H. Taffa, M. Wark, R. A. Fischer, B. M. Weckhuysen, *Phys. Chem. Chem. Phys.* **2019**, 21, 25678-25689.
- 4. "Spectroscopic Bird's Eye of Metal-Organic Frameworks: from Synthesis to Applications"**, M. Rivera-Torrente, B. Seoane, M. Filez, L. D. B. Mandemaker, G. Delen, F. Meirer, B. M. Weckhuysen, *Chem. Soc. Rev.* **2020**, *in preparation*.
- 5. "Micro-Spectroscopic Interrogation of Defect-Engineered Cu₃(BTC)_{2-x}(CYDC)_x Metal-Organic Framework Crystals"**, M. Rivera-Torrente, M. Filez, F. Meirer, B. M. Weckhuysen, *Chem. Eur. J.* **2020**, 26, - 10.1002/chem.201905645.

A2. Oral and Poster Presentations at Conferences

1. "**Impact of Transition Metal Promoters on the MOF-Mediated Synthesis of Solid Cobalt Catalysts: Implications in Syngas Conversion**" Poster presentation at Europacat 2019 (Aachen, Germany, August 2019).
2. "**Critical Impact of Transition Metal Promoters on the MOF-Mediated Synthesis of Solid Cobalt Catalysts: Implications in Syngas Conversion**" Oral presentation at Netherlands Catalysis and Chemistry Conference XX (Noordwijkerhout, The Netherlands, March 2019).
3. "**Critical Impact of Transition Metal Promoters on the MOF-Mediated Synthesis of Solid Cobalt Catalysts: Implications in Syngas Conversion**" Oral presentation at International MOF 2018 (Auckland, New Zealand, December 2018).
4. "**Micro-spectroscopic Interrogation of the Defect-linker Distribution in HKUST-1 Crystals**", Oral presentation at EuroMOF 2017 (Delft, The Netherlands, November 2017).
5. "**MOF Supported Metal Catalysts: Defects Tune Nanoparticle Size**", Oral presentation at Netherlands Catalysis and Chemistry Conference XVIII (Noordwijkerhout, The Netherlands, March 2017).
6. "**Au/MIL-53-Al-catalyzed Dehydrogenation of Formic acid: Role of Defects in a MOF Support**", Oral presentation at DEFNET Workshop in Defect-Network Porous Materials (Gent, Belgium, 2016).

A3. Other Publications by the Author

1. "**Increasing the Availability of Active sites in Zn-Co Double Metal cyanides by Dispersion onto a SiO₂ Support**", C. Márquez, M. Rivera-Torrente, P. P. Paalanen, B. M. Weckhuysen, F. G. Cirujano, D. De Vos, T. De Baerdemaeker, *J. Catal.* **2017**, 354, 92-99.
2. "**Impact of Niobium Promoter on the MOF-Mediated Synthesis of Cobalt Catalysts: Implications in Syngas Conversion**" M. Rivera-Torrente[†], C. Hernández Mejía[†], T. Hartman, K. P. de Jong, B. M. Weckhuysen, *Catal. Lett.* **2019**, 149, 3279-3286; [†], equally contributing first authors.

-
- 3. "Nanoweb Surface-Mounted Metal-Organic Framework Films with Tunable Amounts of Acid Sites as Tailored Catalysts"** L. D. B. Mandemaker, M. Rivera-Torrente, G. Delen, J. P. Hofmann, M. Lorenz, A. Belianinov, B. M. Weckhuysen, *Chem. Eur. J.* **2020**, 26, 691–698.
- 4. "Effects of Extrusion in MOFs as Porous Functional Materials for Gas Sorption"** M. Rivera-Torrente, D. Kroon, R. Hardian, C. Márquez, N. Nikolopoulos, M. -V. Coulet, D. de Vos, P. L. Llewellyn, G. Whiting*, B. M. Weckhuysen*, *in preparation*
- 5. "Effects of Pore Size, Topology and Substituents in Cr-MOFs as Catalysts in Ethylene Polymerization"** M. K. Jongkind, M. Rivera-Torrente, B. M. Weckhuysen*, *in preparation*
- 6. "Visualization of Pore Architecture and Defects in Metal-organic Frameworks: Effects on Permeability and Diffusion"**, M. Rivera-Torrente[†], R. Mayorga González[†], N. Nikolopoulos, K. W. Bossers, J. Yus, B. Ferrari, F. Meirer*, B. M. Weckhuysen*, *in preparation*; [†], equally contributing first authors.

Appendix B. List of Abbreviations

ACN	Acetonitrile
AES	Auger Emission Spectroscopy
AFM	Atom Force Microscopy
ALD	Atomic Layer Deposition
BAS	Brønsted Acid Site
BEA	Zeolite β Framework
BET	Brunnauer-Emmett-Teller
BINAP	2,2'-Bis(diphenylphosphino)-1,1'-binaphthyl
BINOL	[1,1'-Binaphthalene]-2,2'-diol
BJH	Barrett-Joyner-Halenda
BSE	Back-Scattered Electrons
BTC	1,3,5-Benzenetricarboxylate / 1,3,5-Benzenetricarboxylic acid
CCD	Charge Coupled Device
CFM	Confocal Fluorescence Microscopy
CFSE	Crystal Field Splitting Energy
CFT	Crystal Field Theory
CHA	Chabazite Framework Structure
CP	Coordination Polymer
CPC	Coordination Polymer Compound
CUS	Coordinatively Unsaturated Site
CVD	Chemical Vapor Deposition
CVE	Cumulative Variance Explained
CVI	Chemical Vapor Infiltration
CYDC	5-Cyano-1,3,-benzenedicarboxylate/5-Cyano-1,3,-benzenedicarboxylic acid
DEA	Diethyl Aluminum Chloride
DFT	Density Functional Theory
DMF	N-N-Dimethylformamide
DMSO	Dimethyl sulfoxide
DRIFTS	Diffuse Reflectance Infrared Fourier Transform Spectroscopy
DRS	Diffuse Reflectance Spectroscopy

DR	Diffuse Reflectance
DSC	Differential Scanning Calorimetry
DTGS	Deuterated-Triglycine Sulfate
EDX	Energy Dispersive X-ray Spectroscopy
EIS	Electrochemical Impedance Spectroscopy
ENDOR	Electron Nuclear Double Resonance
(CW) EPR	(Continuous Wave) Electron Paramagnetic Resonance
ESI-MS	Electrospray Ionization-Mass Spectrometry
(N)EXAFS	(Near Edge) Extended X-ray Absorption Fine Structure
FAU	Faujasite Framework Structure
FeBTC	Iron (III, II) 1,3,5-benzenetricarboxylate
FER	Ferrierite Framework Structure
GPC	Gel-Permeation Chromatography
HDPE	High Density Polyethylene
HETCOR	2D Heteronuclear Chemical-Shift Correlation
HKUST	Hong Kong University of Science and Technology
HPLC	High-Performance Liquid Chromatography
HYSCORE	Hyperfine Sublevel Correlation
ICP-AES	Inductively Coupled Plasma-Atomic Emission Spectroscopy
INS	Inelastic Neutron Scattering
IR	Infrared
(FT)-IR	Fourier-Transform Infrared
IWI	Incipient Wetness Impregnation
LAS	Lewis Acid Site
LFT	Ligand Field Theory
LFSE	Ligand Field Splitting Energy
LMCT	Ligand-to-Metal Charge Transfer
(CP) MAS	Cross Polarization Magic Angle Spinning
MCM	Mobil Composition of Matter
MCT	Mercury Cadmium Telluride
MFI	Melt Flow Index

MFI	Mobil Five Framework Structure
MIL	Matériaux de l'Institut Lavoisier
MOF	Metal-Organic Framework
MOR	Mordenite Framework Structure
MOT	Molecular Orbital Theory
MTN	Mobil Thirty-Nine Framework Structure
MTV(-MOF)	Multivariate Metal-Organic Framework
NA	Numerical Aperture
NLDFT	Non-Local Density Functional Theory
NMR	Nuclear Magnetic Resonance
NPD	Neutron Powder Diffraction
NU	Northwestern University
PCA	Principal Component Analysis
PCP	Porous Coordination Polymer
PDF	Pair Distribution Function
PDI	Polydispersity Index
PMT	Photomultiplier
PSD	Particle Size Distribution
PTFE	Polytetrafluoroethylene (Teflon®)
PW	Paddle-Wheel
PYDC	3,5-Pyridinedicarboxylate / 3,5-Pyridinedicarboxylic acid
(S)RESPDOR	(Symmetry)-based Resonance-Echo Saturation-Pulse Double-Resonance
SAM	Self-Assembled Monolayer
SAXS	Small-Angle X-ray Scattering
SBA	Santa Barbara Amorphous
SBU	Secondary Building Unit
SEM	Scanning Electron Microscopy
STP	Standard Temperature Pressure (101.325 kPa, 273.15 K)
SURMOF	Surface Mounted Metal-Organic Framework
TCNQ	7,7,8,8-Tetracyanoquinodimethane
TDS	Thermal or Temperature Desorption Spectroscopy

TEM	Transmission Electron Microscopy
TFA	Trifluoroacetic Acid
TGA	Thermogravimetric Analysis
THF	Tetrahydrofuran
TOF	Turnover Frequency
TXM	Transmission X-ray Microscopy
UHMWPE	Ultra-High Molecular Weight Polyethylene
UHV	Ultra-High Vacuum
UiO	Universitetet i Oslo Framework Structure
UV-Vis	Ultraviolet-Visible
UV-Vis-NIR	Ultraviolet-Visible-Near Infrared
WAXS	Wide-Angle X-ray Scattering
XANES	X-ray Absorption Near the Edge Spectroscopy
XAS	X-ray Absorption Spectroscopy
(AP) XPS	(Ambient Pressure) X-ray Photoelectron Spectroscopy
(P)XRD	Powder X-ray Diffraction
XRF	X-ray Fluorescence Spectroscopy
ZIF	Zeolitic Imidazolate Framework

ABOUT THE AUTHOR

Miguel Rivera Torrente was born on the 24th of November 1991, in Madrid, Spain. He started bachelor studies in Chemistry at the Universidad Autónoma de Madrid (UAM) in 2009. In 2012, he received an Erasmus scholarship to continue his studies at the École de Chimie, Polymères et Matériaux (ECPM) – Université de Strasbourg, in France; for two years. In this time, he graduated with a BSc thesis entitled "Sol-Gel Methods for the Synthesis of High-Refractive Index Layers in Commercial OLEDs", for his work carried out at AGC Europe S.A., in Charleroi, Belgium. A year later he obtained his MSc in Chemical Engineering with a thesis entitled "New Downstream Melamine Chemistry", for his work carried out at BASF SE in Ludwigshafen, Germany. Thereafter, he spent six months as a "Wissenschaftlicher Mitarbeiter" at the RWTH Aachen University in Germany, working on the chemistry of isocyanates under the supervision of prof. Walter Leitner. In 2015, he started working on the chemistry and characterization of defects in Metal-Organic Frameworks (MOFs) for catalysis and gas sorption at Utrecht University, The Netherlands, under the supervision of prof. Bert Weckhuysen. The research was funded by the European Union Horizon 2020 research and innovation program under the Marie-Sklodowska-Curie grant agreement 641887 (DEFNET) and the Netherlands Center for Multiscale Catalytic Energy Conversion (MCEC). The results of the research are described in this PhD thesis and were disseminated as oral or poster presentations at several national and international conferences.



